OCTOBER 1, 1989

Analytical CHEMISTRY

Carbon-13 NMR Spectral Simulation

1115 A

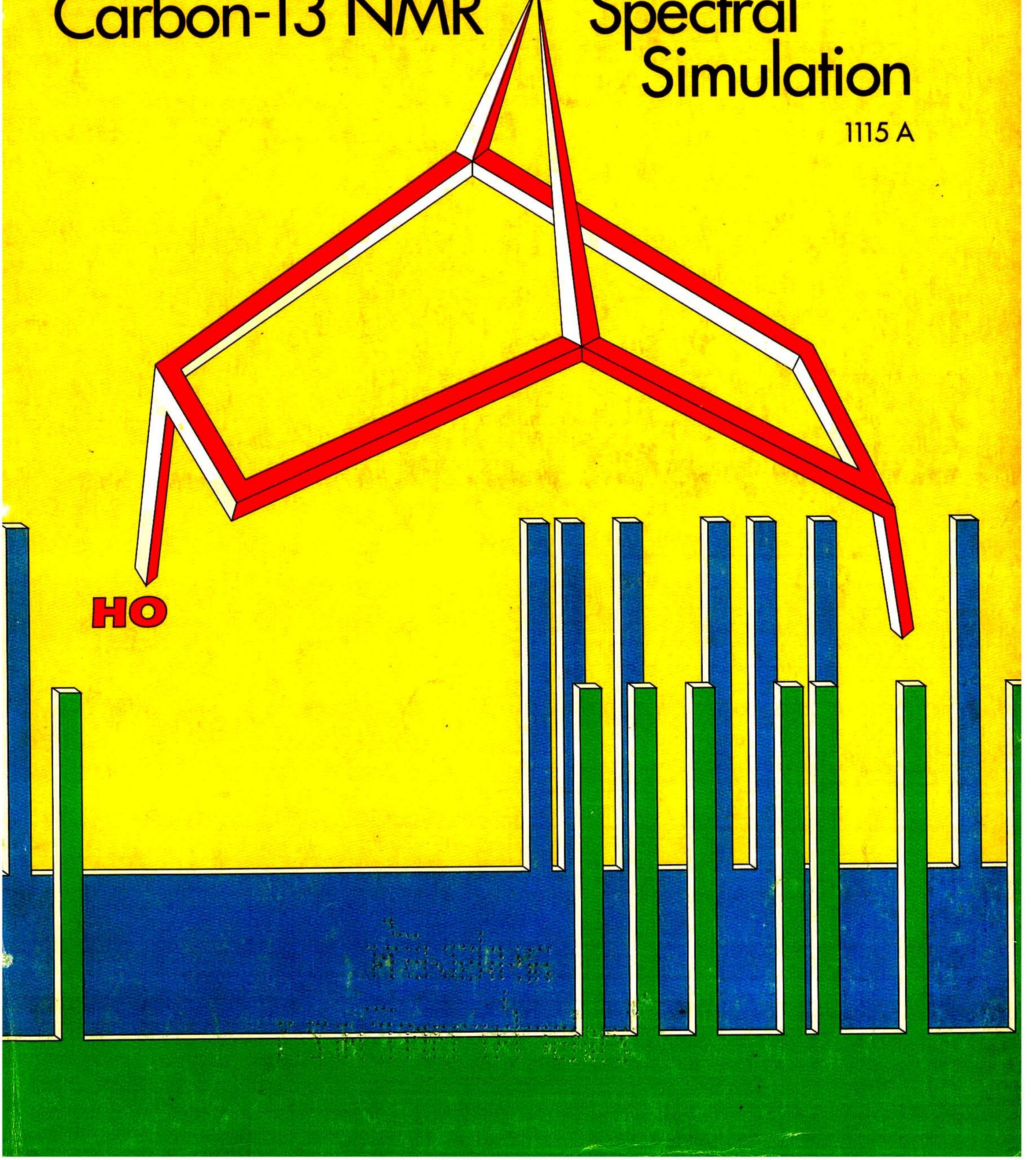

We Take Great Ideas…
& Make Them Even Better.™

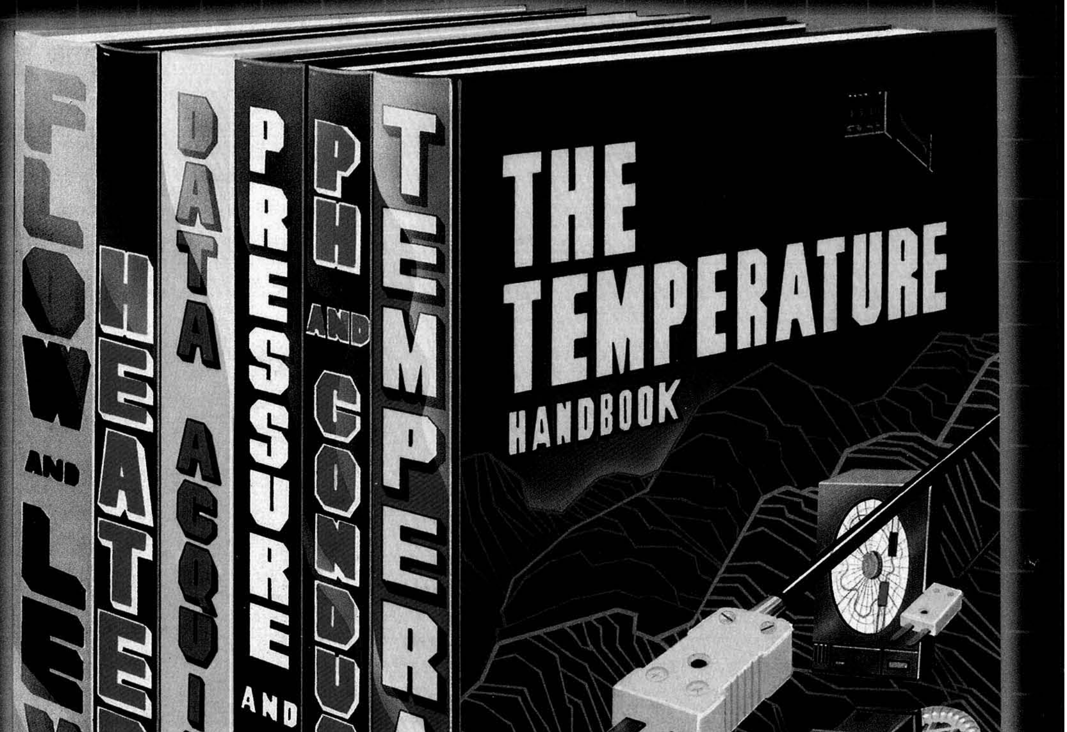
FLOW AND LEVEL
HEATERS
DATA ACQUISITION
PRESSURE AND STRAIN
PH AND CONDUCTIVITY
TEMPERATURE
THE TEMPERATURE HANDBOOK
OMEGA
AN OMEGA GROUP
7.632

OVER 3500 FULL
COLOR PAGES.

NEW! FREE!
NOW HARDBOUND!
The 1990/91 OMEGA
Complete Measurement
and Control Handbooks
& Encyclopedias®

OMEGA
An OMEGA Technologies Company
ne Omega Drive, Box 4047, Stamford, CT 06907
elex 996404 Cable OMEGA FAX (203) 359-7700
sk For Your FREE Qualification Form!
IAL (203) 359-RUSH
(203) 359-7874

COPYRIGHT 1989 OMEGA ENGINEERING, INC. ALL RIGHTS RESERVED

CIRCLE 120 ON READER SERVICE CARD

Now GC detection is more elemental.

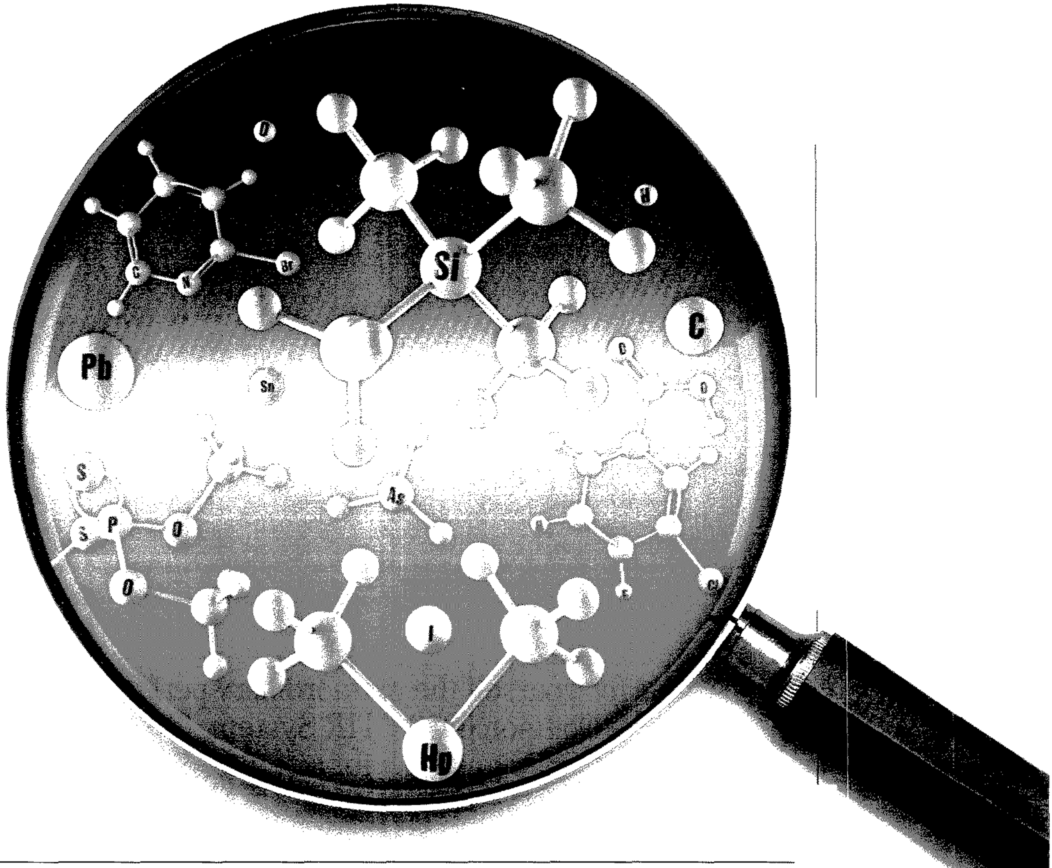

HP's new benchtop atomic emission detector enables you to selectively identify multiple elements in GC effluents. Even some that were previously difficult or impossible to detect. Like carbon. And organometallics. And it's the first GC detector to perform both qualitative *and* quantitative analysis of oxygen.

What's more, up to four elements may be simultaneously detected from a single injection. And sequencing through any number of elements is performed automatically. To confirm MSD or IRD library searches, HP's AED provides elemental information, with the convenience of single-instrument setup.

Ask for a free brochure on this exciting new product. Just call **1 800 556-1234, Ext. 10213.** In California, call **1 800 441-2345, Ext. 10213.**

HEWLETT
PACKARD

© 1989 The Hewlett-Packard Company
AG04905

CIRCLE 65 ON READER SERVICE CARD

COMPARE FTIR PERFORMANCE & PRICE

Mattson's Galaxy 6020® FTIR System offers you more.

Proof that a better-run company can afford to develop innovative products and competitive prices.

Features & Capability	**Mattson 6020**	Perkin Elmer 1760	Nicolet 510	Nicolet 800	Digilab FTS-40
Cube Corner Interferometer	**Yes**	No	No	No	No
Modern User Interface including mouse	**Yes**	No	No	No	No
High Precision 96 bit FFT	**Yes**	No (32 Bit)	No (20 Bit)	No (20 Bit)	No (32 Bit)
Macros	**Yes**	?	Yes	Yes	?
Precision Scan Reference (quadrature)	**Yes**	Yes	No	Yes	No
Sealed Interferometer	**Yes**	Yes	No	No	No
19 Bit ADC	**Yes**	No (16 Bit)	?	No (18 Bit)	Yes
Multi-Component Quantitative Analysis	**Yes**	Yes	Yes	Yes	Yes
Sadtler Libraries	**Yes**	Yes	No	No	Yes
MS-DOS Compatibility †	**Yes**	Third Party	No	No	No
UNIX Compatibility †	**Yes**	No	No	No	Third Party
Macintosh Compatibility †	**Yes**	No	No	No	No
Price	**$27,000**	$45,000*	$30,000*	$80,000*	$40,000*

* Product Comparisons are based on sales information and competitive bid situations. Prices and features may vary significantly with individual negotiations. Please contact vendors directly for more specific information.

† Compatibility meaning primary spectrometer control and data acquisition without intermediate data conversions or alternate operating systems.

See for yourself the extraordinary performance of the Mattson 6020 FTIR System. Then call us for a demo. We'll have a Galaxy 6020 up and running in your lab in 5 minutes.

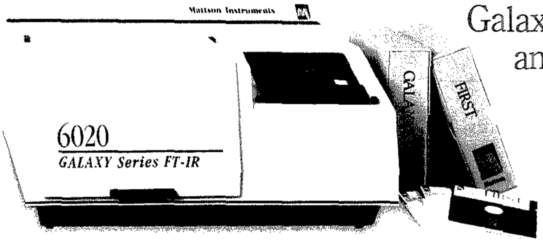

Mattson Instruments, Inc.
1001 Fourier Drive
Madison, WI 53717 U.S.A.
Tel. (608) 831-5515
Fax: (608) 831-2093

Mattson Instruments, Ltd.
Green Farm Road
Newport Pagnell
Bucks MK16 0AL
England
Tel. (44) 908 211414
Fax: (44) 908 618292
Telex: 82304 FORUM G

Mattson

CIRCLE 94 ON READER SERVICE CARD

OCTOBER 1, 1989
VOLUME 61
NUMBER 19

The Audit Bureau
ANCHAM
61(19) 1065A–1124A/2129–2224 (1989)
ISSN 0003-2700

Registered in U.S. Patent and Trademark Office;
Copyright 1989 by the American Chemical Society

ANALYTICAL CHEMISTRY (ISSN 0003-2700) is published semimonthly by the American Chemical Society at 1155 16th St., N.W., Washington, DC 20036. Editorial offices are located at the same ACS address (202-872-4570; FAX 202-872-6325; TDD 202-872-8733). Second-class postage paid at Washington, DC, and additional mailing offices. Postmaster: Send address changes to ANALYTICAL CHEMISTRY Member & Subscriber Services, P.O. Box 3337, Columbus, OH 43210.

Claims for missing numbers will not be allowed if loss was due to failure of notice of change of address to be received in the time specified; if claim is dated (a) North America: more than 90 days beyond issue date, (b) all other foreign: more than one year beyond issue date, or if the reason given is "missing from files."

Copyright Permission: An individual may make a single reprographic copy of an article in this publication for personal use. Reprographic copying beyond that permitted by Section 107 or 108 of the U.S. Copyright Law is allowed, provided that the appropriate per-copy fee is paid through the Copyright Clearance Center, Inc., 27 Congress St., Salem, MA 01970. For reprint permission, write Copyright Administrator, Publications Division, ACS, 1155 16th St., N.W., Washington, DC 20036.

Registered names and trademarks, etc., used in this publication, even without specific indication thereof, are not to be considered unprotected by law.

Advertising Management: Centcom, Ltd., 500 Post Rd. East, Westport, CT 06880 (203-226-7131)

1989 subscription rates include air delivery outside the U.S., Canada, and Mexico

	1 yr	2 yr
Members		
Domestic	$ 27	$ 45
Canada and Mexico	56	103
Europe	83	157
All Other Countries	120	231
Nonmembers		
Domestic	49	83
Canada and Mexico	78	141
Europe	155	280
All Other Countries	192	354

Three-year and other rates contact: Member & Subscriber Services, ACS, P.O. Box 3337, Columbus, OH 43210 (614-447-3776 or 800-333-9511).

Subscription orders by phone may be charged to VISA, MasterCard, Barclay card, Access, or American Express. Call toll free 800-ACS-5558 in the continental United States; in the Washington, DC, metropolitan area and outside the continental United States, call 202-872-8065. Mail orders for new and renewal subscriptions should be sent with payment to the Business Management Division, ACS, P.O. Box 57136, West End Station, Washington, DC 20037.

Subscription service inquiries and changes of address (include both old and new addresses with ZIP code and *recent mailing label*) should be directed to the ACS Columbus address noted above. Please allow six weeks for change of address to become effective.

ACS membership information: Lorraine Bowlin (202-872-4567)

Single issues, current year, $7.00 except review issue and LabGuide, $12.00; **back issues and volumes and microform editions** available by single volume or back issue collection. For information or to order, call 800-ACS-5558 or write the Microform & Back Issues Office at the Washington address.

Nonmembers rates in Japan: Rates above do not apply to nonmember subscribers in Japan, who must enter subscription orders with Maruzen Company Ltd., 3–10 Nihonbashi 2-chome, Chuo-ku, Tokyo 103, Japan. Tel: (03) 272-7211.

ANALYTICAL® CHEMISTRY

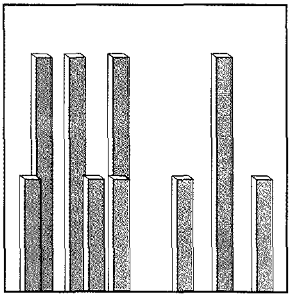

A/C INTERFACE 1115 A

***On the cover.* Carbon-13 NMR spectral simulation** is based on the existence of a direct yet complex relationship between the observed chemical shift of a carbon atom and its chemical environment. Peter C. Jurs and co-workers at The Pennsylvania State University discuss various simulation approaches and their implementation, and predict future research directions

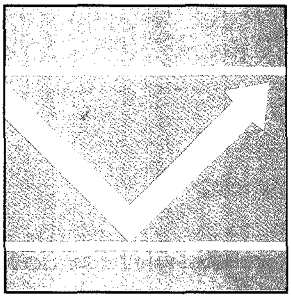

INSTRUMENTATION 1079 A

Waveguides as chemical sensors. The small size, flexible geometry, ability to channel light over long distances, and noise immunity of waveguides make them ideal for remote sensing, clinical applications, environmental monitoring, and process control. Raymond E. Dessy of Virginia Polytechnic Institute and State University reviews how waveguides work and presents current applications

BRIEFS 1068 A

EDITORIAL 1075 A

Near field scanning optical microscopy. Current problems in analytical chemistry require a nondestructive, superresolution technique that can be applied to living systems and can provide morphological and spectroscopic information. This need is being addressed by near field scanning optical microscopy, which provides the spatial resolution necessary to yield information on cell membranes, organelle membranes, and DNA binding in chromosomes

NEWS 1077 A

Division of Analytical Chemistry announces undergraduate awards. ▶ **Frogs' ears** respond to molecular noise. ▶ Implantable **glucose monitor.** ▶ **Sugar-coated semiconductors** used for adhesion research

MEETINGS 1097 A

▶ Conferences. ▶ Short courses and workshops. ▶ Call for papers

FOCUS 1099 A

Scanning electrochemical microscopy. The recently developed scanning electrochemical microscope can spatially resolve electrochemical activity in situ over a surface of interest. Royce C. Engstrom and Christine N. Pharr of the University of South Dakota describe the microscope and present some of the electrochemical data collected

NEW PRODUCTS & MANUFACTURERS' LITERATURE 1110 A

AUTHOR INDEX 2129

BRIEFS

Articles

Phase Synchronization of an Ion Ensemble by Frequency Sweep Excitation in Fourier Transform Ion Cyclotron Resonance 2130

Phase angle synchronization of the ion ensemble occurs by off-resonant acceleration during frequency sweep excitation. Phase synchronization of the ion packet prior to resonant excitation results in better spatial definition of the ion packet.

Curtiss D. Hanson, Mauro E. Castro, and David H. Russell*, Department of Chemistry, Texas A&M University, College Station, TX 77843

Emission Spectrometric Determination of Manganese and Chromium in Steels with a Dual Cathode Glow Discharge Lamp 2137

Mn emission lines, measured with the sputter modulation technique, suffer no spectral interferences originating from Ar lines, indicating that the spectrometric determination of Mn can be easily achieved.

Kazuaki Wagatsuma* and Kichinosuke Hirokawa, Institute for Materials Research, Tohoku University, Katahira 2-1-1, Sendai 980, Japan

Structural Characterization of Model Polyurethanes Using Time-of-Flight Secondary Ion Mass Spectrometry 2142

The masses of repeat units, terminal groups, diisocyanate, and diol can be determined from model polyurethanes. TOF-SIMS combines good sensitivity and extensive mass range so that high molecular weight ions can be observed.

Ioannis V. Bletsos and David M. Hercules*, Department of Chemistry, University of Pittsburgh, Pittsburgh, PA 15260, **Dieter vanLeyen and Alfred Benninghoven,** Physikalisches Institut der Universität Münster, D-4400 Münster, FRG, and **Costas G. Karakatsanis and James N. Rieck,** Mobay Corporation, Pittsburgh, PA 15205

Determination of Stable Carbon and Hydrogen Isotopes of Light Hydrocarbons 2149

A system for the measurement of $^{13}C/^{12}C$ and D/H ratios on light hydrocarbons (C_1–C_3) and CO_2 is described, including the development of a gas preparation line and a special mass spectrometer inlet system.

Ingolf Dumke*, Eckhard Faber, and Jürgen Poggenburg, Federal Institute for Geosciences and Natural Resources (BGR), Hannover, FRG

Evidence for Radical Anion Formation during Liquid Secondary Ion Mass Spectrometry Analysis of Oligonucleosides and Synthetic Oligomeric Analogues: A Deconvolution Algorithm for Molecular Ion Region Clusters 2154

An isotopic deconvolution procedure is applied to the mass spectra of small DNA chains and synthetic oligonucleosides. The discrepancies between the theoretical and measured isotopic distributions are explained.

J. A. Laramée, B. Arbogast, and M. L. Deinzer*, Department of Agricultural Chemistry and the Environmental Health Sciences Center, Oregon State University, Corvallis, OR 97331

Pyruvate Carboxylase as a Model for Oligosubstituted Enzyme–Ligand Conjugates in Homogeneous Enzyme Immunoassays 2160

Pyruvate carboxylase (an enzyme that contains four covalently attached biotins) is inhibited by avidin and is used to assay biotin. Sensitive determinations are possible over a wide range of biotin concentrations.

Sylvia Daunert, Bryan R. Payne, and Leonidas G. Bachas*, Department of Chemistry, University of Kentucky, Lexington, KY 40506-0055

Contribution of Interfacial Resistance to Plate Height in Open Tubular Gas Chromatography 2165

Band broadening by interfacial resistance to mass transfer is shown to have a significant effect. At optimal gas-phase velocities, this effect may contribute four times as much to the HETP value as does the band broadening from diffusion in the liquid phase.

Agneta K. Bemgård* and Lars G. Blomberg, Department of Analytical Chemistry, University of Stockholm, S-106 91, Stockholm, Sweden and **Anders L. Colmsjö,** Department of Analytical Chemistry, National Institute of Occupational Health, S-171 84 Solna, Sweden

Separation of Styrene–Acrylate and Styrene–Methacrylate Copolymers According to Composition by Liquid Adsorption Chromatography 2171

The copolymers are separated using linear gradient elution. The adsorbent is silica gel, and the mobile phase is a mixture of chloroform and ethanol.

Sadao Mori* and Masaaki Mouri, Department of Industrial Chemistry, Faculty of Engineering, Mie University, Tsu, Mie 514, Japan

* Corresponding author

The Sartorians announce the end of an era.

Our PLUS Performance Package has put the calculator in its rightful place among scientific memorabilia. Alongside the abacus, the slide rule, and the ENIAC computer.

For, unlike other balances which merely give you the weight, ours also calculates the answer.

Now standard on many Sartorius balances, the PLUS Performance Package features a choice of three key pad overlays which activate 16 pre-programmed functions and calculations. They make check weighing, animal weighing, parts counting, formulations and other applications faster and easier than ever before. Our analytical balances will even perform molarity and normality calculations.

For more information or a free demonstration, call or write Sartorius Instruments, P.O. Box 770, McGaw Park, IL 60085, (312) 578-4297. Or contact your representative from Baxter Healthcare Corporation, Scientific Products Division, or any authorized dealer.

Unless you're just a sentimentalist.

sartorius

perfect balance.

CIRCLE 148 ON READER SERVICE CARD

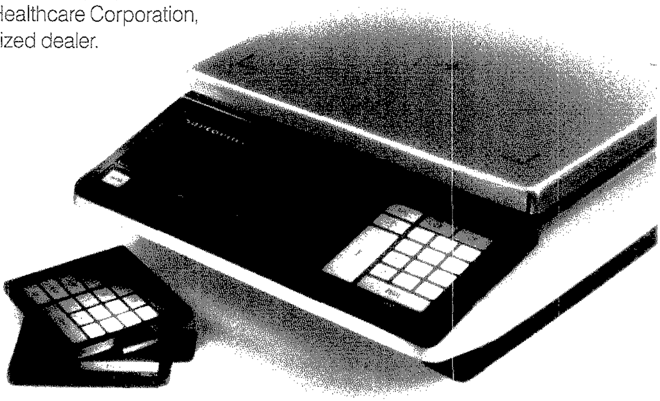

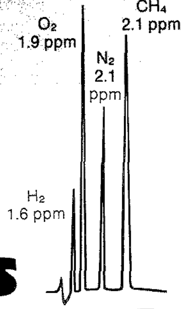

Trace Gas Analysis Down to ppb

The GOW-MAC Series 590 G.C. with Discharge Ionization Detector (DID) detects trace gas impurities in the part-per-billion (ppb) range.

- Non-radioactive, universal detector
- Extremely stable for fast and easy start-up
- Exceptionally quick recovery in the event of detector overload
- System for the analysis of corrosive samples available

The GOW-MAC Series 590 DID Gas Chromatograph is designed for the analysis of trace gas impurities with sensitivity in the part-per-billion range. Common detectable impurities include H_2, Ar, O_2, N_2, CH_4, CO, and CO_2. Ideal for specialty and electronic gas applications. The Series 590 is uniquely engineered to eliminate detector and system contamination, thus affording the utmost in detector sensitivity.

For more information write P.O. Box 32, Bound Brook, NJ 08805-0032 or call 1-201/560-0600, FAX: 1-201/271-2782.

GOW-MAC INSTRUMENT CO.
The World's Leading Manufacturer of Thermal Conductivity Detectors
CIRCLE 56 ON READER SERVICE CARD

BRIEFS

Voltammetric Reduction and Determination of Hydrogen Peroxide at an Electrode Modified with a Film Containing Palladium and Iridium 2176

The modified electrode permits the determination of 0.2–1.8 mM H_2O_2. The correlation coefficient of the calibration curve is 0.999, and the slope is 28.0 ± 0.4 μA L mmol^{-1}.

James A. Cox* and Robert K. Jaworski, Department of Chemistry, Miami University, Oxford, OH 45056

Polarographic Methods for Ultratrace Cobalt Determination Based on Adsorption–Catalytic Effects in Cobalt(II)–Dioxime–Nitrite Systems 2178

The dc and DPP currents of Co increase in the Co(II)–dioxime–$NaNO_2$ systems by as much as 3–4 orders of magnitude, permitting Co determinations with high sensitivity, precision, and selectivity.

Andrzej Bobrowski, Academy of Mining and Metallurgy, Institute of Material Science, Al. Mickiewicza 30, 30-059 Cracow, Poland

Application of a Quartz-Crystal Microbalance for Detection of Phase Transitions in Liquid Crystals and Lipid Multibilayers 2185

The phase transition from the solid to the liquid crystalline state of smectic liquid crystalline molecules or lipid multibilayers deposited on a piezoelectric quartz plate can be observed from the frequency change of the crystal.

Yoshio Okahata* and Hiroshi Ebato, Department of Polymer Chemistry, Tokyo Institute of Technology, Ookayama, Meguro-ku, Tokyo 152, Japan

Amphetamine Selective Electrodes Based on Dibenzo-18-crown-6 and Dibenzo-24-crown-8 Liquid Membranes 2189

Two sensitive and selective membrane electrodes are developed and evaluated. The average recovery is 98.7% and the mean standard deviation is 1.7% for amphetamine sulfate over the range 5 μg/mL to 4 mg/mL.

Saad S. M. Hassan* and Eman M. Elnemma, Department of Chemistry, Faculty of Science, Qatar University, Doha P.O. Box 2713, Qatar

Voltammetry in Supercritical Carbon Dioxide at Platinum Microdisk Electrodes Coated with Perfluorinated Ion-Exchange Membranes 2193

Mass transport of electroactive species to microelectrodes coated with ionically conducting films from supercritical CO_2 is examined. SFC experiments demonstrate the potential usefulness of membrane-coated microelectrodes as chromatographic detectors.

Adrian C. Michael and R. Mark Wightman*, Department of Chemistry, Indiana University, Bloomington, IN 47401

Amazing Reproducibility:

New B&J Columns for Size Exclusion GPC

Your search for a superior GPC column is over. The new Burdick & Jackson GPC Column delivers exceptional reproducibility and long-term, cost-efficient life for analysis across a wide range of polymers. With maximum pore volume and high resolution, the packings provide wider solvent compatibility, higher tolerance to water, and better temperature stability. For added assurance, *every* B&J column is performance tested. Go to the source for all your analytical GPC needs, from columns to standards to high purity solvents.

Contact
Baxter Healthcare Corporation
Burdick & Jackson Division
1953 South Harvey Street
Muskegon, MI 49442 USA.

For technical assistance, call us toll-free at 800.368.0050.

Distributed by
Baxter Healthcare Corporation
Scientific Products Division

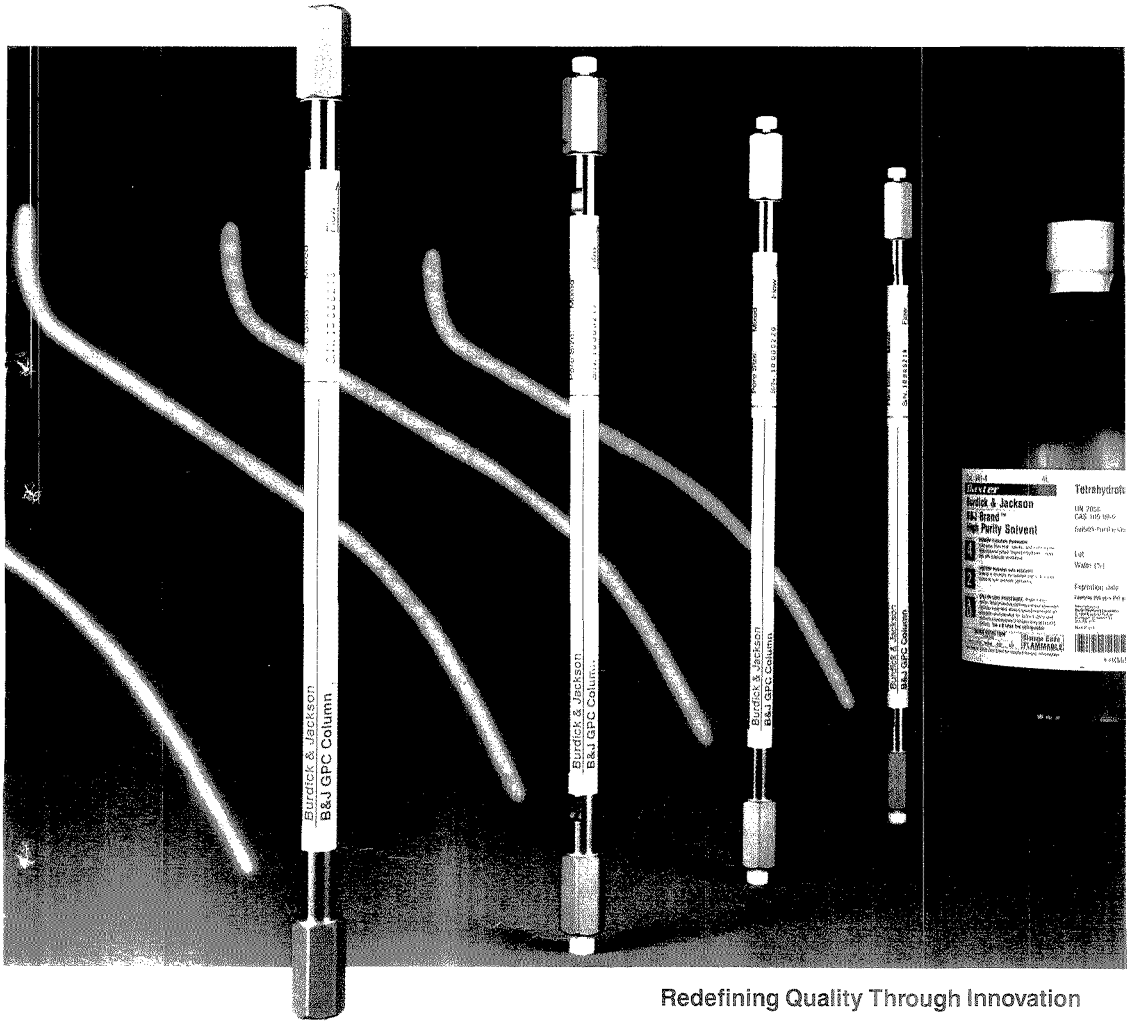
Burdick & Jackson
B&J GPC Column
Burdick & Jackson
B&J GPC Column
Burdick & Jackson
B&J GPC Column
Burdick & Jackson
B&J GPC Column
Baxter
Burdick & Jackson
B&J Brand
High Purity Solvent
FLAMMABLE

Redefining Quality Through Innovation

Baxter

© Copyright 1989. Baxter Healthcare Corporation. All rights reserved.

CIRCLE 20 ON READER SERVICE CARD

MAXIMIZE YOUR SENSITIVITY...

for Volatile Organic Compounds by Dynamic Headspace Concentration

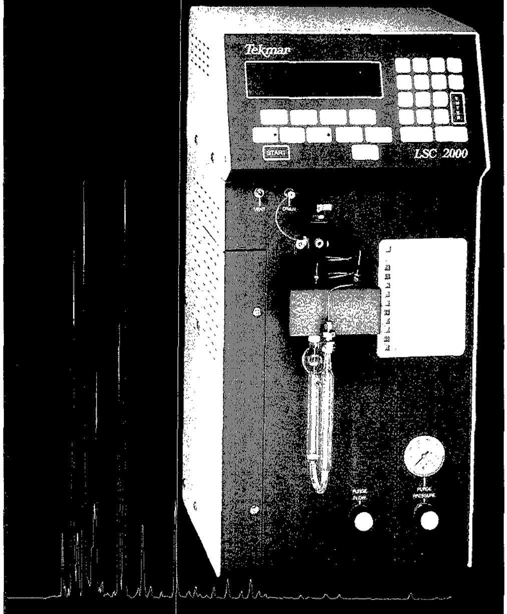

5 ml **Coffee** on Tekmar's LSC 2000 and Capillary Interface

Flavor/Fragrance
Competitive Analysis
Off Flavor/Odor Analysis
Packaging Materials
Pharmaceuticals/Residual Solvents
Building Products/Outgassing Studies
Polymers
Residual Monomers/Solvents

Ask for our FREE bibliography of reprints on a wide range of applications

P.O. Box 371856 • Cincinnati, OH 45222-1856
(800) 543-4461 Sales • (800) 874-2004 Service
Fax (513) 761-5183 • Telex 21-4221

CIRCLE 156 ON READER SERVICE CARD

BRIEFS

Enzyme Dual-Electrode for Analyte Determination 2200

The advantages of a dual microband electrode for biochemical electroanalysis are discussed. Responses of electrodes with different interelectrode space are compared. In the generation–collection mode, glucose is detected up to a concentration of 8 mM.

H. Allen O. Hill*, Naphthali A. Klein, Ioanna S. M. Psalti, and Nicholas J. Walton, Inorganic Chemistry Laboratory, South Parks Road, Oxford OX1 3QR, England

Molecular Formula Determination of Capillary Column Gas Chromatographic Effluents Using Combined Microwave-Induced Plasma Emission and Mass Spectral Data 2207

The elemental responses of a set of small molecules are used to obtain the elemental ratios and composition of larger, structurally unrelated compounds. Combining this information with known molecular weights allows molecular formulae to be determined.

D. B. Hooker and J. DeZwaan*, 7255-209-0, Physical and Analytical Chemistry Research, The Upjohn Company, Kalamazoo, MI 49001

Comparison of Sampling Techniques for Combined Supercritical Fluid Chromatography and Fourier Transform Infrared Spectrometry with Mobile Phase Elimination 2212

Several sampling techniques for SFC/FT-IR measurements involving mobile phase elimination are compared. Conventional transmission spectrometry provides the best performance.

Roger Fuoco, Istituto di Chimica Analitica Strumentale del CNR, Universita di Pisa, Via Risorgimento 35, 56100 Pisa, Italy and **Stephen L. Pentoney, Jr., and Peter R. Griffiths*,** Department of Chemistry, University of California, Riverside, CA 92521-0403

Correspondence

Canonical Correlation Technique for Rank Estimation of Excitation–Emission Matrices 2219

Xin M. Tu and Donald S. Burdick*, Institute of Statistics and Decision Sciences, Department of Mathematics, Duke University, Durham, NC 27706 and **David W. Millican and Linda B. McGown,** Department of Chemistry, Duke University, Durham, NC 27706

Correction. Separation of Two Components of Horse Myoglobin by Isoelectric Focusing Field-Flow Fractionation 2224

J. Chmelík*, M. Deml, and J. Janča, Institute of Analytical Chemistry, Czechoslovak Academy of Sciences, 611 42 Brno, Czechoslovakia

SIEMENS

Ask for performance - ask for the new D 5000 x-ray diffractometer

Detector configurations include:

- PSD (Position Sensitive Detector).
- Solid-state detector for improved detector efficiency.
- Std. scintillation counter.

Versatile goniometer design:

- Operates in horizontal or vertical mode for reflection or transmission measurements.
- Converts from θ:2θ geometry to θ:θ in your lab.
- Converts to parallel beam.

Fully automated design:

- Microprocessor control of data collection.
- Host computer for experimental setup and data analysis.

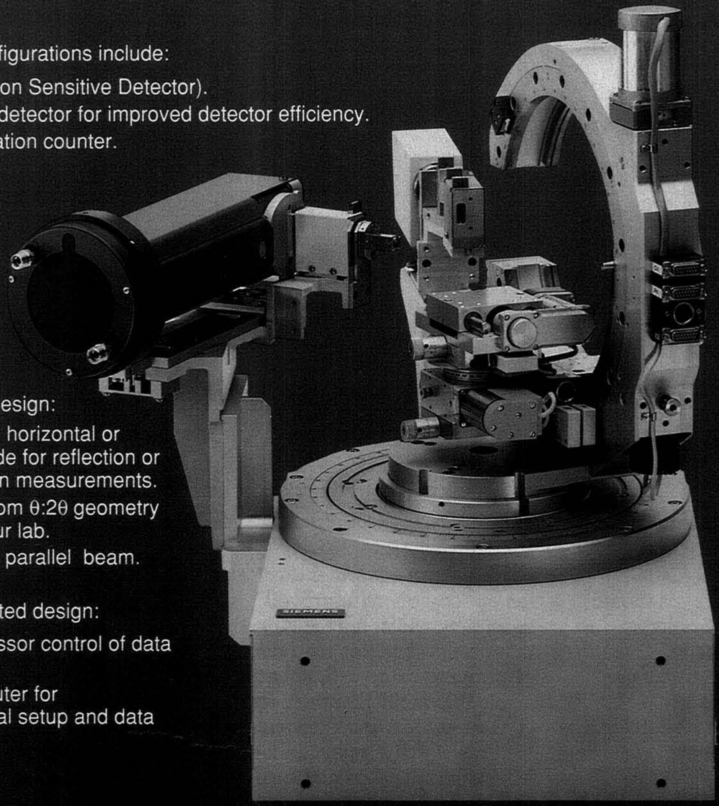

Complete set of attachments for specific applications:

- Eulerian cradle for texture.
- Open Eulerian cradle for texture/stress.
- Automatic sample changer.
- High and low temperature stages.
- Programmable sample rotation.

Available with computer controlled variable aperture slits in incident and diffracted beam paths to control divergence and reduce background.

For maximum performance in your lab, Siemens has engineered a new generation of x-ray diffractometer designed to meet your requirements. The D 5000 features a new goniometer design manufactured to the strictest tolerances. Complete with application specific attachments and advanced software routines, the D 5000 has the precision and flexibility to outperform other systems in every x-ray application.

Your Solution is Siemens

In USA & Canada contact Siemens Analytical X-Ray Instruments, Inc., a joint venture of Siemens & Nicolet.
6300 Enterprise Lane • Madison, WI 53719-1173 • Tel. (608) 276-3000 • FAX (608) 276-3015
Worldwide Contact: Siemens AG, Analytical Systems E 689 • D 7500 Karlsruhe 21 • P.O. Box 21 1262 • Federal Republic of Germany • Tel. (0721) 595-4295

CIRCLE 152 ON READER SERVICE CARD

The VG Trio-2. We added up the benefits. Then we added some more.

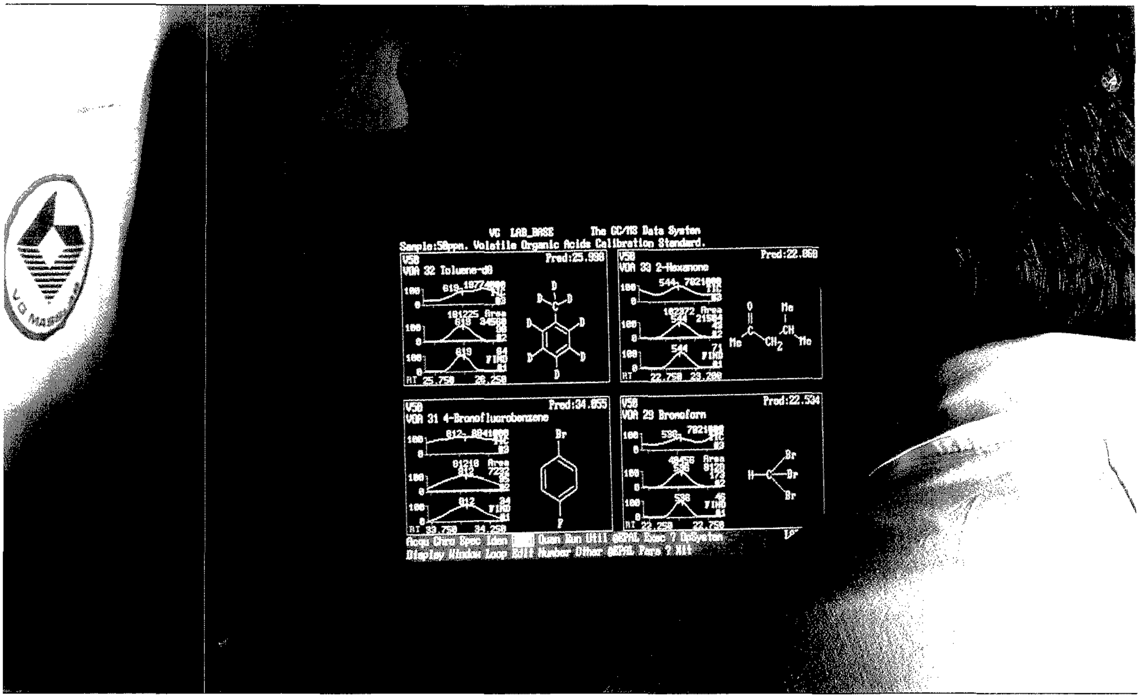
VG MASSLAB
VG LAB_BASE The GC/MS Data System
Sample:50ppm. Volatile Organic Acids Calibration Standard.
V50 VOA 32 Toluene-d8 Pred:25.998
V50 VOA 33 2-Hexanone Pred:22.868
V50 VOA 31 4-Bromofluorobenzene Pred:34.055
V50 VOA 29 Bromoform Pred:22.534
Acqu Chro Spec Iden Quan Run Util @SPAL Exec ? OpSystem
Display Window Loop Edit Number Other @KPAL Para ? Hit

Your equipment is fundamental to your success – it should advance as your applications advance. Which is why, at VG Instruments, we are continually updating our products.

Take the TRIO-2 GC-MS for instance. Our most recent modifications are designed to afford the user not only a wider range of applications but also significant improvements in performance.

TRIO-2's new gold plated ion source – with computer designed ion optics – offers improved sensitivity, whilst the extended mass range enables the resolution of compounds up to 3,000 amu – an invaluable facility for techniques such as LC-MS and Dynamic-FAB.

LINC™, VG's particle beam LC-MS interface, is now available and innovative design has reduced the changeover time between techniques to less than three minutes. Robotic probe systems have also been introduced for the automated analysis of routine samples.

In addition, TRIO-2 is now available with the LAB-BASE™ data handling system. This 'super-computer' technology incorporates 32-bit RISC architecture and multiple parallel processing – giving a speed of data handling unique in mass spectrometry.

Add up the benefits for yourself. **The new TRIO-2** – the latest in the growing family of 'Super-Quads' from VG instruments.

VG INSTRUMENTS
organic mass spectrometry

CIRCLE 170 ON READER SERVICE CARD

A VG INSTRUMENTS GROUP COMPANY

UNITED KINGDOM. VG MassLab Ltd. Tudor Road, Altrincham, Cheshire WA14 5RZ. England Tel: 061-941 3552.
USA. VG Instruments Inc., 32 Commerce Center, Cherry Hill Drive, Danvers, Massachusetts 01923 Tel: (508) 777 8034.
CANADA. VG Instruments Canada Inc., 5929 Transcanadienne, St. Laurent, Quebec H4T 1A1. Tel: (514) 744 5519.
WEST GERMANY. VG Instruments GmbH, Hasengarten Strasse 14, 6200 Wiesbaden. Tel: (6121) 71090.
FRANCE. VG Instruments SA, 5 Avenue Gallieni, 94250 Gentilly. Tel: (33) 147406160.
ITALY. VG Instruments, Viale Dell'Assunta 101, 20063 Cernusco Sul Naviglio, Milano. Tel: (2) 924 8808.
THE NETHERLANDS. VG Instruments BV, PO Box 171, 1380 AD Weesp. Tel: (2940) 80484.
BELGIUM. VG Instruments NV, Excelsiorlaan 1 Box 2, 1930 Zaventem. Tel: (322) 725 2410.
SCANDINAVIA. VG Instruments AB, Box 45199, S-104 30 Stockholm, Sweden. Tel: (46) 8311035
CHINA. VG Instruments Asia Limited, PO Box 2724 Lan Qi Ying, Cheng Fu Lu, Beijing. Tel: 256-4609. Telex: 222 453
KOREA. VG Instruments Korea Limited, Dong-il Building, 58-6 Nonhyun-dong, Kangnam-Ku, Seoul. Tel: (2) 548 2983. Telex: 28523
JAPAN. Jasco International Co. Ltd., 2-4-21 Sennin-cho, Hachioji City. Tokyo 193. Tel: 010813 42666 1321. Telex: 2862515.

EDITORIAL

Near Field Scanning Optical Microscopy

Current problems in analytical chemistry often require ultramicroanalysis (microscopy) in addition to traditional spectroscopic and trace methods. Witness the growing interest in cell biology. It has fostered an expansion of the tools available to the analytical microscopist. The need for high spatially resolved information is obvious: Chemical transport in cells occurs on a submicrometer scale. Current techniques (i.e., EM and SIMS) are destructive and cannot be directly applied to living systems. Our old friend light microscopy in its polarized, fluorescence, and confocal incarnations is quite useful, although it is limited to a spatial resolution of ~0.1 μm. There is a real need for a nondestructive superresolution technique that can be applied to a living system and that is capable of providing morphological and spectroscopic information. This need is currently being addressed by near field scanning optical microscopy (NSOM) (*1, 2*).

NSOM, a superresolution imaging technique, relies on the particle nature of light. Light is passed through an opaque aperture of a diameter, D, less than the wavelength of the incident radiation. Within a short distance of the aperture—the near field—the radiation remains collimated. Thus spatial information, having spatial resolution D, is obtained if the sample is brought within the near field and scanned with respect to the source. By manipulating the source wavelength and the detector assembly, a wide variety of spatially resolved spectroscopies can be realized. Lewis and co-workers (*1*) are currently studying the feasibility of NSOM in the fluorescence mode as applied to biological systems. Using visible laser radiation as a source, a conservative estimate of spatial resolution is 500 Å, which should yield information on cell and organelle membranes and DNA binding in chromosomes, to name only a few. Because this information is chemical in nature, a new chemical microscopy is in hand.

It is most interesting to note that although NSOM is technologically new, the concept is more than 30 years old. O'Keefe originally proposed the idea in a letter to the *Journal of the Optical Society of America* (*3*). He proposed it as "a concept illustrating a method by which it might conceivably be possible to go beyond the resolving power of light.... The realization of this proposal is rather remote...." Technology has taken some 34 years to catch up with O'Keefe's vision. This should remind us of light microscopy's staying power as an analytical technique; through the marriage of physics and analytical chemistry, it will continue to grow and thrive.

References

(1) Betzig, E.; Lewis, A.; Harootunian, A.; Isaacson, M.; Kratschmer, E. *Biophys. J.* **1986**, *49*, 269.

(2) Betzig, E.; Isaacson, M.; Barshatzky, H.; Lewis, A.; Lin, K. *Proc. SPIE—Int. Soc. Opt. Eng.* **1988**, *897* (*Scanning Microsc. Technol. Appl.*), 91.

(3) O'Keefe, J. A. *J. Opt. Soc. Am.* **1956**, *46*, 359.

G. H. Morrison

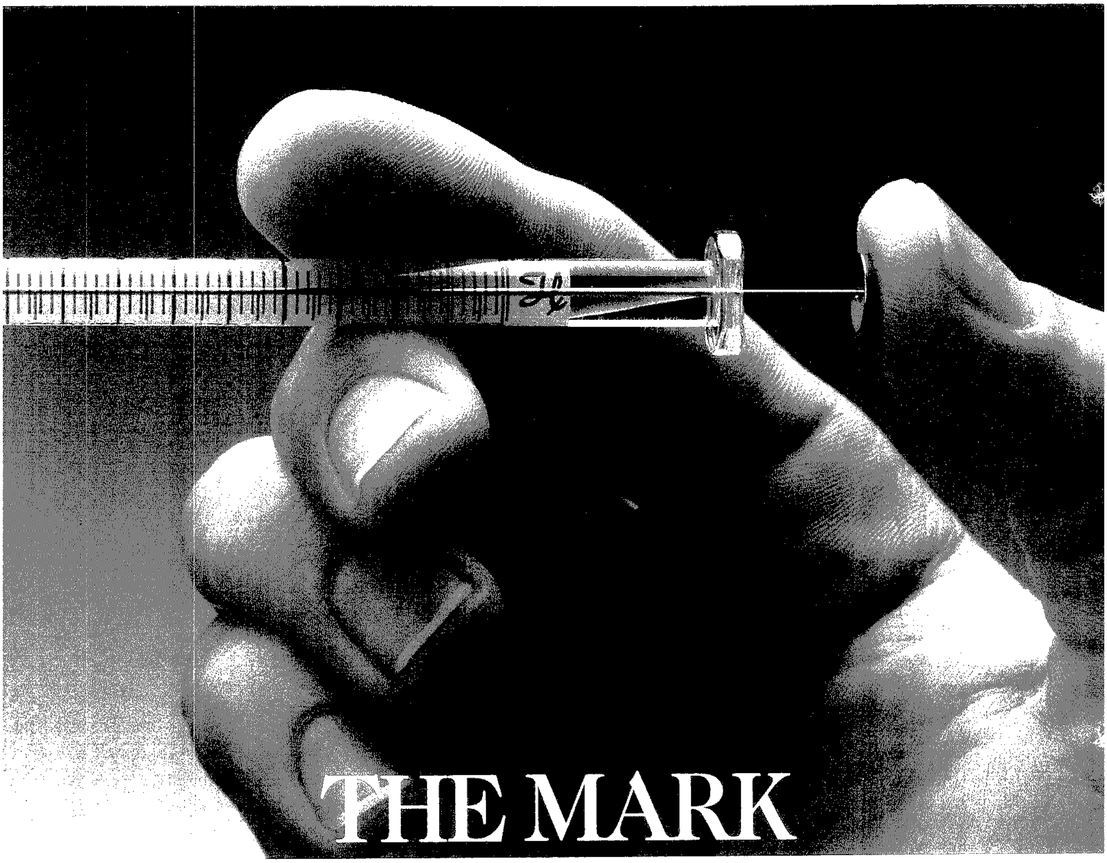

THE MARK
OF THE
EXPERT

Chromatographers the world over choose Hamilton syringes over all others. The reason is plain: the better the syringe, the better the results.

Call or write for your free copy of the Hamilton syringe catalog. Hamilton Company, P.O. Box 10030, Reno, Nevada 89520. (800) 648-5950.

HAMILTON
The measure of excellence.
CIRCLE READER CARD #67
FOR YOUR FREE CATALOG!

ORDER YOUR FREE 1990 HAMILTON
PRODUCT CATALOG TODAY!

Undergraduate Awardees Receive ANALYTICAL CHEMISTRY

The ACS Division of Analytical Chemistry has announced that 397 students have been chosen as winners of the 1989–90 undergraduate awards in analytical chemistry.

The awards are given annually to chemistry students at U.S. colleges and universities to recognize outstanding scholastic achievement and to stimulate interest in the field of analytical chemistry. Awardees will receive 16 issues of ANALYTICAL CHEMISTRY (October 1989 to May 1990) and the Division newsletter. The winners were selected by the faculties of the chemistry departments of their respective institutions.

Hearing the Faintest Noise

Cornell University biophysicists have reported that structures in a frog's ear respond to the faint, pervasive background noise from the random collisions of molecules. Like other experiments that established that the eye's photoreceptor cells can detect single photons or that the nose's chemical receptors will respond to single molecules, these results set lower limits for "hearing."

The researchers, Winfried Denk and Watt Webb, measured the mechanical motion of hairbundles inside the frog's inner ear that respond to sound waves, and the corresponding electrical response from hair cells attached to the bundles. Similar structures are found in many organisms, including humans.

Webb and Denk used a laser differential microinterferometer to record the hairbundle motion. The microinterferometer consisted basically of two matched laser beams capable of detecting motions of approximately 1 pm/s. Output voltages from the hair cells were monitored by microelectrodes.

With this experimental setup, the Cornell researchers demonstrated that hair cells produced signals that precisely correlated with the spontaneous motion of the hairbundles (about 1 nm) due to thermal noise. Says Webb, "While we still do not fully understand how this important transducer works at the molecular level, we now possess key information about its abilities."

Sugar-Coated Semiconductors

Researchers led by Mark Bednarski of the University of California at Berkeley and the Lawrence Berkeley Laboratory are investigating how the common bacterium *E. coli* attaches to silicon wafers coated with various types of organic molecules. Determining whether biological organisms adhere to surfaces will be important in designing new materials and coatings that resist biofouling. This information may also help in the study of infections triggered by the binding of bacteria and viruses to cell surfaces.

In the experiments, semiconductor surfaces are coated with alcohols, lipids, sugars, organic acids, and bases. With all but the sugars, adhesion is nonspecific; bacteria have a stronger hold on the semiconductor surface as acidity, hydrophilicity, and electric charge increase. Bacteria with specific receptors for the sugars mannose and galactose bind to wafers with these sugars, but not to those coated with glucose.

The California scientists characterized the wafer surfaces with X-ray photoelectron spectroscopy, ellipsometry, and scanning electron microscopy (SEM). A contact angle measurement, related to hydrophilicity, predicts whether bacteria will nonspecifically adhere to the surface. Surfaces whose contact angles are less than 30° exhibit the best adhesion, as demonstrated by SEM. Says Bednarski, "Now we have a system to study the conformation and composition of cell–surface molecules, which is not possible by strictly biological techniques."

Implantable Glucose Monitor

Every day an estimated 1 million Americans with Type I insulin-dependent diabetes prick their fingers to monitor blood glucose levels. In time, the finger pricking could destroy nerve endings, robbing the finger of all sensation. A new implantable glucose sensor now under development can perform the same measurement more accurately, with little or no physical discomfort.

The device, labeled the Rechargeable Physiological Sensor (RePS), is being developed by Ebtisam Wilkins and her co-workers at the University of New Mexico's Department of Chemical and Nuclear Engineering and by Wade Radford and engineers at the Johns Hopkins University's Applied Physics Laboratory (APL). The collaborators plan to complete a prototype this year and predict that a commercial unit will be marketed in about four years.

The sensor, designed by Wilkins, consists of a polyvinyl coating impregnated with an ionic glucose salt wrapped around a Pt electrode. Changes in glucose concentration shift the equilibrium between the associated and dissociated forms of the glucose salt, which is monitored electrochemically. A hydrogel or membrane coating prevents leaching of the salt.

When implanted just under the skin in the abdominal region, the RePS measures changes in tissue glucose levels. According to Wilkins, the tissue levels lag about 20 min behind blood glucose values.

A lithium battery-powered telemetry system built by APL transmits the glucose information to a hand-held receiving unit. The RePS is also rechargeable, unlike most other sensors currently under development.

For Your Information

The American Association for Clinical Chemistry (AACC) has issued a **guide for employers setting up "blind" employee drug testing programs.** *Employer's Guide to Evaluating Laboratory Performance* is available from AACC, 2029 K Street, N.W., Seventh Floor, Washington, DC 20006 (202-857-0717; 835-8744).

REVEALING
THE TRUE CHARACTER...

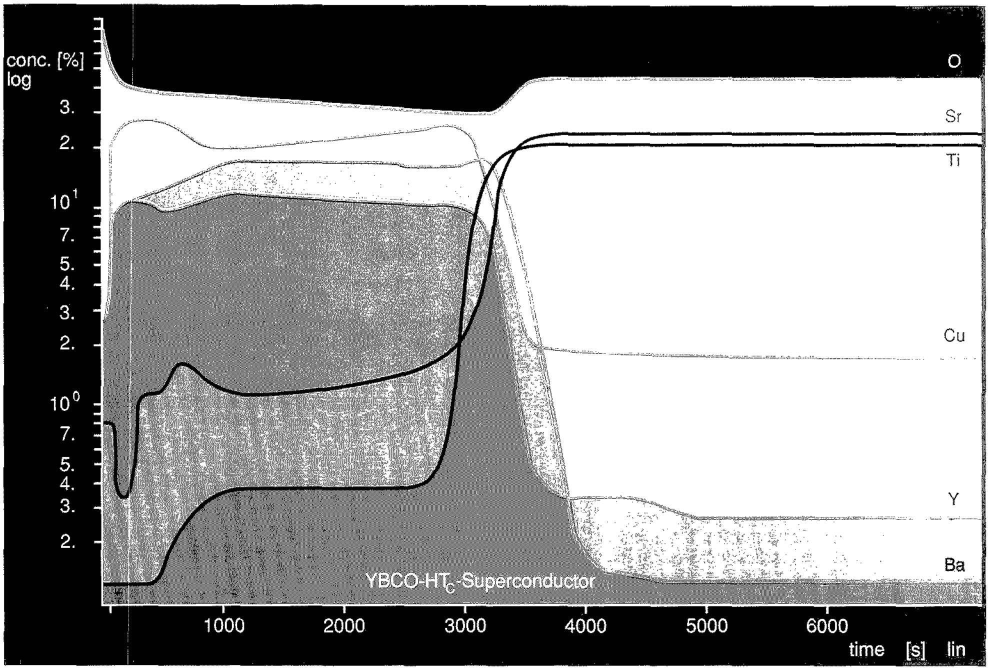

CD Bonn
190.9 61 23.007.02

Sputtered Neutrals Mass Spectrometry (SNMS) – a New Method for Quantitative Depth-Profile Analysis

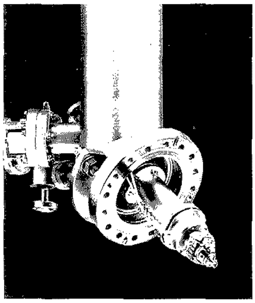

Homogeneity and chemical composition of different layers determine the quality of the new high-temperature superconductors. Accurate quantification of each individual layer is crucial. One by one, atomic layers are stripped away by ion bombardment.The resultant neutral particles can then be analyzed by the SSM 200 detection system.
Only now is the true character revealed!
In other words, the depth profile. Quantitatively!
All made possible by the SSM 200, whose modular construction can be adapted to both Leybold surface analysis or any other UHV system.

Interested? Call: PA (412) 327-5700

- LEYBOLD VACUUM PRODUCTS INC.
  LAS GROUP
  5700 Mellon Road, Export, PA 15632

- LEYBOLD AG
  Bonner Strasse 498, D-5000 Cologne 51

LEYBOLD

Innovative Vacuum Technology

A Degussa Company

CIRCLE 92 ON READER SERVICE CARD

INSTRUMENTATION

Raymond E. Dessy
Chemistry Department
Virginia Polytechnic Institute and
State University
Blacksburg, VA 24061

Waveguides are thin cylinders or films made of glass or plastic that efficiently conduct light (*1*). Developed originally for telecommunications and optical computing applications, they have found another home in analytical chemistry as chemical and physical sensors. Their small size, flexible geometry, ability to channel light over long distances, and noise immunity make these sensors ideal for remote sensing, clinical applications, environmental monitoring, and process control.

The purpose of this article is to demonstrate the breadth of applications served by waveguides as chemical sensors and to provide a brief tour of current implementation techniques. After a short review of how waveguides work, some current case histories are presented dealing with practical analytical situations that may help stimulate problem solving.

Waveguide optics and geometries

When light is directed into a medium consisting of a core material surrounded by a cladding of lower refractive index (RI), the radiation can propagate down the guide in a series of multiple internal reflections. Light launched at an angle greater than a critical angle, determined by the core/cladding index ratio, will leak out of the waveguide after a short distance; light launched at less than this angle will remain channeled in the waveguide. The incident light accepted as a guided wave is said to fall within the guide's cone, or angle, of acceptance (Figure 1).

Waveguides for analytical applications can be cylindrical fibers or very thin planar structures. In the former (Figure 2a), analytes interact at the butt end or at the cylindrical surface of the fiber. Fibers made for telecommunication purposes are usually protected by plastic jackets, commonly an underjacket of silicone and an outer jacket of polycarbonate. The outer jacket provides tough mechanical protection; the fiber is protected from this jacket's high thermal expansion coefficient by the rubbery inner jacket. The thermal diffusivity of both jackets also shields the fiber from temperature-induced changes in RI and elasto-optic characteristics. These jackets must usually be stripped off prior to fabrica-

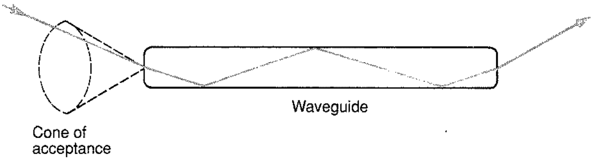

Figure 1. Ray diagram of light propagation.

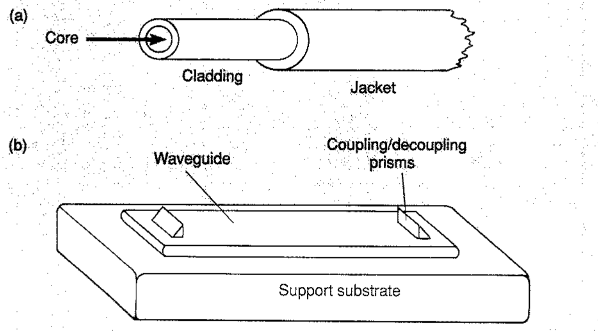

Figure 2. Basic waveguide construction.
(a) Cylindrical waveguide and (b) planar waveguide.

0003-2700/89/A361-1079/$01.50/0
© 1989 American Chemical Society

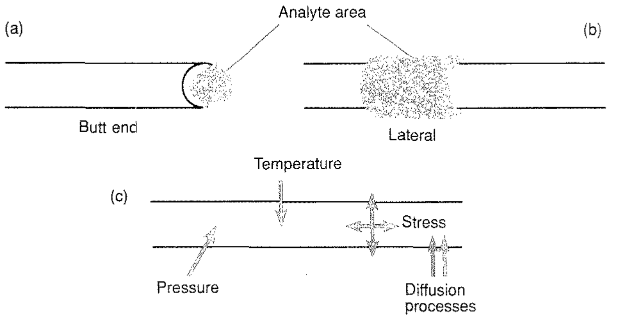

Figure 3. Chemical and physical waveguide sensors.
(a) Extrinsic detector with analyte at the butt end of the fiber, (b) extrinsic detector with analyte at the lateral surface of the fiber, and (c) physical properties affecting the intrinsic properties of a waveguide.

tion of a chemical sensor. Core diameters range from several to several hundred micrometers.

In planar waveguides (Figure 2b), a thin film several micrometers thick on a support substrate is used as the waveguide. These films can be created by casting, spin-coating, vapor deposition, or surface diffusion. Organic and inorganic polymeric films coated on a substrate are common. Silver ions diffused into a glass surface by electrical fields alter the RI enough to produce a rugged, rather inert waveguide. To couple the light into such planar guides, high index-of-refraction prisms (coupling prisms) are commonly used, although small gratings on the surface of the guide or direct butt coupling techniques are also effective.

Direct sample illumination. Waveguides can be used to deliver a stream of photons of a particular color to an analyte. If the waveguide is a cylindrical fiber made from glass or organic polymers, this most commonly occurs at the distal tip of the fiber where the absorbance, fluorescence, or Raman characteristics of the analyte are important (Figure 3a). Light is usually launched into the fiber by shining a tightly focused beam onto the proximal butt end. In many ways, this approach resembles the classic source, cuvette, and detector geometry encountered in more conventional spectrometers.

Indirect interactions—the evanescent wave. An alternative approach is also currently arousing interest. At each internal reflection in the waveguide, interference between the incident and reflected internal beam creates a nonpropagating standing wave in the medium, perpendicular to the reflecting surface. The energy associated with this wave tails out into the surroundings, where it can interact with chemicals in the environment. This tailing phenomenon is called the evanescent wave (Figure 4). This type of interaction has been a historical component of attenuated total reflectance (ATR) and internal reflection spectroscopy pioneered by Harrick and Fahrenfort, who developed the concept around thick slab waveguides. Analytes adsorbed onto the lateral waveguide surface or in the bulk surroundings (Figure 3b) change the light propagation characteristics of the waveguide by their absorbance and their dielectric or RI behavior. The amount of light leaking into the environment is easily affected by these changes, and such alterations can be measured at the distal end of the waveguide. Alternatively, the radiation escaping perpendicular to the waveguide, or the fluorescence or Raman effects this excites, can be measured.

Modes. In waveguides made from thick slabs or large-diameter cylinders of glass a few millimeters in cross-section, light can be received at any angle within the cone of acceptance. Because the walls of such guides are far apart, there are only a few reflections at the surface before the light beam escapes at the end. This limits the extent of interaction of the beam with materials adsorbed onto or near the surface.

In such large media, light can adequately be treated as a particle, moving in straight lines until reflected or refracted. As the guide's dimension grows smaller, the wave and quantum nature of light becomes useful in describing

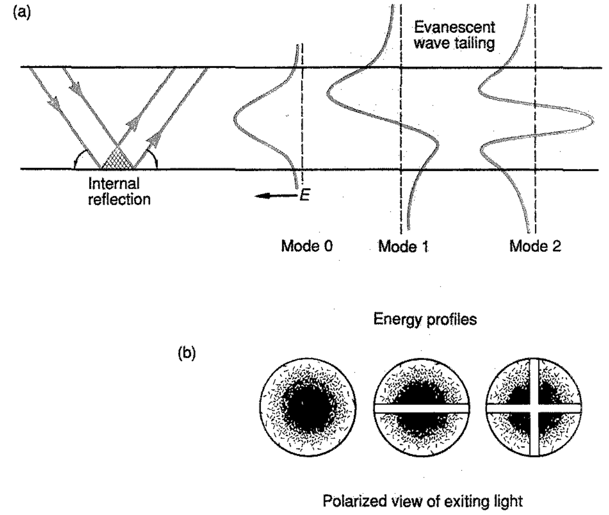

Figure 4. Modes and evanescent waves.
(a) An internal reflection portraying light as a ray. Associated modes give rise to evanescent wave tailing, portraying light as a wave phenomenon. (b) Quantum effects arise when the waveguide and the light it is guiding are of the same dimension.

Evanescent Waves—Seeing Is Believing

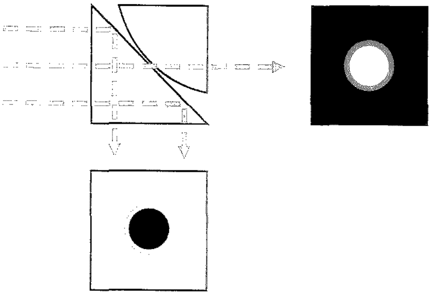

The evanescent wave can be seen in a simple experiment first performed by Newton. A totally reflecting prism is placed in contact with a lens and illuminated with white light. The transmitted light is a white "spot" with a red edge; the reflected light has a black "hole" with a blue edge. The spot and hole are much bigger than the area of contact between the prism and lens. This increased size results from the penetration of the evanescent wave into the lower RI media at the reflecting surface of the prism, and the colored edges result from the dependence of the penetration depth on wavelength.

various phenomena.

What appear to be quantum effects become evident as the thickness of a planar waveguide or diameter of a cylindrical fiber approaches the wavelength of the guided wave (several micrometers). Only certain launch angles lead to propagating waves within the medium; a physical chemist might say that only discrete modes of propagation can be supported (Figure 4a). Each mode has a different nodal energy distribution pattern across the waveguide. Simple viewing experiments with polarizers (Figure 4b) reveal that the visual field produced at the exit of such fiber waveguides by the first few modes, such as those labeled 0, 1, and 2 in Figure 4, reflect the symmetry of *s*, *p*, and *d* orbitals. Increasing mode number is also associated with a greater amount of energy external to the core via the evanescent wave. This is analogous to the increased tunneling shown by the higher energy levels of a particle in a box or the increasing spatial distribution exhibited by the *s*, *p*, and *d* orbital series. Changing the launch angle of light into the waveguide can affect the power distribution between the various modes, preferentially favoring one mode over the others and altering the penetration depth into the surroundings. This spatial effect has been used to examine the spectral characteristics of the chemicals making up the bulk of a waveguide as well as to probe its surface layers and interfaces with surrounding material. If light is viewed as a particle obeying ray optics, these thin waveguides have many more internal reflections than thick guides and hence are more sensitive to changes in the bulk surroundings.

Moderate diameter fibers will support many modes and are therefore called multimode fibers. The exact number is easily calculated from the thickness of the fibers, the wavelength of light, and the RIs of the fibers' components. Over very long distances, power redistribution between modes tends to occur—a process called mode mixing. A fiber can be forced to support only one mode by making its diameter very small and adjusting the RI ratio between core and cladding to approximately one. In these monomode fibers, the phase coherency of a laser beam is maintained over long distances. Such fibers can be used to make simple, inexpensive interferometers for measurement of chemical and physical parameters of materials.

Waveguides can be divided into various categories depending on the medium's RI profile. Both step-index and graded-index fibers are available. In the former, there is an abrupt change in RI; in the latter, there is a gradual change. The RI profile will affect the spacing of the launch angles of light

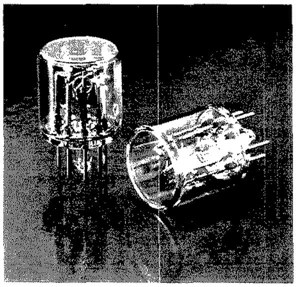

SUPER-QUIET XENON LAMPS FOR PHOTOMETRIC INSTRUMENTS

Outstanding luminance from UV to IR

Hamamatsu flash mode Super-Quiet Xenon Lamps provide a minimum of 10^9 flashes! Arc stability is 5 times higher, service life 10 times longer than conventional lamps. Available in three sizes for:

- Stroboscopes
- Chromatographs
- Photoacoustic Spectroscopes
- Strobe Cameras
- Photomasking Devices
- Fluorospectrophotometers
- Color and SO_2 Analyzers
- Other light-sensitive instruments

For Application Information, Call
1-800-524-0504
1-201-231-0960 in New Jersey

HAMAMATSU

HAMAMATSU CORPORATION
360 FOOTHILL ROAD
P. O. BOX 6910
BRIDGEWATER, NJ 08807
PHONE: 201/231-0960
International Offices in
Major Countries of
Europe and Asia.

© Hamamatsu Photonics, 1986

CIRCLE 63 ON READER SERVICE CARD

associated with the various modes.

Extrinsic versus intrinsic sensing. Most chemical applications of fiber sensors use them as extrinsic detectors (Figure 3a, b). These fibers guide light to small or inaccessible spots where the light, exiting perpendicularly from the butt end of the fiber, can interact with materials external to the fiber by absorbance, fluorescence, or Raman effects. Alternatively, the evanescent wave can interact in similar ways with material in the lateral surroundings. However, sensors can also be based on intrinsic changes in the fiber (Figure 3c). Internal changes in length, RI, or elasto-optic parameters of the waveguide, brought about by environmental changes, can alter light propagation characteristics. Physicists have built pressure, temperature, and magnetic sensors based on such principles using various interferometer designs, and chemical sensors can be built using this approach.

Waveguide configurations

The applications of waveguides as chemical sensors or probes depends on using the physical chemistry or photochemistry associated with analytes in both conventional and novel ways. A key element is combining novel geometries of the physical sensor with new chemistry in the transduction mechanism.

As we examine some typical chemical applications of waveguides, Figures 5–7 will illustrate some of the various optical designs possible. Single- and double-fiber geometries are employed (Figure 5). In the former, the exciting radiation and the emitted radiation share a single conduit. In the latter, one fiber carries the exciting radiation while another carries the emitted radiation to the light detector. With fibers, the reagents producing an optical response by the analyte can be immobilized in many ways (Figure 6). Often, separation of the reagent from the bulk solution by a membrane is involved. Clever ways of replenishing the reagent have been developed.

With planar guides, many configurations are also possible (Figure 7). In some applications, the intensity of the exiting light is measured at a fixed angle; in other cases, the intensity is measured as a function of angle.

Applications

Some waveguide detectors are true sensors that provide a continuous reversible response; others are probes that are based on irreversible chemistry, although the response may be continuous. The recent examples described here were chosen to demonstrate that the true genius behind waveguide detectors lies in the reagent chemistry and geometry. Each case was selected to demonstrate an important type of contribution in this rapidly developing area. Only the corresponding scientist is acknowledged in each case, but many others contributed to these efforts.

S. Michael Angel, Lawrence Livermore National Laboratory, Livermore, CA 94550

Downhole temperature measurements in geothermal wells (*2*). Optrode thermometers based on the temperature-dependent fluorescence characteristics of inorganic ions doped into a host matrix are easily built. The ruby-based optrode functions from 100–600 °C and at 400 °C has an accuracy of 1–2 °C. New temperature-measuring optrodes can be constructed by doping Eu(III) and Er(III) into an inert ceramic-like material such as calcium zirconium titanate. The intensity of the Eu fluorescence bands at 610 and 595 nm increases as temperature increases, whereas the Er fluorescence bands at 548 and 560 nm decrease. The ratio of the Eu and Er band intensities produces a useful calibration curve with an accuracy of 0.2 °C over the 100–300 °C range. Systems employing a single fiber to illuminate and collect fluorescence as well as a double-fiber optrode that separates these functions are possible.

Remote quantitation of organochlorides (*3*). The absorbance of basic pyridine solutions is changed when that molecule is exposed to different organochlorides. The change results from the formation of an open-chain diazachromophore that has a characteristic fluorescence. The rate of appearance of this emission can be used to quantitate organic halide contaminants over long distance. Clever encapsulation of the reagent at the tip of the fiber produces an inexpensive, disposable probe.

Remote sensing of glucose and penicillin (*4*). Optrodes capable of detecting glucose and penicillin can be developed by covalently attaching a polymer membrane to the tip, which contains an appropriate enzyme and a pH-sensitive fluorescence dye. A signal is produced when the enzyme catalyzes the conversion of a substrate into a product that affects the microenvironmental pH of the membrane and consequently lowers the fluorescence intensity of the dye.

Detection of ground water contaminants by surface-enhanced Raman spectroscopy (SERS) in the near-IR range (*5*). A 1-mW 785 nm wavelength diode laser can be used as the exciting source for generation of surface-enhanced Raman signals from tris(2,2′-bipyridyl)ruthenium(II) and various pyridine derivatives on silver and gold electrodes. The technique eliminates the fluorescence problem, usually associated with such studies, that results from emissions from the fiber and the surrounding solution; near-IR excitation avoids most luminescence regions in these environments. Portable solid-state near-IR la-

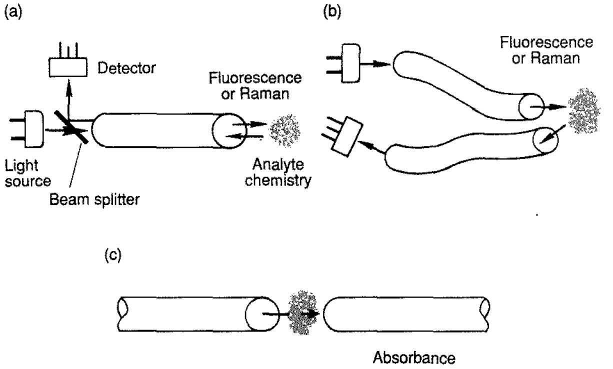

Figure 5. Various cylindrical waveguide geometries.

(a) Single-fiber sensor where exciting and emitted light share a common conduit, (b) double-fiber sensor where the fluorescence and Raman excitations have their own pathway, and (c) dual-fiber absorbance measurement.

MODEL 305
Modular HPLC Pump

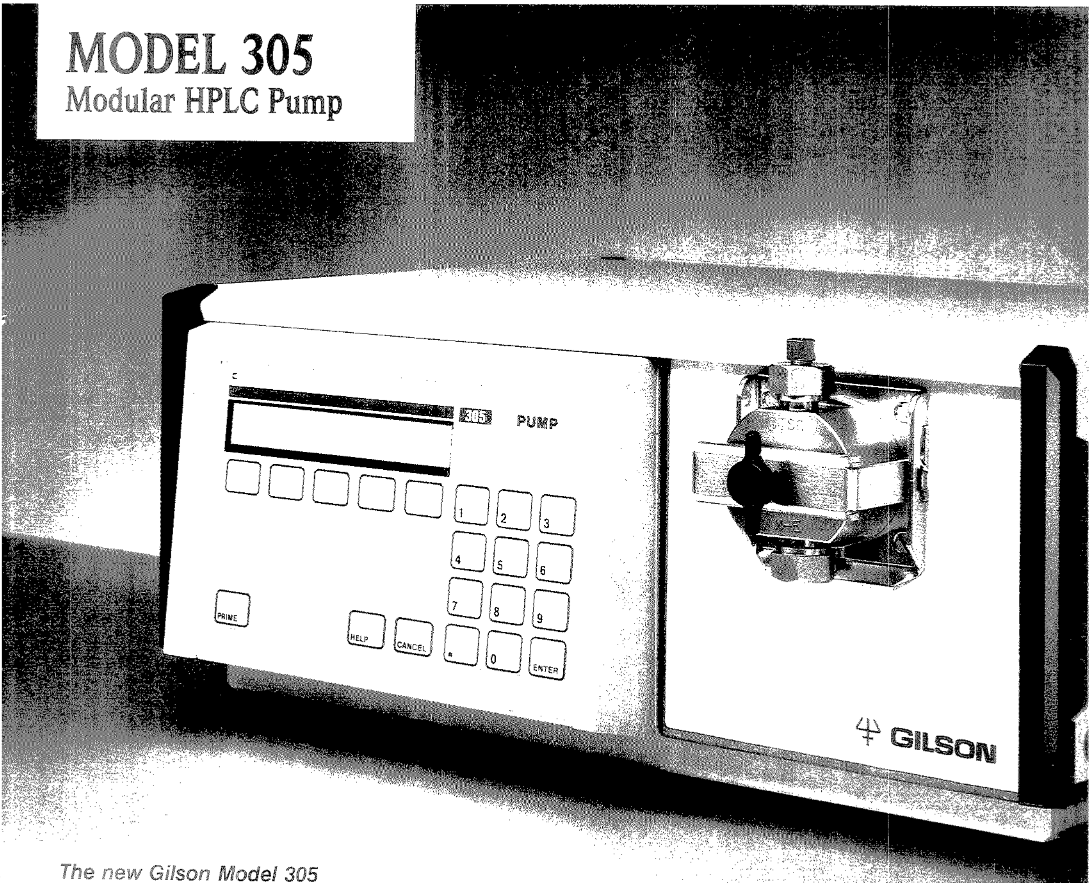

The new Gilson Model 305 Master Pump. For analytical or preparative HPLC in the isocratic, binary or ternary modes.

The Pump.

Now you can program gradients without a computer. Upgrade your isocratic system without major expense. Switch from analytical to preparative and back again. Use the special dispense mode for repetitive injection in automatic preparative systems.

The heads.

For micro-analytical up to laboratory preparative scale (0.025 - 200 mL/min). For aqueous or salt-concentrated solutions. In titanium for ion-free work. All completely interchangeable so you can choose the optimum combination for your separation.

This compact new pump (only 32 cm wide) can handle any HPLC application.

To find out more about Gilson's new Master Pump, please contact your nearest Gilson representative.

GILSON

U.S.A. - Box 27. 3000 West Beltline Hwy - Middleton, WI 53562 - Tel. : 608-836-1551
Tlx : 26-5478 - Fax : 608-831-4451 - FRANCE - BP 45 - 95400 Villiers-le-Bel - Tel. : (1) 34 29 50 00
Tlx : 606 682 - Fax : (1) 39 94 51 83
CIRCLE 61 ON READER SERVICE CARD

ser sources offer the possibility of remote sensing because of a waveguide's high near-IR transmission and the large magnitude of the SERS signals at these energies.

Mark A. Arnold, University of Iowa, Iowa City, IA 52242

Remote sensing of ammonia (*6*). Both *p*-nitrophenol and 6-carboxyfluorescein are pH-sensitive indicators that respond to changes in the concentration of ammonia in the environment. If these are used in conjunction with a microporous membrane of Teflon, an optrode based on absorbance changes can be constructed that has a lower limit of detection of 5 μM. Simplex optimization techniques have focused on the important parameters in such optrode design. The resulting sensor, useful in wastewater analyses, compares well with conventional electrode systems. The optrode has equivalent sensitivity and response time but superior recovery time and S/N ratio.

A general optrode sensor for biomedically important compounds (*7*). An NADH-based optrode can be constructed by immobilizing lactate dehydrogenase at the tip of a bifurcated optical waveguide. This enzyme catalyzes the reaction

$$\text{lactate} + \text{NAD}^+ \rightleftharpoons \text{pyruvate} + \text{NADH} + \text{H}^+$$

Depending on the pH, this reaction proceeds quantitatively in either direction. By adjusting the solution conditions, either a lactate or pyruvate detector can be prepared. The analysis is based on changes in fluorescence due to NADH. NADH sensors based on bacterial luciferase can also be made. The reactions

$$\text{NADH} + \text{FMN} \rightarrow \text{NAD}^+ + \text{FMNH}_2$$

$$\text{FMNH}_2 + \text{O}_2 + \text{RCHO} \rightarrow \text{FMN} + \text{RCOOH} + \text{H}_2\text{O} + \text{light}$$

(where FMN is flavin mononucleotide) are catalyzed by oxoreductase and luciferase, respectively. Measurement of light emission is the basis of the analyses.

Urea biosensors can be made by immobilizing urease at the tip of an optrode and using fluorescence techniques based on the pH-sensitive dyes 5-carboxyfluorescein, 2′,7′-bis(carboxyethyl)-5-carboxyfluorescein, 6-carboxyfluorescein, and 2′,7′-bis(carboxyethyl)-6-fluorescein. Absorbance sensors based on bromothymol blue and nitrazine yellow are also possible.

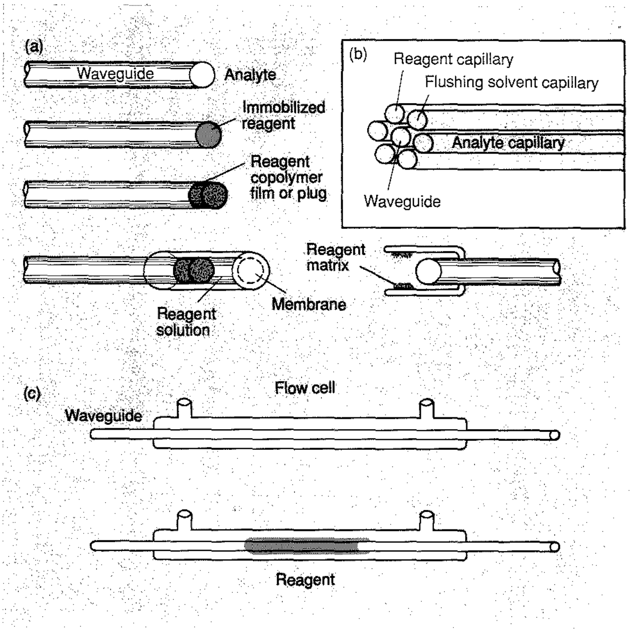
(a)
Waveguide
Analyte
Immobilized reagent
Reagent copolymer film or plug
Reagent matrix
Reagent solution
Membrane
(b)
Reagent capillary
Flushing solvent capillary
Analyte capillary
Waveguide
(c)
Flow cell
Waveguide
Reagent

Figure 6. Common waveguide detector configurations.

(a) Various possible reagent/analyte placements for cylindrical waveguides at the butt end of the fiber, (b) "Gatling Gun" concentric assembly for refreshing sensor reagents and solutions, and (c) flow-cell options for cylindrical waveguides.

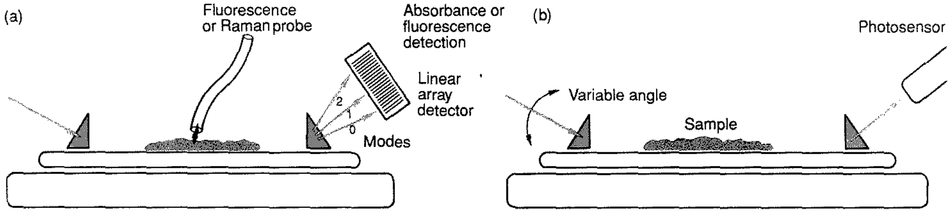
(a)
Fluorescence or Raman probe
Absorbance or fluorescence detection
Linear array detector
2
1
0
Modes
(b)
Photosensor
Variable angle
Sample

Figure 7. Planar waveguide detection schemes.

(a) Fixed-angle measurements and (b) variable-angle sensing rotates either the source or the optical photosensor.

Paul W. Bohn, University of Illinois, Urbana, IL 61801

Absorption spectrometry of bound monolayers (*8*). Monolayer film assemblies are important in studies directed toward the modification of the optical, electronic, or mechanical properties of a surface. Fields such as microlithography, monolayer catalysis, electrical insulators, and biomimetic membranes depend on an understand-

TASK
MASTER.

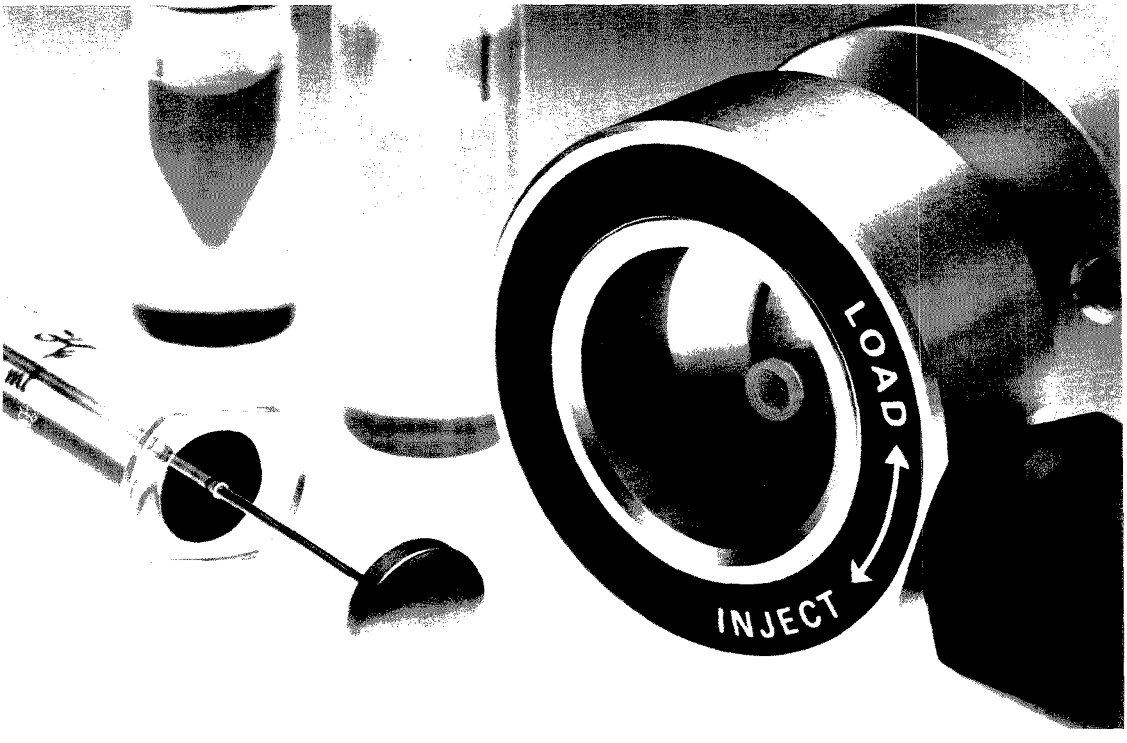

The Rheodyne 7125 LC sample injector is equipped with two operating modes to master every injection task.

In the "partial-fill" mode, the sample from a syringe fills a sample loop only partially. No sample is lost. The amount injected is the exact volume dispensed from the syringe.

You use this mode when you need to conserve sample or change sample volume frequently. You can inject from 1 μL to 2.5 mL with a precision of 1%.

In the "complete-fill" mode, sample from a syringe fills the loop completely–using excess sample. The amount injected is the exact volume of the loop.

You use this mode when you need the maximum volumetric precision of 0.1%, or you wish to load sample without having to read syringe calibrations carefully. You can inject from 5 μL to 5 mL using one of ten interchangeable sample loops.

Variations of the Model 7125 perform yet other tasks. Model 8125 minimizes sample dispersion with micro columns. And Model 9125 uses inert plastic flow passages to prevent the mobile phase from contacting metal.

For more information about these versatile injectors, phone your Rheodyne dealer. Or contact Rheodyne, Inc., P.O. Box 996, Cotati, California, 94931, U.S.A. Phone (707) 664-9050.

CIRCLE 140 ON READER SERVICE CARD

RHEODYNE
THE LC CONNECTION COMPANY

Chemical Structure Information
Interfaces, Communication, and Standards

With the advent of computer graphics, the proliferation of PC's, and the development of user-friendly software, the average chemist can now build chemical data bases, search structures and substructures, and generate chemical reports. Yet, the abundance of these systems has created a new problem—too many systems and too few standards.

This insightful reference directly addresses the problem of interfaces, communication and standards. It is authored by people with diverse backgrounds, from software developers to information specialists.

As a state-of-the-art publication, some of the topics covered include for flexibility in file formats to enable free exchange of chemical data, the interrelated forces that restrict compatibility, the attributes of a standard interface, chemical structure browsing, the use of a host language interface, PC-to-mainframe communication programs, and the standard molecular data format as an integration tool.

Contents • Design Considerations for Multipurpose Structure Files • Information Integration in an Incompatible World • Chemical Structure Browsing • Integration and Standards • A Standard Interface to Public, Corporate, and Personal Files • Towards the Universal Chemical Structure Interface • A Universal Structure/Substructure Representation for PC-Host Communication • Chemical Structure Information at the Bench; A New Integrated Approach • Building a Comprehensive Chemical Information System • The Standard Molecular Data Format (SMD Format) as an Integration Tool in Computer Chemistry • The Effort to Define a Standard Molecular Description File Format

Wendy A. Warr, *Editor*, ICI Pharmaceuticals
Developed from a symposium sponsored by the Division of Chemical Information of the American Chemical Society
ACS Symposium Series No. 400
132 pages (1989) Clothbound
ISBN 0-8412-1664-9 LC 89-14988
US & Canada $34.95 Export $41.95

O·R·D·E·R F·R·O·M
American Chemical Society
Distribution Office, Dept. 36
1155 Sixteenth St., N.W.
Washington, DC 20036
or CALL TOLL FREE
800-227-5558
(in Washington, D.C. 872-4363) and use your credit card!

ing of these monolayers. The thickness, surface density, and orientation of molecular monolayers can be evaluated by absorption measurements made on monolayers deposited on 150 μm-thick glass slab waveguide surfaces. Enhancements 1000 times greater than conventional spectroscopy are observed. The waveguides were prepared from glass coverslips using a careful precleaning procedure. After monolayer deposition, light was coupled into the films using high-RI leaded glass prisms. Both visible and UV propagation experiments can be made, and it is also easy to use fiber optic waveguide elements to capture fluorescence or Raman optical emissions from the thin films.

W. Patrick Carey, Los Alamos National Laboratory, Los Alamos, NM 87545

Determining high concentrations of nitric acid (*9*). Entrapment of a Hammett indicator, such as chromazurol-s, in a polymer blend of polybenzimidazole and polyimide, followed by silane coupling of this mixture to the lateral surfaces of an optical fiber, creates a detector that can be used to measure the protonating power of the bulk environment.

Evanescent coupling of guided waves within the fiber is altered by absorption and RI changes that result from protonation. Although the original launch angle is not sustained in the multimode cylindrical guides used, they offer greater sensitivity than conventional ATR methods because of the increased number of reflections.

Raymond E. Dessy, Virginia Polytechnic Institute and State University, Blacksburg, VA 24061

A sensitive enthalpimeter for biosensor applications (*10*). If an enzyme is immobilized onto the surface of a monomode fiber, reaction of the enzyme with a substrate in solution will create heat that modifies the light-propagating characteristics of the fiber. If coherent light is launched into two fibers, one enzyme-coated and the other uncoated, it is easy to create an interferometer (Figure 8). The light emerging from both fibers is recombined, and an interferometric bar pattern is observed. As heat is generated in one fiber and not the other, this bar pattern shifts, and the shift can be related to the substrate concentration.

A flow-injection analysis (FIA) detector (*11*). Planar waveguides can be constructed from high-quality microscope slides by creating a waveguide area on the surface. This can involve spin coating of an organic polymer film, an inorganic polymer film, or electric-field diffusion of silver ion into the glass matrix for a short distance. High-index coupling prisms can be used to guide light into the waveguide, and decoupling prisms can be used to guide the light out at the other end. Ammonia reacts according to the Berthelot reaction to produce a blue color that can be detected by a 1-mW guided He–Ne laser beam. Waveguides of this type can be tuned to use any of a number of modes, and use of mode 3 configurations results in a minimum detectable quantity of 10^{-4} M NH_3 (Figure 7). The ruggedness of the detector makes it suitable for an FIA system.

Measurement of adsorption and exchange processes occurring on silica surfaces (*12*). The system described above clearly indicated that

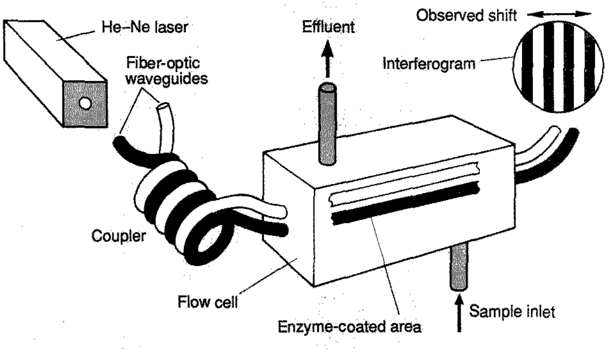

Figure 8. Fiber-optic-based enthalpimeter.
(Reprinted from Reference 10b.)

strong adsorption of analytes on the waveguide surface could occur. Using cylindrical glass waveguides, it is possible to preload the cylindrical surface of a stripped fiber with heavy metal ions from Groups I, II, III, or IV. These ions can be selectively replaced by other ions or stripped off with chelating reagents, giving useful information on equilibria and rates of exchange. Adsorption/desorption studies of organic molecules at pretreated glass surfaces is possible; studies with dyes indicate that the extent and nature of their aggregation, their surface orientation, and their solvation can be studied. Essentially, the outside of a glass fiber waveguide is similar to the inside of a microbore capillary column, and the evanescent wave associated with the guided waves internal to the fiber provides an excellent probe technique. Because cylindrical waveguides make excellent FIA detectors, such experiments are simple to perform.

John F. Giuliani, Naval Research Laboratory, Washington, DC 20375

An inexpensive, easily prepared planar waveguide (*13*). Partially polymerized samples of vinyl esters (Derakane, Dow) admixed with a photocatalyst such as uranyl perchlorate are placed on the surface of a microscope slide and formed into a thin layer by floating a coverslip on the surface. A laser beam then photopolymerizes a small narrow section of the film. The coverslip is removed and the unpolymerized material washed away; the remaining film is a waveguide sensor for ammonia and toluene. The probe optical beam is butt coupled into the thick film, and the monitored beam exits from the opposite end. In the case of toluene, swelling of the waveguide may be the source of the detector's response. With ammonia, an ionic interaction with pendant carboxyl functions probably affects the film's optical transmission characteristics. Although the sensors have minimum detection limits of several thousand parts per million, these limits can be enhanced several orders of magnitude by reductions in thickness and increases in length of the films.

Similar detectors are constructed using commercial polyene–polythiol mixtures (Norland). These materials contain their own photocatalyst, a benzophenone, and can be polymerized with mercury arc lamps. These waveguides have been used to detect chloroform and acetone.

Measurement of the solubility parameters of new polymeric solid films (*14*). Cylindrical glass capillaries, 90 × 1-mm o.d., 0.8 mm i.d., are coated

Leak-tight Valves & Fittings for Analytical Instrument Applications

The leak-tight technology of the SWAGELOK Companies is built into all the products you see here.

They work with each other to give you design flexibility. You can select sizes, shapes, materials and ratings to handle *your* service conditions.

They're all manufactured to the same standards of precision and quality control. You can count on consistent tolerances, compatible end connections, and reliable seals.

They're available locally from Authorized Sales and Service representatives. You can save money through efficient purchasing, controlled inventories, and on-time delivery.

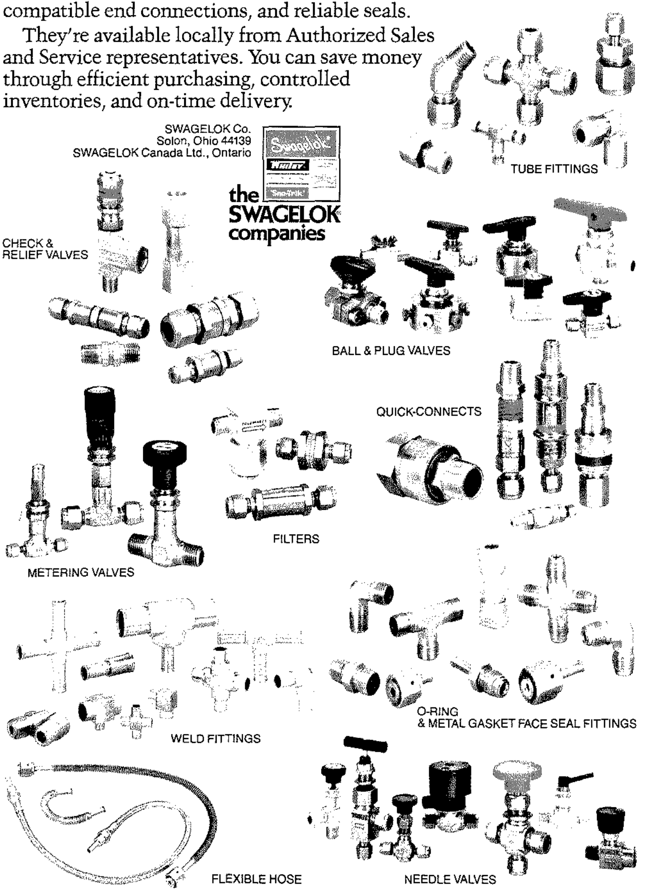

© 1988 SWAGELOK Co., all rights reserved SW4-fa

These Products are subjects of patent or patents pending

CIRCLE 154 ON READER SERVICE CARD

Choosing a graduate school?

Need to know who's doing research critical to yours?

New edition just published!

The ACS Directory of Graduate Research 1989

All the information you need on chemical research and researchers at universities in the U.S. and Canada . . . in a single source.

Includes listings for chemistry, chemical engineering, biochemistry, pharmaceutical/medicinal chemistry, clinical chemistry, and polymer science.

Lists universities with names and biographical information for all faculty members, their areas of specialization, titles of all papers published within the last two years, and individual telephone numbers, FAX numbers, and computer addresses.

Provides a statistical summary of academic chemical research—with information by department on numbers of full- and part-time faculty, postdoctoral appointments, graduate students, and M.S. and Ph.D. degrees granted.

What you'll find inside . . .

Information on . . .

- 683 academic departments
- 11,936 faculty members
- 68,276 publication citations

Listings for . . .

- chemistry
- chemical engineering
- biochemistry
- pharmaceutical/medicinal chemistry
- clinical chemistry
- polymer science

1436 pages (1989) Clothbound
Price:
US & Canada $55.00
Export $66.00

No academic institution or chemically oriented business can afford to be without the ACS Directory of Graduate Research 1989! Order today by calling TOLL FREE (800) 227-5558. In Washington, D.C., call 872-4363. Or use the coupon below.

Please send me ______copy(ies) of the ACS Directory of Graduate Research 1989.
Price: US & Canada $55.00 Export $66.00.

☐ Payment enclosed (make checks payable to American Chemical Society).

☐ Purchase order enclosed. P.O.# ______

Charge my: ☐ MasterCard/VISA ☐ American Express ☐ Diners Club/Carte Blanche

Account # ______ Expires ______

Signature ______

Phone ______

Ship books to:

Name ______

Address ______

City, State, ZIP ______

ORDERS FROM INDIVIDUALS MUST BE PREPAID. Please allow 4-6 weeks for delivery. Prices are quoted in U.S. dollars. Mail this order form with your payment or purchase order to:

American Chemical Society, Distribution Office Dept. 705,
P.O. Box 57136, West End Station, Washington, D.C. 20037.

705

Are you washing money down the drain?

Figure it out for yourself...

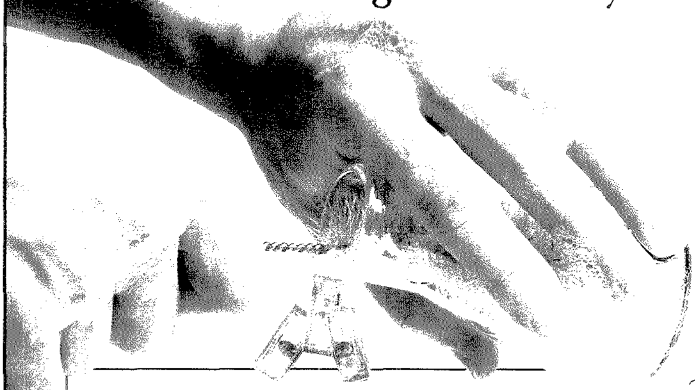

Your Cost for Hand Washing:

A. Number of pieces washed per day ....______

B. Amount of time spent washing them ......______

C. How much do you pay the person who washes labware? ....$______ hr.

D. **Your cost for labor (BxC)** ....$______

E. Electricity to heat cold water ($.17 per load) ______
(Load capacity = that of FlaskScrubber/SteamScrubber)

F. Water ($.10 per load) ....______
(Load capacity = that of FlaskScrubber/SteamScrubber)

G. Detergent ($.14 per load)................______
(Load capacity = that of FlaskScrubber/SteamScrubber)

Your total daily cost for hand washing (add lines D thorugh G) ....$______

*Electricity, water, detergent prices represent an average. Your actual costs may vary depending on your location.

Your Cost Using the FlaskScrubber and SteamScrubber:

A. Number of pieces washed per day ....______

B. Number of FlaskScrubber/SteamScrubber loads washed per day ....______
Capacity:

FlaskScrubber	SteamScrubber
34 100 ml flask = 1 load	125 100 ml beaker = 1 load
25 200 ml flask = 1 load	75 250 ml beaker = 1 load
20 500 ml flask = 1 load	25 1,000 ml beaker = 1 load

C. Amount of time for loading based on eight pieces per minute ....______

D. How much do you pay the person who would load the FlaskScrubber/SteamScrubber? ...$______ hr.

E. **Your cost for labor (CxD)**.............$______

F. Electricity ($.23 per load)...............______

G. Water ($.06 per load) ....______

H. Detergent ($.17 per load)...............______

Your total daily cost using the FlaskScrubber and/or SteamScrubber (add lines E thru H) ..$______

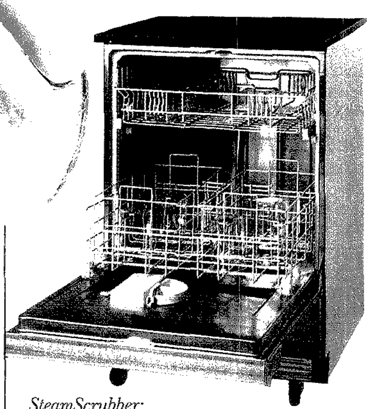

SteamScrubber:
Your general purpose labware washer.

How much could LABCONCO'S FlaskScrubber™ and SteamScrubber™ be saving you?

Fill out the above chart and compare for yourself the cost of hand washing to using a Labconco SteamWasher.

Not only will Labconco's SteamWashers save you money, but will provide you with consistently cleaner glassware. Both the FlaskScrubber and SteamScrubber use steam to get into the hardest to reach places. The steam moistens and loosens even the toughest baked on chemicals to be washed away. This is followed by purified water rinse and dry cycles which guarantee you sparkling clean, uncontaminated glassware. All without moving glassware to a separate oven and without leaving your lab.

Labconco FlaskScrubbers and SteamScrubbers are backed with our commitment to quality as well as a nationwide service network. For more information contact your laboratory supply dealer or call toll free **1-800-821-5525.**

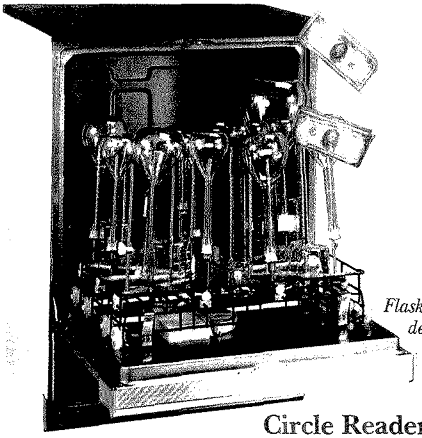

FlaskScrubber: Specially designed to clean narrow-necked labware.

LABCONCO®

Labconco Corporation
8811 Prospect
Kansas City, MO 64132
(816) 333-8811, Telex: 4-2568

Circle Reader Service # 88

with a thin polymer film by drawing the capillary out of a polymer solution. The resulting films are 0.06–0.1 μm thick. Light is coupled into the butt end of the capillary where it interacts evanescentally with the film. As the amount and nature of organic solvents in contact with the films change, the relative transmission of the waveguide is altered. This results from changes in the total internal reflectance properties of the polymer-film/glass interface, which presumably result from the partial solubilization of the adsorbed vapor into the film. The process most likely softens the material, permitting better optical contact with the glass.

Leon N. Klatt, Oak Ridge National Laboratory, Oak Ridge, TN 37831

Measurement of LiBr concentration in aqueous solutions used for heat transfer (*15*). Stripped fiber-optic waveguides are placed at user-selectable sites within operating heat absorption machines; the RI of the solution is then determined by measuring light loss from the unclad segment. Changes in fluid RI alter the angle at which light rays are totally internally reflected at the core/fluid interface, thereby altering the light transmission efficiency of the fiber. The average standard deviation of such a sensor is 0.1% (w/w) LiBr over a range of 30–50% (w/w) LiBr. The RI measurement has a precision of 0.0003 units. An ammonia sensor, based on the same principle, has a precision of 0.2% (w/w) NH_3.

Jinn-Nan Lin, University of Utah, Salt Lake City, UT 84112

Optical detection of interfacially bound biological molecules in remote environments (*16*). Total internal reflection fluorescence (TIRF) shows potential as the basis for remote fluoroimmunoassay techniques. Evanescent excitation of fluorescently labeled antigens complexed with surface immobilized antibodies (or vice versa) on integrated planar waveguide optics is easily accomplished. Variable-angle TIRF can be used to determine the concentration and thickness of an adsorbed fluorescent layer (Figure 7b). The concentration–distance profile of fluors at the interface results directly from the numerical inverse Laplace transform of the fluorescence angular spectrum representation wherein one of the angles (observation or incidence) is varied while the other angle is held fixed. Immunoglobulin protein films on quartz hemicylinders and polystyrene spun-coated films on planar waveguides have been used. The latter have demonstrated an ability to explore Langmuir–Blodgett deposited cyanine dye fatty acid derivative monolayers and surface-adsorbed films of dye-labeled immunoglobulin.

Marc D. Porter, Iowa State University, Ames, IA 50011

Remote pH and calcium ion sensing (*17*). A remote pH sensor can be based on immobilizing a direct azo dye, such as Congo Red, in a porous cellulosic polymer film. This is mounted in a flow cell, in-line with an entrance-and-exit fiber optic light pipe. Response times are typically less than 1.3 s, with a stability of a few percent over a 4-pH unit range. A similar approach results in a calcium ion sensor. Calcichrome is immobilized in a porous anion exchange polymer film; the scattered light, after reflection from the film, is monitored spectrophotometrically. Response is linear from 10^{-3} to 10^{-1} M Ca at pH 12.

It is also possible to monitor pH by measuring the internal reflectance spectrum of immobilized Congo Red dye in a base-hydrolyzed film of cellulose acetate mounted at the ZnSe element of a commercial CIRCLE cell (Spectra Tech). Peaks in the region from 1300 to 1275 cm^{-1} resulting from the N–N stretch in the azo moiety are observed. Protonation relaxes the selection rules, and this results in IR activity.

W. Rudolf Seitz, University of New Hampshire, Durham, NH 03824

Remote measurement of TNT (*18*) and a generic film. Membranes of poly(vinyl chloride) containing poly(oxyethylenamine) react with TNT to produce a reddish-brown product. This reaction can be monitored by a single fiber measuring changes in absorption; TNT levels as low as 0.1 ppm can be detected.

Crosslinking poly(vinyl alcohol) with glutaraldehyde produces a film with many possible applications, because the casting technique allows control of the amount of both indicator and substrate.

Michael J. Sepaniak, University of Tennessee, Knoxville, TN 37996

Antibody-based sensors for benzo[*a*]pyrene metabolites (*19*). A naturally fluorescent hydrolysis product of DNA adducts formed during benzopyrene metabolism is benzopyrenetetraol (BPT). A fiber-optic sensor is based on diffusion of BPT into the fiber's reagent phase, which contains monoclonal anti-BPT antibody. This reagent phase can be membrane entrapped or immobilized on 7-μm silica beads. The 325-nm line of a He–Cd laser provides excitation of the complex. The rate of change of sensor response is then measured; typical limits of detection are 10^{-10} M for 15-min incubations. Regenerable sensors that are being fabricated use a concentric layer of regenerating and rinsing capillaries around the central fiber-optic waveguide (Figure 6).

David R. Walt, Tufts University, Medford, MA 02155

Immobilization of reagents to fiber-optic probe tips (*20*). Direct attachment of an indicator monolayer to a fiber surface produces a sensor with very low signal levels. Some form of copolymerization process is often used to enhance the amount of reagent and to eliminate the diffusion membrane commonly employed. Surface activation can be accomplished by vapor-phase silanization reactions. [γ-(Methacryloxy)propyl]trimethoxysilane and (aminopropyl)triethoxysilane are silanizing reagents that yield vinyl and amino surfaces, respectively. However, plasma deposition is a superior method for homogeneous surface coverage. Fibers are treated inside a plasma chamber with monomer vapors, and an electric discharge through the vapor forms a highly reactive plasma that affects the glass surface. For example, an alkylamine surface can be created by treating the glass with a hexane plasma followed by an ammonia plasma. A variety of derivatized, spectrophotometrically active molecules can react with such surfaces. To this end, the plasma-treated fiber tips are placed in a solution containing monomer, crosslinking agent, functionalized indicator reagent, and polymer initiator appropriate to the analyte for which the sensor is being designed.

Delivery of reagents to fiber-optic probe tips. Work in this lab has also suggested another way to deliver fresh reagent to the working area. Dyes incorporated into ethylene–vinyl acetate copolymers are slowly released on contact with aqueous solutions, and pH-sensitive detectors based on this principle have been demonstrated. This suggests that continuous-release strategies will free optrode sensors from the confines imposed by the need for reversible systems, the penalties associated with hysteresis or side reactions, and the difficulties associated with tip replacement.

Conclusion

Waveguide sensors are obviously limited only by the imagination of the chemist. Fiber-drawing technology is only in its infancy; polarization-preserving fibers, dual fibers, IR fibers, and metal-jacketed fibers all have exciting poten-

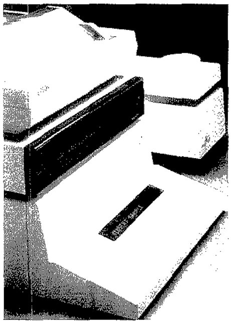

New Thermal Analysis System

Modular METTLER TA4000 grows with your needs — from entry level DSC package under $25,000 to multi-tasking PC-aided system with graphics. Add DSC, TG or TMA modules anytime — new TC11 Evaluation/Control Center contains all software. For maximum versatility, add an IBM PS/2 and TA72.1 GraphWare. **Mettler Instrument Corp., Box 71, Hightstown, NJ 08520. 1-800-METTLER (NJ 609-448-3000).**

CIRCLE 100 ON READER SERVICE CARD

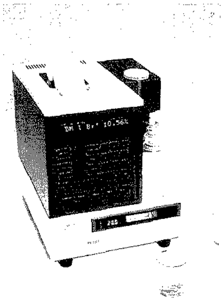

Density Meters: Temp Control Benchtop, Handheld Portable

New METTLER/KEM DA300 4-place density/specific gravity meter (shown) has temp control to 90°C, stores 7 methods, calculates concentrations and temp conversions, displays and prints results. Sample pump, changer, BRIX, API, % alcohol optional. DA110 3-place portable displays results, stores 99 analyses for later output to printer/computer. **Mettler Instrument Corp., Box 71, Hightstown, NJ 08520. 1-800-METTLER (NJ 609-448-3000).**

CIRCLE 103 ON READER SERVICE CARD

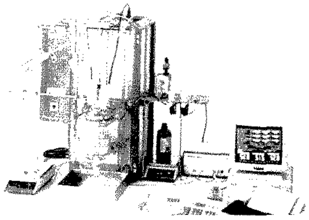

Benchtop Pilot Plant

The METTLER RC1 Reaction Calorimeter tests new processes, optimizes existing ones. As an automated laboratory reactor, it controls all process variables, collects data on-line, provides plant scale-up data on the lab bench. Develop/optimize processes, assess hazards, do small-scale synthesis/production. **Mettler Instrument Corp., Box 71, Hightstown, NJ 08520. 1-800-METTLER (NJ 609-448-3000).**

CIRCLE 101 ON READER SERVICE CARD

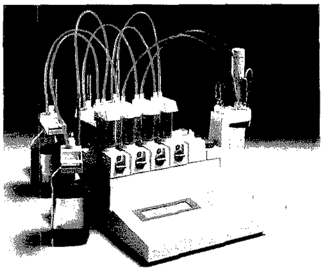

Multitasking 4-Burette Model Leads Autotitrator Line

New DL70 can create methods while running titrations. Auto-switching of four burettes and electrodes for increased throughput and more complex titrations with one keystroke, plus sample changer capability. The DL70 stores 35 methods. Also available: single-burette DL25 (50 methods) and DL21 (one method), plus TS² software for unlimited methods, PC graphics/data storage. **Mettler Instrument Corp., Box 71, Hightstown, NJ 08520. 1-800-METTLER (NJ 609-448-3000).**

CIRCLE 102 ON READER SERVICE CARD

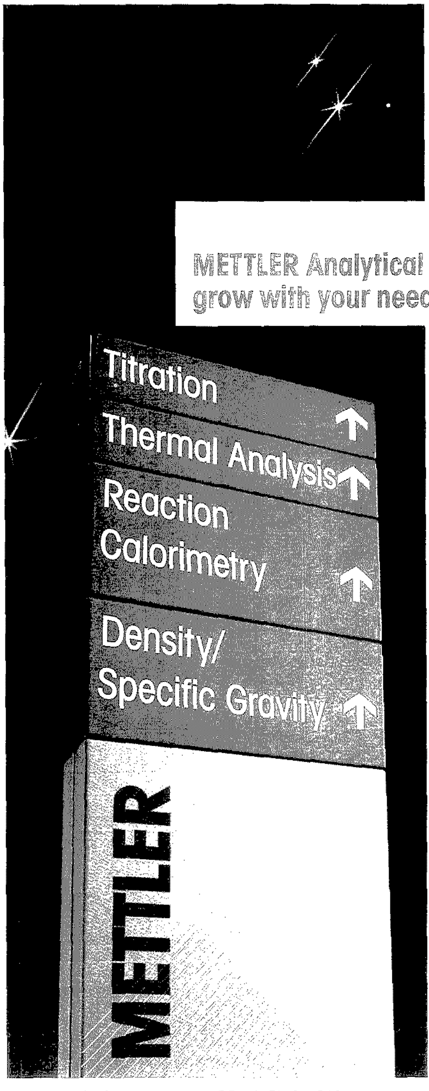

Get quality results today, cost-effectively... expand into tomorrow's systems.

METTLER Analytical Instruments grow with your needs.

Autotitrators include new multi-burette models, single-method to 50-method models, Karl Fischer instrument. Optional software permits PC data storage, graphics.
Thermal Analysis systems perform DSC, TMA, TG by simply adding modules, and work with PCs for graphics and curve comparisons.
Reaction Calorimetry. The RC1 is both a benchtop pilot plant for process development and an automated lab reactor.
Density/specific gravity. Lab meters calculate concentration, BRIX, API, % alcohol. Handheld model simplifies field and production line tests.
Backed by METTLER Service Plus®.

Mettler Instrument Corporation
Box 71, Hightstown, N.J. 08520
1-800-METTLER
(N.J. 609-448-3000)

METTLER

6820.72

CIRCLE 104 ON READER SERVICE CARD

tial. This area presents a unique interface between the practices of chemistry and physics. Several recent summaries of research (*21–23*) will help those interested in building their own new sensors based on optical waveguides.

The author would like to thank all the investigators who shared reprints, preprints, and personal communications, thus making preparation of the manuscript possible. He would also like to acknowledge the efforts of Lloyd Burgess, now at the Center for Process Control Analytical Chemistry at the University of Washington; Steve Choquette, now at the National Institute of Standards and Technology Biosensor Labs; and Jim Petersen, whose work initiated waveguide research at VPI & SU. Their results are reported briefly in this paper. Their willingness to educate their colleagues typifies a remarkable research group.

References

(1) Chabay, I. *Anal. Chem.* **1982,** *52,* 1071–80 A.

(2) a. Angel, S. M.; Garvis, D. G. *Appl. Spectros.* **1989,** *43,* 430–35; b. Angel, S. M.; Hirschfeld, T. B. U.S. Patent 4 729 668, 1988.

(3) Milanovich, F. P.; Garvis, D. G.; Angel, S. M.; Klainer, S. M.; Eccles, L. *Anal. Instrumen.* **1986,** *14,* 137–47.

(4) Kulp, T. J.; Camins, I.; Angel, S. M. *Anal. Chem.* **1987,** *59,* 2849–52.

(5) Angel, S. M.; Myrick, M. L. *Anal. Chem.* **1989,** *61,* 1648–52.

(6) a. Arnold, M. A.; Ostler, T. J. *Anal. Chem.* **1986,** *58,* 1137–40; b. Rhines, T. D.; Arnold, M. A. *Anal. Chem.* **1988,** *60,* 76–81.

(7) a. Arnold, M. A. *Anal. Chem.* **1985,** *57,* 565–66; b. Arnold, M. A. *Proceedings SPIE,* **1988,** *906,* 128–33; c. Wangsa, J.; Arnold, M. A. *Anal. Chem.* **1988,** *60,* 1080–82.

(8) Stephens, D. A.; Bohn, P. W. *Anal. Chem.* **1989,** *61,* 386–90.

(9) Carey, W. P.; DeGrandpre, M. D.; Jorgensen, B. S. *Anal. Chem.* **1989,** *61,* 1674–78.

(10) a. Burgess, L. W. Ph.D. Thesis, Virginia Polytechnic Institute and State University, 1984; b. Dessy, R. E. *Anal. Chem.* **1985,** *57,* 1188 A.

(11) Choquette, S. J. Ph.D. Thesis, Virginia Polytechnic Institute and State University, 1988.

(12) Petersen, J. V. Ph.D. Thesis, Virginia Polytechnic Institute and State University, 1989.

(13) a. Giuliani, J. F.; Kim, K. H.; Butler, J. E. *Appl. Phys. Lett.* **1986,** *48,* 1311–13; b. Giuliani, J. F. *Sensors & Actuators,* **1988,** *15,* 25–31.

(14) Giuliani, J. F. *J. Polym. Sci. Part B: Polym. Phys.* **1988,** *26,* 2197–2201.

(15) Klatt, L. N.; Bostick, D. T.; Perez-Blanco, H. *Proceedings SPIE* **1987,** *787,* 2–7.

(16) a. Ives, J. T.; Reichert, W. M.; Lin, J. N.; Hlady, V.; Reinecke, D.; Suci, P. A.; Van Wagenen, R. A.; Newby, K.; Herron, J.; Dryden, P.; Andrade, J. D. In *Optical Fiber Sensors*; Chester, A. N.; Martellucchi, S.; Vera Scheggi, A. M., Eds.; M. Nijhoff: Boston, 1987; pp. 391–97; b. Andrade, J. D.; Herron, J.; Lin, J. N.; Yen, H.; Kopecek, J.; Kopeckova, P. *Biomaterials,* **1988,** *9,* 76–79.

(17) a. Jones, T. P.; Porter, M. D. *Anal. Chem.* **1988,** *60,* 404–6; b. Chau, L. K.; Porter, M. D., Iowa State University, personal communication, 1988; c. Jones, T. P.; Porter, M. D. *Appl. Spectros.* **1989,** *43,* 576–79.

(18) a. Zhang, Y.; Seitz, W. R. *Anal. Chim. Acta,* in press; b. Zhang, Y.; Seitz, W. R.; Grant, C. L.; Sundberg, D. C. *Anal. Chim. Acta* **1989,** *217,* 217–27; c. Zhujun, Z.; Zhang, Y.; Wangbai, M.; Russell, R.; Sundberg, D. C. *Anal. Chem.* **1989,** *61,* 202–5.

(19) Tromberg, B. J.; Sepaniak, M. J.; Alarie, J. P.; Vo-Dinh, T.; Santella, R. M. *Anal. Chem.* **1988,** *60,* 1901.

(20) a. Munkholm, C.; Walt, D. R.; Milanovich, F. P.; Klainer, S. M. *Anal. Chem.* **1986,** *58,* 1427–30; b. Luo, S.; Walt, D. R. *Anal. Chem.* **1989,** *61,* 174–77.

(21) *Chemical Sensors and Microinstrumentation*; Murray, R. W.; Dessy, R. E.; Heineman, W. R.; Janata, J.; Seitz, W. R., Eds.; ACS Symposium Series 403, American Chemical Society: Washington, DC, 1989.

(22) Seitz, W. R. *C.R.C. Crit. Revs. in Anal. Chem.* **1988,** *19,* 135–73.

(23) Angel, S. M. *Spectroscopy* **1987,** *2,* 38–47.

Raymond E. Dessy received his B.S. degree in pharmacy in 1953 and his Ph.D. in chemistry in 1956 from the University of Pittsburgh. After nine years at the University of Cincinnati, he joined the faculty of Virginia Polytechnic Institute and State University in 1966. From 1982 to 1986, he was contributing editor of ANALYTICAL CHEMISTRY'S A/C INTERFACE *feature and is currently associate editor of* Chemometrics and Intelligent Laboratory Systems. *His research group is now working on the development of new sensors for analytical instruments, artificial intelligence for chemical processes, novel uses of robots in the lab, and better means of acquiring and handling laboratory data. He is internationally recognized for his teaching on laboratory automation.*

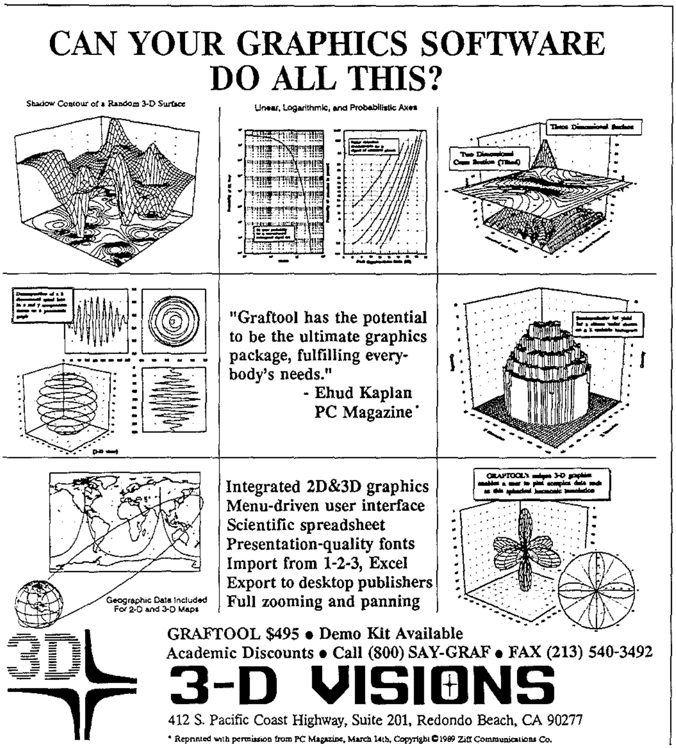
CAN YOUR GRAPHICS SOFTWARE DO ALL THIS?

"Graftool has the potential to be the ultimate graphics package, fulfilling everybody's needs."
- Ehud Kaplan
PC Magazine*

Integrated 2D&3D graphics
Menu-driven user interface
Scientific spreadsheet
Presentation-quality fonts
Import from 1-2-3, Excel
Export to desktop publishers
Full zooming and panning

GRAFTOOL $495 • Demo Kit Available
Academic Discounts • Call (800) SAY-GRAF • FAX (213) 540-3492

3-D VISIONS

412 S. Pacific Coast Highway, Suite 201, Redondo Beach, CA 90277

* Reprinted with permission from PC Magazine, March 14th, Copyright ©1989 Ziff Communications Co.

CIRCLE 36 ON READER SERVICE CARD
Shadow Contour of a Random 3-D Surface
Linear, Logarithmic, and Probabilistic Axes
Geographic Data Included For 2-D and 3-D Maps

CORRECTION

Fluorescence Lifetime Filtering
Linda B. McGown (*Anal. Chem.* **1989,** *61,* 839 A–847 A)

Equation 2 should read:

$$E(t) = A(1 + m_{ex} \sin \omega t)$$

Equation 3 should read:

$$F(t) = A' \times [1 + m_{ex} m \sin (\omega t - \Phi)]$$

All for one?... or one for all!

Switch from one-at-a-time AA to all-at-once ICP.

When it's your job to produce fast and accurate elemental analyses, why should you end up with a scattered set of single-element determinations? All the analytical results you need come in one package, almost instantaneously, when you use simultaneous ICP. Comprehensive results. More sensitive, more reliable, and much less expensive to obtain.

It may be time to investigate the difference. Take a critical look at the rate of your sample throughput and how it may be affecting your high cost per analysis. Like so many other laboratories, you're likely to discover that it's time to move sharply from one-at-a-time AA to simultaneous ICP. Baird's line of ICP instrumentation is way ahead in making single-element analysis obsolete for most applications. And with the Baird UDX ultrasonic nebulizer, this includes a major portion of your graphite furnace overload.

Share in the new all-togetherness that Baird brings to modern ICP. Call or write. You'll get nothing but the facts. Baird Corporation, Analytical Instruments Division, 125 Middlesex Turnpike, Bedford, Massachusetts 01730. (617) 276-6163.

BAIRD ICP

An Imo Industries Company

CIRCLE 22 ON READER SERVICE CARD

SIXTH IN A SERIES OF ONE-MINUTE MESSAGES ON ION ANALYSIS

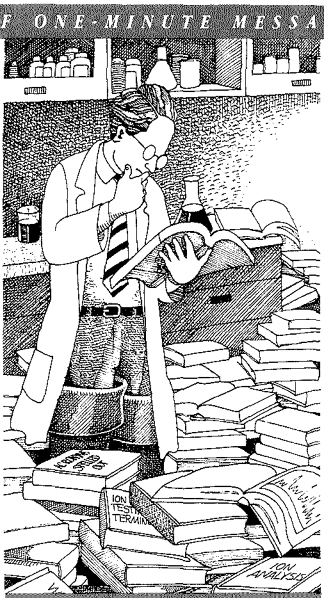

HOW TO DECIPHER ION TESTING TERMINOLOGY

We know. You thought buying an automated ion analyzer would be simple. But then, the complicated scientific language turned your search into a gulf of confusion, correct? And you began to ask yourself "is there an easier way through this?" Well, yes there is.

Find a voice of reason.

At ALPKEM, we have intentionally developed capability across a spectrum of ion analysis technologies. We do not have to advocate any single approach. Instead, we can listen to you, explain options, and concentrate on fitting your lab with the process that works best for you.

We serve the water, pharmaceutical, tobacco, oceanography, fertilizer and industrial quality control markets. We offer instruments for segmented microcontinuous flow analysis. Or unsegmented flow injection analysis, or ion chromatography. You name it. If it is an ion test, we do it.

Seek first to understand.

We listen before we talk. We find out what is happening in your lab: the work you are doing, the problems you are facing, the help you are looking for.

Then, depending on need, we lay out instrument options and discuss the technology tradeoffs. Clearly. So you truly understand your own situation, and can make an equipment choice you will still feel good about years from now.

Be willing to learn.

Let us send you our booklet *A SHORT COURSE ON CONTINUOUS FLOW ANALYSIS.* It is a concise description of the merits of major ion analyzer technologies used today. It is free. And, for an even closer look, ask for a demonstration.

Call us.

ALPKEM can help you see through the clutter of analysis equipment claims, and find a real solution for your ion testing. Just call your nearest Perstorp Analytical Sales Company. No terminology glossary required.

ALPKEM®

A Perstorp Analytical Company
P.O. Box 1260, Clackamas, OR 97015 USA
PHONE: 503-657-3010, FAX: 503-657-5288
TLX: 910-380-9084

CANADA: Labserco Ltd., 416-842-1951 ◆ W.GERMANY: Perstorp Analytical GmbH, 06106-13072 ◆ GREAT BRITAIN: Perstorp Analytical Ltd., 0454-417798
FRANCE: Perstorp Analytical SA, 1-42 602424 ◆ HOLLAND: Perstorp Analytical BV, 01860-14822 ◆ SWEDEN: Tecator AB, 042-423 30
AUSTRALIA: Linbrook, 3-544-3811 ◆ JAPAN: JEOL Trading Ltd., 03-567-4741 ◆ TAIWAN, KOREA: ALPKEM Asia Ltd., 02-771-4491

CIRCLE 1 ON READER SERVICE CARD

MEETINGS

Conferences

■ **Analysis and Its Commercial Significance in the '90s.** Nov. 8–10, 1989. Ferndown, Dorset, U.K. *Contact: C. J. Jackson, c/o Health & Safety Executive, Broad Lane, Sheffield S3 7HQ, U.K.*

■ **Meeting of the American Academy of Forensic Sciences.** Feb. 19–24. Cincinnati, OH. *Contact: American Academy of Forensic Sciences, 225 South Academy Blvd., Colorado Springs, CO 80910*

■ **2nd International Symposium on Applications of Analytical Techniques to Industrial Process Control (ANATECH '90).** April 3–5. Noordwijkerhout, The Netherlands. *Contact: Willem van der Linden, Laboratory for Chemical Analysis—CT, University of Twente, P.O. Box 217, NL-7500 AE Enschede, The Netherlands*

■ **Annual Meeting of the American Oil Chemists Society.** April 22–26. Baltimore, MD. *Contact: American Oil Chemists Society, 1608 Broadmoor, P.O. Box 3489, Champaign, IL 61821*

■ **International Symposium on Measurement of Toxic and Related Air Pollutants.** April 30–May 3. Raleigh, NC. *Contact: Bruce Gay, Atmospheric Research Exposure Assessment Laboratory, U.S. EPA, Research Triangle Park, NC 27709*

■ **Meeting of the Electrochemical Society.** May 6–11. Montreal, Canada. *Contact: Electrochemical Society, 10 South Main St., Pennington, NJ 08534*

■ **5th European Congress of Biotechnology.** July 8–14. Copenhagen, Denmark. *Contact: Edvard Falch, Novo Industri A/S, Novo Alle 1, DK-2880 Bagsvaerd, Denmark*

■ **Meeting of the American Association for Clinical Chemistry.** July 22–26. San Francisco, CA. *Contact: AACC, 1725 K St., N.W., Washington, DC 20006*

■ **17th Annual Meeting of the Federation of Analytical Chemistry and Spectroscopy Societies.** Oct. 7–12. Cleveland, OH. *Contact: Charles J. Belle, Lucas Aerospace PEC, 4259 W. 192nd St., Fairview Park, OH 44126 (216-662-1001)*

■ **3rd International Symposium on Analytical Methods in Biotechnology (Anabiotec '90).** Oct. 28–31. San Francisco, CA. *Contact: Shirley Schlessinger, 400 East Randolph Dr., Suite 1015, Chicago, IL 60601 (312-527-2011)*

Short Courses and Workshops

■ **Workshop on Gas Chromatographic Analysis of Bacterial Fatty Acids.** Rockville, MD. Nov. 1–3. *Contact: Doug Drabkowski, American Type Culture Collection, 12301 Parklawn Dr., Rockville, MD 20852 (301-231-5566)*

■ **Course on Quality Control for Asbestos Analysis Laboratories.** Los Angeles, CA. Nov. 1–3.

■ **Course on Sampling and Evaluating Airborne Asbestos Dust.** Los Angeles, CA. Nov. 6–10.

■ **Course on Industrial Hygiene Sampling Strategies.** Los Angeles, CA. Nov. 15–17.

For information on the above courses in Los Angeles, contact University of Southern California, Institute of Safety and Systems Management, Professional Programs, 3500 South Figueroa St., Suite 202, Los Angeles, CA 90007 (213-743-6523).

Call for Papers

■ **International Conference on Tropospheric Ozone and the Environment.** Los Angeles, CA. March 19–22. The conference will feature papers on topics that include air quality data analysis, modeling and monitoring studies, ozone ecological and health effects, and attainment strategies. Prospective authors should submit 300–500-word abstracts by Nov. 15 to Ronald Berglund, Union Carbide Corp., 3200 Kanawha Trpk. 770-320, South Charleston, WV (304-747-4985).

■ **International Symposium on Measurement of Toxic and Related Air Pollutants.** Raleigh, NC. April 30–May 3. The symposium will feature invited and contributed papers on topics that include hazardous waste emissions, acid deposition, source measurements, quality assurance, ambient measurements, indoor air pollution, radon measurements, complex chemical data analysis, and global climate change and stratospheric ozone. Prospective authors should submit 200-word abstracts, including title, author(s), and affiliation(s), to Bruce Gay, Atmospheric Research Exposure Assessment Laboratory, U.S. EPA, Research Triangle Park, NC 27709, or R.K.M. Jayanty, Research Triangle Institute, P.O. Box 12194, Research Triangle Park, NC 27709. Deadline for submission of abstracts is Nov. 30.

■ **7th Symposium on Radiation Measurements and Applications.** Ann Arbor, MI. May 21–24. Symposium topics include data acquisition; analysis systems and methods; particle-induced X-ray emission and radiation-induced fluorescence; analytical standards and elemental analysis; and applications in areas such as energy and environmental technology. Prospective authors should submit 300–500 word summaries by Jan. 26 to Helen Lum, 3034 Phoenix Memorial Laboratory, University of Michigan, Ann Arbor, MI 48109 (313-764-6214).

■ **3rd International Symposium on Polymer Analysis and Characterization.** Brno, Czechoslovakia. July 23–25. The symposium will consist of poster sessions, invited lectures, and roundtable discussions on recent advances in polymer characterization techniques and selected applications. Topics include chromatography, spectroscopy, light scattering, rheology, thermal analysis, and solution properties of polymers. Authors wishing to contribute poster presentations should submit titles by Nov. 30 to Howard Barth, E. I. du Pont de Nemours & Co., Experimental Station E228/238, P.O. Box 80228, Wilmington, DE 19880 (302-695-4354) or Josef Janca, Inst. Analytical Chemistry, Czechoslovak Academy of Sciences, Leninova 82, 611 42 Brno, Czechoslovakia.

These events are newly listed in the JOURNAL. See back issues for other events of interest.

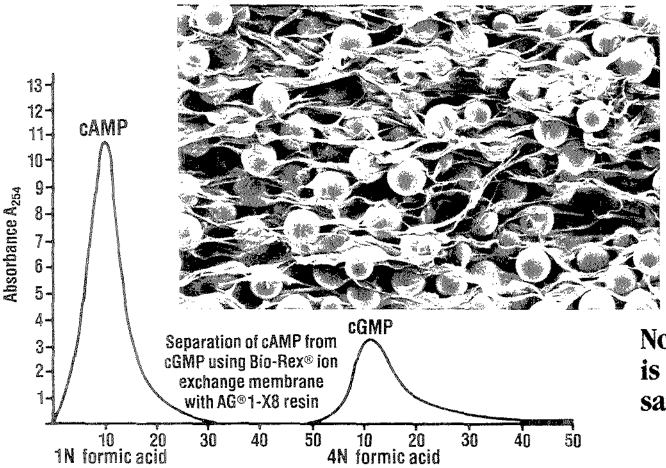

Separation of cAMP from cGMP using Bio-Rex® ion exchange membrane with AG®1-X8 resin

Now chromatography is as easy as sample filtration.

Unique membrane allows chromatography without the column.

There's nothing remotely like the new porous Bio-Rex® chromatography membranes from Bio-Rad. These membranes consist of 90% chromatographic media in a web of PTFE, which results in high capacity and high flow rate.

As the electron micrograph shows, these membranes provide a new support system for column chromatographic media. Because the membranes are porous, they allow **simultaneous** separation and filtration, saving you valuable time. And you can forget about column packing and filtering resin beads, saving even more time!

The Bio-Rex chromatographic membranes are equally effective for both batch and flow-through processes.

At a glance:

- High capacity, high flow rate
- Results equivalent to packed columns
- Resistant to organic solvents
- Choice of three ion exchange membrane types—strong anion, strong cation, and chelating
- Available in free membrane or sample preparation disc form
- pH stable 1-14

An alternative to traditional column chromatographic methods, these convenient, easy-to-use membranes will save you time, effort, and expense. Find out more. Call 800-843-1412 and request Bulletin 1428.

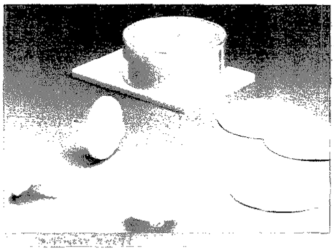

BIO-RAD

Chemical Division

1414 Harbour Way South
Richmond, CA 94804
(415) 232-7000
800-843-1412

Also in Rockville Centre, NY; Hornsby, Australia; Vienna, Austria; Brussels, Belgium; Mississauga, Canada; Watford, England; Paris, France; Munich, Germany; Hong Kong; Milan, Italy; Tokyo, Japan; Utrecht, The Netherlands; and Glattbrugg, Switzerland.

It's the Chemistry that Counts.™

CIRCLE 24 ON READER SERVICE CARD

Scanning Electrochemical Microscopy

Royce C. Engstrom and Christine M. Pharr
Department of Chemistry
University of South Dakota
Vermillion, SD 57069

Modern electroanalytical chemistry relies on increasingly complicated interfacial designs to achieve improved selectivity, sensitivity, and adaptability. Chemical modifications, polymer films, composite materials, and microelectrode arrays are examples of schemes in which the electrode–solution interface possesses spatial heterogeneity on a dimensional level ranging from the microscopic to the atomic. The chemical and physical *structure* of such surfaces can now be characterized with spatial resolutions ranging from the micrometer to the atomic levels using techniques such as optical and electron microscopy, ESCA, Raman microprobe, and scanning tunneling microscopy (STM). However, these techniques do not directly provide information about electrochemical *activity*. Knowledge of structure–activity relationships could ultimately lead to optimized designs of electroanalytical devices and increase our ability to interpret data generated with complicated electrode designs.

FOCUS

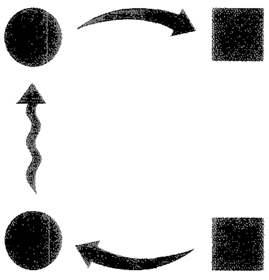

There are many examples of questions related to the spatial distribution of electrochemical activity. For instance, what fraction of a composite electrode surface is in electrochemical communication with the solution? Are electrochemical "hot spots" present on surfaces where events such as nucleation occur? Do defects exist in a polymer film, thereby circumventing the role of the film? What are the spatial relationships between centers of chemical activity and electrochemical activity on modified electrodes?

Several techniques are used to spatially resolve electrochemical activity. For example, scanning microreference electrodes (*1–3*), iontophoretic application of an electroactive probe species (*4, 5*), and imaging of refractive index gradients (*6*) provide resolution in the range of tens to hundreds of micrometers. Resolution in the range of visible light microscopy is obtained through visualization of electrodeposited material (*7*), imaging of electrogenerated chemiluminescence (*8, 9*), and the monitoring of localized laser-induced photocurrents (*10, 11*).

Scanning electrochemical microscopy (SECM) is the name applied by Bard and co-workers (*12*) to the process of using a microelectrode to amperometrically or voltammetrically detect material immediately adjacent to the surface of interest. Because an electrochemical process is involved, the technique is carried out in situ, enabling the study of electrochemical activity with high spatial resolution. The current at the microelectrode is faradaic in nature, in contrast to the tunneling currents measured in STM. Although STM has been applied successfully in situ, measures to eliminate faradaic currents must be taken because these currents can easily swamp out tunneling currents (*13, 14*).

The concept behind what has come to be called SECM was first demonstrated in 1986, when microelectrodes were used to amperometrically detect

0003-2700/89/A361-1099/$01.50/0
© 1989 American Chemical Society

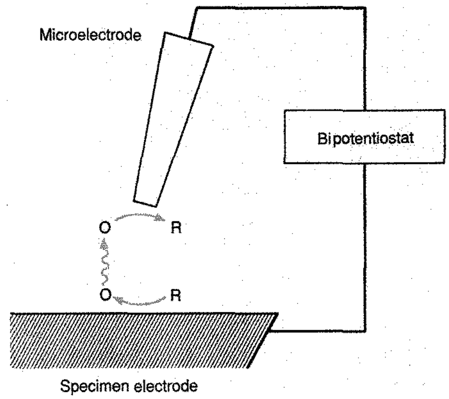

Figure 1. Schematic of the scanning electrochemical microscope operated in the generator–collector mode.

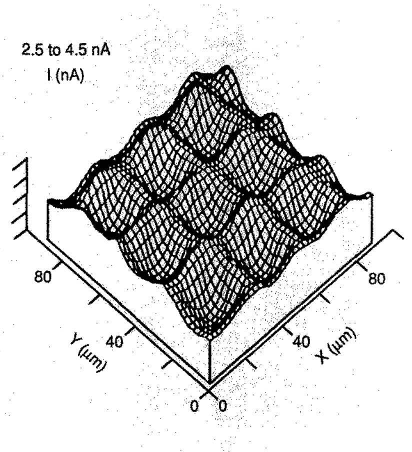

Figure 2. Scans of a gold minigrid obtained in the feedback mode of SECM.

Current is enhanced over the gold lines because of recycling of electroactive material. (Adapted from Reference 20.)

chemical species produced at a specimen electrode (*15*). The potentials of both electrodes are controlled independently (with respect to some reference electrode) using a bipotentiostat (Figure 1). In the presence of a reversible redox couple, the electrodes are operated in a generator–collector mode. The specimen potential is stepped or scanned to a value that causes the "forward" electrochemical reaction to occur, while the microelectrode potential is held constant at a value that causes the "reverse" reaction to occur. Thus, material generated at the specimen electrode diffuses to the microelectrode tip, generating a microelectrode current. Mapping of electrochemical activity is accomplished by incrementally moving the microelectrode over the specimen surface and repeating the specimen potential waveform at each location. If the microelectrode is positioned over a region of electrochemical activity, the microelectrode generates a current. Over a region of inactivity, however, no microelectrode current flows, or it arises only after a time delay associated with lateral diffusion of material from the generation site to the microelectrode.

The microelectrode probes are made of carbon fibers, either in a beveled disk configuration as is commonly used for in vivo voltammetry (*16*) or as electrochemically etched cylinders with tip diameters of 1–3 μm. Positioning of the microelectrode is controlled in three dimensions with a stepper-motor-driven positioner capable of 1-μm increments. Potassium ferrocyanide is present in solution at millimolar concentrations. Spatial resolution of electrochemical activity is demonstrated over specimen electrodes prepared as platinum arrays and over heterogeneous electrodes prepared from reticulated vitreous carbon. Both one- and two-dimensional "maps" of electrochemical activity are created with a spatial resolution of approximately 20 μm. The technique is also used to spatially resolve concentrations in the direction perpendicular to the specimen electrode surface, permitting the characterization of transient species residing in the diffusion layer of the specimen electrode (*17*). Resolution in the perpendicular direction is on the order of 2–3 μm, and a temporal resolution of 20 ms is obtained. The shape of experimentally determined concentration profiles is used to distinguish between two possible mechanisms for the chemical decomposition of the product of the specimen electrode reaction.

Bard and co-workers (*18, 19*) recently increased the versatility of SECM by employing modes of operation other than the simple generator–collector scheme described above. For example, instead of holding the microelectrode potential constant, its potential is scanned while the specimen electrode is generating, allowing for voltammetric characterization of species in the diffusion layer. Another mode of operation involves application of a sinusoidal waveform to the generator electrode while monitoring the concentration of electrogenerated species with the microelectrode. In this latter case, the microelectrode current is a damped sinusoid whose amplitude decreases with increasing distance from the specimen.

An especially interesting approach to SECM is the "feedback mode" (*19*), in which the microelectrode directly electrolyzes a species present in bulk solution and does not serve as the collector of something generated at the specimen. The specimen is not operated as a generator; therefore, it does not have to be connected to a power source. In fact, the specimen need not be a conductor at all.

When the distance between the two electrodes is large compared with the size of the microelectrode diffusion layer, the microelectrode current is unaffected by the specimen regardless of whether the specimen is conductive or nonconductive. However, when the microelectrode is close enough so that the specimen is within the diffusion layer of the microelectrode, the microelectrode response is affected in a way that depends on the nature of the specimen. If the specimen is conductive and held at the appropriate potential, the microelectrode current is enhanced because of recycling of electroactive materials between the two electrodes. If the specimen is nonconductive, the microelectrode current is diminished, because the substrate blocks diffusion of electroactive material from bulk solution to the microelectrode.

Figure 2, taken from the work of Kwak and Bard (*20*), illustrates the feedback mode over a conductive specimen. Scans are taken over a section of

RF POWER
As You Like It.

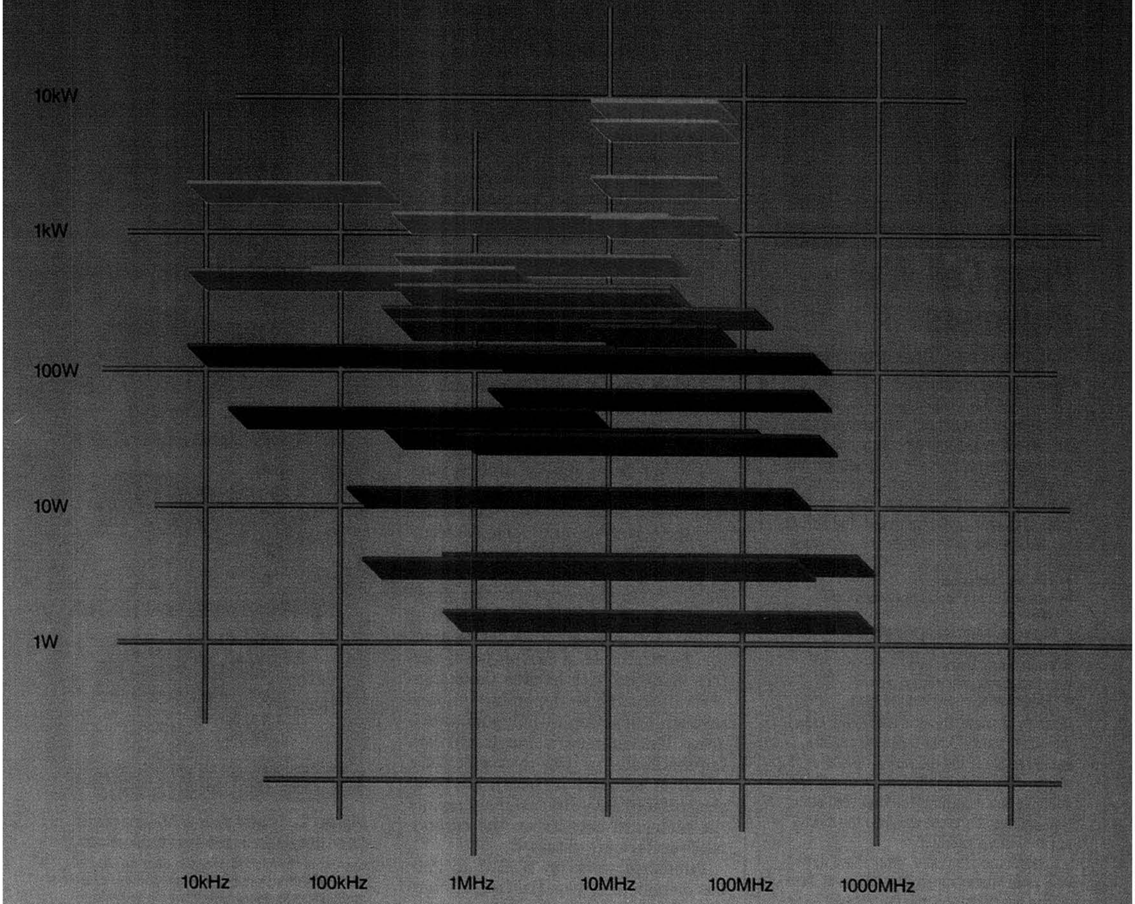

All solid state. Unconditionally stable. Compact. Tremendously versatile. Whatever your need for RF Power, ENI offers you a choice of Class A power amplifiers unsurpassed in quality. Our wide line spans a frequency spectrum from 10kHz to 1GHz with power outputs that range from 300 milliwatts to over 4000 watts.

These units can be driven by virtually any signal source. They're completely broadband and untuned, amplifying inputs of AM, FM, TV, SSB, and pulse modulations with minimum distortion. Their unconditional stability and fail-safe design make them impervious to severe mismatch conditions, and capable of delivering rated power to any load impedance from an open to a closed circuit.

For our latest catalog, please contact us at any of the offices listed below.

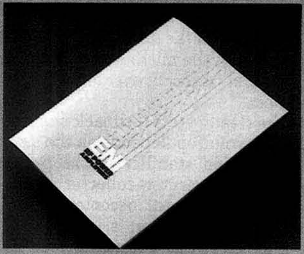

ENI
POWER SYSTEMS

The advanced design of RF power amplifiers and plasma generators

UNITED STATES HEADQUARTERS: ENI, INC., 100 Highpower Road, Rochester, NY 14623-3498 USA, Tel: (716) 427-8300, Tlx: 671 1542 ENI UW, Telfax: 716-4277839
WEST COAST: ENI, INC., 2065 Martin Ave., Suite 101, Santa Clara, CA 95050, Tel: (408) 727-0993, Telfax: (408) 727-1352
EUROPE: ENI EUROPE LTD., Mundells Court, Welwyn Garden City, Hertfordshire AL7 IEN England, Tel: (0707) 371558, Tlx: 24849 ENI UK G, Telfax: 707339286
JAPAN: ENI-JAPAN, 10-20, Shibasaki-cho 3 Chome Tachikawa City, Tokyo, Tel: (81) 0425 229011, Fax: (81) 0425 222636
ENI-JAPAN, Fujita Bldg. 4F, 7-27 Nishitenma 3-chome, Kita-ku, Osaka 530, Japan, Tel: (06) 367-0823, Fax: (06) 367-0827

CIRCLE 45 ON READER SERVICE CARD

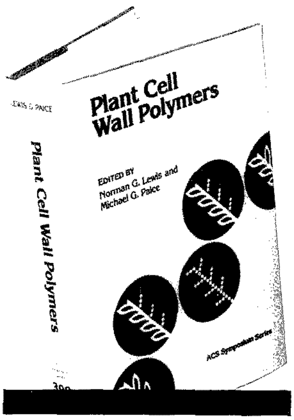

Plant Cell Wall Polymers

Biogenesis and Biodegradation

This timely volume offers a thorough review of this whole subject area. All aspects of biosynthesis and biodegradation are covered including morphology, enzymology, molecular mechanisms and molecular genitics.

Beginning with an overview chapter, you'll learn how the synthesis of the main constitutents of the cell wall is controlled. The remaining 46 chapters offer an extensive discussion on:

- plant cell development
- plant phenolic componds: metabolism and reactions
- biogenesis and structure of protolignin and cutin
- cellulose biogenesis and structure
- plant-microbe interactions
- biodegradation of lignin and tannins
- biodegradation of cellulose and xylan

A variety of plant tissues is addressed, including woody plants. Other topics discussed include the role of the cell wall in resistance of plants, the relationship between cell wall constituents and digestibility of food, solid state NMR studies of the cell wall, and the mechanisms of biodegradation.

This volume provides a comprehensive review while promoting an interchange of ideas among scientists who may traditionally be unaware of each other's work.

Norman G. Lewis, *Editor*, Virginia Polytechnic Institute and State University

Michael G. Paice, *Editor*, Pulp and Paper Research Institute of Canada

Developed from a symposium sponsored by the Division of Cellulose, Paper, and Textile Division of the American Chemical Society

ACS Symposium Series No. 399
664 pages (1989) Clothbound
ISBN 0-8412-1658-4 LC 89-17541
US & Canada **$119.95** Export **$143.95**

O·R·D·E·R F·R·O·M

American Chemical Society
Distribution Office, Dept. 34
1155 Sixteenth St., N.W.
Washington, DC 20036
or CALL TOLL FREE

800-227-5558

(in Washington, D.C. 872-4363) and use your credit card!

gold minigrid, where the grid spacing is 25 μm and the width of the individual gold lines is 7.6 μm. When the platinum microelectrode is located over a grid line, recycling of ferrocyanide/ferricyanide provides an increased microelectrode current compared with the current obtained when the microelectrode is over a space in the grid.

Figure 3 illustrates scanning over a nonconductive specimen, in this case a 50-μm glass fiber resting on a glass slide. As the 5-μm-radius platinum microelectrode traverses the region of the glass fiber, interference with diffusion of ferrocyanide to the microelectrode leads to decreased current (*20*). Results from digital simulation (*19*) show that for a conductive substrate, constructive feedback becomes significant when the microelectrode is closer than approximately 3–5 times its own radius. When the substrate is nonconductive, interference with diffusion to the microelectrode can be detected at even greater interelectrode distances.

SECM is being applied to study nonelectrochemical aspects of surfaces as well. Wang et al. (*21*) have characterized the distribution of biological activity on modified carbon paste electrodes by probing their surfaces with a microelectrode. In this example, the specimen acts as a biochemical generator rather than an electrochemical generator. For example, a carbon paste surface modified with banana tissue converts dopamine to dopamine quinone through the action of polyphenol oxidase. The quinone is monitored voltammetrically at the microelectrode, which is rastered incrementally over the surface. Two-dimensional maps of the biological activity on the carbon-paste surface are obtained.

Published work on SECM to date has demonstrated spatial resolution in the micrometer range, a level far from that of STM even when the latter is carried out in situ. STM relies on currents that become negligible over distances measured in angstroms, whereas SECM relies on the diffusion of chemical species to the microelectrode tip, a process that can occur over much larger distances.

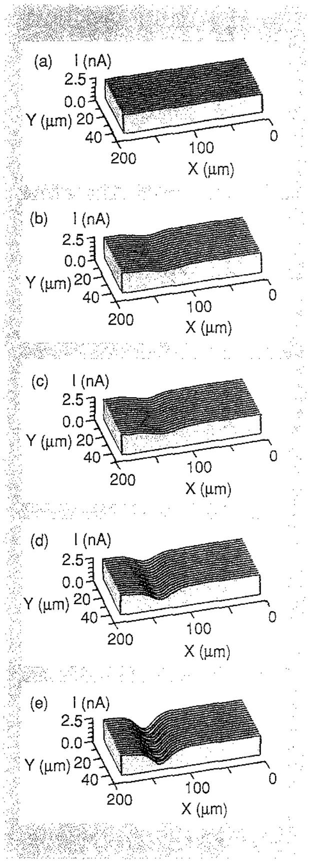

Figure 3. Scans over a 50-μm glass fiber obtained in the feedback mode.
Current is diminished over the fiber as interference with diffusion to the probe occurs. Interelectrode distance decreases from top to bottom (a–e). (Adapted from Reference 20).

In the steady-state feedback mode of SECM, resolution depends on the size, geometry, and stability of the probe tip. In the generator–collector mode, time of measurement becomes important as well; resolution is improved if the microelectrode current is read at short times after the specimen begins generating (*22*), before the generated species diffuses away from its site of origin. Yet short-time measurements become difficult because of capacitive coupling of generator currents to the microelectrode. As the specimen electrode potential is stepped, an induced current spike at the microelectrode prevents measurements before a few milliseconds, during which time the generated species will have diffused over micrometer distances. Decreasing the capacitive coupling of the microelectrode as well as decreasing tip size should improve resolution into the submicrometer range. An additional advantage of the feedback mode over the generator–collector mode is that capacitive coupling is not operative when the specimen is not conducting.

In addition to using SECM as a char-

INTRODUCING A NEW LINE OF LABORATORY INSTRUMENTS FROM AN OLD NAME IN INSTRUMENTATION.

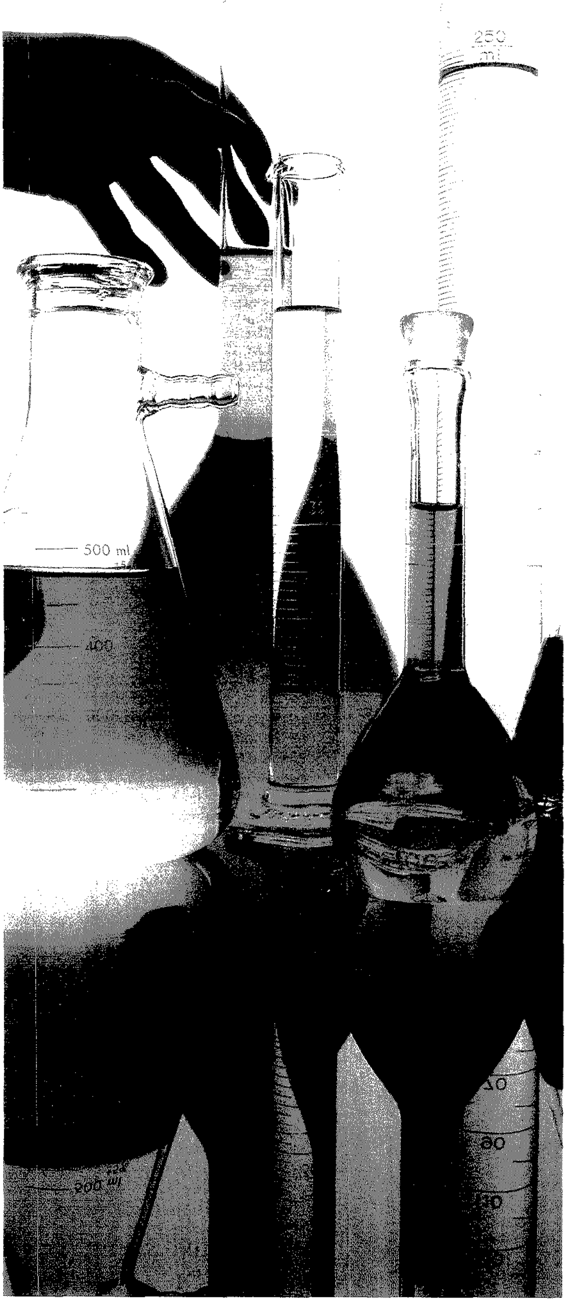

Now you have a new source for laboratory instrumentation...one that has built an 80-year reputation for producing high-quality, economical detection, testing and measurement equipment...BACHARACH. We're proud to announce we are now manufacturing the Coleman® line of analytical instruments, including the 3D HPLC™ and three spectroscopy-based products for laboratory use. Buy our lab equipment and you'll get not only a superior product for your investment, but also superior customer service...including in-house sales, repair and technical staff. Quality, economy and service...Bacharach Coleman Instruments.

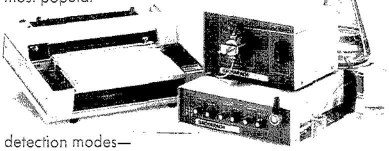

The 3D HPLC System is the first of its kind to combine three of the most popular detection modes—UV, fluorescence and conductivity—into a single, compact unit. The System comes complete with pump, injector, cartridge column, recorder and patented TriDet trifunctional detector for under $7000.

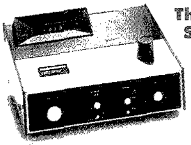

The Model 35 Spectrophotometer provides excellent photometric accuracy and is suitable for most quantitative measurements in the visible range.

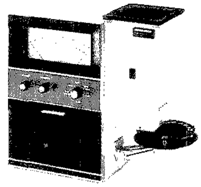

The Model 51Ca Flame Photometer delivers precise, fast, quantitative determination of sodium, potassium, lithium and calcium from a single sample.

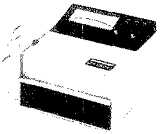

The Model MAS-50B Mercury Analyzer System utilizes the "Hatch and Ott Cold Vapor Technique" for high resolution and easy operation.

For more information, call your local lab equipment dealer or contact:

Bacharach Coleman Instruments
625 Alpha Drive, Pittsburgh, PA 15238
(412) 963-2000 Fax: (412) 963-2091

BACHARACH
Coleman® Instruments

CIRCLE 18 ON READER SERVICE CARD

acterization tool, the faradaic process occurring between the tip and a substrate has been used in microfabrication. The potential difference between tip and substrate can result in the electrochemical deposition of metal on the substrate surface. Bard and co-workers have created silver structures of micrometer dimensions by reducing silver ions at the surface of a Nafion matrix (*23*), and they have photoelectrochemically etched GaAs surfaces (*24*).

As it evolves, SECM should become a valuable technique for characterization of surface activity. Certainly, one of its most important capabilities is to describe the location of activity on a surface, allowing correlation with known structural features. Although there are interesting problems in the micrometer domain, the resolution of SECM must still be improved considerably if we are to study many of the problems relevant to electroanalytical chemistry and to complement available structural information. In addition to simply identifying the location of activity, SECM should be able to provide information about microscopically local electron transfer kinetics, rates of mass transfer through microscopic channels, the fate of chemical species involved in interfacial reactions, and the kinetics of adsorption–desorption processes.

References

(1) Isaacs, H. S.; Kissel, G. *J. Electrochem. Soc.* **1972**, *119*, 1628.
(2) Isaacs, H. S.; Kendig, M. W. *Corrosion* **1980**, *36*, 269.
(3) Isaacs, H. S. *Localized Corrosion-Cause of Metal Failure*, ASTM STP **1972**, *516*, 158.
(4) Engstrom, R. C. *Anal Chem.* **1984**, *56*, 890.
(5) Engstrom, R. C.; Weber, M.; Werth, J. *Anal. Chem.* **1985**, *57*, 844.
(6) Kragt, H. J.; Earl, D. J.; White, H. S.; Smyrl, W. H. *Abstracts of Papers;* 22nd Great Lakes Regional Meeting of the American Chemical Society, Duluth, MN; American Chemical Society: Washington, DC, 1989; Abstract 16.
(7) Rubinstein, I. *J. Appl. Electrochem.* **1983**, *13*, 689.
(8) Engstrom, R. C.; Johnson, K. W.; DesJarlais, S. *Anal. Chem.* **1987**, *59*, 670.
(9) Engstrom, R. C.; Pharr, C. M.; Koppang, M. D. *J. Electroanal. Chem.* **1987**, *221*, 251.
(10) Butler, M. A. *J. Electrochem. Soc.* **1983**, *130*, 2358.
(11) Butler, M. A. *J. Electrochem. Soc.* **1984**, *131*, 2185.
(12) Liu, H. Y.; Fan, R. R.; Lin, C. W.; Bard, A. J. *J. Am. Chem. Soc.* **1986**, *108*, 3838.
(13) Heben, M. J.; Penner, R. M.; Lewis, N. S.; Dovek, M. M.; Quate, C. F. *Appl. Phys. Lett.* **1989**, *54*, 1421.
(14) Itaya, K.; Tomita, E. *Surf. Sci.* **1988**, *201*, L507.
(15) Engstrom, R. C.; Weber, M.; Wunder, D. J.; Burgess, R.; Winquist, S. *Anal. Chem.* **1986**, *58*, 844.
(16) Kelly, R. S.; Wightman, R. M. *Anal. Chim. Acta* **1986**, *187*, 79.
(17) Engstrom, R. C.; Meaney, T.; Tople, R.; Wightman, R. M. *Anal. Chem.* **1987**, *59*, 2005.
(18) Bard, A. J.; Fan, F. F.; Hwak, J.; Lev, O. *Anal. Chem.* **1989**, *61*, 132.
(19) Kwak, J.; Bard, A. J. *Anal. Chem.* **1989**, *61*, 1221.
(20) Kwak, J.; Bard, A. J. *Anal. Chem.* **1989**, *61*, 1794.
(21) Wang, J.; Wu, L-H.; Li, R. New Mexico State University, personal communication, 1989.
(22) Tople, R., Honors Thesis, University of South Dakota, 1989.
(23) Craston, D. H.; Lin, C. W.; Bard, A. J. *J. Electrochem. Soc.* **1988**, *135*, 785.
(24) Lin, C. W.; Fan, F-R. R.; Bard, A. J. *J. Electrochem. Soc.* **1987**, *134*, 1038.

Royce C. Engstrom is professor and chairman of the Department of Chemistry at the University of South Dakota. He received his B.S. degree in chemistry from the University of Nebraska at Omaha in 1975 and his Ph.D. in chemistry from the University of Wisconsin—Madison in 1979. His research interests are in electroanalysis, microanalytical chemistry, and the relationship between electrode surface structure and electrochemical activity.

Christine M. Pharr is a research associate at the University of South Dakota. She received her B.A. degree from Mount Marty College (South Dakota) in 1979 and her M.A. degree from the University of South Dakota in 1989. Her research interests are in electrochemistry and biochemistry. She has applied luminescence imaging to the study of electrode processes.

RENT

Analytical Instruments
lease or rent-to-own

✓ **Free** Instrument delivery & setup in selected areas.

✓ GC•MSD•FTIR•AA•ICP•LC•IR

✓ Choose from many major manufacturers

✓ Hewlett-Packard GC•MSD Systems in stock

✓ New Catalog of Chromatography Supplies.

1-800-551-2783

On-Site® Instruments
ENVIRO**RENTAL**®
689 North James Road Columbus, Ohio 43219-1837
(614) 237-3022

CIRCLE 122 ON READER SERVICE CARD

Reaching Perfection in MS and SEM.
"A man's reach should exceed his grasp..."
Robert Browning

Galileo detectors for Mass Spectrometry and Electron Microscopy.

What silicon chips did for computers, Galileo high-performance detectors are doing for GC/MS, MS and SEM analysis.

Whether your projects involve environmental or pharmaceutical analysis, analysis of organic compounds or general spectroscopy applications, a Galileo detector will speed sample identification while providing accurate and precise analysis.

When research projects require frequent sample analysis over a long period of time, you'll want the latest and best technology backing you up. Galileo is the innovator in analytical instrument detectors. If you demand high performance and are concerned about down time, rapid analysis, dynamic range and cost, insist on Galileo scientific detectors. You'll wonder how you ever got along without us.

Write us and ask how to ensure that your instruments have Galileo scientific detectors.

Galileo Electro-Optics Corp.
Scientific Detector Products Group
P.O. Box 550, Dept. AA
Sturbridge, MA 01566
(508) 347-9191

GALILEO
Galileo Electro-Optics Corp.

CIRCLE 58 ON READER SERVICE CARD

NEED AN ARTICLE FROM AN EARLIER ISSUE?

GET IT FROM CAS DOCUMENT DELIVERY SERVICE®

Does your research depend on locating an article published in this journal a few years back? The CAS Document Delivery Service can provide copies of articles from *all ACS journals from initial publication to the present.*

You'll also find CAS DDS an excellent source for documents related to chemistry and allied disciplines drawn from *the more than 10,000 scientific and technical publications received at Chemical Abstracts Service each year.*

Order articles, patents, and reports back to 1975 (1970 for Soviet material). Most orders are on their way within 24 hours. Call for more information. Ask about our FREE 1989 Directory of Publications.

**Chemical Abstracts Service®
2540 Olentangy River Road
P.O. Box 3012
Columbus, OH 43210**

**Phone: (toll-free) 800-848-6538, ext. 3670
or 614-447-3670**

Chemical Abstracts Service is a division of the American Chemical Society.

A&D
4.0032 g
SAMPLE
MODE
CAL
PRINT
RE-ZERO
FR-300
310g×0.0001g

Ultra Wide Range! The FR Series of Precision Multi-functional Analytical Balances

Another first from A&D – Analytical precision balances with multi weighing units, multi-functions and optional wireless remote control.

By using the latest electronic technology combined with easy-to-use multi-function features and extensive ergonomic design – the FR series will revolutionize the ways you can use an analytical balance. Multi weighing units; Comparator mode; Percentage add/subtract mode; Counting mode; Environmental conditions adjustment (including last-digit blanking during course weighing); Auto power ON; – and much, much more.

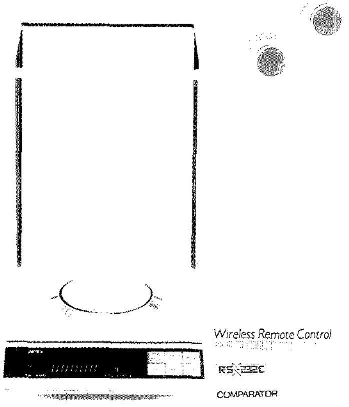
Wireless Remote Control
RS-232C
COMPARATOR

Wireless remote control with total command at the push of a single button.

Start with an optional wireless remote control that simplifies and expands operation of every feature the balance has available – then, enjoy the rest of the full range of options available for the FR Series.

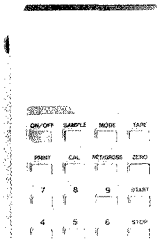
ON/OFF
SAMPLE
MODE
TARE
PRINT
CAL
NET/GROSS
ZERO
7
8
9
START
4
5
6
STOP

A&D ENGINEERING, INC.
1555 McCandless Drive, Milpitas, CA 95035
Fax (408) 263-0119 Telex. 346940 AANDO SNJ
EAST COAST BRANCH OFFICE
2165-M West Park Court, Stone Mountain, GA 30087
(800) 426-4480 In Georgia (404) 498-9732
Fax (404) 498 4877

CIRCLE 3 ON READER SERVICE CARD

Opportunities for Analytical Chemists

in Brussels, Belgium, Newcastle upon Tyne and Egham *(Surrey)*, UK

THE OPENINGS	Procter & Gamble has entry-level openings for Analytical Chemists in its European Technical Center near Brussels, Belgium; and in its UK Technical Centers outside Newcastle upon Tyne, and at Egham *(Surrey)*.
THE CANDIDATES	The successful candidates will have excellent academic records, with a Ph.D. or equivalent in analytical chemistry. Other disciplines are acceptable if combined with experience in modern analytical techniques such as capillary GC, HPLC or MS. He or she will have good communication skills, be fluent in English and, if applying for the European Technical Center, be fluent in at least one of the following languages: Dutch, French, German, Italian, Spanish, Greek or Portuguese. The candidates should be free of military service obligations. Employment is contingent upon possession of citizenship or immigration visa for European Community or Scandinavian countries, Austria, or Switzerland.
THE POSITIONS	The persons taking up these initial assignments will use state-of-the-art analytical technology, design analytical procedures, and manage highly qualified personnel in an international working environment related to research and development projects for our European-wide operations.
THE COMPANY	Procter & Gamble is a research and development based international corporation with more than $21 billion in world-wide sales in household consumer products and an R&D budget of over $625 million.
THE TECHNICAL CENTERS	These Technical Centers are responsible for all aspects of Product Development (product formulation, processing, packaging, human and environmental safety) for all Procter & Gamble companies in Europe, the Middle-East and North Africa.
THE OFFER	We offer starting positions for a research and development career in a successful, strong, and growing company and in an environment which will stimulate personal and professional growth. We have a policy of 'promotion from within' based on contribution and potential. Salaries are highly competitive and coupled with an excellent benefits package which provides for pensions, health care, and paid relocation.
APPLICATIONS	To apply, please send your resume and publication list to: Dr. T. J. Logan European Analytical Positions THE PROCTER & GAMBLE COMPANY P.O. Box 398707, Cincinnati, Ohio 45239-8707

Allow 6-8 weeks for response.

No agency referrals, please.

Procter & Gamble

NEW PRODUCTS

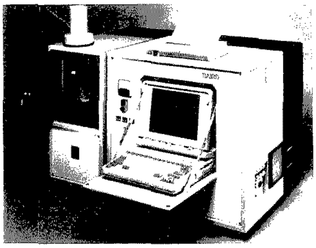

MOA military oil analyzer can determine up to 15 elements in wear metals and hydraulic fluids within 30 s. The system features an internal diagnostic system and solid-state, plug-in electronics. Baird 401

Oxygen. Model 318R analyzer provides on-line monitoring of ppm levels of O_2 contamination in gas streams such as hydrogen, ethylene, argon, and mixed hydrocarbons. Features include modular circuitry and four switch-selectable measuring ranges. Teledyne Analytical Instruments 404

Particle size. CHDF 1100 submicrometer particle size analyzer uses capillary hydrodynamic fractionation to manipulate very small particles in fluids and determine the statistical distribution of their sizes. Analysis time is < 8 min from injection of the sample to full graphics output. Matec Applied Sciences 405

X-ray Diffractometer. D 5000 X-ray diffractometer operates in a horizontal or vertical mode and includes a 3.0-kW X-ray generator and a radiation safety enclosure. The system can be used with a multiposition sample changer and solid-state or position-sensitive detectors. Siemens 406

Spectrophotometers. Bruins Instruments Omega 10 UV–vis and UV–vis/near-IR spectrophotometers feature double grating monochromators and high-resolution color monitors. Integrating spheres, an automatic cuvette changer, and reflectance accessories are available. InterCon 409

Data management. DMS-4000 multichannel pH/ion monitoring and control system is a data management system that is capable of on-line data acquisition, monitoring, and control. The system provides multipoint sensor calibration, allowing conversion of analog voltage inputs to specific measurements such as pH, ion concentration, and temperature. Fluid Management Systems 407

Catalytic reactions. REACTIR Model 3000 permits in situ analysis of homogeneous and heterogeneous catalytic reactions under conditions of high pressure and high temperature. An internal reflectance IR probe mounted inside the reactor continually senses chemical changes without affecting the reaction. Spectra-Tech/Autoclave Engineers 408

Imaging. Astromed CCD 2200 is an ultra-low-light-level imaging system that includes a camera, computer, and image-processing software. The system is suitable for use in microscopy, spectroscopy, X-ray and electron beam imaging, and immunoassay. Microscience 410

GC. Model 8610 gas chromatograph features multilevel temperature programming, digital pneumatics, and a built-in purge and trap accessory. The low mass column oven adapts to both wide-bore capillary and packed columns and operates at temperatures ranging from 25 °C to 250 °C. SRI Instruments 411

Data system. Model 737 chromatography data acquisition system and controller provides control of sampling and operation for batch analysis with real-time monitoring of detector outputs. Calibration and analysis reports can be generated at any time using most dot matrix or laser printers. Axxiom Chromatography 412

Oven. Buchi Model TO-51 drying oven, which operates at temperatures ranging from ambient to 300 °C, provides a direct view of the material being dried. The drying tube has an inner diameter of 43 mm and is attached to the end cap with a vacuum-tight flange fitting for easy opening. Brinkmann Instruments 413

Software

Graphics. Graftool is an interactive scientific and engineering 3D graphics program that can generate, manipulate, and analyze hundreds of variants of 13 different graph types. The software also provides an integrated scientific spreadsheet for generating or importing data. 3-D Visions 415

Statistics. BMDP/PC 88.2 is a statistical software package that provides missing value analysis; stepwise logistic regression; cluster, factor, and spectral analysis; descriptive statistics; plots and histograms; and linear and nonlinear regression. BMDP Statistical Software 416

Manufacturers' Literature

GC. Brochure describes a variety of detectors for GC, including flame ionization, thermal conductivity, electron capture, nitrogen–phosphorus, and flame photometric detectors. 8 pp. Tracor Instruments 418

Preservatives. Bulletin discusses LC-based determination of sorbic acid and benzoic acid in foods and beverages. Concentrations of 1 ppm can be determined in < 5 min. Bio-Rad Laboratories 419

Newsletter. *BioTrack* (Vol. 4, No. 2) includes an article on synthesis of peptide amides using Rink resin and FMOC chemistry. Information on an automated cryopreservation system and DNA synthesis products is also provided. Fisher Scientific 420

Process analysis. Brochure discusses features, applications, and principles of operation of the Process/6800 series TC/TOC analyzers for on-line monitoring of aqueous samples. 6 pp. Ionics 423

For more information on listed items, circle the appropriate numbers on one of our Readers' Service Cards

Don't inject variables into your chromatography. Use Millex® filter units.

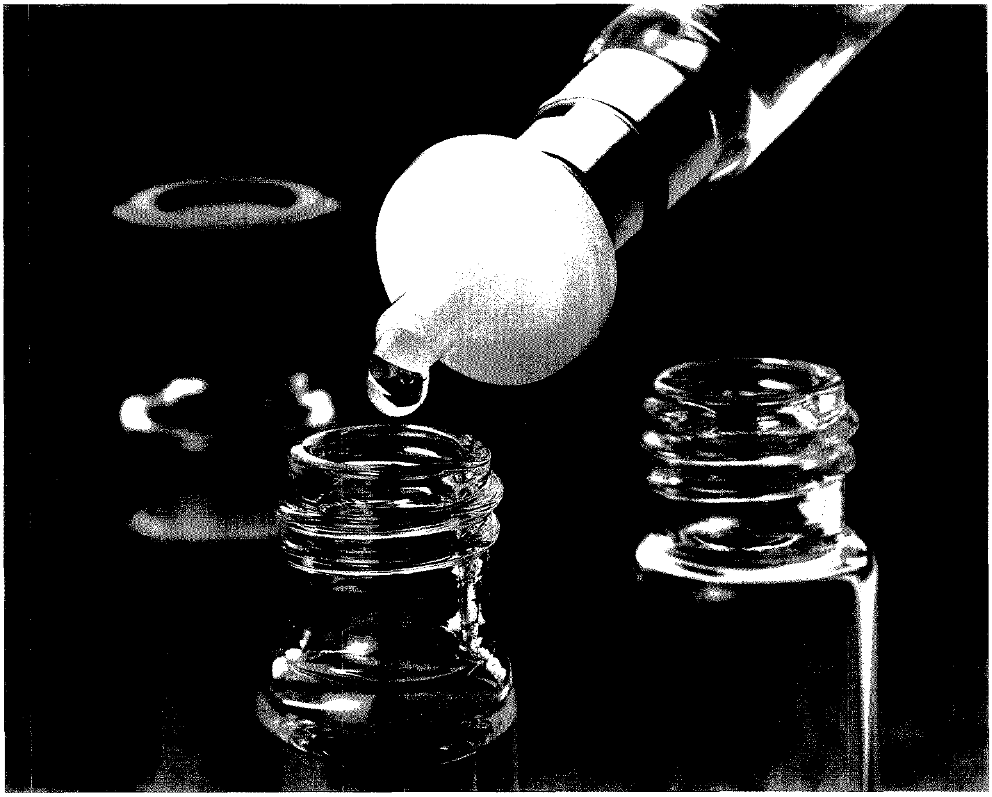

© 1986 Millipore Corporation

Use Millex HPLC filters, and put an end to particle contamination problems. Maximize column life while improving the consistency of your chromatographic results.

Designed for fast, reliable sample clarification, Millex units remove all particulate contaminants down to the rated pore size. Devices are available in 4 mm, 13 mm, and 25 mm configurations, for sample volumes ranging from less than 1 ml up to 100 ml, and offer these advantages:

Maximum sample recovery. Hold-up volume of 4 mm Millex units is less than 10 µl after air purge. For 13 mm units, less than 50 µl. For 25 mm units, less than 0.1 ml.

Ultraclean design. Membranes are incorporated into solvent-resistant housings. There are no glues, binders, or dyes to add unwelcome extractables to your analyses.

Wide chemical compatibility. Millipore's unique Durapore® membrane is non protein-binding, and compatible with most organic, aqueous, or isocratic solutions. Other membrane types are available to clarify a broad range of samples and solvents.

Try Millex HPLC filters in your lab—free. We'll send you a free prep kit and a brochure on sample management and reagent purification. Call (800) 225-1380. In Massachusetts, (617) 275-9200. Or write Millipore Corporation, 80 Ashby Rd., Bedford, MA 01730.

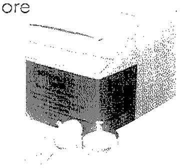

CIRCLE 96 ON READER SERVICE CARD

LC. Brochure highlights OmniPac multidimensional columns, which contain both reversed-phase and ion-exchange properties. Specifications are given for the OmniPac PAX-500 and PAX-100 columns. 4 pp. Dionex 422

Catalogs

Biotechnology. Catalog features scientific instruments for biotechnology research, including transilluminators, photodocumentation systems, and liquid-handling equipment. Fotodyne 425

Instrumentation. Catalog lists light sources, monochromators, and detection systems. Included are UV–IR sources, arc lamp power supplies, and computer-controlled data acquisition systems for scanning monochromators. 460 pp. Oriel 426

Ultra high vacuum. Catalog contains vacuum systems and chambers, ion pumps and controls, measurement instruments, valves, flanges, and fittings. A number of technical tables are included. 168 pp. Perkin-Elmer 428

Laboratory products. Catalog features ovens; water baths; refrigerators; and general-purpose, CO_2, and low-temperature incubators. Precision Scientific 427

Scientific equipment. Catalog features temperature, humidity, air flow, and pH instruments. A series of waterproof and shock-resistant thermometers is included. Testoterm 429

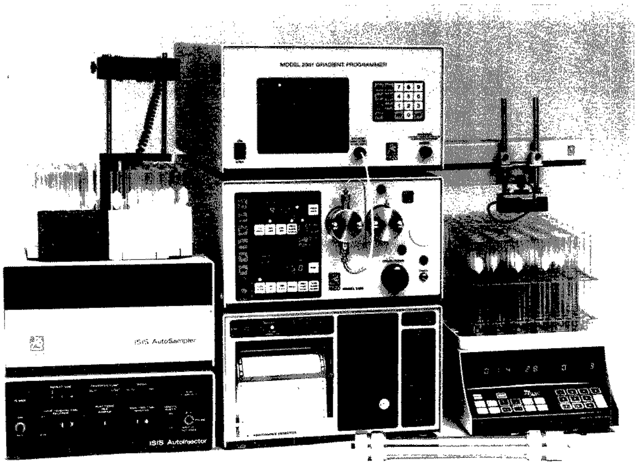

Preparative HPLC system automates sample purification in the milligram to gram range on columns up to 1 in. in diameter. The autoinjector carries up to 114 vials and can load up to 10 mL of sample per injection. Isco **402**

THE UNIVERSITY OF DAYTON RESEARCH INSTITUTE
ENVIRONMENTAL SCIENCES

- TOXIC WASTE INCINERATION
  - INCINERABILITY TESTING
  - BY-PRODUCT IDENTIFICATION
  - TRIAL BURN SUPPORT
- THERMAL STABILITY
  - FIRE SAFETY
  - EVOLVED GAS ANALYSIS
  - LAB-SCALE PROCESS SIMULATION
- ANALYTICAL SERVICES
  - GC-FID/MS/FTIR
  - CUSTOM ANALYSIS
  - TGA

The University of Dayton
ENVIRONMENTAL SCIENCES GROUP
RESEARCH INSTITUTE
300 College Park
Dayton, Ohio 45469-0001
(513) 229-2846

CIRCLE 34 ON READER SERVICE CARD

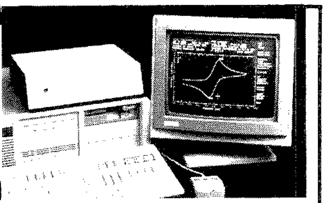

SPEED
FLEXIBILITY
CONTROL

For Your Electroanalytical Studies . . .

- *Cyclic Voltammetry*
- *Linear Scan Voltammetry*
- *Differential Pulse Voltammetry*
- *Square Wave Voltammetry*
- *Chronopotentiometry and Chronocoulometry*

The Model CYSY-1 system puts you in complete control of your electrochemical research with its "all-in-one" system design, combining the power and versatility of the personal computer with the three-electrode potentiostat. It gives you an effective, easy-to-use means of electroanalytical control, data acquisition and calculation. The high-sensitivity version is *perfect for microelectrode work*, down to picoampere current levels. And you can export the data to your other software programs for statistics, spreadsheet analysis, or presentation graphics.

Use of high-resolution color effectively highlights operating functions and experimental results. Pointing with the computer mouse speeds your selection and provides easy zooming and baseline drawing.

Write or phone now for our free brochure.

C.S.
Cypress Systems, Inc.
P.O. Box 3931
Lawrence, Kansas 66046
(913) 842-2511

CIRCLE 28 ON READER SERVICE CARD

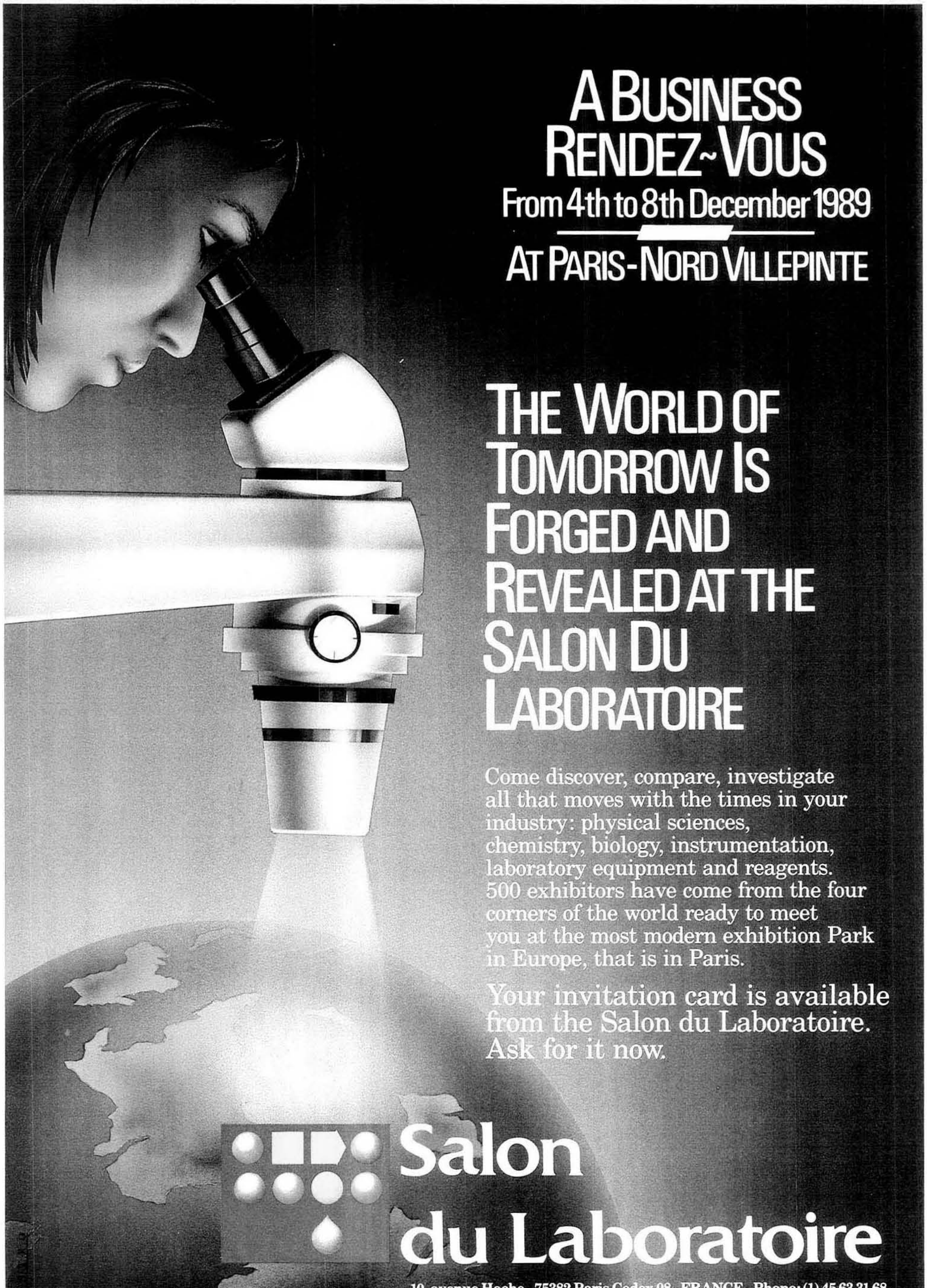

A BUSINESS
RENDEZ~VOUS
From 4th to 8th December 1989
AT PARIS-NORD VILLEPINTE

THE WORLD OF TOMORROW IS FORGED AND REVEALED AT THE SALON DU LABORATOIRE

Come discover, compare, investigate all that moves with the times in your industry: physical sciences, chemistry, biology, instrumentation, laboratory equipment and reagents. 500 exhibitors have come from the four corners of the world ready to meet you at the most modern exhibition Park in Europe, that is in Paris.

Your invitation card is available from the Salon du Laboratoire. Ask for it now.

Salon du Laboratoire

10, avenue Hoche - 75382 Paris Cedex 08 - FRANCE - Phone: (1) 45 63 31 68

CIRCLE 150 ON READER SERVICE CARD

LC-MS

ONLY VESTEC REALLY MAKES IT WORK FOR YOU.

How? By utilizing the technology and design know-how unique to the people who invented thermospray LC-MS!

The Vestec Model 201 is designed to be the ultimate LC detector. This instrument can detect and assist in identification of compounds in low picogram quantities, over a wide range of flow rates and solvents, including 100% water. You can eliminate tedious extraction and sample-preparation procedures and still routinely obtain peak-purity information for coeluting peaks.

This advanced technology is what works for scientists such as Cornell University's George Maylin, Ph.D., who uses the Model 201 for the productivity required in his equine drug-testing program.

Although copied, our instrument capabilities have never been duplicated. That's why Vestec can demonstrate overall high performance for the Dedicated Model 201 LC-MS. Find out how we really make Vestec's technology work for you.

VESTEC
CORPORATION

Vestec Corporation, 9299 Kirby Drive
Houston, Texas 77054, 713-796-9677

CIRCLE 168 ON READER SERVICE CARD

George Maylin, Ph.D.,
Director of the Equine Drug Testing Program,
Cornell University

Carbon-13 NMR Spectral Simulation

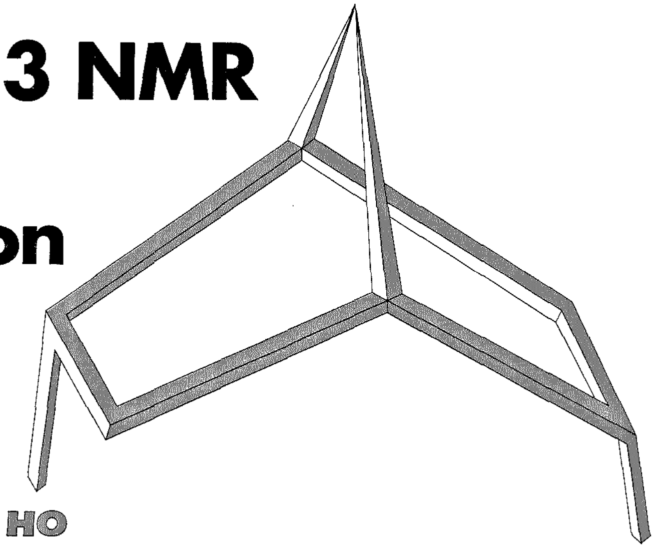

Peter C. Jurs, G. Paul Sutton, and Martha L. Ranc
Department of Chemistry
The Pennsylvania State University
University Park, PA 16802

Since its inception, NMR spectroscopy has become one of the most useful analytical techniques available to the chemist. It is especially useful for solving complex structure elucidation problems, because it yields detailed structural information about the surroundings of specific atoms within molecules. Chemical shifts, intensities, and multiplicities of NMR resonances are all helpful in structure elucidation. Many nuclei can be used in modern NMR analyses, including ^{1}H, ^{11}B, ^{13}C, ^{15}N, ^{17}O, ^{19}F, ^{29}Si, and ^{31}P; however, the two most commonly used today are ^{1}H and ^{13}C.

Both ^{1}H and ^{13}C NMR provide the organic chemist with a wealth of structural information that can be used to support and complement data from other analytical techniques such as infrared and mass spectrometry. Over the years, the field of NMR spectroscopy has seen many advances in instrumentation and methodology, many of which can be attributed to the introduction and application of computers and computational methods. Indeed, the increased use of computers in NMR spectroscopy has dramatically increased the amount of useful information generated as well as the speed with which this information can be obtained and analyzed. Despite these many advances, however, problems remain. With more sophisticated instrumentation comes more spectral information that, in turn, leads to more data to manage and interpret.

When given an NMR spectrum of an unknown compound to interpret, the chemist is confronted with the difficult task of transforming the series of peaks, splitting patterns, and intensities into a chemically meaningful structure, consistent with other available analytical information. This process often leads to several possibilities regarding the exact identity of the unknown compound, but it may not provide a conclusive answer. NOE (nuclear Overhauser effect) experiments can aid in the interpretation of ^{1}H NMR spectra, whereas proton decoupling techniques can be helpful in deducing chemical structure from ^{13}C NMR spectra.

A/C INTERFACE

However, direct spectral interpretation can still be quite difficult and tedious, especially for complex molecules. Pattern recognition methods have been applied to the interpretation of ^{13}C NMR spectra (*1–3*) but have proven somewhat limited in providing information on the specific identity of an unknown. The development and application of various additivity rules and substituent effect parameters for predicting ^{13}C NMR chemical shift values have also been extensively investigated for many classes of compounds.

In addition, visual comparisons with standard library reference spectra and computer-aided library searching have been used to provide additional assistance in spectral interpretation. However, the use of library comparisons requires that the reference spectral library be as large and as accurate as possible. This may severely restrict the usefulness of library search results.

An alternative to library search and retrieval methods is spectral simulation. In this approach, the chemist proposes several likely candidate structures using the spectrum of the unknown and then generates an approximate, or simulated, NMR spectrum for each candidate. These simulated spectra are then compared to the authentic spectrum of the unknown compound to confirm its identity. The generation of simulated spectra can also prove helpful in cases where previously reported spectral assignments are ambiguous.

Spectral simulation

^{13}C NMR spectral simulation is based on the existence of a direct yet complex relationship between the observed chemical shift of a carbon atom and its chemical environment. The exact nature of this relationship is not yet completely understood; however, it is possible to draw mathematical and statistical correlations between the structural surroundings of a carbon atom and its observed spectral properties. Once these relationships have been devel-

0003-2700/89/0361-1115A/$01.50/0
© 1989 American Chemical Society

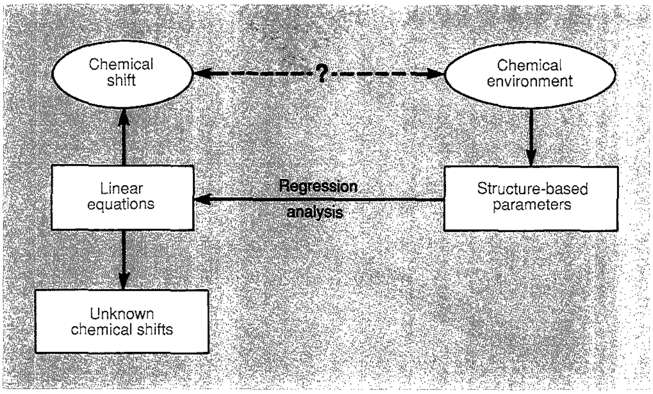

Figure 1. The parametric approach to spectral simulation.
The complex relationship between the chemical environment and the observed chemical shift is investigated through the calculation of structural descriptors and the development of linear model equations.

oped, they can be used to predict the chemical shifts for carbons in other compounds.

One approach to the simulation of ^{13}C NMR spectra involves the use of library shift retrievals (*4, 5*). These techniques differ from ordinary library searches in that they use libraries of specially coded structural environments rather than collections of complete reference spectra. Each environment contains an associated set of one or more chemical shifts. Simulated spectra are created by coding each structurally unique carbon atom in the candidate structure and searching the environment library for the closest environmental match. The sets of chemical shifts from each environmental match can then be assembled to yield simulated spectra. The quality and size of the spectral libraries are important considerations in applying these methods, as are the nature and scope of the environment coding algorithms used. However, an important drawback of library shift retrieval methods is that they have primarily been set up to work on specific databases, thus limiting their general utility.

Work has also been done involving the application of quantum mechanical methods to ^{13}C NMR spectral simulation (*6, 7*). This approach is based on molecular orbital theory calculations (e.g., INDO and MINDO/2), but has been limited thus far only to small, simple molecular structures because of the large amounts of computational time required. In contrast to programs for calculating spin–spin coupling, the routines for calculating nuclear shielding are not widely available to researchers, thereby limiting the use of this approach to spectral simulation.

The most widely used approach to ^{13}C NMR spectral simulation involves parametric methods. In this approach, the goal is to relate observed chemical shift values to numerically encoded structural parameters, called descriptors. The general procedures involved in parametric simulation methods are shown in Figure 1. The process involves investigating the complex relationship between molecular structure and chemical shift by numerically describing the structural environment of each unique carbon atom in a molecule. The resulting calculated parameters are then related to the observed chemical shift values through the use of regression techniques. This leads to the development of chemical shift model equations of the form

$$S = b_0 + b_1X_1 + b_2X_2 + \ldots + b_dX_d$$

where S is the predicted chemical shift of a given carbon atom, b_i is the ith coefficient of regression, X_i is the value of the ith numerical descriptor, and d is the number of descriptors in the model. Once generated, these models can be used to predict the chemical shifts for carbon atoms in structurally similar environments that were not used to create these equations.

The early work in this area, pioneered by Grant and Paul (*8*), Lindeman and Adams (*9*), and Ejchart (*10, 11*), focused on the modeling of ^{13}C NMR chemical shifts for linear and branched alkanes and some heteroatomic derivatives. These methods involved the use of simple descriptors, such as atom counts, which could be calculated by hand. Further work by Smith and Jurs (*12*), and later by Small and Jurs (*13*), incorporated the use of three-dimensional molecular modeling and the calculation of more sophisticated descriptors, such as those designed to encode geometrical features of molecules. These currently used approaches are entirely computer-based and provide model generation, spectral prediction, and library search capabilities. Similar work has been reported recently in the literature by Bernassau and co-workers (*14, 15*).

These methods of spectral simulation involve a multistep process of structure entry and modeling, descriptor calculation, statistical screening, model development and evaluation, and spectral prediction, as illustrated in Figure 2. Thus, a series of structurally related compounds with known ^{13}C NMR chemical shifts can be used to derive predictive equations that can later be used to generate approximate ^{13}C NMR spectra, thereby providing assistance in solving complex structure elucidation problems. In the remainder of this article, we will discuss the parametric spectral simulation approach and the methodology currently used in our laboratory, highlighting many of

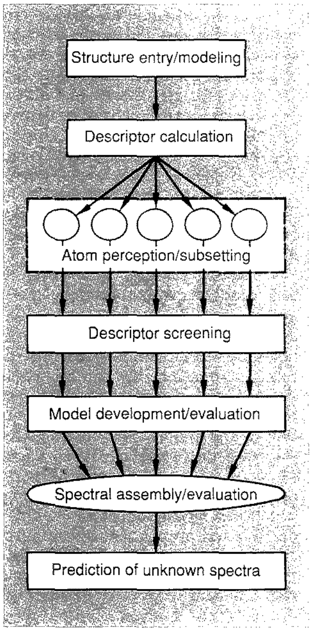
Structure entry/modeling
Descriptor calculation
Atom perception/subsetting
Descriptor screening
Model development/evaluation
Spectral assembly/evaluation
Prediction of unknown spectra

Figure 2. Flow diagram describing the multistep procedure used in ^{13}C NMR spectral simulation.
Each atom subset is modeled separately, and the results are combined to give complete simulated spectra.

DIALOG INTRODUCES ANOTHER TABLE OF BASIC ELEMENTS FOR YOUR LAB.

There's no symbol for *information* in the Periodic Table. Yet nothing could be more crucial to your research than complete, accurate technical and business information.

That's why many chemists consider DIALOG® an essential element in the modern lab.

As the world's largest online knowledgebank, DIALOG gives you access to a whole world of critical information. Right in your own lab.

For starters, you can tap into the crucial scientific data. DIALOG has detailed information on everything from compound identification to chemical safety data, property data, substance and substructure.

Then you can expand your focus by accessing important, related data that will enable you to look at your work in a broader context.

For example, you can investigate patents, competitive projects, new product markets, and worldwide industry trends. In fact, you can investigate any topic, anytime.

And you won't have to sacrifice depth for the sake of breadth. DIALOG is updated continuously, so the data is always comprehensive and current. And many citations can be conveniently retrieved in full text.

Call today for more information and a free Periodic Table Reference Card. Once you've examined them, you'll see how DIALOG can become a basic element of all your research.

Call us toll free at 800-3-DIALOG, (800-334-2564). Or request information by Fax at 415-858-7069.

DIALOG INFORMATION SERVICES, INC.
A Knight-Ridder Company

The world's largest online knowledgebank.

© 1989 Dialog Information Services, Inc., 3460 Hillview Avenue, Palo Alto, California 94304. All rights reserved. DIALOG is a servicemark of Dialog Information Services, Inc. Registered U.S. Patent and Trademark Office.

CIRCLE 32 ON READER SERVICE CARD

the factors that must be considered during each phase of the simulation process. Finally, we will address some of the limitations of this approach and discuss the direction that this area of research is likely to follow in the future.

Parametric simulation methodology

The data set. The first step is to gather a set of compounds for study, usually through a literature search. When assembling the data set, several factors must be taken into consideration, the most obvious being the availability of ^{13}C NMR data for the class of compounds of interest. Another important consideration is the reliability of the data: If the spectral data reported are from more than one laboratory, problems resulting from experimental and instrumental variations may be present. This may require that the ^{13}C chemical shift data be calibrated (*16*) to remove these experimental variables. In addition, the degree of structural homogeneity of the compounds in the data set must be considered, because a group of molecules with widely varying structural features (substituents and functional groups) will make it difficult to describe these features in a consistent manner.

Once the data set has been assembled, the structures and their spectra are entered and stored in the computer. The chemical structures are input by sketching on a graphics terminal, using software to generate the internal representation. Next, approximate three-dimensional atomic coordinates are generated via molecular mechanics calculations. Then the compounds are divided into a training set and a prediction set. The majority of the compounds comprise the training (or reference) set that is used to generate the regression models, and the remaining compounds are put aside to provide an external prediction set. The prediction set compounds are usually chosen randomly, but other criteria may be used; for example, compounds with unreported or ambiguous chemical shift assignments are good candidates for inclusion in the prediction set.

Because each structurally unique carbon atom gives rise to a distinct ^{13}C NMR resonance, the modeling process must rely on atomic descriptors. Therefore, each unique carbon atom in the reference set must be perceived, thereby yielding an atom pool. This perception is performed by an algorithm that systematically investigates the immediate surroundings of each carbon center. Multiple occurrences of structurally equivalent carbons could skew or bias the calculated regression models; therefore, duplicate carbon atoms are not included in this pool of carbon centers.

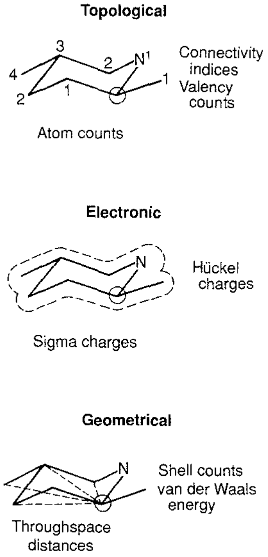

Figure 3. Examples of topological, electronic, and geometrical atom-based structural descriptors used in ^{13}C NMR spectral simulation studies.

Descriptor generation. The next step is to calculate a series of carbon-center descriptors for each atom in the pool. Each descriptor encodes some facet of the chemical environment of the given carbon center and can be used with other descriptors to predict the shift of that particular carbon. These descriptors range from simple (e.g., atom counts) to complex (e.g., Hückel charge descriptors) and are classified as topological, electronic, or geometrical (Figure 3).

Topological descriptors depend solely on atom types and connections. Because these descriptors do not encode geometrical features, they are not influenced by the molecular modeling process. Descriptors that fall into this category include atom and bond counts and connectivity indices (which encode the degree of branching). Electronic parameters, such as calculations of the sigma charge on various atoms near the carbon center of interest, comprise the second category of descriptors. Geometrical descriptors are used to differentiate atoms that are topologically identical but exist in different geometrical environments, such as those in *cis* and *trans* isomers. This type of descriptor is based on the three-dimensional atomic coordinates of the molecule and includes parameters such as interatomic throughspace distances and calculations of van der Waals energies. Although geometrical descriptors are almost always important in generating accurate chemical shift models, their accuracy is highly dependent upon the molecular modeling process.

Atom subsetting. Once carbon-center descriptors have been calculated for every atom in the pool, the pool is divided into subsets. One large problem—the prediction of the chemical shifts of a wide range of carbon centers—is thereby broken down into a series of smaller, more manageable problems (i.e., the prediction of the chemical shifts of smaller sets of similar carbons). Almost any criterion can be used to divide the atom pool; however, one useful (and chemically intuitive) scheme is to divide the carbons based on connectivity. Dividing the pool based on the atom's location in the molecule relative to a given functional group or structural feature (*16–18*) is another criterion that has been used successfully. For example, in the case of a data set made up of carbonyl-containing compounds, it makes sense to consider dividing the carbon atoms into groups based on their location relative to this electron-withdrawing functionality.

Each subset of carbon centers is subsequently treated separately but in an identical manner. Blindly employing available computational power to generate the greatest number of descriptors is not the key to obtaining good predictive models. If this were done, there is a high probability that a good fit to the observed chemical shift data would be obtained purely by chance. Therefore, it is necessary to screen the set of calculated descriptors using various statistical methods and chemical intuition. Such screening is done without using the dependent variable—the ^{13}C NMR chemical shift data—and is therefore objective and unbiased. The goal of these screening procedures is to maximize the amount of structural information encoded while minimizing the number of descriptors used. These procedures include the removal of information-poor descriptors (i.e., those possessing few, if any, nonzero values or for which most of the values are identical). For example, if only a few carbons in a given atom subset are in molecules that have primary carbon atoms located five bonds away, a descriptor encoding this particular structural feature would contain mostly zero values. Consequently, this descriptor would probably be of little value in characterizing the chemical shifts for this subset of carbons, because it is not representative of the entire atom subset. Equally important for obtaining sound predictive models is the minimization of information overlap between pairs or among groups of descriptors; this is accomplished by examining pairwise and multiple correlations among descriptors. This screening allows a statistically sound set of descriptors to be sent to the model construction phase.

Model generation. Model construction involves several methods of multiple linear regression analysis. The general methods used are stepwise or forward-selection regression analysis, either of which can be coupled to a progressive deletion procedure to help obtain superior models. Stepwise regression is the most widely used automated method for selecting recession variables (descriptors). Using this method, a sequence of regression models is generated with descriptors added or deleted at each step. The criterion for addition or deletion is the partial F statistic, with the F-to-enter and the F-to-delete independently set at the user's discretion. The F-to-enter is a quantitative measure of the predictive value a particular descriptor would bring to a new model. The F-to-delete ensures that each descriptor in a model is contributing enough to warrant its retention. The maximum number of descriptors in any given regression model is determined by the ratio of the number of observations (or unique carbon centers) modeled to the number of descriptors in the equation. Usually, this ratio is set at 5:1 to prevent overfitting or overdetermining the chemical shift data. Forward selection is a simplified version of stepwise regression wherein a variable, once entered into the model, is never tested for deletion. Progressive deletion allows each variable in the current best model to be withheld in turn to allow the quality of the resulting models to be tested.

Model evaluation. The regression methods described previously can generate up to several hundred models for each carbon atom subset. Obviously, there is a need to reduce the number of models that must be examined further. Preliminary screening of models can be performed based on the standard error, s, and the coefficient of multiple correlation, R, or the coefficient of multiple determination, R^2. The standard error, s, is a measure in ppm of the difference between the predicted and observed chemical shifts. Models that exhibit a high standard error (usually those with an s value greater than 1 or 2 ppm) are eliminated, as are those with a low R or R^2 (usually under 0.9). These limits depend on the particular atom subset used and the values relative to the statistics exhibited by the other models being examined. This screening is used to reduce the number of models to a manageable number, allowing further evaluation in choosing the models that best fit the data.

Further model evaluation methods can be broken down into colinearity diagnostics, outlier detection diagnostics, internal validation, and visual inspection. The two main colinearity diagnostics methods involve the examination of simple and multiple correlations. Simple correlations are pairwise correlations among the descriptors in a given model. Descriptors that are highly correlated contain redundant information, indicating that it may be possible to remove a given descriptor from a model without significantly detracting from its performance. Descriptors with extremely high correlations should have been eliminated at the descriptor-screening step; however, significant correlations might still exist and could indicate potential problems, especially when considered in conjunction with other diagnostics and internal validation results. Multicolinearities involve three or more descriptors. High colinearities occur when two or more descriptors in a model can be used to predict another descriptor. Models containing descriptors with extremely high multicolinearities are usually discarded.

The versatility of a model could be decreased because of skewing of the model if statistical outliers are present. Currently, several methods of outlier detection are used, including standardized residual, which is the residual adjusted to the standard error of estimate; studentized residual, which uses the standard error computed without the current observation; and several measures of leverage that detect undue influence on the model equation due to one observation. Models with a large number of observations judged to be outliers by one or more of these diagnostics should be examined to be sure that they are not unduly influenced by these outliers. This is especially true if the potential outliers are indicated as such by several of the diagnostics.

At this stage of model evaluation, internal validation procedures are per-

IF YOU CAN'T LIVE WITH
OUR STANDARDS,
WE'LL CHANGE THEM.

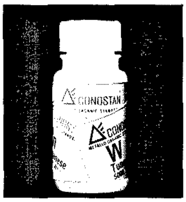

If your spectrometric analysis of metals in oils requires a blend of elements we don't routinely offer— we'll custom blend it for you. Conostan custom blending allows you to test for unusual combinations and concentrations of elements with minimal interference and repeatable results. For a complete list of Conostan single and multi-element standards, write or call for our free brochure. If you don't find what you need, we'll blend something special just for you.

Standards to Burn
CONOSTAN®

Conostan Division
Conoco Specialty Products Inc.
P.O. Box 1267
Ponca City, OK 74603
Phone: (405) 767-3078
Fax: (405) 767-5843

CIRCLE 30 ON READER SERVICE CARD

formed. These methods involve withholding one or several of the chemical shifts originally used to create the model. New models, or submodels, are then generated based on the remaining chemical shifts and are used to predict the values for the chemical shifts withheld. If the submodels have difficulty in predicting the chemical shifts that had been temporarily withheld, this indicates that the original model did not fit the data very well. Two internal validation procedures commonly used are jackknifing and duplexing. Jackknifing is based on the deletion of each single observation in turn, with its subsequent prediction from the recalculated model; the difference between the observed and predicted chemical shifts is referred to as the jackknifed residual and serves as a diagnostic measure for the model. A model containing large jackknifed residuals may not be very useful for external prediction. Duplexing involves splitting the set of data in half and using one half to calculate a submodel; the other half of the data set is then used to predict the chemical shifts of the atoms using the submodel. The chemical shift data is usually split such that each half has similar statistical characteristics. The standard error from the submodel formation step and the prediction error of the chemical shifts left out should, ideally, be similar in value; in turn, both should be similar to the standard error of the overall model. If these three values differ significantly, the model may be skewed, and large differences may suggest that the model should be discarded.

Visual inspection of results includes examining residual plots and the plots of predicted versus observed chemical shifts. Ideally, the latter plot should yield a straight line, as implied by a high *R* value. However, this is not necessarily the case. It is quite possible to obtain high values for *R* or R^2 and yet not be modeling the chemical shift data accurately. This underscores the fact that numerical statistics alone are not the entire solution to the problem of model evaluation. Residual plots (residuals versus predicted shifts) should not have discernible patterns; in other words, they should look randomly distributed. Notable curvature or unequal spread in a residual plot may indicate that alternative regression procedures (such as weighted least squares) be considered or that variable transformations be used. Other solutions to these kinds of problems include the development of new descriptors or the consideration of alternate atom subsetting schemes.

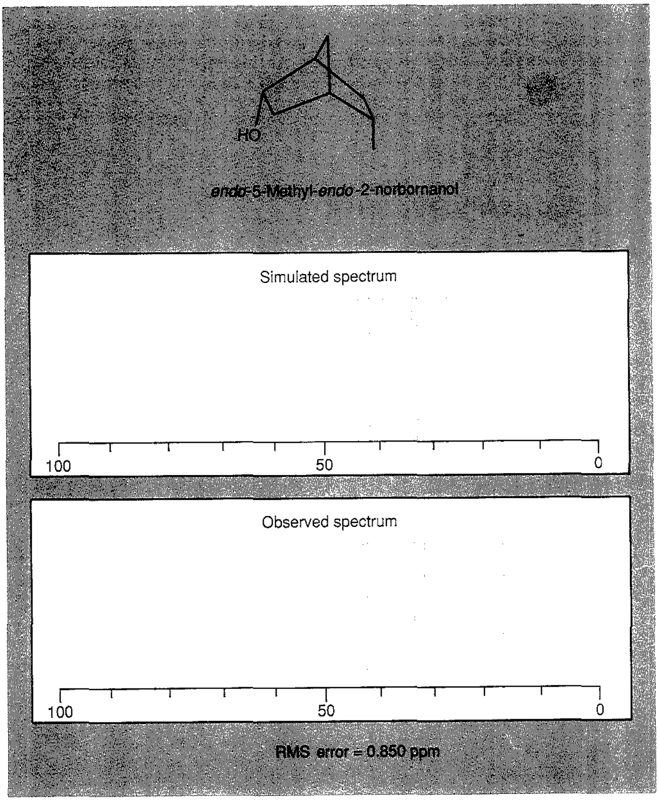

Figure 4. Simulated versus observed ^{13}C NMR spectra for *endo*-5-methyl-*endo*-2-norbornanol.

Once the number of equations has been reduced to two or three per carbon atom subset, they are further evaluated by determining how well they work together to simulate complete spectra. The predicted chemical shift values obtained from the equations in each atom group are combined to form a complete simulated spectrum for each compound in the training set. One method of determining how well the models function as a unit is by direct spectral comparison between each simulated and corresponding observed spectrum. Figure 4 depicts the simulated and observed spectra for *endo*-5-methyl-*endo*-2-norbornanol (*19*). A visual comparison of the two spectra will show that there are differences between them but does not provide a quantitative measure of how closely the simulated spectrum approximates the observed spectrum. The standard or residual mean square (rms) error between each pair of spectra serves as one quantitative measure for determining spectral simulation accuracy. In general, an average rms spectral error of 1 ppm or less is desirable.

A second method of spectral evaluation involves a library search procedure that retrieves the five closest spectral matches to each simulated spectrum in the reference set from a library of observed spectra. When comparing results, the number of matches in the top five is a useful criterion. Combinations of models that yield high rms spectral errors and perform poorly in library searches indicate that one or more of the models used should be replaced and other combinations should be tested. Another potentially important method of evaluating spectral simulation accuracy involves the assembly of partial simulated spectra (*17, 18*). To date, this approach has not been explored thoroughly.

The final and most important step in model evaluation is external validation. This involves the prediction of chemical shifts for atoms that were not used in the development of the models. External validation allows for the evaluation of the external predictive ability of the models generated earlier, because a good fit to observed data does not necessarily guarantee successful prediction of chemical shifts for unknowns. The compounds set aside as the prediction set at the start of the study are now used. As with the training set, unique carbons must be perceived and then grouped according to the atom subsetting scheme used in generating the models. The descriptors contained in the predictive model equations previously judged useful are then calculated. Each model is then used to predict the shifts for the appropriate atom subset, and the results are combined to yield the simulated spectra for the prediction set compounds. The spectral simulation accuracy and the external predictive ability of the models can then be evaluated as before by using direct spectral comparisons and library search methods.

The techniques described here have been applied to several sets of compounds to address a number of important aspects involved in ^{13}C NMR spectral simulation. The initial investigations (*12*, *13*, *20*) demonstrated the overall feasibility of the approach. Sophisticated structural descriptors were calculated and related to the observed chemical shifts in a statistically robust manner. Later work (*21*, *22*) focused on methods for determining duplicate structural environments and reducing the amount of data required to give accurate chemical shift models. A study involving cyclopentanes and cyclopentanols (*17*) demonstrated that accurate chemical shift models could be obtained for conformationally flexible compounds, even though the ^{13}C NMR shift data were conformationally averaged. Further investigations successfully modeled compounds containing oxygen atoms in ether linkages in monosaccharides (*16*) and in carbonyl functional groups in cyclic ketones (*18*). These studies also showed that the use of alternate carbon atom subsetting schemes was both feasible and useful for the modeling process. The modeling of chemical shifts for nitrogen-containing compounds is currently under way using a data set of methyl-substituted piperidines (*23*).

Future directions

The spectral simulation approach described here has shown promising results in a number of studies and points the way to many research possibilities. Most of the work performed thus far has involved small data sets using homogeneous structures; in addition, only limited work has gone into examining data sets possessing appreciable amounts of conformational flexibility. Future research in this area will require the expansion of both the size and the structural diversity of the data sets, including the modeling of compounds with heteroatoms and varying functional groups, in addition to those studied so far. Another important aspect of this research is the development of new and more complex structural descriptors. Structural environments of carbon atoms will undoubtedly need to be characterized more completely to provide a clearer insight into the complex relationships that exist between molecular structure and chemical shift. The development and evaluation of more sophisticated electronic parameters will be especially significant.

Another area of investigation addresses questions regarding the application of previously generated models to new and more complex chemical structures: Of a series of stored equations, are any suitable for predicting

LABORATORY SERVICE CENTER

NMR ANALYSIS
MULTINUCLEAR LIQUID or
MULTIFIELD SOLID STATE
SPECTRAL DATA SERVICES, INC.
818 Pioneer
Champaign, IL 61820
(217) 352-7084

Laboratory Service Center (Equipment, Materials, Services, Instruments for Leasing), Maximum space — 4 inches per advertisement. Column width, 2-3/16″; two column width, 4-9/16″. Artwork accepted. No combination of directory rates with ROP advertising. Rates based on number of inches used within 12 months from first date of first insertion. Per inch: 1″ — **$155; 12″ — $153; 24″ — $150; 36″ — $145; 48″ — $140.**

CALL OR WRITE JANE GATENBY

ANALYTICAL CHEMISTRY
500 Post Road East
P.O. Box 231
Westport, CT 06880
203-226-7131/FAX: 203-454-9939

HELP WANTED ADS

ROP display at ROP rates. Rate based on number of insertions within contract year. Cannot be combined for frequency.

Unit	1-Ti	6-Ti	12-Ti
1″ (25 mm)	$180	$160	$150
	24-Ti	48-Ti	72-Ti
	$140	$130	$125

CALL OR WRITE JANE GATENBY

ANALYTICAL CHEMISTRY
500 Post Road East
P.O. Box 231
Westport, CT 06880
203-226-7131
FAX: 203-454-9939

FREE DATA, FAST

To quickly amass data on all of the products you need, consult the Lab Data Service section on our *Analytical Chemistry* reader reply card insert.

USE LABORATORY SERVICE CENTER

Metal Clusters in Proteins

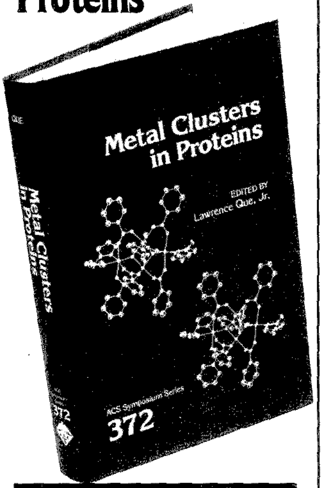

Over the past 20 years, the study of metals in the maintenance and regulation of many biological processes has gained significant importance. Now through this exciting new book, you can get an in-depth look at the different functions of metal ions as well as learn the background on the tools used to elucidate the properties of metal clusters. Specialists in biochemistry and spectroscopy of proteins and scientists involved in the design and synthesis of structural and functional models for the metal sites offer the latest information on new techniques and developments. With 19 chapters, this book is divided into four detailed sections:

- metalloproteins and two spectroscopic techniques used to characterize them
- binuclear sites of metalloproteins that contain copper
- metal-oxo centers of metalloproteins
- metal-sulfur clusters

Metal Clusters in Proteins provides an up-to-date summary. It will be of interest to biochemists, spectroscopists, crystallographers, molecular biologists, and inorganic and organic chemists in all stages of expertise. This book may also serve as a starting point for classroom discussions on bioinorganic chemistry.

Lawrence Que, Jr., *Editor, University of Minnesota*

Developed from a symposium sponsored by the Division of Inorganic Chemistry of the American Chemical Society

ACS Symposium Series No. 372
414 pages (1988) Clothbound
ISBN 0-8412-1487-5 LC 88-14504
US & Canada **$84.95** Export **$101.95**

Order from: American Chemical Society
Distribution Office Dept. 93
1155 Sixteenth St., N.W.
Washington, DC 20036
or CALL TOLL FREE

800-227-5558

and use your credit card!

the chemical shift of a given carbon atom in a molecule that has not previously been examined? If so, which of these models is likely to give the most accurate prediction? One possibility includes the application of artificial intelligence methods to aid in the model selection process. Another aspect of this research, related to the questions of model suitability and selection, involves further investigations into the generation and evaluation of partial simulated spectra. Accurate creation of simulated subspectra could prove useful in answering questions regarding the identities of substructural fragments in complex molecules. In addition, it may be possible to use various combinations of simulated subspectra in conjunction with library search results to help determine what new types of regression models should be developed and what new classes of compounds should be investigated. Although it is clear that important advances in the field of computer-aided ^{13}C NMR spectral simulation have been made, several unanswered questions remain that should prove both challenging and interesting to pursue.

The work described in this article was supported by the National Science Foundation under Grant CHE-8815785.

References

(1) Brunner, T. R.; Wilkins, C. L.; Lam, T. F.; Soltzberg, L. J. *Anal. Chem.* **1976**, *48*, 1146–50.
(2) Wilkins, C. L.; Brunner, T. R. *Anal. Chem.* **1977**, *49*, 2136–41.
(3) Sjöström, M.; Edlund, U. J. *Magn. Reson.* **1977**, *25*, 285–97.
(4) Zupan, J.; Heller, S. R.; Milne, G.W.A.; Miller, J. A. *Anal. Chim. Acta* **1978**, *103*, 141–49.
(5) Gray, N.A.B.; Crandell, C. W.; Nourse, J. G.; Smith, D. H.; Dageforde, M. L.; Djerassi, C. J. *Org. Chem.* **1981**, *46*, 703–15.
(6) Ando, I.; Nishoka, A.; Kondo, M. *Bull. Chem. Soc. Jpn.* **1974**, *47*, 1097–1104.
(7) Ando, I.; Webb, G. A. *Theory of NMR Parameters;* Academic Press: New York, 1983.
(8) Grant, D. M.; Paul, E. G. *J. Am. Chem. Soc.* **1964**, *86*, 2984–89.
(9) Lindeman, L. P.; Adams, J. Q. *Anal. Chem.* **1971**, *43*, 1245–52.
(10) Ejchart, A. *Org. Magn. Reson.* **1980**, *13*, 368–71.
(11) Ejchart, A. *Org. Magn. Reson.* **1981**, *15*, 22–24.
(12) Smith, D. H.; Jurs, P. C. *J. Am. Chem. Soc.* **1975**, *100*, 3316–21.
(13) Small, G. W.; Jurs, P. C. *Anal. Chem.* **1983**, *55*, 1121–27.
(14) Bernassau, J. M.; Fetizon, M.; Maia, E. R. *J. Phys. Chem.* **1986**, *90*, 6129–34.
(15) Bastard, J.; Bernassau, J. M.; Bertranne, M.; Maia, E. R. *Magn. Reson. Chem.* **1988**, *26*, 992–1002.
(16) McIntyre, M. K.; Small, G. W. *Anal. Chem.* **1987**, *59*, 1805–11.
(17) Egolf, D. S.; Jurs, P. C. *Anal. Chem.* **1987**, *59*, 1586–93.
(18) Sutton, G. P.; Jurs, P. C. *Anal. Chem.* **1989**, *61*, 863–71.
(19) Egolf, D. S.; Brockett, E. B.; Jurs, P. C. *Anal. Chem.* **1988**, *60*, 2700–2706.
(20) Small, G. W.; Jurs, P. C. *Anal. Chem.* **1983**, *55*, 1128–34.
(21) Small, G. W.; Jurs, P. C. *Anal. Chem.* **1984**, *56*, 1314–23.
(22) Small, G. W.; Jurs, P. C. *Anal. Chem.* **1984**, *56*, 2307–14.
(23) Ranc, M. L.; Jurs, P.C. The Pennsylvania State University, unpublished results.

Peter C. Jurs (center), professor of chemistry at The Pennsylvania State University, received his Ph.D. from the University of Washington in 1969. His research interests include computer applications in chemistry, studies of correlations between molecular structure and biological activity or physicochemical properties, and applications of pattern recognition and multivariate statistics to analytical data interpretation.

G. Paul Sutton (right) received his B.S. degree from the University of Delaware in 1985 and is a fourth-year graduate student pursuing a Ph.D. in analytical chemistry. His research interests include the development and application of computer-aided multivariate statistical methods to NMR spectral simulation problems and to the study of chromatographic retention properties.

Martha L. Ranc (left) received her B.S. degree in chemistry and computer science from Chestnut Hill College (Pennsylvania) in 1986. She is currently pursuing a Ph.D. in chemistry and is working in the area of ^{13}C NMR simulation.

INDEX TO ADVERTISERS IN THIS ISSUE

CIRCLE INQUIRY NO.	ADVERTISERS	PAGE NO.
3	***A&D Engineering, Inc.**	1106A
1	***Alpkem Corporation**	1096A
18	**Bacharach Coleman Instruments** Karl J. Skutski & Associates, Inc.	1103A
22	**Baird Corporation** W. J. Hearn & Company, Inc.	1095A
24	***Bio-Rad Chemical Division** Pan & Associates	1098A
20	**Burdick & Jackson Division/Baxter** Nordstrom/Cox Marketing	1071A
30	***Conostan Division/Conoco Specialty Products** Robert Lamons & Associates	1119A
28	**CYpress SYstems, Inc.**	1112A
36	**3-D Visions, Inc.**	1094A
32	***Dialog Information Services, Inc.** Humpal, Leftwich & Sinn, Inc.	1117A
45	**ENI** Quinlan Foels & Company	1101A
58	***Galileo Electro-Optics Corp.** Legasse Associates Advertising, Inc.	1105A
60	***Gilson Medical Electronics, Inc.**	1083A
61	****Gilson Medical Electronics, SA**	1083A
56	***Gow-Mac Instrument Company** Scientific Marketing Services, Inc.	1070A
63	**Hamamatsu Corporation** Ketchum/Mandabach & Simms	1081A
67	***Hamilton Company** Robert E. LaPointe & Company	1076A
65	***Hewlett-Packard Company** Brooks Communications	1065A
88	**Labconco Corporation** Prospect Avenue Associates	1091A
90	***Leco Corporation**	OBC
92	***Leybold Vacuum Products, Inc.** CD Werbeagentur GmbH	1078A
94	***Mattson Instruments, Inc.** Cunningham & Welch Design Group	1066A
100–104	***Mettler Instrument Corporation** Sardi & Bleecker	1093A
96	***Millipore Corporation** Mintz & Hoke, Inc.	1111A
120	***Omega Engineering, Inc.** Media Business House	IFC
122	***On-Site Instruments**	1104A
–	**Proctor & Gamble** Hogan, Nolan & Stites	1109A
140	**Rheodyne, Inc.** Bonfield Associates	1085A
150	**Salon du Laboratoire** GERP	1113A
148	***Sartorius Instruments** Robert E. LaPointe & Company	1069A
152	**Siemens Analytical X-Ray Instruments, Inc.**	1073A
154	***Swagelok Company** Falls Advertising Company	1087A
156	***Tekmar Company** Kenyon Hoag Associates	1072A
34	**The University of Dayton Research Institute**	1112A
168	**Vestec Corporation** Barbeau-Hutchings Advertising, Inc.	1114A
170	**VG Masslabs** Burgess Daring Advertising, Ltd.	1074A

Directory section, see page 1121A.
** See ad in ACS Laboratory Guide.*
*** Company so marked has advertisement in Foreign Regional edition only.*
Advertising Management for the American Chemical Society Publications

CENTCOM, LTD

President
Thomas N. J. Koerwer

Executive Vice President *Senior Vice President*
James A. Byrne **Benjamin W. Jones**
Clay S. Holden, *Vice President*
Robert L. Voepel, *Vice President*
Joseph P. Stenza, *Production Director*

500 Post Road East
P.O. Box 231
Westport, Connecticut 06880
(Area Code 203) 226-7131
Telex No.643310
FAX: 203-454-9939

ADVERTISING SALES MANAGER
Bruce E. Poorman

ADVERTISING PRODUCTION MANAGER
Jane F. Gatenby

SALES REPRESENTATIVES

Philadelphia, PA . . . Patricia O'Donnell, CENTCOM, LTD., GSB Building, Suite 405, 1 Belmont Avenue, Bala Cynwyd, Pa. 19004. Telephone: 215-667-9666, FAX: 215-667-9353

New York, NY . . . John F. Raftery, CENTCOM, LTD., 60 East 42nd St., New York, N.Y. 10165. Telephone: 212-972-9660

Westport, CT . . . Edward M. Black, CENTCOM, LTD., 500 Post Road East, P.O. Box 231, Westport, Ct. 06880. Telephone: 203-226-7131, Telex 643310, FAX: 203-454-9939

Cleveland, OH . . . Bruce E. Poorman, John C. Guyot, CENTCOM, LTD., 325 Front St., Suite 2, Berea, Ohio 44017. Telephone: 216-234-1333, FAX: 216-234-3425

Chicago, IL . . . Michael J. Pak, CENTCOM, LTD., 540 Frontage Rd., Northfield, Ill. 60093. Telephone: 312-441-6383, FAX: 312-441-6382

Houston, TX . . . Michael J. Pak, CENTCOM, LTD. Telephone: 312-441-6383

San Francisco, CA . . . Paul M. Butts, CENTCOM, LTD., Suite 1070, 2672 Bayshore Frontage Road, Mountain View, CA 94043. Telephone: 415-969-4604

Los Angeles, CA . . . Clay S. Holden, CENTCOM, LTD., Newton Pacific Center, 3142 Pacific Coast Highway, Suite 200, Torrance, CA 90505. Telephone: 213-325-1903

Boston, MA . . . Edward M. Black, CENTCOM, LTD. Telephone: 203-226-7131

Atlanta, GA . . . John F. Raftery, CENTCOM, LTD. Telephone: 212-972-9660

Denver, CO . . . Paul M. Butts, CENTCOM, LTD. Telephone: 415-969-4604

United Kingdom

Reading, England . . . Malcolm Thiele, Technomedia Ltd., Wood Cottage, Shurlock Row, Reading RG10 OQE, Berkshire, England. Telephone: 073-434-3302, Telex #848800, FAX: 073-434-3848

Lancashire, England . . . Technomedia Ltd., c/o Meconomics Ltd., Meconomics House, 31 Old Street, Ashton Under Lyne, Lancashire, England. Telephone: 061-308-3025

Continental Europe . . . Andre Jamar, International Communications, Inc., Rue Mallar 1, 4800 Verviers, Belgium. Telephone: (087) 22-53-85, FAX: (087) 23-03-29

Tokyo, Japan . . . Sumio Oka, International Media Representatives Ltd., 2-29 Toranomon, 1-Chome Minato-ku Tokyo 105 Japan. Telephone: 502-0656, Telex #22633, FAX: 591-2530

Search spectra online

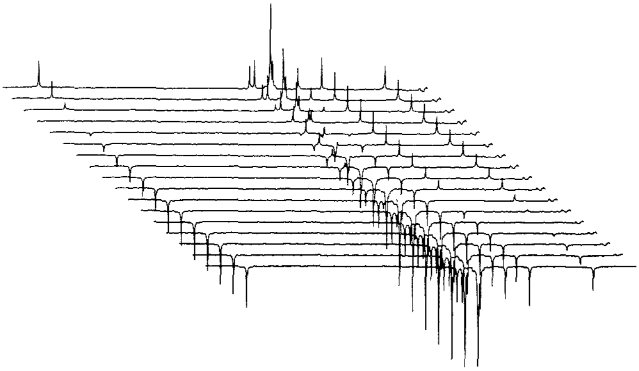

C13-NMR/IR
Now available on STN®

Now there's a new way to identify chemical substances online through their CNMR or IR spectra. Discover the Carbon 13 Nuclear Magnetic Resonance/Infrared file and see how invaluable it can be in your research!

The file and its sources In C13-NMR/IR you'll find almost 120,000 spectra for 90,000 compounds. Data are drawn from significant journals, spectral catalogs, and unpublished spectra from BASF and other industrial labs.

The workshop Not familiar with searching spectra online? Our workshop shows you how to

- find spectra by searching a substance name or molecular formula
- predict a C13 spectrum or shift
- find exact or similar structures
- find substances using CAS Registry Numbers

How to get started The C13-NMR/IR file is available only through the STN International network. If you're already an STN user, arrange access to C13-NMR/IR by calling Customer Service at 800-848-6538 or 614-447-3600. If you aren't yet using STN, return the enclosed coupon.

☐ **Yes!** I'd like more information about C13-NMR/IR on STN International. Please rush me my FREE information package.

Name

Organization

Address

Phone

Mail to: STN International, c/o Chemical Abstracts Service,
Dept. 38389, P.O. Box 3012, Columbus, OH 43210 U.S.A.

In Europe, contact STN International c/o FIZ Karlsruhe, P.O. Box 2465, D-7500 Karlsruhe 1, Federal Republic of Germany. Telephone: (+49) 7247/808-555.

STN®
INTERNATIONAL
The Scientific & Technical Information Network

STN is operated in North America by Chemical Abstracts Service, a division of the American Chemical Society; in Europe, by FIZ Karlsruhe; and in Japan, by JICST, the Japan Information Center of Science and Technology.

Analytical
CHEMISTRY

EDITOR: **GEORGE H. MORRISON**

ASSOCIATE EDITORS: **Klaus Biemann, Georges Guiochon, Walter C. Herlihy, Robert A. Osteryoung, Edward S. Yeung**

Editorial Headquarters
1155 Sixteenth St., N.W.
Washington, DC 20036
Phone: 202-872-4570
Telefax: 202-872-6325

Managing Editor: Sharon G. Boots

Associate Editors: Louise Voress, Mary Warner

Assistant Editors: Grace K. Lee, Alan R. Newman

Editorial Assistant: Felicia Wach

Director, Operational Support: C. Michael Phillippe

Production Manager: Leroy L. Corcoran

Art Director: Alan Kahan

Designer: Amy Meyer Phifer

Production Editor: Elizabeth E. Wood

Circulation: Claud Robinson

Editorial Assistant, LabGuide: Joanne Mullican

Journals Dept., Columbus, Ohio

Associate Head: Marianne Brogan

Journals Editing Manager: Joseph E. Yurvati

Associate Editor: Rodney L. Temos

Staff Editor: Sharon K. Hatfield

Advisory Board: Bernard J. Bulkin, Michael S. Epstein, Renaat Gijbels, Peter R. Griffiths, Thomas L. Isenhour, Nobuhiko Ishibashi, James W. Jorgenson, Peter C. Jurs, Mary A. Kaiser, David L. Nelson, Lawrence A. Pachla, Ralph E. Sturgeon, George S. Wilson, Mary J. Wirth, Andrew T. Zander, Richard N. Zare
Ex Officio: Sam P. Perone

Instrumentation Advisory Panel: James B. Callis, Bruce Chase, R. Graham Cooks, L. J. Cline Love, Sanford P. Markey, Ronald E. Majors, Linda B. McGown, Gary W. Small, R. Mark Wightman

Published by the
AMERICAN CHEMICAL SOCIETY
1155 16th Street, N.W.
Washington, DC 20036

Publications Division

Director: Robert H. Marks

Journals: Charles R. Bertsch

Special Publications: Randall E. Wedin

Manuscript requirements are published in the January 1, 1989 issue, page 91. Manuscripts for publication (4 copies) should be submitted to ANALYTICAL CHEMISTRY at the ACS Washington address.

The American Chemical Society and its editors assume no responsibility for the statements and opinions advanced by contributors. Views expressed in the editorials are those of the editors and do not necessarily represent the official position of the American Chemical Society.

AUTHOR INDEX

Arbogast, B., 2154

Bachas, L. G., 2160
Bemgård, A. K., 2165
Benninghoven, A., 2142
Bletsos, I. V., 2142
Blomberg, L. G., 2165
Bobrowski, A., 2178
Burdick, D. S., 2219

Castro, M. E., 2130
Chmelík, J., 2224
Colmsjö, A. L., 2165
Cox, J. A., 2176

Daunert, S., 2160
Deinzer, M. L., 2154
Deml, M., 2224
DeZwaan, J., 2207
Dumke, I., 2149

Ebato, H., 2185
Elnemma, E. M., 2189

Faber, E., 2149
Fuoco, R., 2212

Griffiths, P. R., 2212

Hanson, C. D., 2130
Hassan, S. S. M., 2189
Hercules, D. M., 2142
Hill, H. A. O., 2200

Hirokawa, K., 2137
Hooker, D. B., 2207

Janča, J., 2224
Jaworski, R. K., 2176

Karakatsanis, C. G., 2142
Klein, N. A., 2200

Laramée, J. A., 2154

McGown, L. B., 2219
Michael, A. C., 2193
Millican, D. W., 2219
Mori, S., 2171
Mouri, M., 2171

Okahata, Y., 2185

Payne, B. R., 2160
Pentoney, S. L., Jr., 2212
Poggenburg, J., 2149
Psalti, I. S. M., 2200

Rieck, J. N., 2142
Russell, D. H., 2130

Tu, X. M., 2219

vanLeyen, D., 2142

Wagatsuma, K., 2137
Walton, N. J., 2200
Wightman, R. M., 2193

Sweep Excitation

Resonance

Curtiss D. Hanson, Mauro E. Castro, and David H. Russell*

Department of Chemistry, Texas A&M University, College Station, Texas 77843

The Fourier transform ion cyclotron resonance (FT-ICR) signal is produced by the coherent motion of a population of ions. The ability to produce a well-defined ion packet by excitation of an initially random ion ensemble is a major limiting factor of high mass FT-ICR. Ions must be both resonant and in phase with the applied radio frequency excitation field to be accelerated to radii suitable for detection by FT-ICR. Synchronization of the phase angles of an ensemble of ions occurs by off-resonant acceleration during frequency swept excitation. Results from computer-simulated ion trajectories suggest that phase synchronization of the ion packet prior to resonant excitation results in better spatial definition of the ion ensemble.

INTRODUCTION

The basis for ion cyclotron resonance (ICR) is the periodic circular orbit of an ion in a homogeneous magnetic field (*1*). The period of the cyclotron orbit corresponds to a specific frequency; thus ion detection by ICR is achieved by relating the frequency of the orbit to the mass of the ion. The FT-ICR signal is produced by accelerating an ion population into a cycloiding packet which induces an image current in the receive plates of the ICR cell (*2–4*). The performance characteristics associated with FT-ICR (e.g., sensitivity (*5*), mass resolution (*6*), mass range (*7*), and Fellgett advantage (*8*)) arise from the ability to produce a spatially defined ion packet from an initially random ion ensemble. Spatial definition of the ion packet is defined by a combination of the radial distribution (distribution of kinetic energy in the $X-Y$ plane) and the radial dispersion (angular distribution) (*9*). In most FT-ICR experiments (performed with electron impact ionization) the radial distribution of the initially formed ions is small and the ions have near-thermal kinetic energies. Consequently, the radial distribution of the ions does not adversely affect ion detection. It is important to note that some ICR experiments (e.g., experiments utilizing methods that involve momentum transfer, such as secondary ion mass spectrometry (SIMS), collisional ionization, or ion injection from an external source (*10–12*)) are not adequately described by models based on electron impact ionization of a static gas.

Although there has been recent success in the detection of high mass nonpolar organic ions by laser desorption FT-ICR (*13*), the ion dynamics involved are different than those experienced with other desorption ionization methods (e.g., SIMS (*14, 15*), ^{252}Cf-PDMS (plasma desorption mass spectrometry) (*16*), etc.). In the case of laser desorption within the ion cell, a large number of ions and neutrals are produced during the desorption process (*17*). Ions that are desorbed in this manner are thermalized by ion–neutral interactions (*18*) and recent results suggest ion–ion interactions also play a role in ion trapping (*19*). Conversely, ions that are produced by SIMS are initially formed with a relatively large distribution of kinetic energies, and because SIMS experiments are performed by using low primary beam densities, the yield for neutral species is not sufficient for ion–neutral relaxation. Similarly, ion motion and the absence of ion–neutral relaxation further complicate experiments performed by using an external ion source instrument. Thus, for SIMS and external ion source instruments it is possible that ions are trapped in the ion cell with initially random phase angles and relatively high (1–10 eV) kinetic energies. Because the ability to "drive" ions into a coherent ion packet is inversely related to the ions translational energy (*20*), ions that are trapped in the ICR cell with significant kinetic energies yield poorly defined ion packets following resonant excitation. The inability to produce coherent motion in a spatially discrete packet of ions results in the loss of both sensitivity and resolution.

The principal factor in the production of a coherent ion packet is the ability to drive an ensemble of ions having initially random velocity vectors (e.g., random phase angles) into coherent motion (i.e., having a narrow angular distribution). Because the final radial distribution of a population of ions is dependent upon how quickly the random ensemble is "driven" into coherent motion (*20*), ion detection by FT-ICR is a direct result of the phase angle synchronization of the initially random ion population. Phase angle synchronization of the ion ensemble is a result of ion interaction with an electric field. In a typical broad-band FT-ICR experiment, ion excitation is achieved by sweeping a radio frequency (rf) oscillator over a range of frequencies corresponding to the mass range of interest. Individual ions experience a net gain of translational energy as their respective frequencies come into resonance. Although ions only receive a net gain in kinetic energy during resonant excitation, ions experience the electric field force during the entire excitation period. In order to understand the processes of phase angle synchronization of the ion ensemble, the effect of ion interaction with a nonresonant rf electric field must be examined.

The process of phase synchronization on the dimensions of the ion packet following excitation is difficult to evaluate in a simple cubic ICR cell. Ions that are produced as a result of electron impact have kinetic energies corresponding to those of the neutrals prior to ionization. Thus, ions are driven into phase coherence quickly and accelerated as a well-defined ion packet; thus the impact of phase synchronization is negligible. On the other hand, ions that are formed with appreciable kinetic energies are introduced into the cell with undefined velocities and spatial locations. Direct measurements of the spatial dimensions of the ion packet in a simple cubic cell are difficult due to the lack of an unambiguous diagnostic procedure for probing the effect of phase advancement and ion excitation. The objective of this paper is to discuss the process of phase advancement and evaluate the effects of off-resonant acceleration prior to resonant excitation on the formation of a coherent ion packet for detection by FT-ICR.

MONTE CARLO CALCULATIONS

In order to address the effect of phase angle on ion excitation, it was necessary to develop a computer program that allowed user-defined initial ion conditions. Of primary importance was the ability to define the initial phase angle of the ion motion with respect to the applied rf excitation. To

0003-2700/89/0361-2130$01.50/0 © 1989 American Chemical Society

investigate the effect of ion excitation in FT-ICR, an ion trajectory model was developed by Eyler and co-workers (*21*) based on the motion of charged particles in a magnetic field (*22*). This program was expanded and modified by Castro and Russell (*23*) to allow precise control of excitation waveform and initial ion conditions (i.e., ion location, initial phase angle with respect to the applied rf electric field, initial kinetic energy of the ion, etc.). This enhanced program permits systematic evaluation of the effect of ion kinetic energy and phase angle on excitation and the production of the coherent ion packet.

The computer program is based on an analytical solution of the equations of motion for ions accelerated by an applied rf electric field. Only ion motion in the X–Y plane is addressed by the program to allow specific studies of radial motion to be performed. To do this the equations of motion for an ion of a given mass, charge, and velocity in a homogeneous magnetic field were derived for ion excitation in a homogeneous rf electric field. The electric and magnetic forces acting on an ion were calculated based on the ions temporal location in the applied fields. On the basis of the forces acting on the ion at the location, an ion trajectory was calculated. From the trajectory calculation, a new ion location was determined. Following an operator-determined time interval, the computer program itteratively calculates a new ion location and ion trajectory. The frequency of the applied rf electric field was incremented to allow frequency sweep excitation studies.

RESULTS AND DISCUSSION

The original theoretical treatment for resonant excitation in ICR was developed by neglecting the effect of the initial phase angles of the ion population (*24–26*). However, recent work suggests that the phase angle cannot be neglected for ions having significant radial translational energies (*13, 20, 28*). Such considerations are consistent with work reported by Eyler (*27*).

Phase synchronization of a incoherent ion ensemble occurs through the process of phase advancement. For example, an ion that is initially out-of-phase with respect to the applied resonant rf excitation must phase advance into synchronous alignment with the electric field prior to a net gain of translational energy (*13, 20, 28*). A change in the relative phase angle of an ion in a cyclotron orbit requires a shift in the period of that orbit. Because the cyclotron frequency is related to the mass-to-charge ratio and the magnetic field strength and *independent* of the translational energy of the ion, acceleration of an ion in a magnetic field (i.e., a change in the ion's translational energy) results in a larger cyclotron radius and *not* a change in frequency. Conversely, the effective frequency of an ion in a combined electric and magnetic field is a *function* of the ion's kinetic energy.

The mechanism for both ion excitation and phase advancement is the application of a *resonant* oscillating electric field. An ion moving in phase with the applied rf is continuously accelerated (acceleration is caused by the synchronous alignment of the ion's motion with the force vectors produced by the rf field) whereas an ion moving out-of-phase ($\gamma \neq 0$) with the applied rf field experiences a synchronous *misalignment* of the velocity and electric field force vectors (*20*). As illustrated in Figure 1, the misalignment of an out-of-phase ion with the applied rf electric field creates a net force perpendicular to the ion motion ($F_{E\perp} = qE_{\perp} = qE \sin \gamma$). The frequency shift required to move an out-of-phase ion into synchronous alignment with the applied electric field is achieved by effect of $F_{E\perp}$ on the ion's angular frequency. The perpendicular component of the applied electric field causes a shift in the angular frequency of the ion (i.e., $\omega_{rf} \neq \omega_{ion}$) allowing phase advancement and synchronization of the ion ensemble to occur.

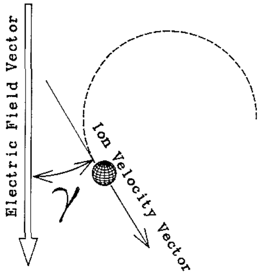

Figure 1. Illustrated is the effect of the misalignment of an out-of-phase ion with the applied rf electric field. The misalignment creates a net force perpendicular to the ion motion ($F_{E\perp} = qE_{\perp} = qE \sin \gamma$) resulting in a frequency shift.

The magnitude of the frequency shift determines how rapidly phase synchronization occurs. Because the magnetic field is velocity dependent, ions having low translational energy experience a strong component of the electric field relative to that of the magnetic field. The perpendicular component of the electric field causes a significant frequency shift and phase advancement occurs rapidly. Conversely, high radial ion velocities increase the force of the magnetic field with respect to the force of the electric field. Under these conditions, the frequency shift induced by the perpendicular component of the rf electric field is reduced (i.e., $\omega_{rf} \approx \omega_{ion}$). Consequently, phase advancement and phase synchronization do not occur instantaneously.

The time required for phase advancement reduces the total amount of translational energy gained during a discrete excitation period. For example, an ion that is initially in-phase with the rf excitation gains translational energy during the entire excitation period (τ_{total}). Conversely, phase advancement occurs over a finite period (τ_{phase}) for an ion that is initially out of phase and the ion gains translational energy during some fraction of the total excite period ($\tau_{total} - \tau_{phase}$). Ions having initially random phases and significant radial velocities therefore yield a significant energy distribution following resonant excitation. An ion ensemble having a distribution of kinetic energies following resonant excitation corresponds to a large radial distribution of the ion packet (i.e., poorly defined spatial dimensions in the X–Y plane).

EFFECT OF MASS AND ENERGY ON PHASE SYNCHRONIZATION

Studies of the effects of mass and energy on ion motion and ion excitation are simplified by Monte Carlo simulations. The computer simulations assume totally homogeneous electric and magnetic field gradients. Ion location is determined by calculating the resultant vectors of the electric and magnetic fields. The effects of mass and energy on phase synchronization are illustrated by observing the effect of rf excitation for an ion which is initially in-phase ($\gamma = 0$) compared to that of an ion which is initially out-of-phase ($\gamma = 180$). Figure 2A contains a temporal plot of the calculated trajectories for two ions (m/z 500) having thermal kinetic energy and a relative phase angle of 180°. The trajectories result from acceleration of the ions with a resonant, single frequency rf field (900 V/m). Because the initial radial velocity is low, $F_{MAG.} \approx F_{ELEC.}$, phase synchronization of the ion with the rf electric field occurs quickly and the ions are excited as a coherent packet. Conversely, ions that have initial radial velocities corresponding to 3 eV of kinetic energies follow markedly different trajectories (see Figure 2B). The ion that is out-of-phase experiences a continuous misalignment with the electric field resulting in a different trajectory compared to that of an ion which is

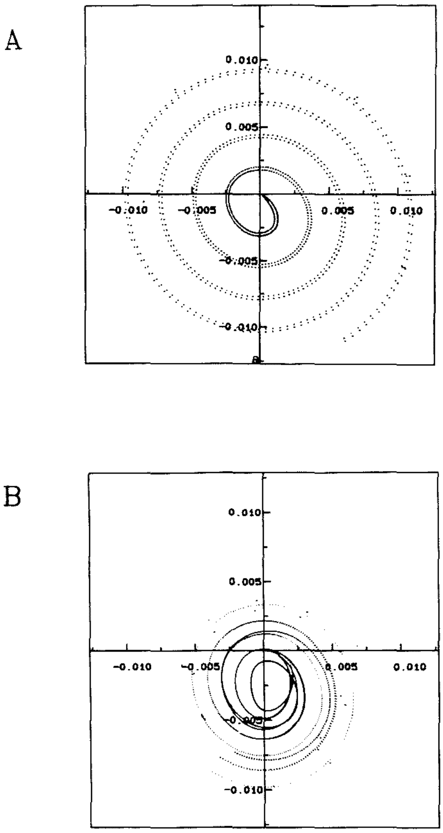

Figure 2. Contained are temporal plots of ion location (axis plotted in cm) from the calculated trajectories in a 3-T magnetic field for two ions (*m/z* 500) having (A) thermal translational energies and (B) significant translational energies (3 eV) with a relative phase angle of 180°.

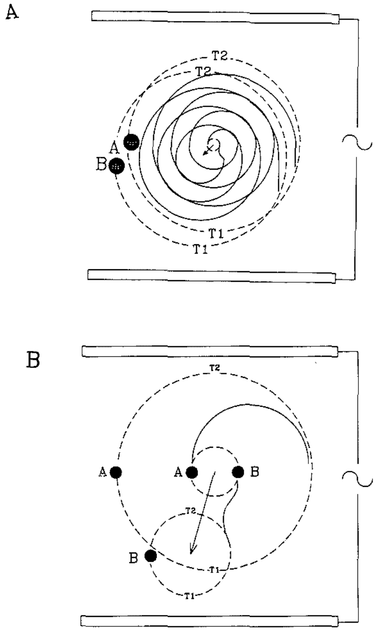

Figure 3. Trajectories for two ions (*m/z* 20 (A) and *m/z* 4000 (B)) having a phase relationship of 180° (γ = 0 and 180° relative to the applied electric field) are illustrated.

initially in phase. The simulations show that instantaneous phase synchronization prior to a net gain of translational energy results is better spatial definition of the ion ensemble following excitation. The spatial distribution of the ion packet following excitation is defined by the relative differences in the temporal locations of the ions comprising the ion ensemble. For example, the ions having well-defined (i.e., coherent) dimensions have negligible differences in their temporal positions relative to the average radius of the ensemble. Such an ion ensemble can be approximated by a rotating monopole (*28*).

The effect of mass on phase synchronization and the ability to produce a coherent ion packet can be studied by observing the simulated trajectories for two ions having relative phases of 180° (γ = 0 and 180° relative to the applied rf field). Illustrated in Figure 3A are the trajectories for two ions of *m/z* 20 accelerated by a resonant rf field. The final orbits (shown as dashed lines) show that at times corresponding to γ = 180° (T1) and γ = 0 (T2), the temporal positions of ion A (initially in phase) and ion B (initially out-of-phase) are separated by a distance that is small with respect to the final dimensions of the orbits. The near identical trajectories for the two ions arise because the shift in the orbit center (illustrated by a solid arrow) and the differences in final radii are both small relative to the final radius of orbit. Figure 3B contains a similar plot for the trajectories for two ions of *m/z* 4000. Although the ion initially out-of-phase (B) is driven into phase synchronous motion relative to an in-phase ion (A), there are significant differences in both the final radii and the centers of the cyclotron orbits. At time T1 both ions contribute to the ICR signal. However, because of the spatial differences in cyclotron orbits, the resultant signal from ion B will be reduced at time T2. Therefore, the inability to produce spatial coherence leads to a reduction in the detected signal.

The effect of mass on the magnitude of the center shift and the deviations in relative radii is illustrated in Figure 4. The plots contained in Figure 4 were obtained by comparing the simulated ion trajectories for two ions (in and out of phase with respect to the applied rf field) which have significant initial kinetic energies (3 eV). Ions of a given *m/z* ratio are accelerated to a final radius that is suitable for detection by FT-ICR (ca. 1 cm). The time required for phase synchronization results in a difference in the energy gained by an ion which was initially in phase and an ion which must undergo phase synchronization prior to gaining energy.

Figure 4A shows the mass dependence for the radial deviation accompanying rf excitation of out-of-phase ions. The mass dependence arises as a result of time required for phase advancement to occur (τ_{phase}). If τ_{phase} is significant relative to the period of a cyclotron orbit, then the time required for phase advancement of an out-of-phase ion increases with mass. It is important to note that the total excitation time (τ_{total}) of the ion ensemble is limited by the time that an inphase ion can be accelerated prior to ejection from the ICR cell. Because τ_{total} is constant for both in-phase and out-of-phase ions, the differences in the net period of excitation ($\tau_{\text{net}} = \tau_{\text{total}} - \tau_{\text{phase}}$) also increase as a function of the mass. The differences in the radii of high mass ions arise because of the dependence

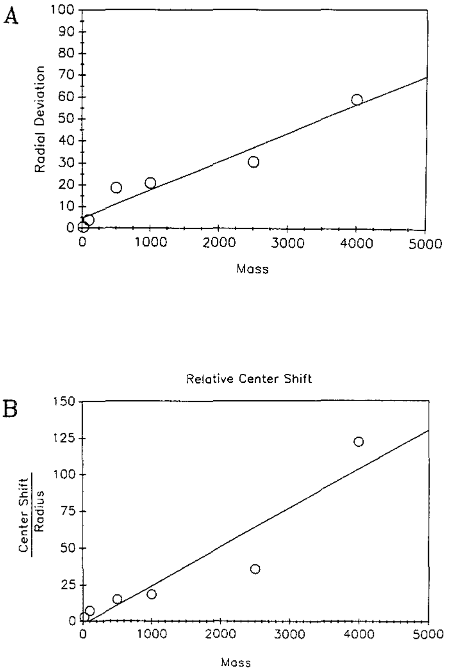

Figure 4. A plot of the effect of increasing mass on (A) the magnitude of the radial deviation (expressed as percent) and (B) on the magnitude of the relative shift in the center of the cyclotron orbit (compared to the final radius of the ensemble) determined for two ions of a given m/z ratio having a phase relationship of 180°. A linear regression of the data from the calculations illustrates the trend.

of the cyclotron radius on τ_{net}. For example, the out-of-phase ion (B) in Figure 3B required a finite time to phase advance (τ_{phase}) which reduces the net period for excitation ($\tau_{\mathrm{total}} - \tau_{\mathrm{phase}}$) compared to that of the in-phase ion (A). Becuase ion B acquired kinetic energy for a shorter period of time, the final radius of ion B is significantly smaller than that of ion A.

Figure 4B correlates the effect of mass on the magnitude of the center shifts for two ions having a phase relationship of 180°. For ions having the same initial kinetic energies, the resulting shift in the center of the cyclotron radius for the out-of-phase ion is directly dependent on the m/z ratio. The distribution of the ion ensemble arises because the center shift of the out-of-phase ions requires a deflection of the ion's momentum. Because the radius of an ion's curvature in a magnetic field is directly related to its momentum, the magnitude of the resulting center shift increases with mass.

The combined effects of both increasing the deviation of the different radii and relative center shifts result in an inability to produce coherent ion motion for high mass ions having initially significant (ca. 3 eV) kinetic energies and random phases. The plot contained in Figure 5 illustrates the decrease in the degree of coherence which is obtained by resonant acceleration as a function of mass. In this plot the degree of coherence is defined by the relationship described by eq 1. In this relationship, r_{ave} is the average radius achieved by the ion ensemble following excitation and r_{dev} is average deviation of the different ions about that radius. Such a deviation is therefore a function of both the center shift and radial deviation (*13, 20, 28*).

$$\text{degree of coherence } (\%) = 10^2(r_{\mathrm{ave}} - r_{\mathrm{dev}})/r_{\mathrm{ave}} \quad (1)$$

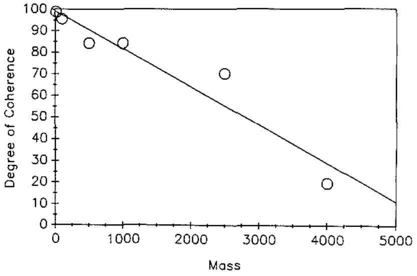

Figure 5. A linear regression of the data obtained from the Monte Carlo plots illustrates the effect of mass on the degree of coherence of the ion ensemble. The data are obtained from the calculated ion trajectories and combine the effects of both the center shift and radial deviation on two ions of a given m/z ratio having a phase relationship of 180°.

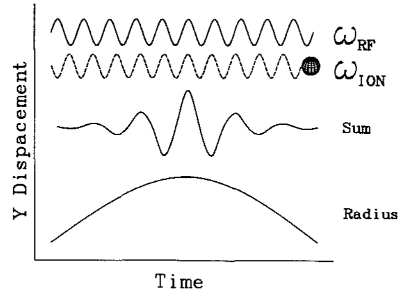

Figure 6. A plot of Y displacement as a function of time is illustrated for the relative position of an ion which is accelerated by a frequency which is discretely different from its cyclotron frequency. The ion moves in- and out-of-phase with respect to the applied electric field. When the ion is in-phase, it will gain translational energy and the associated cyclotron radius will increase. When it is out-of-phase, the misalignment of the electric field force vectors will decelerate the ion resulting in a smaller cyclotron radius.

OFF-RESONANCE EXCITATION AND PHASE SYNCHRONIZATION

The addition of two waveforms of different frequencies results in an interference pattern in time. The pattern of interference (i.e., the beat frequency) arises by the periodic constructive and destructive addition of the two waves. The node of a beat frequency corresponds to a time at which the two waveforms are 180° out of phase, whereas, the maximum amplitude of the beat frequency occurs when the waveforms are in phase. The beat frequency for an ion and an oscillating electric field of different frequency (i.e, off-resonance) is illustrated in Figure 6. The ion moves in and out of phase with respect to the applied rf excitation resulting in ion energy that varies with $\sin^2(t)$ (*29*). When the ion is in phase with the applied rf excitation, it is accelerated to higher translational energy (i.e., a larger cyclotron radius). During the node of the beat frequency, the ion is decelerated to lower translational energy (i.e., a smaller cyclotron radius). Thus, the radius of cyclotron orbit continuously oscillates as it interacts with the electric field. Because of the oscillation of the beat frequency, ions are continually accelerated (excited and deexcited) with no net gain of kinetic energy.

The translational energy acquired by an ion during frequency sweep excitation has been studied by Marshall and co-workers (*30*). The instantaneous power absorption is related to the rate that the frequency is swept and the difference between the applied and cyclotron frequencies (*13, 20, 28*).

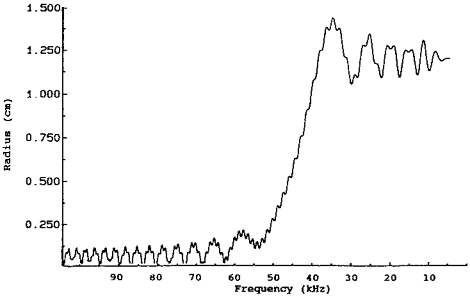

Figure 7. A plot of ion radius (*m/z* 1000, 3-T B field, 0.01 eV initial kinetic energy) during frequency sweep excitation clearly demonstrates the effect of off-resonant excitation. Ions are constantly accelerated by the applied electric field during the entire excitation period. There is only a *net* gain of translational energy when $\omega_{\mathrm{applied}} = \omega_c$. This results in a continuous oscillation of the cyclotron radius similar to single frequency off-resonance excitation.

During frequency-sweep excitation of the ion ensemble, ions of all *m/z* ratios are continuously accelerated and decelerated when $\omega_{\mathrm{applied}} \neq \omega_c$, and a *net* gain of translational energy only occurs when $\omega_{\mathrm{applied}} = \omega_c$. The oscillation of the cyclotron radius during swept excitation can be observed by numerical solutions to the equations of ion motion (*27, 31*). Contained in Figure 7 is a plot of cyclotron radius vs applied frequency during swept excitation. The modulation in the cyclotron radius prior to a net gain of energy clearly demonstrates the effect of off-resonance acceleration on ion motion. It is important to note that ions of all *m/z* ratios are influenced by the electric field, regardless of the applied frequency and that there is no *net* gain of kinetic energy prior to $\omega_{\mathrm{applied}} = \omega_c$.

Phase synchronization of ions trapped in an FT-ICR cell occurs through interaction with an applied electric field. Because no mechanism exists for moving ions out of phase with respect to the electric field, phase synchronization is *directional*. For example, ions that have the same relative phase angle will experience identical force vectors at any time during the oscillation of the electric field. As long as the forces acting on the two ions are the same, they continue to move coherently. Therefore, an initially random ensemble of ions driven into phase coherent motion continue to move in phase in the absence of collisions.

All ions comprising an ion ensemble interact with the applied rf field during a frequency sweep excitation. Because of the off-resonant interaction of the ion ensemble with the swept frequency, ions are "driven" into phase synchronous motion prior to $\omega_{\mathrm{applied}} = \omega_c$. Ions that are driven into phase during frequency sweep excitation remain in phase. The question we now pose is can off-resonance excitation cause phase synchronization of an ion ensemble prior to resonant acceleration for detection, i.e., result in better spatial distribution of the coherent ion packet.

It is important to realize that frequency sweep excitation affects more than ion energy. In experiments using "chirp" or swept excitation, the interaction of the ion with nonresonant electric fields must be considered. The effect of nonresonant phase synchronization prior to resonant acceleration is illustrated by computer-simulated ion motion. Ion packet definition following swept excitation can be evaluated by varying only the sweep duration prior to resonant acceleration. Off-resonant phase synchronization can be evaluated by monitoring packet dimensions as a function of sweep duration prior to $\omega_{\mathrm{applied}} = \omega_c$.

Figure 8 contains plots of trajectories for *m/z* 500 ions (initial kinetic energy of 3 eV) resulting from frequency sweep excitation (1378 V/m, 2.54 cm cell, 3 T) to a final energy of ca. 100 eV. The effect of phase angle and ion velocity is examined by using four ions having phase angles corresponding to $\gamma = 0, 90, 180, 270$. By selection of specific phase angles, it is possible to illustrate the behavior of a random ion ensemble. Figure 8A contains a plot of the temporal ion locations following a swept excitation initiated at a frequency corresponding to *m/z* 50. That is, ions of *m/z* 500 interact with the electric field (with no net gain in translational energy) during the swept excitation between *m/z* 50 and *m/z* 500. At a sweep rate of 884 Hz/μs, ions of *m/z* 500 interact with the electric field of ca. 1 ms prior to resonant acceleration. The plot of ion location contained in Figure 8D is a result of a frequency sweep initiated at a frequency corresponding to *m/z* 300. During the abbreviated frequency sweep, ions of *m/z* 500 interact with the electric field for ca. 0.2 ms prior to a net gain of kinetic energy. These plots illustrate that longer interaction time with the applied electric field results in better definition of the ion packet following excitation.

Contained in Figure 9 is a plot of the effect of sweep duration on the relative dimensions of the ion ensemble. The degree of coherence achieved for four ions ($\gamma = 0, 90, 180, 270$ and 3 eV of kinetic energy) of *m/z* 500 is determined for different interaction times prior to resonant excitation. From this relationship, it is clear that longer interaction times with the rf electric field prior to resonant excitation results in a better defined ion packet for detection by FT-ICR.

PRACTICAL ASPECTS OF OFF-RESONANCE EXCITATION FOR DETECTION OF HIGH MASS IONS

The high sensitivity and high resolution attributed to FT-ICR arise from the ability to produce a well-defined ion packet by excitation of an initially random ion ensemble. Ions must be both resonant and in-phase with the applied rf excitation field to be accelerated to radii suitable for detection. Ions are driven into phase coherence by interacting with a resonant rf frequency. However, phase angle synchronization of the ion ensemble can also occur by off-resonant acceleration during frequency swept excitation. As illustrated by the data contained in Figures 8 and 9, phase synchronization of the ion packet prior to resonant excitation results in a higher degree of coherence of the detected ion packet.

The spatial distribution of an ion population is affected by the interaction time with the applied electric field. In an FT-ICR ion cell, a high mass ion cannot interact with as many oscillations of the resonant rf electric field as a low mass ion prior to ejection from the ion cell. This limitation reduces the ability to produce a spatially defined packet of high mass ions. The impact of phase synchronization and phase advancement therefore increases with increasing mass and energy. High mass ions injected into the ICR cell (from an external ion source or from a surface bombarded by an energetic particle) with significant translational energies yield a poorly defined ion packet following excitation.

The effect of frequency swept phase synchronization on ion detection has been observed experimentally. Early Cs^+ desorption experiments showed a dramatic loss of signal when the translationally hot ions were detected in a high-resolution narrow band mode compared to a broad band detection scheme (*32*). That is, in the narrow-band mode (either direct or heterodyne) off-resonant excitation does not occur. Similar observations have been made for tandem quadrupole/FT-ICR experiments (*33*). Although detection of high mass ions is possible by broad-band frequency sweep excitation (chirp), the signal is greatly attenuated in the narrow-band mode (i.e., near resonant excitation with reduced interaction time with the electric field). Observations such as these are difficult to quantitate but are consistent with one of the problems (which

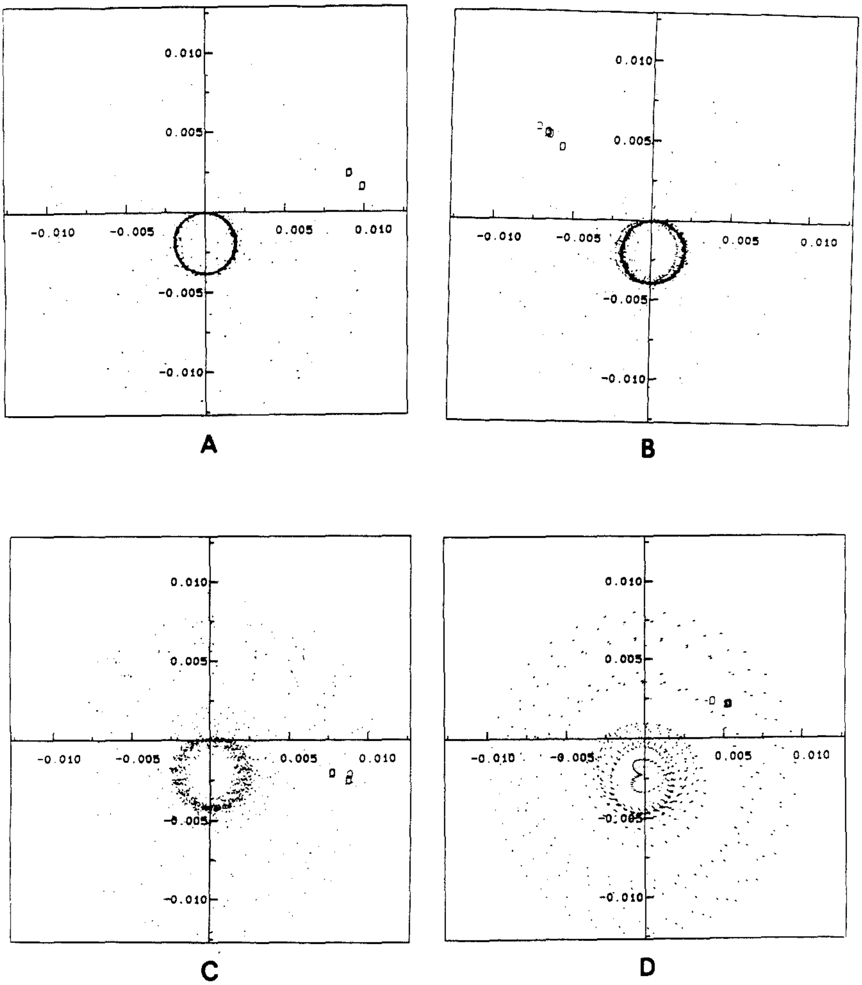

Figure 8. Four plots of temporal ion position (*m/z* 500, 3-T B field) as a result of ion excitation. The effect of frequency sweep excitation on the production of well-defined ion motion can be studied by computer simulations of ion motion. Frequency sweep synchronization of the ion population is evaluated by monitoring the dimensions of the ion packet following excitation solely as a function of the duration of the frequency sweep prior to resonant acceleration. (A) Ions accelerated by a frequency sweep initiated at a frequency corresponding to *m/z* 50. (B) Ions accelerated by a frequency sweep initiated at a frequency corresponding to *m/z* 100. (C) Ions accelerated by a frequency sweep initiated at a frequency corresponding to *m/z* 200. (D) Ions accelerated by a frequency sweep initiated at a frequency corresponding to *m/z* 300.

we attribute to phase synchronization) which presently limit the high mass analytical utility of FT-ICR.

One approach to addressing the problems arising from ions having significant initial radial velocities is through collisional relaxation of the ion's translational energy prior to excitation (*34*). Although this technique is effective for removal of excess translational energy, it introduces more complications into the FT-ICR experiment. For example, the high buffer gas pressures required to collisionally relax ions are incompatible with the ultrahigh vacuum required for detection by FT-ICR. Such techniques require removal of the collision gas prior to detection. Although pulsed-valve experiments of this type have been described, such experiments will not eliminate all the factors important in ion detection. For instance, collisional processes result in scattering of the injected ions. Ions having initially high radial velocities which are scattered by collision with a buffer gas enlarge the spatial distribution of the ion packet, and the initial spatial distribution will be magnified upon rf excitation.

Off-resonant acceleration permits ions to interact with the electric field for extended periods without gaining translational energy. The ion ensemble is phase synchronized prior to excitation and therefore results in a detected packet of ions having more phase-coherent ICR orbital motion. The advantage of off-resonant excitation is that phase synchronization can be performed over a time period of many cyclotron orbits without a net gain in translational energy. The effect of off-resonance excitation has been observed experimentally and the net energy gained by the ion of interest can be neglected if the period of excitation corresponds to a node of

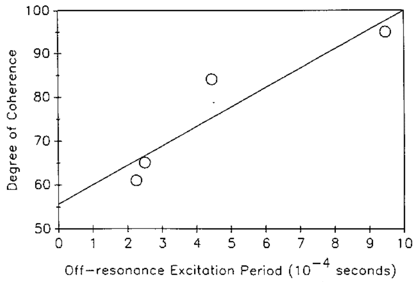

Figure 9. A plot of sweep duration vs the degree of coherence of the ion ensemble following excitation illustrates the effect of off-resonant acceleration.

the beat frequency produced by the difference between $\omega_{\text{cyclotron}}$ and ω_{applied} (*35*)

$$t = 1/|\omega_{\text{cyclotron}} - \omega_{\text{applied}}| \qquad (2)$$

Thus, ions interact with an nonresonant rf electric field for a finite period and receive no increase in translational energy. The extended interaction of the electric field results in phase synchronization of the ion population prior to resonant acceleration. In theory, the extended interaction time of swept excitation and the associated increase in the spatial definition of the ion ensemble could be achieved by a single frequency, off-resonance acceleration prior to detection. The practical applications of this approach are now being evaluated.

LITERATURE CITED

(1) Beauchamp, J. L. *Annu. Rev. Phys. Chem.* **1971**, *22*, 527–561.
(2) Comisarow, M. B.; Marshall, A. G. *Chem. Phys. Lett.* **1974**, *25*, 282.
(3) Comisarow, M. B.; Marshall, A. G. *J. Chem. Phys.* **1976**, *64*, 110.
(4) Comisarow, M. B. *Fourier, Hadamard, and Hilbert Transformations in Chemistry*; Marshall, A. G., Ed.; Plenum Publishing Corp.: New York, 1982.
(5) Hunt, D. F.; Shabanowitz, J.; Yates, J. R.; Zhu, N.; Russell, D. H.; Castro, M. E. *Proc. Natl. Acad. Sci.* **1987**, *84*, 620.
(6) Allemann, M.; Kellerhals, Hp.; Wanczek, K. P. *Int. J. Mass Spectrom. Ion Processes* **1983**, *46*, 139.
(7) Castro, M. E.; Russell, D. H.; Ghaderi, S.; Cody, R. B.; Amster, I. J.; McLafferty, F. *Anal. Chem.* **1985**, *58*, 483.
(8) Marshall, A. G. *Fourier, Hadamard, and Hilbert Transformations in Chemistry*; Marshall, A. G., Ed.; Plenum Publishing Corp.: New York, 1982.
(9) Hanson, C. D.; Kerley, E. L.; Castro, M. E.; Russell, D. H. *Proc. Annu. Conf. Mass Spectrom. Allied Top.*, *36th* American Society for Mass Spectrometry, 1988; p 612.
(10) McIver, R. T.; Hunter, R. L.; Bowers *Int. J. Mass Spectrom. Ion. Processes* **1986**, *64*, 67.
(11) Kofel, P.; Allemann, M.; Kellerhals, Hp.; Wanczek, K. P. *Int. J. Mass Spectrom. Ion Processes* **1985**, *65*, 97.
(12) Alford, J. M.; Weiss, F. D.; Laaksonen, R. T.; Smalley, R. E. *J. Chem. Phys.* **1986**, *90*, 4480.
(13) Ijames, C. F.; Wilkins, C. L. *J. Am. Chem. Soc.* **1988**, *110*, 2687.
(14) McCrery, D. A.; Ledford, E. B.; Gross, M. L. *Anal. Chem.* **1982**, *54*, 1437.
(15) Castro, M. E.; Russell, D. H. *Anal. Chem.* **1984**, *56*, 578.
(16) Loo, J. A.; Williams, E. R.; Amster, I. J.; Furlong, J. J.; Wang, B. H.; McLafferty, F. W.; Chait, B. T.; Field, F. H. *Anal. Chem.* **1987**, *59*, 1882.
(17) Hanson, C. D.; Castro, M. E.; Russell, D. H.; Hunt, D. F.; Shabanowitz, J. In *Fourier Transform Mass Spectrometry: Evolution, Innovation, and Applications*; Buchanan, M. V., Ed.; American Chemical Society: Washington, DC, ACS Symposium Series 359, pp 100–115.
(18) Ledford, E. B.; Remple, D. L.; Gross, M. L. *Anal. Chem.* **1984**, *56*, 2744–2748.
(19) Rempel, D. L.; Huang, S. K.; Gross, M. L. *Int. J. Mass Spectrom. Ion Processes* **1986**, *70*, 163–184.
(20) Hanson, C. D.; Kerley, E. L.; Castro, M. E.; Russell, D. H., submitted to *Anal. Chem.*
(21) Baykut, G.; Watson, C. H.; Eyler, J. R. ASMS 87 Denver, 387.
(22) Wagness, R. K. *Electromagnetic* Fields, 2nd ed.; Wiley & Sons: New York, 1979; Appendix A.
(23) Castro, M. E.; Russell, D. H., unpublished work at Texas A&M University, April 1988.
(24) Beauchamp, J. L. *J. Chem. Phys.* **1967**, *46*, 1231.
(25) Buttrill, S. E. *J. Chem. Phys.* **1969**, *50*, 5690.
(26) Marshall, A. G. *J. Chem. Phys.* **1971**, *55*, 1343–1354.
(27) Baykut, G.; Watson, C. H.; Eyler, J. R. *Proc. Annu. Conf. Mass Spectrom. Allied Top.*, *35th* American Society for Mass Spectrometry, 1987; p 387.
(28) Comisarow, M. B. *J. Chem. Phys.* **1978**, *69*, 4097.
(29) Marshall, A. G. *Chem. Phys. Lett.* **1971**, *55*, 1343.
(30) Marshall, A. G.; Roe, D. C. *J. Chem. Phys.* **1980**, *73*, 1581.
(31) Cody, R. B.; Goodman, S. D.; Ghaderi, S.; Shohet, J. L. *Proc. Annu. Conf. Mass Spectrom. Allied Top.*, *35th* American Society for Mass Spectrometry; 1987; p 779.
(32) Castro, M. E.; Russell, D. H., unpublished results.
(33) Hunt, D. F.; Shabanowitz, J.; Russell, D. H.; Castro, M. E., unpublished results.
(34) Alford, J. M.; Williams, P. E.; Trevor, D. J.; Smalley, R. E. *Int. J. Mass Spectrom. Ion Processes* **1986**, *72*, 33.
(35) Cody, R. B.; Goodman, S. *Analusis* **1988**, *16*, XXX–XXXVI.

RECEIVED for review March 24, 1989. Accepted July 19, 1989. This work was supported by the National Institutes of Health–General Medical Sciences (GM-33780) and the National Science Foundation (CHE-8418457). Some of the equipment was purchased from funds provided by the TAMU Center for Energy and Mineral Resources. We gratefully acknowledge the Texas Agricultural Experiment Station for providing a portion of the funds for purchase of the Nicolet FTMS 1000 mass spectrometer.

Anal. Chem. 1989, 61, 2137–2141 2137

Emission Spectrometric Determination of Manganese and Chromium in Steels with a Dual Cathode Glow Discharge Lamp

Kazuaki Wagatsuma* and Kichinosuke Hirokawa

Institute for Materials Research, Tohoku University, Katahira 2-1-1, Sendai 980, Japan

Analytical applications of a dual-cathode hollow cathode discharge lamp are investigated and discussed. The lamp consists of three electrodes (anode, intermediate electrode, and cathode). Two individual power supply devices are employed with a pulsed discharge mode to separate the sputtering process occurring in the lamp from the excitation step in the hollow cathode plasma. Discharge voltages are supplied between the anode and the intermediate electrode to generate the plasma in the intermediate electrode. The cathode sputtering is controlled by bias voltages between the intermediate electrode and the cathode (sample). Emission intensities from the sputtered materials strongly depend upon the variation in the bias voltage, while those from the plasma gas hardly change. This effect can lead to selective detection of the emission lines of the sample from the overall emission signals with a modulation technique. Determination of manganese and chromium in steels is attempted by use of the dual-cathode discharge lamp with the sputter modulation method.

Glass-sealed hollow cathode lamps have been extensively employed as a primary light source for atomic absorption spectrometry. The properties of small widths of the spectral lines, their high intensities, the stability of the discharge, and the simple power supply device have made the lamp a radiation source mostly suitable for this purpose. In the field of emission spectrometry, many works have been also reported as an analytical application of glow discharges (*1–5*).

Since the sample introduction in the plasma is caused by the cathode sputtering, the low-pressure glow discharges have been utilized to perform direct elemental analyses of solid samples. The sputter atomization process has some advantages over thermal volatilization method in arc or spark discharge plasmas. Refractory metals such as tungsten, tantalum, can be easily atomized through atom/ion bombardments against the cathode surface in the glow discharge plasmas. The elemental sputtering yields vary less greatly for various elements (*6, 7*). Therefore, a stable and uniform sampling stage can be expected to be provided in the glow discharge spectrometry. Furthermore, it is well-known that when the pressures of the plasma gas are kept constant, the discharge voltage and/or current definitely control the amount of the sputtered materials (*8*). The sputtering with pulsed discharge voltages could periodically change the atomic density of the sputtered materials in the plasma (*9, 10*).

We have reported the configuration and the operating conditions of a dual-cathode hollow cathode lamp (*11*). The lamp comprises three electrodes: anode, intermediate electrode, and cathode (sample) (cf. Figure 1). Two individual power supply devices are employed. The main hollow cathode discharge plasma, which is supported by the discharge voltages supplied between the anode and the intermediate electrode, generates in the cylindrical, hollow intermediate electrode. On the other hand, the voltages supplied between the intermediate electrode and the cathode (sample) are modulated with a square wave form. The sputtering process could be controlled periodically without the main plasma conditions. This effect leads to the selective detection of emission lines from the sputtered atoms and ions. Many emission lines of the plasma gases are also observed from the glow discharge plasmas (*12*). In some cases, these gas emission may interfere with accurate intensity measurements of the analytical lines. Therefore, it is worth while to attempt to separate the spectral lines of the sample species from the gas emission lines.

In this paper, we will indicate quantitative determination of manganese and chromium in steels with the modulation technique of discharge voltages supplied to the dual-cathode hollow cathode lamp. When argon is used as a plasma gas, spectral interferences originating from Ar I and Ar II lines can be eliminated with this method.

EXPERIMENTAL SECTION

The structures of our dual-cathode glow discharge lamp and the instrumentation have been reported in detail elsewhere (*11*). The operating conditions for this work are described briefly.

A schematic diagram of the apparatus is represented in Figure 1. The hollow cathode plasma created in the intermediate electrode results from the pulsed voltage supplied between the anode and intermediate electrode. The intermediate electrode was grounded (0 V). The wave pattern of the discharge voltage was a rectified half-sine wave form. The peak voltage was ca. 300 V. The average current (110 ± 5 mA) and the frequency (788 Hz) of this pulsed discharge, which determine the characteristics of the plasma, were predetermined from the performance of the power supply device used. The negative bias voltage (−150 V) is supplied between the intermediate electrode and cathode (sample) with a different power source. The wave pattern of the bias voltage was a square wave form of 108 Hz.

The spectral lines from the lamp would be expected to be doubly modulated at frequencies of 788 and 108 Hz. The excitation step in the hollow cathode plasma can be modulated at 788 Hz, whereas the sputtering process is modulated principally at 108 Hz. The dispersed emission signals were amplified with a preamplifier and then separated into each component. A lock-in amplifier, which was tuned to a frequency of 788 Hz or 108 Hz, was used to select the desired component from the overall signals.

Pure argon was employed as a plasma gas. The gas pressure was selected to be 2.7×10^2 Pa to obtain maximum emission intensities.

Binary alloy standard samples (Fe-Mn and Fe-Cr alloys) were employed to estimate the calibration factors for each analytical line. These samples were received from The Iron and Steel Institute of Japan (FXS-306~309 and FXS-335~337, standard samples for X-ray fluorescence analysis). Determination of manganese and chromium in two series of low-alloyed steel samples; SRM-1160 standard reference materials from US National Bureau of Standards and ASC-150 alloy steel standard samples from The Iron and Steel Institute of Japan, was attempted in this study. The sample surfaces were mechanically polished with waterproof emery papers.

The intermediate electrode, made from aluminum, can be easily demounted and interchanged. When a new electrode was inserted in the holder, a prolonged predischarge stage was required to obtain stable and intense emission signals, probably due to the surface contaminations such as water or hydrocarbons on the inside wall of the electrode. Therefore, the predischarge was carried out for ca. 60 min. However, the intermediate electrodes

0003-2700/89/0361-2137$01.50/0 © 1989 American Chemical Society

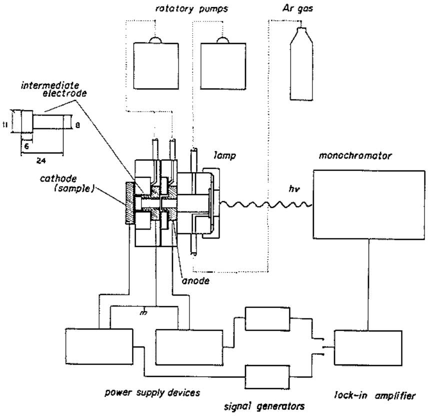

Figure 1. Block diagram of the apparatus employed. The dimensions listed for the intermediate electrode are in millimeters.

which had been cleaned by the prolonged predischarge could be used after the predischarges for less than 10 min. The intermediate electrode were gradually exhausted by the cathode sputtering, thus affecting the discharge conditions, and thereby changing the observed emission intensities. It was difficult to maintain stable discharges with the progress of the electrode exhaustion, and then the electrodes were exchanged. However, an electrode could be used continuously for more than 600 min.

RESULTS AND DISCUSSION

Manganese. In the glow discharge plasmas, the most sensitive emission lines of manganese appear in the wavelength region between 403.1 and 403.5 nm. These atomic resonance lines can be employed as analytical lines in the emission spectrometry (*13*). However, several emission lines derived from argon also appear in these wavelengths, thus leading to the spectral interferences against the detection of the Mn lines. Especially, this effect must be taken into consideration when a monochromator having relatively low resolution power is employed to analyze the spectrum.

The Mn I emission lines analyzed and Ar I and Ar II lines in the neighborhood of the analytical lines are listed in Table I. The emission line at 403.1 nm seems to be free from overlapping with the Ar lines. However, it is found that the emission intensities of Mn I 403.3 nm are distorted in the existence of Ar II 403.4 nm. Such background emission from the Ar lines becomes a serious problem, especially when small amounts of manganese must be determined.

Figure 2 shows spectrum scans of a Mn-free steel (Mn < 0.005 wt %) recorded with two different detection modes in the wavelength range 399–406 nm. It is found that the spectra measured with the plasma modulation mode at 788 Hz (Figure 2a) are more complex than those with the sputter modulation mode at 108 Hz (Figure 2b). This phenomenon can be explained by the disappearance of the Ar emission lines with the sputter modulation method. The Mn I analytical lines would exist in the wavelength region near 403.3 nm. Therefore, it is significant to note that no emission lines appear at 403.3 ± 0.5 nm in Figure 2b, whereas two or three emission lines are clearly observed in Figure 2a. As denoted in Table I, these lines are identified to Ar II 403.4 nm and Ar II 403.5 nm. Accordingly, little background interferences occur on quantitative analyses of the Mn I emission lines detected with the sputter modulation.

Table I. Emission Lines of Manganese and Argon and Iron Lines in the Neighborhood of the Analytical Lines

wavelength, nm	assignment, eV upper	assignment, eV lower
Mn I 403.1	4p $^6P_{7/2}$, 3.08	4s $^6S_{5/2}$, 0.00
Mn I 403.3	4p $^6P_{5/2}$, 3.07	4s $^6S_{5/2}$, 0.00
Mn I 403.5	4p $^6P_{3/2}$, 3.07	4s $^6S_{5/2}$, 0.00
Fe I 399.7	4p $^3H_5$, 5.83	4s $^3G_4$, 2.73
Fe I 400.5	4p $^3F_2$, 4.65	4s $^3F_3$, 1.56
Fe I 401.0	4p $^5P_2$, 5.31	4s $^5P_1$, 2.22
Fe I 401.4	4p $^3D_2$, 6.11	4s $^3P_2$, 3.02
Fe I 402.2	4p $^3H_4$, 5.84	4s $^3G_3$, 2.71
Fe I 404.6	4p $^3F_4$, 4.55	4s $^3F_4$, 1.48
Ar II 399.5	4p $^2P_{1/2}$, 23.85	4s $^2S_{1/2}$, 20.74
Ar II 401.4	4p $^4D_{7/2}$, 19.49	3d $^4D_{7/2}$, 16.41
Ar II 403.4	5s $^4P_{1/2}$, 22.68	4p $^4D_{3/2}$, 19.61
Ar II 403.5	4p $^2D_{5/2}$, 21.50	4s $^2D_{3/2}$, 18.43
Ar II 404.3	4p $^2D_{3/2}$, 21.49	4s $^2D_{3/2}$, 18.43
Ar I 404.4	5p $[3/2]_2$, 14.69	4s $[3/2]_1$, 11.62
Ar II 405.3	4p $^2P_{3/2}$, 23.80	4s $^2S_{1/2}$, 20.74
	(internal standard line)	
Fe I 414.4	4p $^3F_4$, 4.55	4s $^3F_3$, 1.56

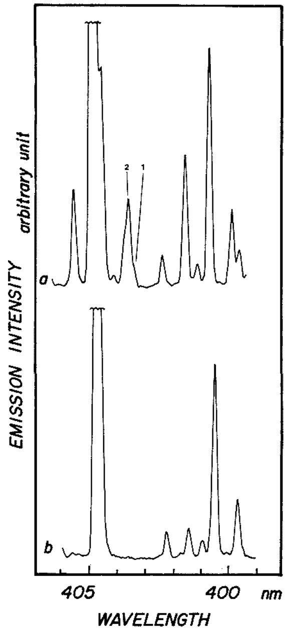

Figure 2. Spectrum of Mn-free steel sample detected with the plasma modulation mode (a) and the sputter modulation mode (b): emission lines (1) Ar II 403.4 and (2) 403.5 nm.

In the case of an alloy sample containing 0.2 atom % Mn, similar spectral scans are indicated in Figure 3. It can be recognized that the Mn I emission lines are added in the spectrum of the Mn-free steel sample. However, the relative intensities among these lines are different, depending on the detection methods. With the plasma modulation mode (Figure 3a), peak intensity of Mn I 403.3 nm is observed to be a little more intense compared to that of Mn I at 403.1 nm, whereas this relation on the relative intensities is reversed between the two Mn I lines with the sputter modulation method (Figure 3b). The apparent increase in the intensity of Mn I 403.3 nm results from the fact that the Mn I 403.3 nm line overlaps with the Ar II 403.4 nm line. Relative intensities of the emission lines detected with a conventional dc amplifi-

Table II. Analytical Result on Mn Determination in Steels

sample	certified value		this study		major alloyed elements, atom %
	atom %	Mn/Fe	Mn/Fe	RSD, %	
SRM-1161[a]	0.38	4.0×10^{-3}	3.9×10^{-3}	2.3[b]	Ni, 1.72; Cu, 0.32; Mo, 0.18
			3.9×10^{-3}	2.0[c]	
−1162	0.99	1.1×10^{-2}	1.0×10^{-2}	3.1	Ni, 0.69; Cr, 0.82; Cu, 0.18
			1.0×10^{-2}	3.2	
−1163	1.22	1.28×10^{-2}	$1.2_7 \times 10^{-2}$	1.4	Cu, 0.43; Ni, 0.39; Cr, 0.29
			$1.2_8 \times 10^{-2}$	1.3	
−1164	1.38	1.46×10^{-2}	$1.4_7 \times 10^{-2}$	0.9	V, 0.33; Ni, 0.13
			$1.4_8 \times 10^{-2}$	1.0	
−1165	0.032	3.5×10^{-4}	4×10^{-4}	5.4	Al, 0.41; Ti, 0.25
			4×10^{-4}	5.7	
−1166	0.121	1.22×10^{-3}	1.2×10^{-3}	3.8	
			1.2×10^{-3}	2.6	
−1167	0.293	3.02×10^{-3}	3.0×10^{-3}	2.2	Al, 0.35; Ti, 0.32; Nb, 0.19
			3.0×10^{-3}	3.3	
−1168	0.50	5.2×10^{-3}	5.2×10^{-3}	2.3	Ni, 1.02; Cr, 0.61; Cu, 0.24; V, 0.19
			5.1×10^{-3}	1.5	
ASC-150[d]	0.20	2.3×10^{-3}	2.3×10^{-3}	2.1	Ni, 4.09; Cr, 0.51
			2.3×10^{-3}	3.3	
−151	1.45	1.55×10^{-2}	$1.6_1 \times 10^{-2}$	2.5	Ni, 2.83; Cu, 0.43
			$1.6_2 \times 10^{-2}$	1.4	
−152	0.47	5.0×10^{-3}	4.9×10^{-3}	3.2	Ni, 1.85; Cr, 0.74; Mo, 0.56; Cu, 0.38
			4.9×10^{-3}	2.6	
−153	0.82	8.7×10^{-2}	8.3×10^{-3}	1.5	Ni, 1.05; Cr, 1.23; Mo, 0.56; V, 0.25
			8.3×10^{-3}	1.3	
−154	1.09	1.18×10^{-2}	$1.1_5 \times 10^{-2}$	2.3	Cr, 2.17; Ni, 0.50; Mo, 0.41; V, 0.37
			$1.1_6 \times 10^{-2}$	2.5	
−155	0.11	1.1×10^{-3}	1.2×10^{-3}	2.8	Cr, 3.32; V, 0.49; Cu, 0.27; Mo, 0.25
			1.2×10^{-3}	3.0	

[a] SRM-1160 samples are received from US National Bureau of Standards. [b] Mn I 403.1 nm. [c] Mn I 403.3 nm. [d] ASC-150 samples are received from The Iron and Steel Institute of Japan.

cation method are almost the same as those obtained with the plasma modulation method (*11*). In fact, the spectral interferences from the Ar II 403.4 (403.5) nm lines occur also with the dc detection method. On the other hand, it could be deduced from Figures 2 and 3 that the spectrum obtained with the sputter modulation mode provides true intensity profiles.

Determination on manganese in several low-alloyed steel samples was attempted with the sputter modulation method. Quantitative analyses determination by using an internal standard emission line are recommended to compensate for fluctuations of cathode sputtering. In this study, the Fe I emission line at 414.4 nm was selected as the internal standard (see Table I). Accordingly, the intensities of the Mn I lines observed are expressed as the intensity ratios (Mn I/Fe I), which leads to estimation of the atomic ratios (Mn/Fe) with the calibration factors.

Calibration graphs were prepared for Mn I 403.1 nm and Mn I 403.3 nm using a series of Fe–Mn binary alloys containing 0.20, 0.52, 1.04, and 2.14 atom % Mn. Linear relationships are obtained between the intensity ratios and the atomic ratios in the concentration range 0–2.14 atom % Mn. Further, the calibration factors can be of use up to ca. 10 atom % Mn. The reproducibility is satisfactory and the correlation coefficients are estimated to be more than 0.999. The intercept on the *Y* axis is almost zero when the intensity measurements are carried out with the sputter modulation method. Such background-free detections could contribute to precise determination especially at low Mn concentration.

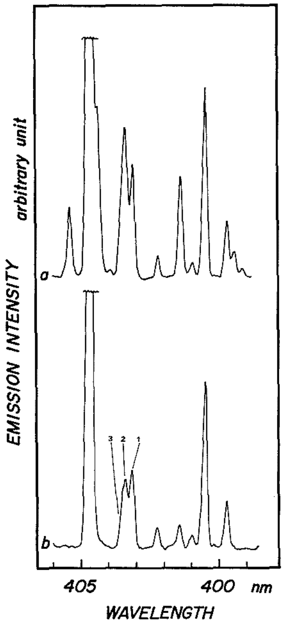

Figure 3. Spectrum of Fe–0.20 atom % Mn binary alloy sample detected with the plasma modulation mode (a) and the sputter modulation mode (b): emission lines (1) Mn I 403.1, (2) Mn I 403.3, and (3) Mn I 403.5 nm.

Table II gives the analytical results on Mn concentration in some standard reference steel samples. These results are calculated from measuring the peak heights of the analytical emission lines for seven to nine replicates. It is found that the contents of Mn obtained are generally in good agreement with the certified values. Nevertheless, the values determined in SRM-1165 are higher than the certificate value. This is probably due to errors on the intensity estimation because the emission intensities of the Mn I lines are very weak. As shown in Table II, the analytical values obtained with the Mn I 403.1 nm line agree with those obtained by use of the Mn

Table III. Analytical Result on Mn Determination in Stainless Steels

	recommended value		this study		
sample	atom %	Mn/Fe	Mn/Fe	RSD, %	major alloyed elements, atom %
FX-2[a]	0.72	8.7×10^{-3}	8.8×10^{-3}	3.4[b]	Ni, 0.19; Cr, 14.33; Cu, 0.17 Cr, 14.33; Cu, 0.17
			8.6×10^{-3}	3.1[c]	
FX-4	0.86	1.0×10^{-2}	1.0×10^{-2}	2.0	Ni, 0.41; Cr, 18.33; Cu, 0.09
			1.0×10^{-2}	1.7	
FX-6	1.69	2.50×10^{-2}	$2.5_6 \times 10^{-2}$	1.6	Ni, 8.61; Cr, 20.51; Mo, 0.14; Cu, 0.14
			$2.5_3 \times 10^{-2}$	1.8	
FX-8	1.23	1.83×10^{-2}	$1.8_9 \times 10^{-2}$	2.6	Ni, 9.16; Cr, 20.30; Cu, 0.13
			$1.8_8 \times 10^{-2}$	2.7	
FX-12	1.46	2.20×10^{-2}	$2.0_9 \times 10^{-2}$	2.3	Ni, 10.68; Cr, 19.21; Mo, 1.30; Cu, 0.19
			$2.0_9 \times 10^{-2}$	2.4	
FX-16	1.58	2.53×10^{-2}	$2.4_3 \times 10^{-2}$	1.8	Ni, 12.09; Cr, 19.62; Mo, 1.47; Cu, 1.06
			$2.4_2 \times 10^{-2}$	2.0	

[a] Reference samples are received from The Iron and Steel Institute of Japan. [b] Mn I 403.1 nm. [c] Mn I 403.3 nm.

Table IV. Emission Lines of Chromium and Argon and Iron Lines in the Neighborhood of the Analytical Lines

	assignment, eV	
wavelength, nm	upper	lower
Cr I 425.4	4p $^7P_4$, 2.91	4s $^7S_3$, 0.00
Cr I 427.5	4p $^7P_3$, 2.90	4s $^7S_3$, 0.00
Cr I 429.0	4p $^7P_2$, 2.89	4s $^7S_3$, 0.00
Fe I 425.1	4p $^3G_3$, 4.47	4s $^3F_3$, 1.56
Fe I 426.1	4p $^7D_5$, 5.31	4s $^7D_5$, 2.40
Fe I 427.2	4p $^3G_5$, 4.39	4s $^3F_4$, 1.49
Fe I 428.3	4p $^5S_2$, 5.07	4s $^5P_3$, 2.18
Fe I 429.5	4p $^3G_4$, 6.15	4s $^3H_5$, 3.27
Fe I 430.0	4p $^3H_5$, 6.15	4s $^3H_5$, 3.27
Ar I 425.9	5p $[1/2]_0$, 14.74	4s $[1/2]_1$, 11.83
Ar I 426.6	5p $[3/2]_2$, 14.53	4s $[3/2]_1$, 11.62
Ar II 426.7	4p $^4D_{5/2}$, 19.55	4p $^4P_{5/2}$, 16.64
Ar I 427.2	4p $[3/2]_1$, 14.52	4s $[3/2]_1$, 11.62
Ar II 427.8	4p $^2P_{3/2}$, 21.35	4s $^2D_{5/2}$, 18.45
Ar II 430.1	4p $^2D_{5/2}$, 21.50	3d $^2F_{5/2}$, 18.62
	(internal standard line)	
Fe I 414.4	4p $^3F_4$, 4.55	4s $^3F_3$, 1.56

I 403.3 nm line. It also indicates that the relative standard deviations (RSD) are 0.9–5.7%, but less than 3.8% except for SRM-1165. The intensities of argon lines are very sensitive to the change in the plasma conditions, especially such as impurity gases in the plasma (*14*). Because of intensity fluctuations of overlapping argon lines, such spectral interferences may worsen the data precision obtained with conventional glow discharges. Therefore, it is expected that the modulation technique used in this study provides good precision.

Influences of the other alloyed elements were roughly investigated from the kind and the amount of the major-alloyed elements in the samples. The analytical result of manganese in ACS-150, which contains 4.09 atom % Ni (cf. Table II), can imply that nickel hardly affects the Mn determination. Furthermore, little influences of chromium are deduced from the result in ACS-155 containing 3.32 atom % Cr.

We attempted the determine the concentration of Mn in some commercial stainless steels. Table III represents the analytical results obtained. These values are in good agreement with the recommended values. In the case of the high-alloyed steels, it seems that the other alloyed elements such as Ni or Cr exert no influence on the Mn determinations.

In glow discharge plasmas, it is not necessary in most cases to note so-called matrix effects, which means that excitation reactions in the plasma mainly depend not upon the collisions among analyte atoms introduced in the plasma but on those between analyte atoms and plasma gas species. Therefore, small variations in the plasma composition, which are caused by the other alloyed elements in the sample, are insignificant. Unless the Mn I lines analyzed overlap with lines of the other alloyed elements, it is possible to determine the Mn concentration by use of the calibration factors obtained with the Fe–Mn binary alloy standard samples. In the hollow cathode plasma source employed, it is found that the Mn I lines are free of spectral interferences from emission lines of iron, nickel, chromium, molybdenum, copper, and vanadium.

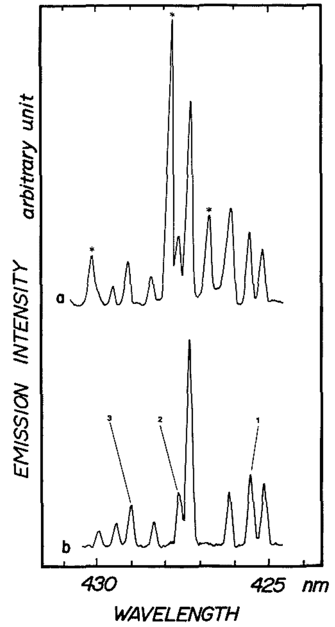

Figure 4. Spectrum of Fe–0.56 atom % Cr binary alloy sample detected with the plasma modulation mode (a) and the sputter modulation mode (b). Emission lines marked by asterisks (*) are identified to Ar I or Ar II lines or overlap in part with Ar emission lines. Emission lines are as follows: (1) Cr I 425.4, (2) Cr I 427.5, and (3) Cr I 429.0 nm.

Chromium. Table IV summarizes Cr I emission lines employed for the determination of chromium in steel samples, together with Ar II and Fe I emission lines in the neighborhood of the Cr I lines. Figure 4 illustrates spectral scans obtained with the plasma modulation mode (a) and the sputter modulation mode (b) in an Fe–0.56 atom % Cr alloy sample. They

Table V. Analytical Result on Cr Determination in Steels

	certified value		this study	
sample	atom %	Cr/Fe	Cr/Fe	RSD, %
SRM-1161	0.15	1.5×10^{-3}	1.6×10^{-3}	3.5[a]
			1.6×10^{-3}	5.4[b]
			1.6×10^{-3}	3.0[c]
−1162	0.82	8.7×10^{-3}	8.5×10^{-3}	5.0
			8.5×10^{-3}	4.7
			8.4×10^{-3}	5.5
−1163	0.29	3.1×10^{-3}	3.0×10^{-3}	3.2
			3.0×10^{-3}	3.1
			3.0×10^{-3}	2.6
−1164	0.086	0.91×10^{-3}	$0.9_6 \times 10^{-3}$	3.3
			$0.9_8 \times 10^{-3}$	6.3
			1.0×10^{-3}	6.1
−1166	0.012	0.13×10^{-3}	$0.2_0 \times 10^{-3}$	4.3[a]
−1167	0.041	0.42×10^{-3}	$0.4_8 \times 10^{-3}$	5.3
			$0.5_4 \times 10^{-3}$	5.0
			$0.5_4 \times 10^{-3}$	11.3
−1168	0.60	6.3×10^{-3}	6.2×10^{-3}	3.4
			6.3×10^{-3}	2.6
			6.2×10^{-3}	3.1
ASC-150	0.51	5.5×10^{-3}	5.6×10^{-3}	3.6
			5.6×10^{-3}	3.6
			5.6×10^{-3}	3.7
−151	0.12	1.3×10^{-3}	1.4×10^{-3}	4.7
			1.5×10^{-3}	5.8
			1.5×10^{-3}	6.6
−152	0.74	7.9×10^{-3}	7.8×10^{-3}	3.3
			7.7×10^{-3}	2.7
			7.8×10^{-3}	3.8
−153	1.23	1.30×10^{-2}	$1.2_9 \times 10^{-2}$	3.3
			$1.2_6 \times 10^{-2}$	3.3
			$1.2_6 \times 10^{-2}$	3.2
−154	2.17	2.34×10^{-2}	$2.2_8 \times 10^{-2}$	2.4
			$2.2_9 \times 10^{-2}$	3.2
			$2.2_2 \times 10^{-2}$	3.0
−155	3.32	3.59×10^{-2}	$3.5_7 \times 10^{-2}$	3.4
			$3.6_2 \times 10^{-2}$	3.7
			$3.5_9 \times 10^{-2}$	2.4

[a] Cr I 425.4 nm. [b] Cr I 427.5 nm. [c] Cr I 429.0 nm.

also indicate that the Ar II emission lines (shown by asterisks in Figure 4a) are not detected with the sputter modulation method. All of the triplet Cr I lines can be available for the determination of chromium under the conditions with no background contribution. However, in the plasma modulation mode, the Ar II 427.8 nm line distorts to measure the true peak intensities of the Cr I 427.5 nm at lower Cr concentration.

The contents of chromium in the steel samples were determined by the same procedure as in manganese. Iron–chromium binary alloy samples containing 0.56, 1.10, and 3.36 atom % Cr were employed to obtain the analytical curves and thereby the calibration factors. The resultant calibration graphs give linear relations over the range of 0–3.36 atom % Cr.

The analytical results are listed in Table V. Though the intensity ratios were investigated for each of the triplet Cr I lines, only the Cr I 425.4 nm line was measured in SRM-1166 because the emission intensities of the other Cr I lines were not great enough to be utilized for the Cr determination. It is found from Table V that the values obtained with the sputter modulation method are generally in good agreement with the certified values. The average RSD can be computed to be 3.9% if a RSD (11.3%) obtained in SRM-1167 can be excluded due to an anomalous value. Effects of the other alloyed elements for the Cr determinations seem to follow the conclusion obtained in manganese. No influences of nickel, molybdenum, vanadium, and copper could be recognized for all of the Cr I lines over the concentration range of each element as shown in Table II.

Since emission lines of sputtered materials can be selectively detected with the sputter modulation method, the resultant spectra are less complicated. Spectral interferences from emission lines of plasma gases can be eliminated. This effect is of great use for elemental analyses in some instances such as the determination of manganese in steels.

LITERATURE CITED

(1) Thornton, K. *Analyst* **1969**, *94*, 958.
(2) Harrison, W. W.; Prakash, N. J. *Anal. Chim. Acta* **1970**, *49*, 151.
(3) Harrison, W. W.; Daughtey, E. H. *Anal. Chim. Acta* **1973**, *65*, 35.
(4) Caroli, S.; Alimonti, A.; Violate, N. *Spectrosc. Lett.* **1980**, *13*, 313.
(5) Caroli, S.; Senofonte, A.; Delle Femmine, P. *Analyst* **1983**, *108*, 196.
(6) Laegeid, N.; Wehner, G. K. *J. Appl. Phys.* **1961**, *32*, 365.
(7) Rosenberg, D.; Wehner, G. K. *J. Appl. Phys.* **1962**, *33*, 1842.
(8) Boumans, P. W. J. M. *Anal. Chem.* **1972**, *22*, 317.
(9) Gough, D. S. *Anal. Chem.* **1976**, *48*, 1926.
(10) Wagatsuma, K.; Hirokawa, K. *Anal. Chem.* **1984**, *56*, 2732.
(11) Wagatsuma, K.; Hirokawa, K. *Spectrochim. Acta*, *Part B* **1988**, *43B*, 831.
(12) Wagatsuma, K.; Hirokawa, K. *Anal. Chem.* **1985**, *57*, 2901.
(13) Wagatsuma, K.; Hirokawa, K. *Anal. Chem.* **1984**, *56*, 908.
(14) Wagatsuma, K.; Hirokawa, K. *Anal. Chem.* **1989**, *61*, 326.

RECEIVED for review March 22, 1989. Accepted June 27, 1989.

Anal. Chem. **1989**, *61*, 2142–2149

Structural Characterization of Model Polyurethanes Using Time-of-Flight Secondary Ion Mass Spectrometry

Ioannis V. Bletsos and David M. Hercules*
Department of Chemistry, University of Pittsburgh, Pittsburgh, Pennsylvania 15260

Dieter vanLeyen and Alfred Benninghoven
Physikalisches Institut der Universität Münster, D-4400 Münster, FRG

Costas G. Karakatsanis and James N. Rieck
Mobay Corporation, Pittsburgh, Pennsylvania 15205

Time-of-flight secondary ion mass spectra of a series of polyurethanes based on three diols and four diisocyanates were obtained from thin polyurethane films cast from solution on silver substrates. Intact oligomer ions and large polyurethane fragments consisting of an integral number of repeat units, both cationized with Ag^+ and Na^+, were detected in the mass range $m/z = 500$–3200. The mass of the repeat unit of a polyurethane can be determined from m/z values of oligomer or fragment ions or from the spacing between consecutive peaks generated from fragments or oligomers cationized with the same cation. The combined mass of the terminal groups can be determined from the mass difference between oligomer and fragment peaks. Identities of the diol and diisocyanate in a polyurethane can be obtained by comparing different fragmentation patterns in the spectrum; differences and similarities between polyurethanes can thus be assessed. Transesterification products of polyurethanes and trifluoroacetic acid were identified from secondary ion mass spectra to be diesters consisting of an integral number of polyurethane repeat units and an additional diol.

INTRODUCTION

Polyurethanes (PURs) are versatile polymers having many applications. PURs present a challenge for structural characterization because of the number of possible formulations and range of their complexity. The main objective in the characterization of PURs is identification of the isocyanate and hydroxy components of the repeat unit, chain extenders, and their sequence in the PUR backbone.

Infrared spectroscopy (IR) has been applied widely to the characterization of PURs but, in some cases, with limited success (*1, 2*). Base hydrolysis of PURs and identification of the resulting diamines and diols by IR, nuclear magnetic resonance spectroscopy (NMR), or mass spectrometry (MS) have been used (*3–6*). In general, methods involving hydrolysis of PURs are time-consuming and cannot satisfy the need for detailed structural characterization of the repeat unit and its sequence in the PUR backbone. Proton and ^{13}C NMR have been used to identify and estimate the composition of polyether and polyester PURs (*7, 8*). Solid-state ^{13}C and deuterium NMR have been used to characterize molecular motion and phase separation between hard and soft segments in PURs and evaluate their composition in the different domains (*9, 11*).

The pyrolysis products of carbamates have been identified as the corresponding isocyanates and alcohols (*12–15*). Studies of deuterated (*17*) and N-substituted model PURs (*18–20*) using pyrolysis mass spectrometry (Py-MS) have shown that pyrolytic pathways depend strongly on the PUR structure. PURs based on various diisocyanates, diols, and formulations of PURs and epoxy resins have been studied by using Py-MS (*21–24*). The diisocyanate and some chain extenders could be identified from the spectra; identification of diols, however, was difficult (*23, 24*). Laser MS, Py-MS, and Curie point pyrolysis have been used to characterize etherurethane–urea copolymers used as biological implants (*25–27*). The pyrolysis of a flexible PUR foam was investigated by gas chromatography/mass spectrometry (GC/MS) (*16*). Several columns and long analysis times were required, and only volatile nonpolar pyrolyzates could pass through the gas chromatograph. Two comprehensive review articles have appeared on the characterization of PURs and other polymers by Py-MS (*28, 29*).

The characterization of PURs using Py-MS has some limitations. The additional fragmentation induced by electron impact following pyrolysis often produces fragments not specific to the original PUR. Aliphatic diisocyanates generally do not give molecular ions, and it is difficult to identify them from their low m/z fragments. The precise lengths of polyol chains cannot be determined by Py-MS since all polyols below some minimum molecular weight (ca. 700) give similar ions in their mass spectra (*24*). In general, Py-GC/MS provides structural details about PURs but is restricted to a mass range equivalent to less than one repeat unit.

The present study is part of a program aimed at surface and structural characterization of polymers by using time-of-flight secondary ion mass spectrometry (TOF-SIMS). PURs were chosen because they are important polymers but difficult to characterize; thus PURs provide a challenging test for TOF-SIMS. TOF-SIMS combines good sensitivity for high masses and extensive mass range, such that high molecular weight ions can be observed. Traditionally, characterization of PURs has been based on a multitechnique approach where information obtained from different techniques is used in a complementary manner to compose the overall PUR structure. TOF-SIMS provides in one spectrum a clear and unambiguous way to obtain structural details difficult to extract from other techniques.

In this report TOF-SIMS is presented as a viable technique for structural characterization of PURs prepared from polycondensation of diols and diisocyanates (i.e., PUR-Is). Structures of diols, diisocyanates, and some typical PUR-Is are shown in Figure 1. We believe this to be the first report of PUR mass spectra obtained in the medium mass range (e.g., $m/z = 500$–3200). Information obtained from a single TOF-SIMS spectrum allows identification of the PUR repeat unit, its diol and diisocyanate components, and their sequence in

0003-2700/89/0361-2142$01.50/0 © 1989 American Chemical Society

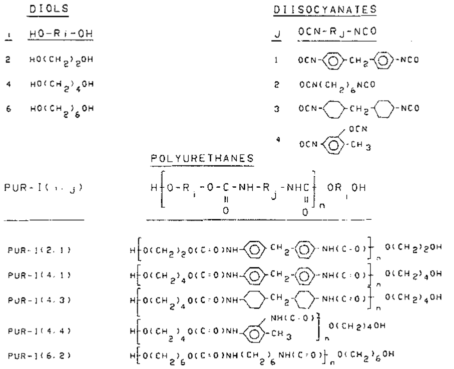

Figure 1. Structures of diols, major isomers of diisocyanates used, and some typical polyurethanes.

the repeat unit. Furthermore, this report establishes that fragmentation patterns can be applied to polymer characterization by MS in a way similar to fragmentation in low mass organic molecules. The characterization of PURs prepared from polyesters and diisocyanates will be presented in a subsequent communication.

EXPERIMENTAL SECTION

I. Synthesis of PUR-Is. Twelve PUR-Is were prepared by using well-established polycondensation reactions of each of three diols with each of four diisocyanates. The diols were ethylene glycol, 1,4-butanediol, and 1,6-hexanediol. The diisocyanates were 4,4′-diphenylmethane diisocyanate (MDI), hexamethylene diisocyanate (HX), dicyclohexylmethane diisocyanate (94% 4,4′- and 6% 2,4′-isomers; RMDI), and toluene diisocyanate (80% 2,4- and 20% 2,6-isomers; TDI). The PUR-Is based on MDI and HX were isolated as powders, while those based on RMDI and TDI were glasses. The powder PUR-Is were prepared in toluene, while the glassy polymers were prepared neat. In all cases stannous octoate was used as the catalyst.

For PUR-Is based on MDI and HX the diisocyanate was dissolved in toluene, followed by an amount of diol to give NCO/H = 0.98. The reaction mixture was heated to 90–100 °C for 2 h, followed by filtration and drying of the solid powder.

Bulk polymerization was used for PUR-Is based on RMDI and TDI. The diisocyanate was added with stirring to a weighed amount of diol to give ca. NCO/H = 0.98. The reaction mixture was placed into a Teflon coated tray and heated for 30 min at 110 °C before cooling to room temperature. Then the glassy polymers were cut into pieces for subsequent characterization.

The general structure of PUR-Is is given by 1. Figure 1 shows the structures of the diols, HO–R_i–OH, major isomers of diisocyanates used, OCN–R_j–NCO, and some typical PUR-I(i,j)s. PUR-Is are identified by the diol and diisocyanate indices i and j, respectively. The structures that are within brackets in Figure 1 and consist of the diol and diisocyanate (i.e., hard segment) are the repeat units of the different PUR-Is. For example, reaction of 1,4-butane diol (i = 4) and MDI (j = 1) produces PUR-I(4,1) shown in Figure 1; structures of PUR-I(2,1), PUR-I(4,3), PUR-I(4,4), and PUR-I(6,2) are shown similarly.

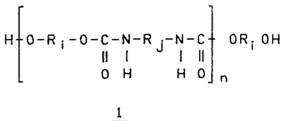

$$\mathrm{H}\left[\mathrm{O{-}R}_i\mathrm{{-}O{-}}\underset{\underset{\displaystyle \mathrm{O}}{\|}}{\mathrm{C}}\mathrm{{-}}\underset{\underset{\displaystyle \mathrm{H}}{|}}{\mathrm{N}}\mathrm{{-}R}_j\mathrm{{-}}\underset{\underset{\displaystyle \mathrm{H}}{|}}{\mathrm{N}}\mathrm{{-}}\underset{\underset{\displaystyle \mathrm{O}}{\|}}{\mathrm{C}}\right]_n\mathrm{OR}_i\mathrm{OH}$$

1

II. Sample Preparation. TOF-SIMS spectra of PUR-Is were obtained from thin PUR-I films cast from solution on a silver substrate. All 12 PUR-Is were dissolved in tetrahydrofuran (THF). For the transesterification experiment PUR-I(4,1) and PUR-I(4,3) were placed in trifluoroacetic acid (TFA) overnight. The concentrations of PUR-Is in THF and TFA solutions were in the range 1 × 10^{-2} to 1 × 10^{-3} M with respect to the repeat unit. A 1–5 μL quantitiy of each solution was deposited on 100 mm^2 of a silver substrate which had been previously cleaned by etching in nitric acid (20 vol %). Approximately 1–5 μg of each PUR-I was deposited on the silver substrate for analysis.

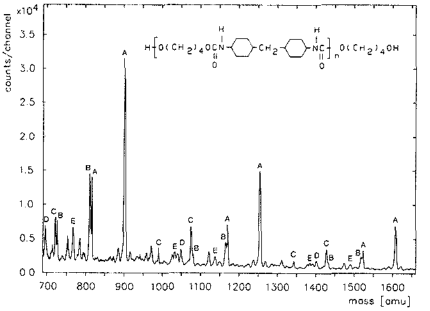

Figure 2. TOF-SIMS spectrum of PUR-I(4,3) in the mass range m/z = 690–1660. The oligomer series is identified by A, the repeat unit series by B, and the fragmentation series by C, D, and E.

III. Instrumentation. The time-of-flight mass spectrometer used was especially designed for SIMS applications and is described in detail elsewhere (*30, 31*). It has high transmission and detects ions in a preset mass range (e.g., 0–10000 amu) in a single spectrum for each primary ion pulse. A continuous beam of pimary argon ions is produced in a conventional electron impact source. Acceleration to 8 keV and focusing are accomplished by slit electrodes. By application of a 5-kV voltage pulse for 1 μs to a parallel plate deflection system, a short bunch of ions is chopped from the continuous beam and deflected into a magnetic sector field where it is mass separated. The path lengths of the ions in the packet are matched in the magnetic field so that time focusing is achieved. This system produces packets of 100–10000 argon primary ions focused on a spot of about 1 mm^2 on the target. The pulse repetition rate can be adjusted to 40 kHz, the pulse duration is <10 ns, and the energy of ions is approximately 12 keV.

Secondary ions are extracted from the sample and accelerated to ±5 kV, depending on the mode of operation, into a time-of-flight mass analyzer of the Poschenrieder type (*31*). The acceleration potential is applied via an electrode located above the sample, and it is measured with respect to the sample holder at ground potential. The masses of the secondary ions are determined by measurement of the flight time through an electrostatic sector field and two linear drift spaces. This arrangement provides first-order focusing of energy and angle, improving the mass resolution which is limited initially by the energy spread of the secondary ions. Mass calibration is achieved by using hydrocarbon peaks in the low mass range and Na^+ (m/z = 23) and Ag^+ (m/z = 107, 109) peaks.

To enhance the detection efficiency, especially for high masses, a postacceleration potential of up to ±20 kV is applied to the entrance of the detector unit. The detector consists of a channel plate for ion to electron conversion and optical signal coupling to a scintillator and photomultiplier. Single ion counting is used to enhance the signal-to-background ratio and to reduce mass discrimination of ions having the same m/z but slightly different times of flight. A target area of about 1 mm^2 is bombarded by 12-keV Ar^+ ions with an average current of 5 × 10^{-12} A for 60–300 s, corresponding to a primary ion current density of <1 × 10^{-9} A/cm^2 (static SIMS).

RESULTS AND DISCUSSION

I. TOF-SIMS Spectra of PUR-Is. TOF-SIMS spectra of PUR-Is were obtained in the medium mass range m/z = 500–3200. A segment from a typical spectrum is shown in Figure 2. The peaks in the spectra of PUR-Is can be separated into three well-defined series, depending on the process involved in ion production: oligomer, repeat unit, and fragmentation series. Desorption of intact low molecular weight

Table I. Oligomer Series (A) and Repeat Unit Series (B) for Polyurethanes Based on Diols and Diisocyanates (PUR-Is)[a]

	oligomer series (A)		repeat unit series (B)	
n	Na	Ag	Na	Ag
		PUR-I(2,1)[b]		
1	397 (85000)	481, 483 (114000, 112000)		
2	709 (44000)	793, 795 (36000, 36100)	647 (35000)	731, 733 (54000, 61000)
3	1021 (13400)	1106 (9600)[c]	959 (5700)	1044 (3100)
4	1333 (2950)	1418 (2200)	1271 (1900)	1356 (380)
5	1645 (560)	1730 (400)	1583 (1800)	1668 (90)
6	1957 (100)	2042 (90)	1895 (440)	
7			2207 (40)	
		PUR-I(2,2)		
2	545 (16000)		483 (250000)	567, 569 (54300, 56000)
3	775 (5600)		713 (85000)	797, 799 (9900, 11000)
4	1005 (1700)		943 (9100)	1028 (1500)
5	1235 (400)		1173 (500)	1258 (300)
6	1465 (140)		1403 (250)	1488 (40)
7	1695 (50)		1633 (50)	
8			1863 (30)	
		PUR-I(2,3)		
2	733 (400)	817, 819 (700, 650)		
3	1057 (100)	1142 (170)		
		PUR-I(2,4)		
2		641, 643 (3000, 3000)		579, 581 (9100, 8600)
3		878 (1500)		816 (3700)
4		1114 (830)		1052 (1500)
5		1350 (350)		1288 (850)
6		1586 (150)		1524 (400)
7		1822 (100)		1760 (200)
8		2058 (50)		1996 (100)
9		2294 (40)		2232 (50)
10				2468 (40)
		PUR-I(4,1)		
1	453 (32000)	537, 539 (42100, 38300)	363 (12300)	447, 449 (12300, 10300)
2	793 (16100)	878 (22300)	703 (28200)	787, 789 (46400, 52400)
3	1133 (3300)	1218 (5600)	1043 (1500)	1128 (2100)
4	1473 (970)	1558 (1450)	1383 (190)	1468 (500)
5	1813 (300)	1898 (500)		1808 (120)
6	2153 (100)	2238 (200)		2148 (80)
7	2493 (30)	2578 (50)		
8	2833 (20)	2918 (30)		
9		3258 (20)		
		PUR-I(4,2)		
1	371 (61000)	455, 457 (151000, 133000)		
2	629 (39000)	713, 715 (65000, 60400)	539 (129000)	623, 625 (191000, 177000)
3	887 (6000)	971, 973 (14000, 12500)	797 (77000)	881, 883 (14000, 14300)
4	1145 (1650)	1230 (2400)	1055 (700)	1140 (1040)
5	1403 (600)	1488 (250)	1313 (150)	1398 (300)
6		1746 (60)	1571 (90)	1656 (50)
7			1829 (70)	
		PUR-I(4,3)		
1		549, 551 (34000, 30000)		
2	817 (12300)	901, 903 (30000, 27000)	727 (5600)	811, 813 (13000, 11900)
3	1169 (6000)	1254 (14000)	1079 (1800)	1163, 1165 (3500, 3500)
4	1521 (2600)	1606 (6200)	1431 (850)	1516 (1700)
5	1873 (1000)	1958 (2700)	1783 (400)	1868 (650)
6	2225 (400)	2310 (1000)	2135 (180)	2220 (300)
7	2577 (150)	2662 (600)	2487 (140)	2572 (120)
		PUR-I(4,4)		
2	641 (6100)	*d*	551 (49000)	635, 637 (16200, 15000)
3	905 (2600)		815 (4600)	900 (5800)
4	1169 (1250)		1079 (1900)	1164 (1900)
5	1433 (530)		1343 (800)	1428 (800)
6	1697 (200)		1607 (380)	1692 (350)
7	1961 (100)		1871 (270)	1956 (180)
8	2225 (60)		2135 (100)	2220 (100)
9			2399 (50)	
		PUR-I(6,1)		
1	509 (3000)	593, 595 (3000, 2500)		
2	877 (1500)	962 (1500)	759 (22000)	844 (25000)
3	1245 (200)	1330 (300)	1127 (1000)	1212 (1000)
4	1613 (100)	1698 (50)	1495 (70)	1580 (60)

Table I (Continued)

	oligomer series (A)		repeat unit series (B)	
n	Na	Ag	Na	Ag
5			1863 (50)	
		PUR-I(6,2)		
1		511, 513 (8000, 7000)		
2	713 (4000)	798 (2100)	595 (134000)	679, 681 (141000, 129000)
3	999 (800)	1084 (700)	881 (50000)	966 (44000)
4		1370 (100)	1167 (2100)	1252 (1700)
5		1656 (70)	1453 (300)	1538 (120)
6		1942 (50)	1739 (100)	1824 (100)
7		2228 (30)	2025 (50)	2110 (50)
		PUR-I(6,3)		
1	521 (11000)	605, 607 (7300, 5800)		
2	901 (2300)	986 (1600)	783 (8700)	867, 869 (7200, 6900)
3	1281 (350)	1366 (240)	1163 (500)	1248 (460)
4	1661 (50)	1746 (40)	1543 (100)	1628 (50)
5	2041 (40)			
		PUR-I(6,4)		
2	725 (1200)	810 (500)	607 (15000)	691, 693 (3800, 3700)
3	1017 (300)	1102 (160)	899 (2950)	984 (680)
4	1309 (120)	1394 (100)	1191 (600)	1276 (200)
5	1601 (50)	1686 (40)	1483 (150)	1586 (60)
6	1893 (40)	1978 (30)	1775 (50)	1860 (30)

[a] The m/z of each peak is given; intensity (counts/channel) is given in parentheses. Noise is approximately 100 counts/channel at m/z = 800. [b] Structures correspond to those given in Figure 1. [c] Doublet due to Ag^+ isotopes is not resolved. [d] Not resolved from E with Na cationization.

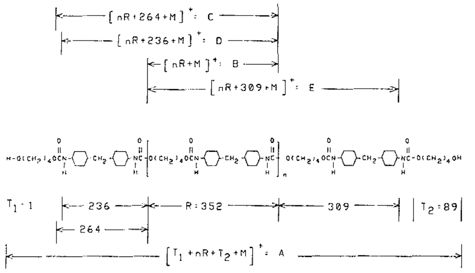

Figure 3. Structures of oligomer A and fragments B, C, D, and E, observed in TOF-SIMS spectrum of PUR-I(4,3).

oligomers gives rise to the oligomer series. The repeat unit series consists of peaks due to large PUR-I fragments containing an integral number of repeat units. The possibility that these are not fragments but PUR-I cyclic oligomers or linear PUR-Is having isocyanato and hydroxyl terminal groups is very low, because excess diol was used in the synthesis. The fragmentation series consists of less intense peaks corresponding to fragments that consist of an integral number of repeat units plus part of one additional repeat unit. Figure 3 shows the structures of the PUR-I(4,3) fragments and oligomers that generate the three series of peaks in the TOF-SIMS spectra. The oligomer series is identified by A, the repeat unit series by B, and the fragmentation series by three sets of fragments C, D, and E. All peaks are cationized with either Ag or Na.

Consecutive peaks having a consistent mass difference throughout the spectrum can be grouped in the same series. A mass difference of m/z 84 indicates that the same oligomer or fragment is cationized with Ag^+ and Na^+. The oligomer and repeat unit series are the most intense in the spectrum, followed by the fragmentation series. Oligomer peaks can be distinguished from repeat unit peaks because they appear at higher m/z values than the corresponding repeat unit peaks. Repeat unit peaks appear at m/z values which, after subtraction of the mass of the metal cation, are multiples of the nominal mass of the repeat unit. Peaks of the fragmentation series are usually of lower intensity than the oligomer and repeat unit peaks and appear on both the high and low mass sides of the repeat unit peaks. The mass difference between fragmentation and repeat unit series corresponds to reasonable mass losses from fragments of the repeat unit series. Peaks corresponding to the three series described dominate the spectrum in the mass range m/z = 500–3200 and provide complementary information useful for determining PUR-I structures. For example, structural information deduced from the fragmentation and repeat unit series can be used to identify similarities and differences between the diols and diisocyanates of the various PUR-Is, as will be detailed below.

A. Oligomer Series. Peaks due to cationized oligomers were observed for all PUR-Is studied. The existence of low molecular weight oligomers (ca. n = 1–10 ...) was verified by gel permeation chromatography for PUR-Is representative of the series examined [e.g., PUR-I(2,1), PUR-I(4,1)]. The oligomers consist of an integral number of repeat units and both terminal groups. The masses of the terminal groups can be determined from the difference between the corresponding peaks of the oligomer and repeat unit series. The mass of the repeat unit of the polymer can also be determined from the spacing between consecutive peaks in the oligomer series.

The structure of the oligomers of PUR-I(4,3) is given in Figure 3. The peaks of the oligomer series are labeled A in Figure 2. The oligomer series is tabulated in Table I for the PUR-Is studied. An oligomer and a fragment of the repeat unit series differ by the masses of the terminal groups. For example, PUR-I(4,3) oligomers consisting of two repeat units and cationized with Ag^+ give two peaks at m/z = 901, 903 of the oligomer series. Fragments of the same PUR-I(4,3) consisting of two repeat units and cationized with Ag^+ give rise to peaks at m/z = 811, 813 of the repeat unit series. The difference between the oligomer and repeat unit peaks of 90 amu is equal to the combined masses of the two terminal groups, H and $O(CH_2)_4OH$.

Molecular weight averages can be calculated for PUR-Is from m/z values and intensities of oligomer peaks. This will be the topic of a subsequent communication, where molecular weight averages of PURs determined from TOF-SIMS spectra will be compared to those measured by conventional techniques such as gel permeation chromatography.

B. Repeat Unit Series. The repeat unit series was observed for all PUR-Is studied except PUR-I(2,3). The peaks in this series correspond to an integral number of PUR-I repeat units, cationized with Ag$^+$ or Na$^+$. The mass of the repeat unit can be determined from the m/z of a peak in this series or from the spacing between consecutive peaks involving the same cation; thus the PUR-I can be identified.

The peaks of the repeat unit series are labeled B in Figure 2. The fragments in this series are produced by cleavage of two urethane bonds at alternate urethane links along the PUR-I chain. The structure of the fragments in the repeat unit series for PUR-I(4,3) is

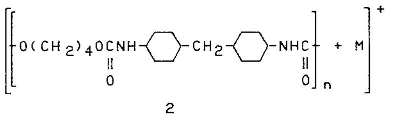

2

where n = 2, 3, 4, ..., 7 and M = Ag, Na.

The peaks for the repeat unit series for all PUR-Is studied are tabulated in Table I. For some PUR-Is the repeat unit series is the most intense in the spectrum; for others the oligomer series appears as the most intense. Cationization by Ag$^+$ and Na$^+$ gives two peaks for each fragment, separated by 84 amu. Therefore, a mass difference of 84 amu between a singlet and the first peak of a doublet on the high mass side of the singlet indicates cationization of the same fragment by both Ag$^+$ and Na$^+$. For example, **2** (n = 2, M = Na) gives rise to a peak at m/z = 727; cationization of the same fragment by Ag$^+$ gives peaks at m/z = 811, 813. Depending on availability of metal cations and stability of cationized fragments, peaks due to silver cationized fragments may appear as more intense than those due to fragments cationized with sodium, and vice versa.

Since the fragments of the repeat unit series consist of an integral number of repeat units, the spacing between two consecutive peaks cationized with the same cation is equal to the mass of the repeat unit. For example, the peaks at m/z = 811, 813 for **2** (n = 2, M = Ag) and m/z = 1163, 1165 for **2** (n = 3, M = Ag) have a spacing of 352 amu, which is the mass of the repeat unit for PUR-I(4,3). The mass of the repeat unit can be also determined from the m/z of a peak by subtracting the mass of the metal cation (i.e., 107 or 109 for Ag$^+$, or 23 for Na$^+$) and dividing by an appropriate integer n (i.e., n = 2, 3, 4, ...). For example, the peak at m/z = 727 for **2** (n = 2, M = Na) gives the mass of the repeat unit equal to 352 amu.

C. Fragmentation Series. The fragmentation series is generated by PUR-I fragments consisting of an integral number of repeat units plus a fraction of one additional PUR-I unit. This series occurs in the medium mass range (m/z = 500–3200); not all fragments of the fragmentation series are observed for all PUR-Is. Generally peak intensities for fragmentation series are lower than for the repeat unit and oligomer series. The particular fragmentation pattern of this series allows determination of the mass of the repeat unit of a PUR-I, as well as the masses of the diol and diisocyanate.

The fragmentation series is produced by cleavage of two different bonds separated by at least one repeat unit, as opposed to the repeat unit series which is produced by cleavage of the same urethane bonds. Depending on which bonds cleave, three kinds of fragments can be produced: C, D, and E. These fragments differ by a fraction of an additional repeat unit. This fraction corresponds to the diisocyanate plus two hydrogens for C, the diisocyanate minus CO plus two hydrogens for D, and the PUR-I repeat unit minus NHCO for E. The structures of C, D, and E fragments for PUR-I(4,3) are shown in Figure 3. The peaks of the fragmentation series are tabulated in Table II and labeled C, D, and E in the spectrum of Figure 2.

The mass difference between a B fragment consisting of (n + 1) repeat units and a C fragment of the same PUR-I consisting of n repeat units corresponds to the mass of the diol minus two hydrogens. For example, the mass difference between m/z = 1163, 1165 of **2** (n = 3, M = Ag) and m/z = 1075, 1077 of **3** (n = 2, M = Ag), both of PUR-I(4,3), is 88 amu, which is the mass of 1,4-butanediol minus two hydrogens.

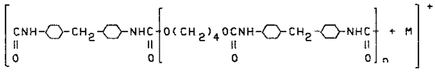

3

The mass difference between a B and a C fragment both consisting of the same number of repeat units of a PUR-I corresponds to the mass of the diisocyanate plus two hydrogens. For example, the mass difference between m/z = 811, 813 of **2** (n = 2, M = Ag), and m/z = 1075, 1077 of **3** (n = 2, M = Ag), both of PUR-I(4,3), is 264 amu, which corresponds to the mass of RMDI plus two hydrogens.

D. Comparison between PUR-Is. The masses of the repeat unit, diol and diisocyanate of a PUR-I, can be determined from the repeat unit and fragmentation series. Therefore, PUR-Is can be identified from the masses of their repeat units and for different PUR-Is differences or similarities can be established from the masses of their diols and diisocyanates. This can be used to compare PUR-Is and identify structural differences and similarities between them.

If the mass differences between a B fragment consisting of (n + 1) repeat units and a D fragment consisting of n repeat units are the same for two or more different PUR-Is, then the diols of their repeat units must be the same. The reverse is true also; that is, if the mass differences are not the same, then the diols of their repeat units must differ. For example, the Na$^+$ cationized B fragments of PUR-I(4,1), PUR-I(4,3), and PUR-I(4,4) give peaks at m/z = 1043, 1079, and 815, respectively (see Table I), for n = 3. The Na$^+$ cationized D fragments of PUR-I(4,1), PUR-I(4,3), and PUR-I(4,4) give peaks at m/z = 927, 963, and 699, respectively (see Table II), for n = 2. The mass difference of 116 amu between the B and D fragments for each PUR-I indicates that the diols are the same and corresponds to the mass of 1,4-butanediol − 2H + CO. The Na$^+$ cationized B fragments of PUR-I(2,1) and PUR-I(4,1) give peaks at m/z = 959 and 1043, respectively, for n = 3. The corresponding D fragments give peaks at m/z = 871 and m/z = 927, respectively, for n = 2. The mass differences between the B and D fragments are 88 amu for PUR-I(2,1) and 116 amu for PUR-I(4,1). The mass differences do not match; therefore, the diols must differ for PUR-I(2,1) and PUR-I(4,1). Specifically, $\Delta m/z$ = 88 corresponds to ethylene glycol − 2H + CO for PUR-I(2,1) and $\Delta m/z$ = 116 corresponds to 1,4-butanediol − 2H + CO for PUR-I(4,1).

If the mass differences between D and B fragments, both fragments consisting of the same number of repeat units, are the same for different PUR-Is, then the diisocyanates must be the same. If the mass differences are not the same, then the diisocyanates must be different. For example, the D fragments of PUR-I(2,1) and PUR-I(4,1) cationized with Na$^+$ give peaks at m/z = 871 and 927, respectively, for n = 2. The B fragments of PUR-I(2,1) and PUR-I(4,1) similarly give peaks at m/z = 647 and 703, respectively, for n = 2. The differences between the D and B fragments for PUR-I(2,1) and PUR-I(4,1) are equal to 224 amu, which indicates that the diisocyanates are the same for the two PUR-Is. The mass dif-

Table II. Fragmentation Series C, D, and E for PUR-I(2,1), PUR-I(4,1), PUR-I(4,3), and PUR-I(4,4)[a]

	C fragments PUR-I(4,3)[b]			D fragments PUR-I(2,1)	
n	Na	Ag	*n*	Na	Ag
1		723, 725 (5200, 5200)	1	559 (15000)	643, 645 (23000, 28000)
2	991 (1800)	1075, 1077 (5500, 5600)	2	871 (3200)	956[d]
3	1343 (1100)	1428 (2800)[c]	3	1183 (5000)	1268
4	1695 (400)	1780 (1100)	4	1495 (1400)	1580
5	2047 (100)	2132 (440)	5	1807 (350)	1892
6	2399 (70)	2484 (170)	6	2119 (70)	2204

D Fragments

	PUR-I(4,1)			PUR-I(4,3)	
n	Na	Ag	*n*	Na	Ag
1			1	611 (2400)	695, 697 (4400, 4000)
2	927 (7000)	1012 (6700)	2	963 (500)	1047, 1049 (2300, 2100)
3	1267 (180)	1352 (160)	3	1315 (400)	1400 (850)
			4		1752 (350)
			5		2104 (180)

	PUR-I(4,4)	
n	Na	Ag
1	435 (11000)	519, 521 (28300, 24300)
2	699 (5000)	783, 785 (10000, 9800)
3	963 (3200)	1048 (4200)
4	1227 (1200)	1312 (1950)
5	1491 (650)	1576 (980)
6	1755 (270)	1840 (650)
7	2019 (110)	2104 (250)
8	2283 (75)	2368 (100)
9	2547 (50)	

E Fragments

	PUR-I(4,3)		PUR-I(4,4)[e]	
n	Na	Ag	Na	Ag
1	684 (1000)	768, 770 (4400, 3900)	461 (14000)	545, 547 (32500, 28500)
2	1036 (300)	1121 (2100)	725 (23000)	809, 811 (25000, 25100)
3		1473 (900)	989 (12250)	1074 (13100)
4		1825 (400)	1253 (5000)	1338 (5200)
5		2177 (140)	1517 (2000)	1602 (2060)
6			1781 (830)	1866 (800)
7			2045 (540)	2130 (350)
8			2309 (100)	2394 (150)
9			2573 (90)	
	PUR-I(2,1)			
1	604 (9400)	688, 670 (11600)		

[a] The m/z of each peak is given; intensity (counts/channel) is given in parentheses. Noise is approximately 100 counts/channel at m/z = 800. [b] Structures correspond to those given in Figure 1. [c] Doublet due to Ag^+ is not resolved. [d] Interference from B with Na cationization. [e] Fragments correspond to an integral number of PUR-I(4,4) repeat units + NHCO + $O(CH_2)_4OC({=}O)NH$.

ference of 224 amu corresponds to the mass of MDI − CO + 2H.

II. Transesterification of PUR-Is. TOF-SIMS spectra of polymers are usually obtained from thin polymer films cast from solution on a silver substrate. A good solvent for a polymer solution disrupts intermolecular forces between polymer chains but leaves the polymer intact. Many polymers are insoluble or difficult to dissolve; therefore, having to dissolve a polymer before a TOF-SIMS spectrum can be obtained can be a serious drawback to the applicability of TOF-SIMS in polymer characterization. Recently TOF-SIMS spectra were obtained from thick, solid polymer films after overcoming problems due to charge accumulation on the polymer surface (*32*). Although this approach holds a great potential for surface and structural characterization of neat polymers, it is still difficult to apply. For polymers difficult to dissolve, an alternative would be to use chemical degradation reactions which occur at specific bonds, do not completely alter the structure of the polymer, and produce chain segments that are large enough to contain information about more than one repeat unit.

THF, TFA, and *N*,*N*-dimethylformamide were tested as solvents for PURs. THF was found to be optimum solvent for PUR-Is. TFA was used to investigate transesterification and hydrolysis reactions of PUR-I(4,1) and PUR-I(4,3). The transesterification reaction products were identified from TOF-SIMS spectra to be chain segments that are diesters of TFA and the diols from the PUR-Is. Some products of partial hydrolysis were identified from the spectra to be diamines and diesters of the diols of the PUR-Is.

Figure 4 shows part of the TOF-SIMS spectrum of PUR-I(4,3) in the range m/z = 590–1510. The spectrum was obtained from a thin film of PUR-I(4,3) cast on silver from a PUR-I(4,3) solution in TFA. The peaks in the spectrum correspond to segments of the PUR-I(4,3) backbone which are cationized with Ag^+ and Na^+ and consist of an integral

Table III. Transesterification Products of PUR-I(4,1) and PUR-I(4,3) with Trifluoroacetic Acid[a]

	PUR-I(4,1)[b]		PUR-I(4,3)	
n	Na	Ag	Na	Ag
1	645 (6000)	729, 731 (6800, 6800)	657 (25000)	741, 743 (18000, 17800)
2	985 (200)	1070 (170)[c]	1009 (3500)	1093, 1095 (2100, 2100)
3	1325 (30)		1361 (350)	1446 (180)
4			1713 (65)	1798 (40)
5			2065 (30)	2150 (20)

[a] The m/z of each peak is given; intensity (counts/channel) is given in parentheses. Noise is approximately 110 counts/channel at m/z = 800. [b] Structures correspond to those given in Figure 1. [c] Doublet due to Ag^+ is not resolved.

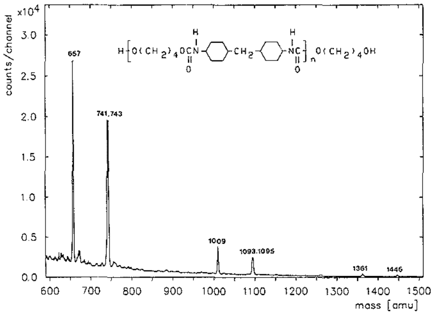

Figure 4. TOF-SIMS spectrum of PUR-I(4,3) obtained from thin film cast from trifluoroacetic acid solution on a Ag substrate. The spectrum is in the mass range m/z = 590–1510. Peaks correspond to Ag^+ and Na^+ cationized diesters of trifluoroacetic acid and diols of PUR-I(4,3).

number of repeat units, plus one additional diol and two trifluoroacetates, 4, where $n = 1, 2, ..., 5$ and M = Ag, Na. The peaks of the TOF-SIMS spectra of PUR-I(4,1) and PUR-I(4,3) in TFA are tabulated in Table III.

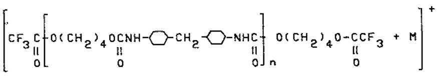

4

The products indicate that transesterification of PUR-Is with trifluoroacetic acid occurs at specific urethane links along the polymer backbone such that some diisocyanates remain intact and two diol ends are exposed for ester formation. Partial hydrolysis of PUR-I(4,3) to diamine and diol is evident from peaks at m/z = 211 due to 5 and m/z = 282 which is

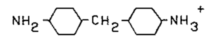

5

due to the diester of trifluoroacetic acid and 1,4-butanediol. Detection of large segments of PUR-I chains as diesters of TFA indicates that transesterification of PUR-Is with TFA is the dominant reaction. Hydrolysis of PUR-Is in TFA is rather mild, and it does not proceed completely to diamines and diols (*1*, *3*). The mass of the repeat unit of PUR-I(4,3) can be determined from the spacing between consecutive peaks due to 4 or from the m/z of a peak by appropriate subtraction of the masses of the metal cation, additional diol, and trifluoroacetates.

Transesterification reactions are potentially useful for characterization of insoluble PURs. Although transesterification degrades oligomers, it produces large enough chain segments from which structural information similar to that of large polymer fragments of the repeat unit series can be obtained. The transesterification approach points out to a direction of using derivatization or selective degradation reactions such that TOF-SIMS spectra can be obtained from insoluble polymers.

CONCLUSIONS

TOF-SIMS has been presented in this report as a viable technique for structural characterization of polyurethanes. TOF-SIMS combines the structural specificity of mass spectrometry with a sufficient mass range that large segments of polymer chains can be observed and identified from the spectra.

TOF-SIMS spectra of PUR-Is extend to several thousand atomic mass units. Intact cationized oligomers and fragments of PUR-Is were observed up to m/z = 3200. The masses of the repeat unit and terminal groups can be determined from the spacing between consecutive peaks in a series or the m/z of a fragment or oligomer peak in TOF-SIMS spectra. The masses of the diol and diisocyanate can be determined by comparing peaks originating from different fragmentation patterns. Therefore, PUR-Is can be identified, and differences and similarities in the diols or diisocyanate of PUR-Is can be assessed from the spectra. Transesterification of PUR-Is with trifluoroacetic acid occurs at specific ester bonds producing diesters of trifluoroacetic acid consisting of an integral number of repeat units and an additional diol. Polyuretane formulations that are difficult to dissolve can be characterized by using transesterification with trifluroacetic acid and subsequent identification of the diesters using TOF-SIMS.

The characterization of PURs based on polyesters, diisocyanates, and diol chain extenders, and PURs having pendant groups or cross-links, will be presented in future publications.

Registry No. PUR-I(2,1) (copolymer), 25036-33-3; PUR-I(2,1) (SRU), 25035-54-5; PUR-I(2,2) (copolymer), 25821-11-8; PUR-I(2,2) (SRU), 25868-19-3; PUR-I(2,3) (copolymer), 53465-21-7; PUR-I(2,3) (SRU), 121987-95-9; PUR-I(2,4) (copolymer), 9072-91-7; PUR-I(2,4) (SRU), 24969-33-3; PUR-I(4,1) (copolymer), 25805-16-7; PUR-I(4,1) (SRU), 25868-09-1; PUR-I(4,2) (copolymer), 25805-16-7; PUR-I(4,2) (SRU), 25868-09-1; PUR-I(4,3) (copolymer), 81122-07-8; PUR-I(4,3) (SRU), 81062-43-3; PUR-I(4,4) (copolymer), 37338-53-7; PUR-I(4,4) (SRU), 54633-10-2; PUR-I(6,1) (copolymer), 25805-34-9; PUR-I(6,1) (SRU), 25805-52-1; PUR-I(6,2) (copolymer), 27104-50-3; PUR-I(6,2) (SRU), 26183-63-1; PUR-I(6,3) (copolymer), 121987-94-8; PUR-I(6,3) (SRU), 121987-96-0; PUR-I(6,4) (copolymer), 25867-03-2; PUR-I(6,4) (SRU), 52622-33-0.

LITERATURE CITED

(1) Gorish, P. J. *Anal. Chem.* **1959**, *31*, 1298.
(2) Dussel, H.-J.; Wenzel, N.; Hummel, D. O. *Angew. Makromol. Chem.* **1982**, *106*, 107.
(3) Mulder, J. L. *Anal. Chim. Acta* **1967**, *38*, 563.
(4) Dawson, B.; Hopkins, S; Sewell, P. R. *J. Appl. Polym. Sci.* **1970**, *14*, 35.
(5) Jackson, M. B.; Solomon, D. H. *Anal. Chem.* **1972**, *44*, 1074.
(6) Mumford, N. A.; Chatfield, D. A.; Einhorn, I. N. *J. Appl. Polym. Sci.* **1979**, *23*, 2099.
(7) Brame, E. G.; Ferguson, R. G.; Thomas, G. J. *Anal. Chem.* **1967**, *39*, 517.
(8) Delides, C.; Pethrick, R. A.; Cunliffe, A. V.; Klein, P. G. *Polymer* **1981**, *22*, 1205.
(9) Eisenbach, C. D.; Gronski, W. *Makromol. Chem., Rapid Commun.* **1983**, *4*, 707.
(10) Dumais, J. J.; Jelinski, L. W.; Leung, L. M.; Gancarz, I.; Galambos, A.; Koberstein, J. T. *Macromolecules* **1985**, *18*, 116.

(11) Kintanar, A.; Jelinski, L. W.; Gancarz, I.; Koberstein, J. T. *Macromolecules* **1986**, *19*, 1876.
(12) Dyer, E.; Newborn, G. E. *J. Am. Chem. Soc.* **1958**, *80*, 5495.
(13) Thorne, M. P. *Can. J. Chem.* **1967**, *45*, 2537.
(14) McKay, A. F.; Vavasour, G. R. *Can. J. Chem.* **1953**, *31*, 688.
(15) Fletcher, M. A.; Lakin, M. W.; Plant, S. G. P. *J. Chem. Soc.* **1953**, 3898.
(16) Hileman, F. D.; Voorhees, K. J.; Wojcik, L. H.; Birky, M. M.; Ryan, P. W.; Einhorn, I. N. *J. Polym. Sci., Polym. Chem. Ed.* **1975**, *13*, 571.
(17) Voorhees, K. J.; Lattimer, R. P. *J. Polym. Sci., Polym. Chem. Ed.* **1982**, *20*, 1457.
(18) Ballistreri, A.; Foti, S.; Maravigna, P.; Montaudo, G.; Scamporino, E. *J. Polym. Sci., Polym. Chem. Ed.* **1980**, *18*, 1923.
(19) Foti, S.; Maravigna, P.; Montaudo, G. *J. Polym. Sci., Polym. Chem. Ed.* **1981**, *19*, 1679.
(20) Foti, S.; Giuffrida, M.; Maravigna, P.; Montaudo, G. *J. Polym. Sci., Polym. Chem. Ed.* **1983**, *21*, 1583.
(21) Foti, S.; Maravigna, P.; Montaudo, G. *Macromolecules* **1982**, *15*, 883.
(22) Reed, C. *Br. Polym. J.* **1974**, *6*, 1.
(23) Evans, N.; Williamson, J. E. *Adv. Mass Spectrom.* **1980**, *8A*, 1023.
(24) Marshal, G. L. *Eur. Polym. J.* **1983**, *19*, 439.
(25) Graham, S. W.; Hercules, D. M. *Spectrosc. Lett.* **1982**, *15*, 1.
(26) Dussel, H.-J.; Wenzel, N.; Hummel, D. O. *Angew. Makromol. Chem.* **1985**, *129*, 121.
(27) Richards, J. M.; McClennen, W. H.; Meuzelaar, H. L. C.; Gregonis, D. E.; Reichert, W. M.; Helle, M. A. *Macromolecules* **1985**, *18*, 496.
(28) Montaudo, G.; Puglisi, C. In *Developments in Polymer Degradation*; Grassie, N., Ed.; Elsevier Applied Science: London, New York, 1987, chapter 2, pp 35–80.
(29) Schulten, H.-R.; Lattimer, R. P. *Mass Spectrom. Rev.* **1984**, *3*, 231.
(30) Steffens, P.; Niehuis, E.; Friese, T.; Benninghoven, A. In *Ion Formation from Organic Solids*; Benninghoven, A., Ed.; Springer-Verlag: Berlin, 1983; Vol. 25, pp 111–117.
(31) Steffens, P.; Niehuis, E.; Friese, T.; Greifendorf, D.; Benninghoven, A. *J. Vac. Sci. Technol., A* **1985**, *3*, 1322.
(32) Bletsos, I. V.; Hercules, D. M.; Magill, J. H.; vanLeyen, D.; Niehuis, E.; Benninghoven, A. *Anal. Chem.* **1988**, *60*, 938.

RECEIVED for review September 6, 1988. Revised manuscript received May 11, 1989. Accepted June 1, 1989. This work was supported by the National Science Foundation under Grant CHE-8541141 and by the Deutsche Forschungsgemeinschaft. We are grateful to the Alexander von Humboldt Foundation for a senior fellowship for David M. Hercules, which stimulated this work.

Determination of Stable Carbon and Hydrogen Isotopes of Light Hydrocarbons

Ingolf Dumke,* Eckhard Faber, and Jürgen Poggenburg

Federal Institute for Geosciences and Natural Resources (BGR), Hannover, FRG

A combined system for the measurement of $^{13}C/^{12}C$ and D/H ratios on light hydrocarbons (C_1–C_3) and CO_2 is described. The system is designed for natural gas and sediment gas analyses. It comprises gas chromatographic separation with online combustion of hydrocarbons to CO_2 and H_2O, reduction of H_2O to H_2 on zinc in closed ampules, and mass spectrometric determination of isotope ratios ($\delta^{13}C$, δD) using a mass spectrometer inlet system especially designed for low hydrogen gas quantities. Isotope analyses can be carried out in the range of 3–10000 μL of CO_2 and 100–10000 μL of H_2 (gas quantities converted from sample compounds during preparation, STP). Including all preparation steps, reproducibility of isotope values for large sample quantities (>100 μL of produced CO_2 and >1000 μL of produced H_2) is ±0.2‰ for $\delta^{13}C$ and ±3‰ for δD. With decreasing gas quantities the reproducibility is lower, e.g. ca. ±1‰ for $\delta^{13}C$ (at 5–10 μL) and ca. ±7‰ for δD (at 100–150 μL). The isotope values tally with data of other laboratories (±0.2‰ for $\delta^{13}C$).

INTRODUCTION

Stable isotope ratios of light hydrocarbons are often successfully used in oil and gas exploration. The $^{13}C/^{12}C$ ratio of methane is the most widely used parameter for the genetic classification of naturally occurring hydrocarbon gases in terms of isotope values. It allows the distinction between bacterial and thermal hydrocarbons (*1–4*) and is related to the generation mechanisms and to the maturity of source rocks of thermal gases, respectively (*5–7*). Schoell (*2*) and Whiticar et al. (*8*) have shown that additionally the $^2H/^1H$ ratio of methane in combination with the $^{13}C/^{12}C$ ratio characterizes different pathways of bacterial methane formation. Furthermore carbon isotope values of higher homologues (ethane, propane) can be related to source rock maturities as well (*9*). They also show up mixtures of thermal gases and allow the isotope data of the mixing partners and related source rock maturity data to be calculated (*10*).

Isotope data have been measured on quite different types of samples including reservoir gases, headspace and desorbed gases from drill cuttings, cores from deep wells, and near surface sediments. Reviews on possible applications and published literature can be found elsewhere (*7, 9, 11, 12*).

The determination of isotope ratios requires an analytical system including gas chromatography, quantitative combustion, water reduction, and mass spectrometry. In contrast to the wide-ranging literature on applications of light hydrocarbon isotope data, only a small amount of literature is available on details about the analytical technique. For carbon isotope analysis a circulation combustion system with cupric oxide and oxygen (*13*) has been widely used for methane and other organic compounds for various investigations (*1, 14–17*). Silverman and Oyama (*18*) describe gas chromatographic separation coupled with an online combustion for carbon isotopic determination on methane as an automated sampling and preparation system for use in microbial metabolism studies.

Up to four components (C_1, C_2, C_3, and CO_2), separated on a gas chromatographic column, can be prepared for ^{13}C analysis with a system published by Faber (*19*) and Faber and Stahl (*20*). At the BGR first measurements on D/H ratios on natural gas samples were carried out in 1976 (*21*). Deuterium analysis on methane especially designed for low-volume samples has been developed by Faber et al. (*22*). The system described below is the continued development of these earlier techniques and allows the determination of carbon and hydrogen isotopic ratios on methane, ethane, and propane and the carbon isotopic ratio of CO_2 from one gas sample within one preparation cycle. The capability of isotope analysis in

0003-2700/89/0361-2149$01.50/0 © 1989 American Chemical Society

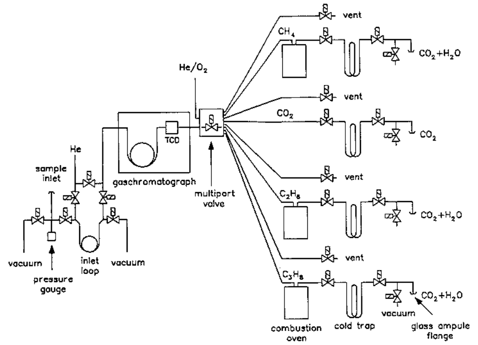

Figure 1. Scheme of the gas preparation line (for detailed explanation see text).

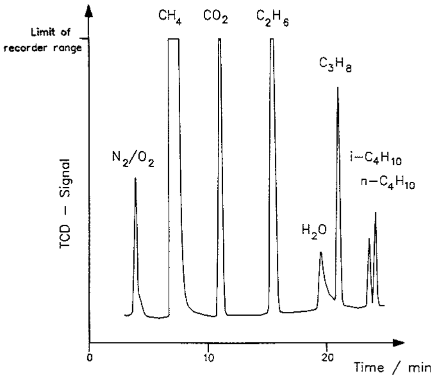

Figure 2. Chromatogram of the laboratory standard gas E245 (for composition see Table II, no valve switching).

a wide range of hydrocarbon concentrations, including very low gas quantities, makes it suitable for natural gases as well as headspace and shallow sediment gases.

EXPERIMENTAL SECTION

For the determination of stable isotope ratios, hydrocarbons have to be converted to CO_2 and H_2 required by stable isotope mass spectrometers. The complete technique can be divided into three parts, which are put into effect independent from each other: a gas preparation line to separate the desired components by gas chromatography with online combustion of hydrocarbons to CO_2 and H_2O, a reduction system to convert the combustion water to H_2, and stable isotope mass spectrometers.

Gas Preparation. A scheme of the gas preparation line is shown in Figure 1. The whole range of sample pressures from several atmospheres (test gases) down to some 10 mbar (sediment gases) can be handled by the evacuable inlet system with easily changeable inlet loops of different sizes. Loop volumes of 3, 10, and 30 mL ($^1/_4$ in. o.d. stainless steel) have been found to be useful. An additional 3-mL loop packed with Porapak Q allows transfer of all the hydrocarbons from a sample vessel into the inlet loop by freezing the latter in liquid nitrogen, a significant procedure for small samples with hydrocarbon quantities near the lower detection limit.

Helium is the carrier gas for separation on the column ($^1/_4$ in. o.d. stainless steel, 2.5 m length, Porapak Q) and passes the hydrocarbon components through the combustion lines. A thermal conductivity detector (TCD) monitors the gas components N_2/O_2, CH_4, CO_2, C_2H_6, H_2O, C_3H_8, i-C_4H_{10}, n-C_4H_{10}, i-C_5H_{12}, n-C_5H_{12}. Figure 2 shows a typical gas chromatogram (laboratory standard gas E245, see below). N_2 and O_2 as well as higher hydrocarbon homologous (C_{5+}) are not fully resolved. Unsaturated compounds (C_2H_4 and C_3H_6) may occur shortly before but well separated from the corresponding saturated compounds. The chromatogram is not used for quantitative evaluation because correct peak integration is impeded by extra peaks and base-line shifts due to necessary valve switching during the preparation cycle.

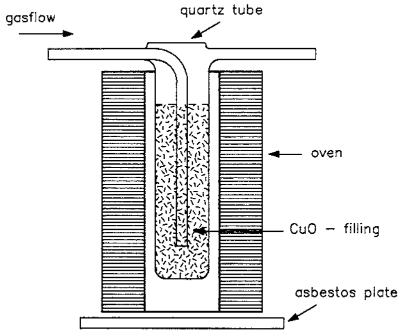

Figure 3. Sectional drawing of the combustion oven.

The column is temperature programmed from −50 °C (2 min initial time) to 220 °C (10 min final time) with rise of 15 °C/min for 8 min followed by 5 °C/min for another 8 min and again 15 °C/min until the final temperature is reached. This temperature program assures separation of the early compounds air (N_2/O_2), methane, and CO_2.

Experiences with earlier systems (*20*) have shown that it is essential to eliminate memory effects occurring when the various hydrocarbon components are combusted successively in the same oxidation line. Therefore the desired components (methane, ethane, and propane) are separated into individual pathways at the exit of the chromatographic column. A multiport valve (VALCO type AH2 CSC-8-HPA) switches the carrier gas to one of three separate combustion lines and an additional cold trap for CO_2. Vent valves prevent passing of blank contributions or undesired components (e.g. unsaturates) through a combustion line. Complete removal of combustion products from the oven chamber is achieved by a second He flow which is connected to all outlet ports of the multiport valve except the one momentarily linked to the gas chromatograph. This flow path can be also used with oxygen for daily regeneration of the oxidation catalyst.

The construction of the electrical combustion furnace (manufactured by H.-D. Buchwald, Bolsehle 55, 3071 Husum, FRG) is shown in Figure 3. The vertical arrangement saves space and avoids gaps in the flow path which may occur due to shrinking of the CuO filling. Copper(II) oxide (CuO) is the most popular catalyst for oxidation of hydrocarbons and has been extensively studied, mainly because of its application in elemental analyzers. Ebel (*23*) has given a good review on this subject. Oxidation of methane has been examined by Kainz and Horvatitsch (*24*), Horacek et al. (*25*), Pechanec (*26*), and also by Matthews and Hayes (*27*). Methane, mostly the major component within samples considered here, is known to be difficult to combust quantitatively and requires relatively high combustion temperatures. The necessary temperature depends on the type of grain size of the CuO used. Wire form CuO has been chosen here because it allows the use of a considerable amount in the oven to combust several large samples (some 10 mL of methane) without regeneration and does not lead to unacceptable high flow resistance. Temperature is chosen at 880 °C.

Cold traps to trap combustion products (CO_2 and H_2O) at liquid nitrogen temperature are made of glass (Duran, 6 mm o.d.). No undesired effects (loss of CO_2, isotopic shifts) caused by the procedure of freezing both combustion products in one cold trap have been observed. In fact, bulk of CO_2 and H_2O freeze well displaced onto the tube walls due to the temperature gradient in the first part of the cold trap. This may support a quantitative separation. Combustion products are individually transferred to glass ampules (6 mm o.d., 15 cm length) through heated transfer lines using cryogenic separation (dry ice/2-propanol mixture, ca.

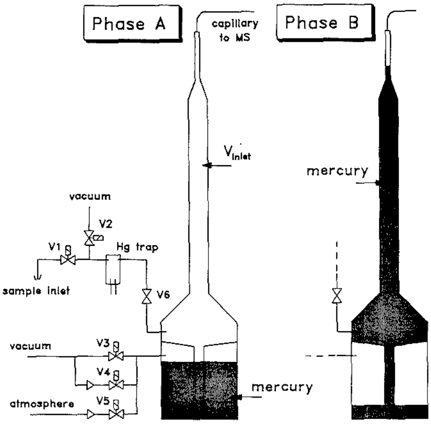

Figure 4. Scheme of the mass spectrometer inlet system: V_1–V_6, valves (for functions see text); V_{Inlet}, inlet volume; phase A, maximum inlet volume for sample inlet; phase B, inlet volume compressed by rising mercury for pressure adjustment after sample inlet.

−80 °C). The glass ampules are sealed by torch.

A rotary pump and a turbo molecular pump are attached to the system. Except for the cold traps all tubes are made of stainless steel ($^1/_{16}$ in. or $^1/_4$ in.). High vacuum tight, air-actuated bellows valves (NUPRO SS-4BK-1C) have been chosen for all evacuable parts of the system. All valves in the system can be either manually switched or activated by computer. The whole process, starting with inlet of the sample and ending with the collection of all combustion products in the cold traps, runs automatically controlled.

Water Reduction. Methods of reducing water to hydrogen for isotope analysis are mostly based on the reaction with hot uranium in flow systems (*28*, *29*) or zinc in flow systems (*30*) or closed ampules (*31*, *32*).

Because sample amounts as small as possible should be processed, flow systems were regarded as disadvantageous due to their large internal volumes and surface areas and the risk of memory effects. Therefore a further development of the method described by Coleman et al. (*32*) has been chosen. The combustion water is transferred to glass reaction tubes with a filling of some granules of cleaned zinc. After the reaction tube was heated at 450 °C for at least 2 h it contains zinc oxide and molecular hydrogen and can be used directly at the mass spectrometer for isotope ratio determination. The cleaning procedure described by Coleman et al. is applied to prepare the zinc granules which are then kept under vacuum until usage. Besides the zinc charge indicated by Coleman et al. (BDH AnalaR shot 0.5–2.0 mm) another charge (Riedel-de-Haen, Zink feingranuliert pa. 31651) has also been found to be usable for the reduction process.

Mass Spectrometry. The determination of isotope ratios is carried out on commercial isotope mass spectrometers. $^{13}C/^{12}C$ ratios are determined on a Finnigan MAT 250 with which the whole range of sample quantity, ca. 3 to ca. 10.000 μL of CO_2 (STP), can be handled with standard equipment using cool finger technique below the quantity of 50 μL CO_2. $^2H/^1H$ determinations are performed on a Finnigan MAT Delta D. With standard equipment the dynamics of volume variation in the inlet system is not suitable for H_2 gas quantities down to less than 100 μL (STP). Therefore a special inlet system for the sample side has been constructed which uses a mercury piston for volume variation (Figure 4). The volume in the upper part (V_{inlet}, ca. 250 mL) is separated from the mercury reservoir in the lower part. V_{inlet} is evacuable via valve V2 and the float valve V6 (phase A) provided that the headspace above the mercury is evacuated via valves V3 or V4 too. After sample inlet via valve V1 the mercury can be raised by carefully floating the lower chamber via valve V3 (phase B). The rising mercury automatically closes the float valve V6. The maximum volume of V_{inlet} is large compared to the volume of sample tube and inlet flange so that more than 95% of the sample is available in V_{inlet} for compression. The maximum volume can be decreased by a factor of ca. 500. This allows pressure adjustment and measurement of samples down to ca. 30 μL of H_2 (STP). The system is made of stainless steel except for the glass standpipe to watch the mercury piston. The standpipe is surrounded by a plexi tube for security. The float valve V6 consists of a free up and down movable Teflon cylinder with silicon cap which is pressed against a ring edge by the raising mercury. The total height of the system is 85 cm so that undesired flushing of the lower chamber will not result in pushing the mercury into the capillary of the mass spectrometer. Valves V4 and V5 are operated electrically with interceptions to allow careful adjustment of the mercury level. Via valve V3 quick pumping down of the mercury is possible. Malfunction of V6 resulting in mercury spill toward V1 and V2 is indicated by electrical contacts within a mercury trap right before V6. The whole inlet system has been manufactured by EMG (Elektronik-Mechanik-Gerätebau GmbH, 2800 Bremen 61, FRG).

Table I. Calibration Data Set for Deuterium Analysis (in Parts per Mil)

standard	δ_{WST}[a]	δ_{SMOW}[b]	$\delta_{SMOW\text{-}SLAP}$[c]	nominal value
V-SMOW	95.3 ± 0.1	0.0	0.0	0.0
NBS 1	46.0 ± 0.3	−45.0	−46.0	−47.1
NBS 1a	−101.3 ± 0.3	−179.5	−183.4	−183.2
GISP	−107.3 ± 0.5	−185.0	−189.1	−189.8
SLAP	−363.4 ± 1.8	−418.8	−428.0	−428.0

$\delta_{SMOW/WST}$[d] = −87.0 f_{corr} = 1.022

[a] δ_{WST}, δ value versus working standard. [b] δ_{SMOW}, δ value versus V-SMOW. [c] $\delta_{SMOW\text{-}SLAP}$, δ value recalculated to the SMOW-SLAP scale using f_{corr}. [d] $\delta_{SMOW/WST}$, δ value of the working standard versus V-SMOW.

Table II. Composition of Laboratory Standard Gas E 245

component	concn, vol %
nitrogen	1.2
carbon dioxide	3.1
methane	89.5
ethane	3.9
propane	1.2
isobutane	0.3
n-butane	0.4
isopentane	0.2
n-pentane	0.1

RESULTS

Isotope ratios are reported in the commonly used δ notation

$$\delta \text{ value} = \frac{R_{sample} - R_{standard}}{R_{standard}} * 1000 \ (‰) \qquad (1)$$

where R is the ratio $^{13}C/^{12}C$ or $^2H/^1H$, respectively. Results are given according to the PDB scale for $\delta^{13}C$ (*33*) and according to the SMOW-SLAP scale for δ^2H (δD) (*34*).

Water Reduction. The apparatus described has been tested with common international water standards (Table I). A calibration of the H_2 gas working standard at the mass spectrometer according to V-SMOW has been established. As a common method of eliminating systematic deviations from the nominal values, a correction factor according to the SMOW-SLAP scale (*34*) has been determined. Delta values recalculated to the SMOW-SLAP scale correspond to the nominal values (*34*, *35*). While the reproducibility of delta values of consecutive samples was mostly better than ±0.5‰, a long-term reproducibility in routine analysis of ±1–2‰ seems to be realistic.

Gas Preparation. Reproducibility. Long-term reproducibility of the system can be deduced from repeated routine

Table III. Isotope Ratios (Mean Values of Multiple Analyses, in ‰) and Standard Deviations (σ_{n-1}) for the Gas Standard E 245

	methane	ethane	propane	carbon dioxide	sample vol, μL_{STP}
$\delta^{13}C_{PDB}$	−44.5 ± 0.13	−32.0 ± 0.25	−29.0 ± 0.25	no values	>100
	a	*a*	*a*	−10.4 ± 0.7	<100
$\delta D_{SMOW\text{-}SLAP}$	−166 ± 2.4	*b*	*b*		>1000
	−166 ± 5.5	−126 ± 6.6	−118 ± 6.6		<1000

[a] See text and Figure 7. [b] No values.

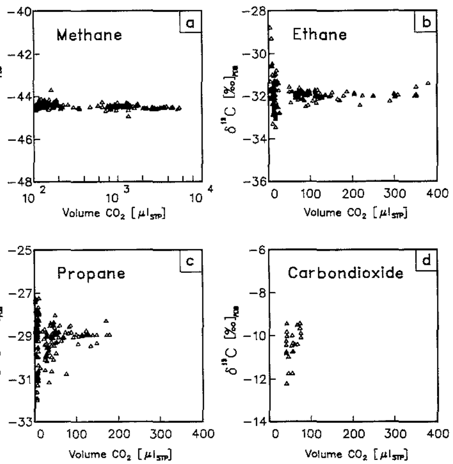

Figure 5. Measurements of $\delta^{13}C$ for methane, ethane, propane, and carbon dioxide of the laboratory standard gas E245 as a function of sample volume (μL of CO_2 produced in preparation, STP).

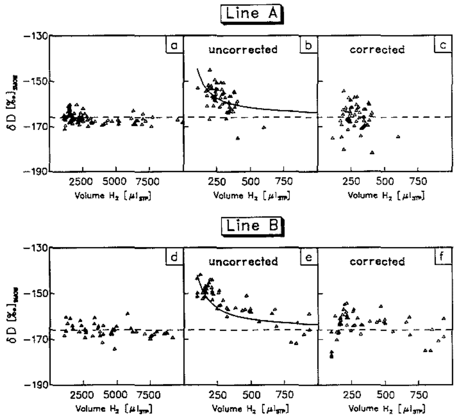

Figure 6. Measurements of δD for methane (laboratory standard gas E245) as a function of sample volume (μL of H_2 produced in preparation, STP) for two different preparation lines (A and B): dotted lines, nominal value, mean of data displayed in graphs a and b; solid lines (graphs b, e), correction curves used for blank correction of measured δ values for sample quantities below 1000 μL of H_2.

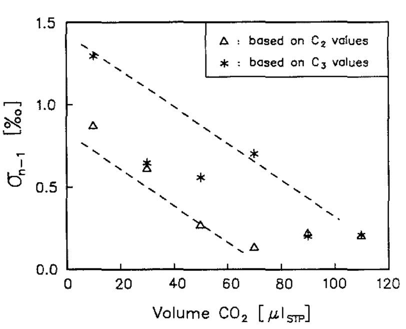

Figure 7. Reproducibility of $\delta^{13}C$ values (expressed as standard deviation σ_{n-1}) as a function of sample volume (μL of CO_2 produced in preparation, STP).

measurements on a laboratory standard. The gas (Laboratory-No. E 245, composition given in Table II) has been used for daily check of the system and Figures 5–7 display results of preparations spread over a time interval of about 2 years. Figure 5 illustrates the measurement of $\delta^{13}C$ for methane, ethane, propane, and CO_2 as a function of sample volume (CO_2 produced in preparation, STP), ranging from some microliters up to about 6 mL. It can be seen that down to ca. 100 μL of produced CO_2 the scattering of the isotope values stays fairly constant while below 100 μL it increases with decreasing sample volume.

Regarding corresponding measurements for δD of methane in Figure 6, a different situation can be found. Two data sets of two different GC–combustion lines (A and B) used at BGR are presented. Sample volumes (H_2 produced in preparation, STP) range from ca. 50 μL up to ca. 10 mL. Down to ca. 1000 μL (Figure 6a,d) scattering is quite homogeneous and a mean value of δD = −166‰ can be calculated. Below 1000 μL (Figure 6b,e) scattering increases and in addition the measured isotope values rise with decreasing sample volume. This is explained by a blank of water in the GC–combustion system which contributes to each sample during the preparation. Sources for this blank are traces of water and hydrocarbons in the He carrier gas and traces of compounds that remain on the GC column and in the combustion oven from previous preparations and are given off slowly. The H_2 blank contribution during a preparation cycle has been determined to be ca. 30 ± 10 μL with a δD value of about −95 ± 14‰ for line A. Mean values for line B are 20 μL with δD of −47‰. This illustrates that the blank contribution strongly depends on the condition of the combustion lines. However, experience shows that the blank contribution stays constant within given limits for quite long time periods. By use of formula 2 for blank correction on δD values for H_2 quantities below 1000 μL the distribution of Figure 6c,f shows about the same mean values as for the large volume samples

$$\delta D_{corr} \sim \frac{\delta D_{MS} V_{mS} - \delta D_{blank} V_{blank}}{V_{MS} - V_{blank}} \qquad (2)$$

with δD_{corr} the corrected delta value, δD_{MS} the measured delta value at the mass spectrometer, V_{MS} the volume of H_2 determined at the mass spectrometer (real sample volume plus blank contribution), δ_{blank} the delta value of blank contribution (=−95‰), and V_{blank} the volume of blank contribution (=30 μL). For CO_2 the blank contribution of a preparation cycle

Table IV. Isotope Values for Natural Gas Standards (NGS1/2/3)[a]

	NGS1			NGS2				NGS3
institute code	C_1	C_2	C_3	C_1	C_2	C_3	CO_2	C_1
Results of an Interlaboratory Comparison ($\delta^{13}C_{PDB}$ in ‰)								
F-6	−28.9	−26.4	−19.9	−43.5	−31.1	−24.3	−7.5	−73.1
I-4	−29.16	−26.02		−44.92	−32.1	−25.9	−8.08	−72.85
NL-1	−29.16	−25.42		−44.76	−31.17		−8.02	−72.67
USA-15	−28.91	−25.93		−44.57	−32.06	−25.7		−72.77
USA-16	−28.97	−26.09	−21.67	−44.58	−31.84	−25.01	−8.38	−72.55
USA-17	−28.6	−26.3		−43.1	−31.7	−23.5	−8.9	−69.6
Evaluation of Data								
mean	−28.95	−26.03		−44.24	−31.66	−24.88	−8.19	−72.26
σ_{n-1}	±0.21	±0.35		±0.75	±0.43	±1.0	±0.51	±1.3
After Outlier Correction								
mean	−28.95	−26.09		−44.71	−31.93	−25.00	−8.16	−72.79
σ_{n-1}	±0.21	±0.16		±0.17	±0.19	±0.7	±0.19	±0.21
BGR Results								
$\delta^{13}C_{PDB}$	−28.9	−25.9	−22.9	−44.6	−31.9	−25.5	−8.1	−72.9
$\delta D_{SMOW-SLAP}$	−140	−114		−178	−125			−178

[a] Results of an interlaboratory comparison, published by HUT (*36*), and measurements at the BGR.

has been determined to be in the order of 0.1–0.2 μL (STP) which is neglectable compared to sample volumes.

A summary of the results with the laboratory standard E245 is given in Table III and Figure 7:

$\delta^{13}C$ isotope ratios can be reproduced by ±0.2‰ for CO_2 quantities of >100 μL (corresponding to 100 μL of methane, 50 μL of ethane, and 33 μL of propane, respectively), whereas below 100 μL the reproducibility decreases according to Figure 7 to ca. ±1‰ at 5–10 μL.

δD isotope ratios can be reproduced by ±3‰ for H_2 quantities of >1000 μL (corresponding to 500 μL of methane, 333 μL of ethane, and 250 μL of propane, respectively), whereas below 1000 μL the reproducibility decreases to ca. ±7‰ at 100–150 μL.

Gas Preparation. Accuracy. The accuracy of the system can be checked by measuring samples with known isotope values. Unfortunately, gas standards with internationally accepted isotope values have not existed up to now. But in 1985 three natural gas samples of different composition and origin were supplied by the International Atomic Energy Agency (IAEA), Vienna. Results of $\delta^{13}C$ isotope analyses of several laboratories were published by HUT (*36*). Table IV shows these results. Mean and outlier corrected mean (excluding values beyond $2\sigma_{n-1}$) have been calculated and can be compared to results obtained by the BGR preparation system described here. The latter coincide with the outlier corrected means for all measured components within the limits of standard deviation. A major deviation does exist for propane of sample NGS1, but only two considerable differing values measured by other laboratories are available. Isotope ratios for deuterium were not published by HUT (*36*) but the BGR data are included in Table IV.

CONCLUSION

With the method described it is possible to process hydrocarbon components for $\delta^{13}C$ and δD isotope analysis in the range of 3–10000 μL of produced CO_2 and 100–10000 μL of produced H_2, respectively. The reproducibility and accuracy are sufficient to genetically classify hydrocarbons from reservoirs (large gas quantities) and sediment samples (small gas quantities). The lower limit of processable gas quantities is not given by mass spectrometry but by the blank contribution in the gas preparation and the water reduction system. Blank correction, necessary for low-volume hydrogen isotope measurements cannot be applied to lower quantities than ca. 100 μL of H_2 because of the steep slope of the correction curve in this region. Further improvement of hydrogen isotope measurements therefore has to concentrate mainly on reducing the system blank. The fact that correction is possible by using the measured system blank allows the conclusion that the water reduction process does work down to these very small sample amounts without severe systematic error.

ACKNOWLEDGMENT

The authors wish to thank U. Rinow for valuable discussions during the construction phase. Many thanks also to all technicians, especially R. Bauer, who have performed more than 13000 analyses up to now, for their skillful work and several hints for improvements of the system.

LITERATURE CITED

(1) Rosenfeld, W. D.; Silverman, S. R. *Science* **1959**, *130*, 1658–1659.
(2) Schoell, M. *Geochim. Cosmochim. Acta* **1980**, *44*, 649–661.
(3) Rice, D. D. *Gulf Coast Assoc. Geol. Soc., Transactions 30th Annu. Meeting* **1980**, 203–213.
(4) Colombo, U.; Gazzarrini, F.; Gonfiantini, R.; Tongiorgi, E.; Caflisch, L. *Advances in Organic Geochemistry 1968*; Schenck, P. A., Havenaar, I., Eds.; Pergamon Press: Oxford, 1968; 499–516.
(5) Stahl, W. J.; Koch, J. *Erdöl Kohle, Erdgas, Petrochem.* **1974**, *27*, 623.
(6) Stahl, W. J. *Erdöl Kohle, Erdgas, Petrochem.* **1975**, *28*, 188–191.
(7) Stahl, W. J. *Chem. Geol.* **1977**, *20*, 121–149.
(8) Whiticar, M. J.; Faber, E.; Schoell, M. *Geochim. Cosmochim. Acta* **1986**, *50*, 693–709.
(9) Faber, E. *Erdöl Erdgas Kohle* **1987**, *103*(5), 210–218.
(10) Berner, U.; Faber, E. *Advances in Organic Geochemistry 1987*; Mattavelli, L., Novelli, L., Eds.; Pergamon Press: Oxford, 1987. *Org. Geochem.* **1988**, *13*, 67–72.
(11) Fuex, A. N. *J. Geochem. Explor.* **1977**, *7*, 155–188.
(12) Schoell, M. *Geol. Jahrb. Reihe D* **1984**, *67*.
(13) Craig, H. *Geochim. Cosmochim. Acta* **1953**, *3*, 53–92.
(14) Park, R.; Epstein, S. *Geochim. Cosmochim. Acta* **1960**, *21*, 110–126.
(15) Parker, P. L. *Geochim. Cosmochim. Acta* **1964**, *28*, 1155–1164.
(16) Sackett, W. M.; Menendez, R. *Advances in Organic Geochemistry 1971*; Gärtner, H. R., Wehner, H., Eds.; Pergamon Press: Oxford, 1972; pp 523–533.
(17) Coleman, D. D. Ph.D. Dissertation, University of Illinois, Urbana-Champaign.
(18) Silverman, M. P.; Oyama, V. J. *Anal. Chem.* **1968**, *40*(12), 1833–1837.
(19) Faber, E. Ph.D. Dissertation TU Clausthal.
(20) Faber, E.; Stahl, W. J. *Petroleum Geochemistry and Exploration of Europe*; Brooks, J., Ed.; Blackwell Scientific Publications: Oxford, 1983; pp 51–63.
(21) BGR unpublished report, Archives No. 77821, Hannover, 1977.
(22) Faber, E.; Dumke, I.; Ott, A.; Poggenburg, J. Forschungsbericht DGMK-Projekt 298, Hamburg, 1986.
(23) Ebel, S. *Fresenius' Z. Anal. Chem.* **1973**, *264*, 16–28.
(24) Kainz, G.; Horvatitsch, H. *Z. Anal. Chem.* **1960**, *177*, 321–327.
(25) Horacek, J.; Körbl, J.; Pechanec, V. *Mikrochim. Acta* **1960**, 294–298.
(26) Pechanec, V. *Collect. Czech. Chem. Commun.* **1973**, *38*, 2917–2925.
(27) Matthews, D. E.; Hayes, J. M. *Anal. Chem.* **1978**, *50*, 1465–1473.
(28) Bigeleisen, J.; Perlman, M. L.; Prosser, H. C. *Anal. Chem.* **1952**, *24*, 1356–1357.

(29) Friedman, I.; Smith, R. L. *Geochim. Cosmochim. Acta* **1958**, *15*, 218–228.
(30) Friedman, I. *Geochim. Cosmochim. Acta* **1953**, *4*, 89–103.
(31) Rolle, W.; Bigl, F.; Haase, G.; Runge, A.; Hübner, H. *Isotopenpraxis* **1969**, *5* Heft 1, 35–36.
(32) Coleman, M. L.; Shepherd, Th. J.; Durham, J. J.; Rouse, J. E.; Gillian, R. M. *Anal. Chem.* **1982**, *54*, 993–995.
(33) Craig, H. *Geochim. Cosmochim. Acta* **1957**, *12*, 133–149.
(34) Gonfiantini, R. *Nature* **1978**, *271*, 534–536.
(35) Gonfiantini, R. Advisory Group Meeting on Stable Isotope Reference Samples for Geochemical and Hydrological Investigations, IAEA, Vienna 19–21 Sept 1983, Report to the Director General, Vienna 1984.
(36) Hut, G. Consultants Group Meeting on Stable Isotope Reference Samples for Geochemical and Hydrological Investigations, IAEA, Vienna 16–18 Sept 1985, Report to the Director General, Vienna, 1987.

RECEIVED for review January 9, 1989. Accepted June 27, 1989. This work was backed by the German Minister of Research (BMFT, Grant No. 03 E 6237A) and the Deutsche Wissenschaftliche Gesellschaft für Erdöl, Erdgas and Kohle e.V. (Grant No. 298).

Evidence for Radical Anion Formation during Liquid Secondary Ion Mass Spectrometry Analysis of Oligonucleotides and Synthetic Oligomeric Analogues: A Deconvolution Algorithm for Molecular Ion Region Clusters

J. A. Laramée, B. Arbogast, and M. L. Deinzer*

Department of Agricultural Chemistry and the Environmental Health Sciences Center, Oregon State University, Corvallis, Oregon 97331

It is shown that one-electron reduction is a common process that occurs in negative ion liquid secondary ion mass spectrometry (LSIMS) of oligonucleotides and synthetic oligonucleosides and that this process is in competition with proton loss. Deconvolution of the molecular anion cluster reveals contributions from $(M - 2H)^{\bullet-}$, $(M - H)^{-}$, $M^{\bullet-}$, and $(M + H)^{-}$. A model based on these ionic species gives excellent agreement with the experimental data. A correlation between the concentration of species arising via one-electron reduction [$M^{\bullet-}$ and $(M + H)^{-}$] and the electron affinity of the matrix has been demonstrated. The relative intensity of $M^{\bullet-}$ is mass-dependent; this is rationalized on the basis of base-stacking. Base sequence ion formation is theorized to arise from $M^{\bullet-}$ radical anion among other possible pathways.

INTRODUCTION

Reduction of analytes during analysis by liquid secondary ion mass spectrometry (LSIMS) became a topic of discussion almost as soon as the analytical technique itself was introduced. Not all compounds yielded exclusively preformed $(M - H)^{-}$ or $(M + H)^{+}$ cluster ions as first predicted by the original models to describe the ionization phenomenon (*1, 2*). It was shown that chlorophylls with extended π systems gave 3.4 times more $M^{\bullet-}$ than $(M - H)^{-}$ (*3*) and *N*-carboxymethyl-3-dicyanomethylene-5-nitroindolin-2-one yielded exclusively $M^{\bullet-}$ (*4*) under particle bombardment. Positive LSIMS of nucleosides (*5*) and some peptides (*6*) yields enhanced $(M + n)^{+}$ ions that are not explained by the isotopic composition. It was suggested that in these cases low-lying unoccupied molecular orbitals (LUMOs) were available for capture of low-energy electrons to produce $M^{\bullet-}$ ions (*7*) or reduced multiprotonated $(M + n)^{+}$ ions (*5*).

Extensive reduction has been reported for nucleotides (*8*), cationic triarylmethane and Oster dyes (*9*), diquaternary ammonium and other organic salts (*4, 10*), anthracyclines and anthracyclinones (*11*), quinones and tetracyanoquinodimethanes (*4*), or generally for compounds expected to undergo facile reduction in solution. Charge-transfer complexes also have been proposed as sources of $M^{\bullet-}$ and $M^{\bullet+}$ pairs (*12, 13*).

In addition to being a plausible source of thermalized electrons (*7*), the matrix provides radical species and possibly hydrogen atoms through high-energy particle bombardment (*14, 15*). Alternatively, it has been suggested that hydrogen atoms may be abstracted from matrix molecules by radical ions (*16*) as is more typical of free radicals in solution, and some reduction of organic salts and complexes may even occur in glycerol without particle bombardment (*10*). Thus the nature of the matrix significantly affects the degree of reduction of sample molecules. Organic dyes in tetraglyme and diethanolamine (*9*), and Met-enkephalin in thioglycerol (*6*), for example, show $(M + 1)^{+}$ cluster ion patterns that are closer to that expected from the isotopic composition than when these compounds are analyzed in glycerol.

A serious deficiency in dealing with reduction reactions in LSIMS is the lack of a quantitative treatment for the ions being observed. This is important if isotope patterns are used to confirm empirical formulas, or if fragment-ion-forming processes are needed to understand the structural features of the molecule. It is particularly critical when molecular weights of larger molecules are relevant. We have developed a computational method for deconvoluting the ion clusters that allows a quantitative determination of the sample ion composition that was analyzed. This has brought about some new findings about the relative importance of the electron affinities of matrix and sample molecules being analyzed.

EXPERIMENTAL SECTION

Chemicals. The oligodeoxynucleotide carbamate analogues were synthesized as described previously (*17*). Amino functionality on adenine and cytosine was blocked with the benzoyl (Bz) group and on guanine was blocked with the phenylacetyl (PA) group. Backbone linkages consisting of carbamate and *N*-methylcarbamate were examined while terminal 5′ amino groups were blocked with monomethoxytrityl (mmT) and trityl (Ph_3C) groups, respectively. Structural groups corresponding to dA, dG, dT, and dC represent the carbamate analogues to mononucleotides. Phosphodiester oligonucleotides d(pCGCG), $d(pT)_6$, $d(pT)_8$, and $d(pT)_{10}$ were obtained from Sigma Chemical and were used without further purification; d(ACGT), d(AGCT), $d(T)_6$, d(CCGTGG), $d(T)_7$, and $d(T)_8$ were synthesized in-house by fol-

0003-2700/89/0361-2154$01.50/0 © 1989 American Chemical Society

lowing established phosphoramidite procedures (*18*).

dA^{BZ}

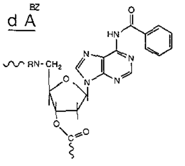

dG^{PA}

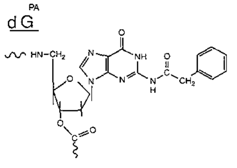

dT

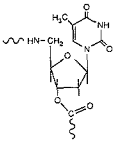

dC^{BZ}

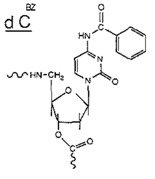

MoC^{BZ}

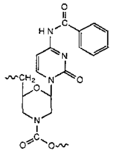

MoU

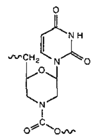

Mass Spectrometry. Negative ion mass spectra were obtained on a KRATOS MS 50 RF with an inhomogeneous magnetic field capable of scanning to m/z 10 000 at 8 keV. Mass resolution, ca. 2000–4000, was maintained to properly resolve the molecular ion cluster of each sample. Data were acquired by a Data General Box 30 minicomputer as uncentroided peak profiles using DS90 software. At least 20 scans were accumulated over a mass range of 200 amu, so that the summed spectra possessed a signal-to-noise ratio of greater than 40:1. This procedure was repeated on three separate occasions and reported as a grand average. The ion current at each integral mass in the spectrum was then obtained by integrating across the peak in order to measure the peak areas. The mass range surrounding the molecular anion region was examined before each sample run to assure freedom from background matrix interference. Mass calibration was achieved with CsI.

Three to ten nanomoles of oligonucleotide was introduced to the ion source on a copper probe tip of 21-mm² surface area. A thin layer of matrix (approximately 2 μL) was applied to the probe tip, and the solid samples were dissolved in this layer prior to analysis. The ammonium salts of the phosphodiester oligonucleotides were first dissolved in distilled water (2 μL) and then applied to the probe tip. The probe tip was cleaned abrasively with a fiberglass pencil followed by an acetone wash. A 7-keV neutral xenon beam sputtered the samples, and the desorbed anions were accelerated to −8 keV and detected by a +28-keV postacceleration detector.

Matrices were obtained from commercial suppliers, usually Aldrich Chemical, with quoted purities of 98% or higher. Glycerol-d_3 (Aldrich Chemical) was 98 atom % deuterium with a D_2O plus H_2O content of no greater than 1.5%. Glycer-d_5-ol (MSD Isotopes) with all methylene backbone hydrogen replaced with deuterium was 97.7 atom % deuterium. These matrices were handled and stored under a nitrogen blanket. Mixed matrices of glycerol–α-thioglycerol (1:1) or dithiothreitol–dithioerythritol (1:3) were also used.

Molecular Orbital Calculations. The published Modified Neglect of Diatomic Overlap (MNDO) method was used to obtain the orbital energies of molecules in their optimum geometric conformation. Equilibrium conformations were located with full optimization of *all* geometric variables. These calculations assume there is no reorganization of the other $N + 1$ electrons upon ionization of the molecule (Koopmans' theorem). The computation hardware and software has been previously described (*19*, *20*). An orbital restriction of up to 75 minimal base functions did not allow us to directly perform the calculations for the complete dimers and tetramers. Truncated oligonucleotide analogues were used in the calculations, viz. 2′-deoxyribose-5′-*O*-methylcarbamate, and 2′-deoxyribose-5′-*N*,*O*-dimethylcarbamate. The nucleic acids dA and dT were approximated as 9-*N*-methyladenine and 1-*N*-methylthymine.

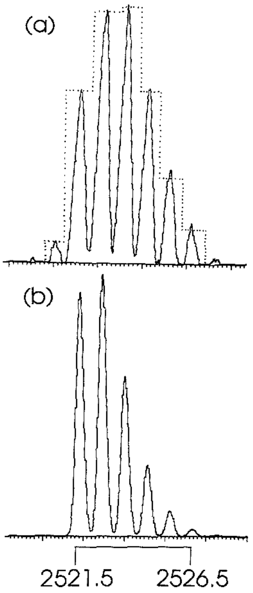

Figure 1. Molecular ion region of oligodeoxynucleotide $d(pA)_8$, as (a) measured experimentally and (b) calculated for the $(M - H)^-$ cluster. The histogram (dotted line) in part a is the theoretical fit using $(M - 2H)^{\bullet-}$, $(M - H)^-$, $M^{\bullet-}$, and $(M + H)^-$ ion abundances from the deconvolution procedure (Figure 2).

RESULTS AND DISCUSSION

Composition of Molecular Ion Cluster Region. A comparison of experimental (Figure 1a) and calculated (Figure 1b) isotopic cluster patterns for the $(M - H)^-$ ion of the oligodeoxynucleotide, $d(pA)_8$ shows poor agreement and indicates there are other ionic species present in the molecular ion region. Extensive one-electron reduction giving the $M^{\bullet-}$ radical anion is indicated by the shift in the center of the isotopic pattern to higher mass. However, inclusion of the contribution from $M^{\bullet-}$ alone in varying relative proportions to the $(M - H)^-$ ion in a theoretical treatment was not sufficient to reproduce the experimental data. If contributions from $(M - 2H)^{\bullet-}$ and $(M + H)^-$ are included, a theoretical molecular ion isotopic cluster pattern as described below can be synthesized that closely matches the experimental results (Figure 1a).

The isotopic clusters of each ionic species have to a first approximation the same pattern, but each is shifted by an integral mass unit (Figure 2a). When these clusters are superimposed with the correct relative contributions of each ion, the predicted cluster pattern in the molecular ion region should be a close match to the experimental data (Figure 2b). The solution of a set of four simultaneous equations using partial pivoting yields the relative contributions of each of the four ionic species (X_1, X_2, ...) (in-house algorithm for HP-41CX hand-held computer, available upon request). The first four experimental peak intensities of the cluster are treated as constants (B_1, B_2, ...), and the theoretically derived

Table I. Deconvolution, Using a Set of Four Simultaneous Equations (Figure 2), of Molecular Ion Cluster Region Data from LSIMS Analysis of Oligodeoxynucleotides

		computed relative abundance					
oligodeoxynucleotide	mass[a]	$(M-2H)^{\bullet-}$	$(M-H)^-$	$M^{\bullet-}$	$(M+H)^-$	$(M+2H)^{\bullet-}$ or $(M+D)^-$	% δ[c]
d(ACGT)	1171.2	1.8	92.7	2.1	3.4	–[d]	3
d(AGCT)	1171.2	3.1	92.3	1.6	3.0	–	3
$d(T)_6$	1760.3	14.6	60.5	17.2	7.7	–	2
d(CCGTGG)	1805.3	16.4	57.0	14.4	12.2	–	4
$d(T)_7$	2064.4	17.2	58.9	16.2	7.7	–	9
$d(T)_8$	2368.4	19.2	49.8	18.7	12.3	–	6
d(pCGCG)	1252.2	3.0	94.0	1.0	2.0	–	5
$d(pT)_6$	1840.3	16.1	51.3	18.9	10.8	2.9	3
$d(pT)_6$[b]	1840.3	16.6	36.8	25.6	12.7	8.3	5
$d(pT)_8$	2448.4	16.6	57.0	14.1	12.3	–	15
$d(pA)_8$	2520.5	7.6	48.4	24.3	19.7	–	8
$d(pT)_{10}$	3056.5	30.3	34.5	24.5	10.7	–	4

[a] First $(M-2H)^{\bullet-}$ peak in ion cluster. [b] Glycer-d_5-ol matrix. [c] Average relative fluctuation of data about the model. [d] Not computed.

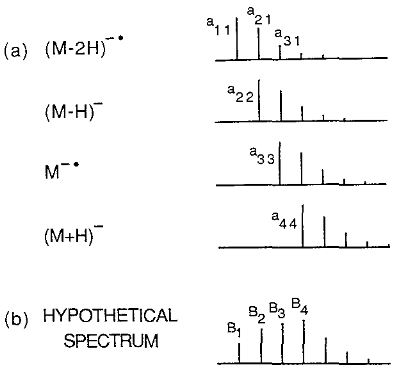

(c)

$$a_{11}X_1 + a_{12}X_2 + a_{13}X_3 + a_{14}X_4 = B_1$$
$$a_{21}X_1 + a_{22}X_2 + a_{23}X_3 + a_{24}X_4 = B_2$$
$$a_{31}X_1 + a_{32}X_2 + a_{33}X_3 + a_{34}X_4 = B_3$$
$$a_{41}X_1 + a_{42}X_2 + a_{43}X_3 + a_{44}X_4 = B_4$$

Figure 2. (a) Exact isotope clusters for $(M-2H)^{\bullet-}$, $(M-H)^-$, $M^{\bullet-}$, and $(M+H)^-$ of $d(pT)_6$ and (b) resultant hypothetical molecular ion region cluster. (c) Matrix used to solve for relative contributions X_1, X_2, ... of $(M-2H)^{\bullet-}$, $(M-H)^-$, ..., respectively, where coefficients $a_{ii}...a_{jj}$ are theoretical intensities and constants B_1, B_2, ... are the first four experimental peak relative intensities.

intensities of peaks in the cluster of each ionic species as coefficients ($a_{ii}\ldots a_{jj}$). The set of simultaneous equations may be written as shown (Figure 2c). Thus, $a_{11}X_1$, $a_{21}X_1$, $a_{31}X_1$, and $a_{41}X_1$ are all terms associated with the $(M-2H)^{\bullet-}$ ion series, and likewise coefficient a_{22} is the first peak in the isotopic cluster of the $(M-H)^-$ distribution. The equations for deconvoluting the molecular ion isotope cluster for $d(pA)_8$, assuming the presence of four ionic species (Figure 1a), are then (peak areas rather than peak heights are used)

$$(M-2H)^{\bullet-} \qquad 93.0X_1 = 8.2$$

$$(M-H)^- \qquad 100.0X_1 + 93.0X_2 = 66.2$$

$$M^{\bullet-} \qquad 61.1X_1 + 100.0X_2 + 93.0X_3 = 98.9$$

$$(M+H)^-$$
$$27.1X_1 + 61.1X_2 + 100.0X_3 + 93.0X_4 = 100.0$$

where the numerical coefficients are the isotopic distributions of ^{12}C, ^{13}C, ^{1}H, ^{2}H, ^{16}O, ^{17}O, ^{18}O, ^{14}N, and ^{15}N from Figure 1b.

This procedure yields the relative contributions of each of the four ionic species for $d(pA)_8$ (Table I). Synthesis of the molecular ion cluster pattern using values X_1, X_2, ... yields a theoretical pattern that matches the observed spectrum almost exactly (Figure 1a histogram) (in-house algorithm for HP-41CX hand-held computer). This visual agreement was confirmed via a chi-square evaluation; since $\chi^2_{\text{expt}} << \chi^2_{0.05}$, the fit of the data to the theoretical distribution is excellent. For all of the compounds analyzed, the average relative error of the model about the data is in no case greater than 15% and typically is 3%.

There are other computational methods that can be used to solve for the ion abundances, including a polynomial fit and a minimized chi-squared method. The latter has been used successfully, but the computational time was greater and it sometimes failed to converge to a solution by going into oscillation.

Reactions of $M^{\bullet-}$. It is assumed that sample molecules with low-lying LUMOs capture low-energy (0–3 eV) ionizing electrons generated by high-energy particle bombardment of the liquid matrix (*7*). The resultant radical anions, $M^{\bullet-}$, depending on their relative stabilities, can (a) survive long enough to be detected, (b) fragment to give product ions, or (c) react bimolecularly to give other molecular ion region product ions. Thus, ionic species $(M+H)^-$ would be the reaction product of radical anion ($M^{\bullet-}$) with the matrix (eq 1) or with matrix-derived hydrogen atoms (*14*, *16*) (eq 2). Studies in deuterated glycerol were carried out to show this.

$$M^{\bullet-} + RH \rightarrow (M+H)^- + R\cdot \qquad (1)$$

$$M^{\bullet-} + H\cdot \rightarrow (M+H)^-$$

or (2)

$$M^{\bullet-} + D\cdot \rightarrow (M+D)^-$$

Molecular ion region spectra of $d(pT)_6$ in glycerol-d_3, which has deuterium on the oxygen atoms, showed extensive deuterium incorporation largely from equilibrium exchange of the protons. The cluster envelope covers a range of 14 amu, and it was impossible to distinguish deuterium incorporated by proton exchange from that incorporated by atom transfer. Notwithstanding, deuterium located on the carbon backbone of glycer-d_5-ol was expected to undergo predominantly atom transfer. A comparison of the molecular ion region profiles of $d(pT)_6$ in glycerol (Figure 3A) and in glycer-d_5-ol (Figure 3B) shows the center of mass has been shifted slightly to higher mass. No partial deuteration on the oxygens was evident, since an identical spectrum was recorded with the use of glycer-d_5-ol that underwent five water wash/lyophilize cycles. Deconvolution of these regions using a five-by-five

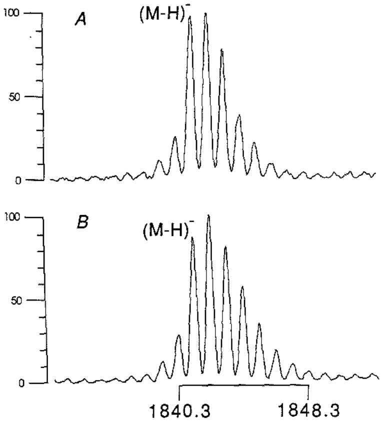

Figure 3. Molecular anion region of d(pT)$_6$ desorbed from (A) glycerol and (B) glycer-d_5-ol.

matrix gives 8.3 ± 1.5% (2σ confidence level) relative abundance of (M + 2)$^-$ ion in glycer-d_5-ol and 10.8 ± 1.2% (2σ confidence level) (M + 1)$^-$ ion abundance in glycerol (Table I). These numbers are similar and support the proposed mechanism (eq 2). There may be other reactions occurring, however, which would account for the isotopic cluster shift to higher mass when glycer-d_5-ol is used as a matrix. A disproportionation reaction between M$^{\bullet -}$ and (M − H)$^-$ would lead to both (M + H)$^-$ and (M − 2H)$^{\bullet -}$. Although two negatively charged species would be expected to approach and react with each other only with difficulty, this should be entirely feasible as the molecular size of the reacting species increases, since the charges may be located distal to the interaction site. In either case, i.e., the reaction of M$^{\bullet -}$ with the matrix (eq 1 and 2) or disproportionation, the intensities of (M + H)$^-$ and (M − 2H)$^{\bullet -}$ should increase with increasing intensity of M$^{\bullet -}$ (Table I). Alternatively, the (M − H)$^-$ ion could react with some other radical (R·) and produce (M − 2H)$^{\bullet -}$. The difficulty with this reaction, however, is that the concentrations of reacting species may be too low for the reaction to be of significance. Finally, simple hydrogen atom loss from an (M − H)$^-$ precursor may be the facile mechanism responsible for (M − 2H)$^{\bullet -}$ production, as is the case with positive ion mass spectra.

Oligodeoxynucleotides. A series of oligodeoxynucleotides ranging in length from tetramers to 10-mers were analyzed by negative ion LSIMS. By use of the deconvolution procedure, the relative contribution of M$^{\bullet -}$ radical anion was found to increase at the expense of the (M − H)$^-$ anion with increasing size of oligodeoxynucleotide (Table I, Figure 4). Benchmark experiments showed there was no systematic discrimination toward higher masses by the instrument in either the positive or negative ion mode. Thus, the experimental and calculated isotopic cluster patterns for the (M − H)$^-$ of β-cyclodextrin (MW 1133.4) and bovine insulin oxidized B-chain (MW 3492.6), and for (RbI)$_n$I$^-$ (n = 6, 11, 17), were almost identical (to within ±1%).

A possible explanation for increasing M$^{\bullet -}$ concentration with chain length is that base stacking in the solution causes overlap of the π orbitals of the bases; this, in turn, lowers the energy levels of the LUMOs, making the oligomer more accessible to the low-energy ionizing electrons. A similar explanation has been used to account for the significantly lower molar absorbance and the shift in λ_{max} to shorter wavelengths in the absorption spectrum of poly A relative to adenosine monophosphate (*21*). It is suggested that base stacking results in splitting of electronic states, creating an exciton band that has both higher and lower energy levels.

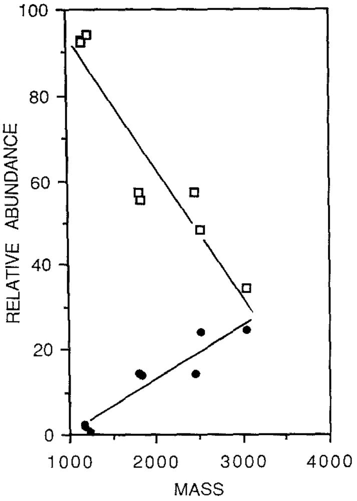

Figure 4. Relative experimental ion abundances of (M − H)$^-$ (□) and M$^{\bullet -}$ (●) from deconvolution of spectral data versus molecular weight of oligodeoxynucleotides.

Carbamate-Linked Oligonucleosides. Dimers and tetramers of carbamate-linked oligonucleosides (*17, 22*) analyzed by negative ion LSIMS show (M − 2H)$^{\bullet -}$, (M − H)$^-$, M$^{\bullet -}$, and (M + H)$^-$ species in the molecular ion cluster region (Table II). A comparison between compounds **2** and **4**, and **3**, and **5**, shows the relative intensity of M$^{\bullet -}$ increases as the length of oligomer increases from dimers to tetramers, the same trend as that observed for oligodeoxynucleotides. The dimer with adenine also shows more M$^{\bullet -}$ than the dimer with thymidine. This is expected because the manifolds of vacant orbitals for adenine are more dense and of lower energy compared to those of thymidine over the same energy range, ca. −0.5 to 4 eV, according to calculations by the MNDO method. It is also observed that the carbamates **3** and **5** show greater electron capture than the corresponding N-methylcarbamates. This is consistent with the lower LUMO energy calculated for secondary amides as opposed to that for tertiary amides, viz. 1.17 versus 1.45 eV, respectively.

Matrix Characteristics. Assuming one-electron reduction, the competition between matrix and sample molecules for the electron becomes relevant. The relative electron affinities (EA) would have to be known in order to evaluate this competition, but electron affinity measurements have not been made for common LSIMS matrices. It has been shown, however, that experimental electron affinities can be correlated with ϵ_{LUMO} (*23*). With use of the MNDO method the LUMO energies were computed for a series of conjugated hydrocarbons, heterocycles, and aliphatic compounds whose electron affinities had been reported. The correlation is excellent (Figure 5), and a least-squares regression analysis gives

$$EA = -1.17\epsilon_{LUMO} - 0.515 \text{ eV} \qquad (3)$$

with a correlation coefficient of 0.98. This method does not take into account the change in correlation energies upon ionization or reorganization energies. From this correlation, however, electron affinities were estimated for common matrix compounds whose LUMO energies had been calculated. A more sophisticated calculation was performed to determine the influence of the captured electron on the orbital energy manifold. The difference in total energies, obtained from

Table II. Deconvolution of Experimental Data of Carbamate-Linked Oligonucleosides[a] into Four Ionic Distributions Using a Set of Four Simultaneous Equations (Figure 2)

no.	oligonucleoside[b]	$(M - 2H)^{\bullet -}$	$(M - H)^-$	$M^{\bullet -}$	$(M + H)^-$	δ %[c]
1	$^{5'}Ph_3CN(CH_3)T\text{-}T\text{-}OH^{3'}$	3.50	92.97	0.38	3.16	1
2	$Ph_3CN(CH_3)A^{Bz}A^{Bz}\text{-}OH$	1.93	93.69	1.14	3.24	6
3	mmT $N(H)A^{Bz}A^{Bz}\text{-}OH$	2.27	86.85	7.92	2.96	5
4	$Ph_3CN(CH_3)A^{Bz}A^{Bz}A^{Bz}A^{Bz}\text{-}OH$	5.64	69.75	15.55	9.06	7
5	mmT $N(H)A^{Bz}A^{Bz}A^{Bz}A^{Bz}\text{-}OH$	6.50	61.07	26.03	6.40	8

[a] Representative structure shown below; see ref 22 for dimer through 11-mer structures. [b] mmT = monomethoxytrityl; Ph_3C = trityl. [c] Average relative fluctuation of data about the model.

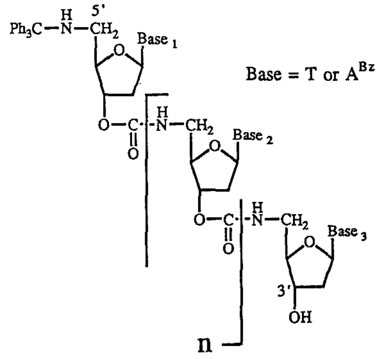

carbamate-linked oligonucleoside

independent MNDO calculations on the ground states, of the neutral and anion was found to correlate with experimental electron affinities as

$$EA = -1.16(\Delta TE\ (\text{anion} - \text{neutral})) - 1.06$$

The oligodeoxynucleotide $d(pT)_6$ was used as a probe to determine the competition for the low-energy electrons between sample and matrix. A plot of the sum of the reduction products, [$M^{\bullet -}$ and $(M + H)^-$] (Figure 6), versus electron affinities of the matrices shows a relationship which suggests that the greater the electron affinity of the matrix, the more likely it is to scavenge electrons and make them unavailable for capture by $d(pT)_6$.

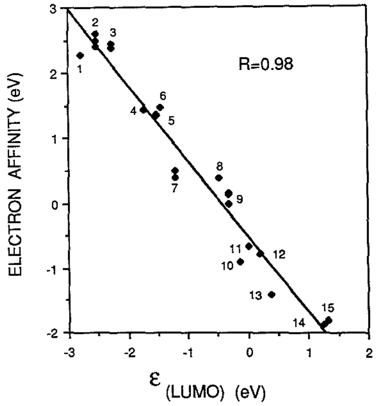

Figure 5. Experimental electron affinities versus ϵ_{LUMO} calculated by MNDO method (*19*, *20*): (1) tetrafluoro-1,4-benzoquinone (*24*); (2) tetrachloro-1,4-benzoquinone (*24*–*26*); (3) chlorine (*27*, *28*); (4) *m*-dinitrobenzene (*26*); (5) *p*-benzoquinone (*24*, *25*); (6) hexachloroethane (*24*, *29*); (7) nitrobenzene (*30*, *31*); (8) biacetyl (*31*); (9) naphthalene (*32*, *33*); (10) chlorobenzene (*34*, *35*); (11) pyridine (*23*); (12) biphenyl (*36*); (13) benzene (*35*); (14) pyrrole (*23*); (15) ethylene (*24*).

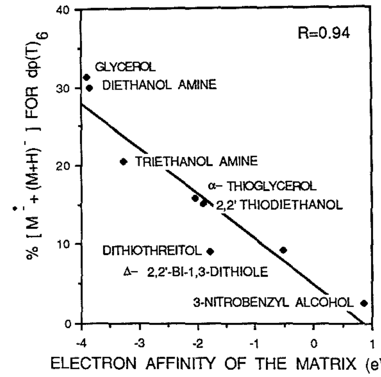

Figure 6. One-electron reduction dependence in the probe oligodeoxynucleotide $d(pT)_6$ as a function of interpolated electron affinity (eq 3) of the matrix.

It has been proposed that thiol groups act as radical scavengers and effectively reduce the hydrogen atoms available in the matrix (*6*). This may be a reason for the significant departure of dithiothreitol from the relationship (Figure 6).

Morpholine-Linked Nucleosides. Since the electron affinity of the matrix can be correlated with the amount of electron reduction observed, the effect of different matrices on a sample molecule expected to have a high electron affinity was of interest. The morpholine-linked nucleic acid analogue **6** was analyzed by LSIMS in 2:1 thioglycerol–glycerol, 3-nitrobenzyl alcohol (3-NBA), 2,2′-thiodiethanol, and sulfolane. The relative abundances of the ionic species are reasonably similar in each of the first three matrices, particularly if the sum of the reduction products is considered (Table III). These results indicate that the nucleic acid analogue, **6**, is highly competitive at capturing electrons and that it must have an electron affinity equal to or greater than 0.87 eV, i.e. the electron affinity of 3-NBA. In sulfolane the degree of reduced ion species is even greater, which at first would suggest that sulfolane has an electron affinity very much lower than that

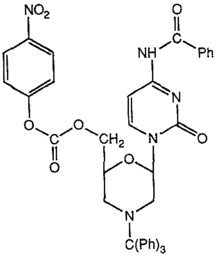

6

Table III. Relative Abundances of Ionic Species for Nucleic Acid Analogue 6 in Different Matrices from Deconvoluted LSIMS Data

	computed relative abundance				
ionic species	2:1 thioglycerol–glycerol	3-nitrobenzyl alcohol	2,2′-thiodiethanol	tetramethylene sulfone	tetramethylene-d_8 sulfone
$(M - 2H)^{\bullet-}$	1.35	1.02	1.54	1.3	1.2
$(M - H)^-$	53.59	52.19	56.00	43.4	35.5
$M^{\bullet-}$	42.04	46.79	39.89	50.3	47.0
$(M + H)^-$	3.02	0	2.57	4.1	11.5
$\Sigma_{(red)}$	45.1	46.8	42.5	54.4	58.5
$(M + 2H)^{\bullet-}$ or $(M + D)^-$	–	–	–	0.9	4.8
% δ^a	2	2	4	1	4

[a] Average relative fluctuation of data about the model.

Table IV. Deconvoluted Molecular Ion Cluster Profiles from LSIMS Analyses of Morpholine-Linked Nucleic Acid Oligomers

		rel abundances obtained with 2:1 thioglycerol–glycerol matrix					rel abundances obtained with 3-nitrobenzyl alcohol matrix				
no.	nucleic acid oligomer	$(M - 2H)^{\bullet-}$	$(M - H)^-$	$M^{\bullet-}$	$(M + H)^-$	% δ^a	$(M - 2H)^{\bullet-}$	$(M - H)^-$	$M^{\bullet-}$	$(M + H)^-$	% δ^a
7	6′HO-MoC^{Bz}-Tr4′	0.3	68.3	28.3	3.1	3	–	–	–	–	–
8	6′HO-MoC^{Bz}MoC^{Bz}-Tr4′	1.6	77.0	15.7	5.7	1	–	–	–	–	–
9	6′HO-MoC^{Bz}MoC^{Bz}MoC^{Bz}MoC^{Bz}-Tr4′	2.3	63.1	22.5	12.1	2	6.5	90.4	1.7	1.4	3
10	6′HO-MoC^{Bz}MoC^{Bz}MoC^{Bz}MoC^{Bz}-MoC^{Bz}MoC^{Bz}-Tr4′	0.0	49.7	50.3	0.0	6	15.3	79.9	4.8	0.0	5
11	6′HO-MoU-DPM4′	6.2	88.8	0.6	4.4	4	3.0	95.7	0.0	1.3	11
12	6′(Mo)(CH$_3$)PO$_2$-MoU-DPM4′	4.2	91.6	0.0	4.2	1	–	–	–	–	–
13	6′H$_2$N-N(CH$_3$)-C(O)O-MoC^{Bz}-Tr4′	5.1	72.8	18.9	3.2	14	7.1	86.8	5.4	0.7	10

[a] Average relative fluctuation of the data about the model.

of the other three matrices, ca. 2.1 eV. But, as has been observed recently (*37*), the mechanism associated with $M^{\bullet-}$ formation may involve the decomposition of sulfolane to sulfur dioxide radical anion followed by electron transfer to nucleic acid 6 to give the ion. The electron affinity of sulfur dioxide is 1.1 e*V*, which suggests that the EA of 6 is even greater. In sulfolane-d_8 as a matrix, the pattern of deuterium atom transfer is similar to that observed for d(pT)$_6$ (Table I).

The fragmentation of **6** also is revealing. The molecular ion region with *m/z* 736.2 for the $(M - H)^-$ shows the large contribution from the other ions (Figure 7). The alkoxide fragment ion cluster with *m/z* 571.2 is described exactly by the isotopic contribution, and no other ions except the alkoxide anion are present. The $M^{\bullet-}$ may be the precursor to the alkoxide ion. To test this possibility, a matrix would be required that competes effectively for the electrons and prevents formation of $M^{\bullet-}$.

A series of morpholine-linked nucleic acid monomers and oligomers was analyzed by negative LSIMS, and the molecular ion cluster profiles were deconvoluted (Table IV). Homopolymers **8–10** show increasing $M^{\bullet-}$ and decreasing $(M - H)^-$ with increasing chain length as expected, and accordingly, in 3-NBA the relative intensities of reduction products are reduced. Except for the fact that nucleic acid analogue **6** shows an $M^{\bullet-}$ concentration that deviates from this trend, these results conform to those observed for oligodeoxynucleotides and carbamate-linked oligonucleosides. The series **11–13** is of some interest. The $M^{\bullet-}$ abundance for **11** and **12** is small, but for **13** it is significant. The benzoate group extends the π orbital system, which probably lowers the LUMO energy and increases the electron affinity. Nucleic acid analogue **6** has this extended π system as well as the nitrobenzyl group, which may explain why it is so competitive at absorbing ionizing electrons.

CONCLUSIONS

This investigation has shown that the relative contributions of suspected ionic species generated from sample molecules being analyzed by LSIMS may be determined by deconvoluting the molecular ion region cluster. The results have implications for LSIMS analyses of large organic or biological macromolecules. When isotopic patterns are used to either confirm empirical formulas or determine isotopic enrichment, careful considerations must be given to the ions present. The presence of species formed via one-electron reduction, [$M^{\bullet-}$ and $(M + nH)^-$] for example, will shift the center of the envelope cluster to higher mass. Deconvolution of the molecular ion cluster can be used to estimate the relative intensities of ions present. It has also been shown that the electron affinities of the matrices have a significant effect on the molecular ion cluster profiles of sample molecules being analyzed by negative LSIMS.

The $M^{\bullet-}$ may undergo fragmentation (*7*). Sequence ions of oligodeoxynucleotides, for example, could be fragmentation products from the $M^{\bullet-}$. Likewise, ion series of carbamate-linked nucleosides are easily explained as fragment ions of the $M^{\bullet-}$. In fact, the difficulty in trying to account for the

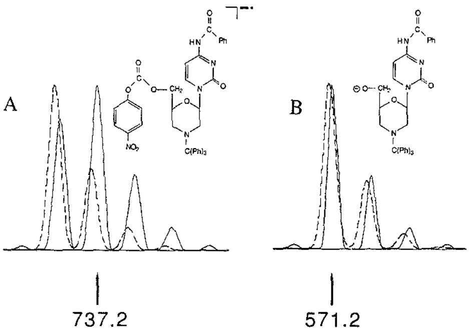

Figure 7. Partial spectrum of morpholine-linked mononucleoside **6** showing experimental clusters (solid line) and calculated isotopic distribution (hatched line, offset for clarity): (A) molecular anion region and (B) fragment anion.

5′ ion series in spectra of carbamate-linked nucleosides prompted this investigation (*22*). Unfortunately, B/E linked scan analysis using a two-sector double-focusing mass spectrometer does not provide answers to these questions because of its poor precursor ion resolution. A four-sector tandem instrument with high parent ion selectivity would provide some additional information, but this instrument was not available for this work.

ACKNOWLEDGMENT

We thank T. Fleischmann and R. McParland for preparation of oligodeoxynucleotides. We also thank T. L. Laramée for photographing the spectra and S. Lindsay for processing the manuscript.

LITERATURE CITED

(1) Barber, M.; Bordoli, R. S.; Sedgewick, R. D.; Tyler, A. N. *J. Chem. Soc., Chem. Commun.* **1981**, 325–327.
(2) Williams, D.; Bradley, C.; Bojesen, C.; Santikharn, S. *J. Am. Chem. Soc.* **1981**, *103*, 5700–5704.
(3) Brereton, R. G.; Bazzar, M. B.; Santikharn, S.; Williams, D. *Tetrahedron Lett.* **1983**, *24*, 5775–5778.
(4) Clayton, E.; Wakefield, A. J. C. *J. Chem. Soc., Chem. Commun.* **1984**, 969–970.
(5) Cerny, R. L.; Gross, M. L. *Anal. Chem.* **1985**, *57*, 1160–1163.
(6) Musselman, B. D.; Watson, J. T. *Biomed. Environ. Mass Spectrom.* **1987**, *14*, 247–248.
(7) Williams, D. H.; Findeis, A. F.; Naylor, S.; Gibson, B. W. *J. Am. Chem. Soc.* **1987**, *109*, 1980–1986.
(8) Fenselau, C. *J. Nat. Prod.* **1984**, *47*, 215–225.
(9) Pelzer, G.; De Pauw, E.; Dung, D. V.; Marien, J. *J. Phys. Chem.* **1984**, *88*, 5065–5068.
(10) Callahan, J. H.; Hool, K.; Reynolds, J. D.; Cook, K. D. *Anal. Chem.* **1988**, *60*, 714–719.
(11) Dass, C.; Seshadri, R.; Israel, M.; Desiderio, D. M. *Biomed. Environ. Mass Spectrom.* **1988**, *17*, 37–45.
(12) Main, D. E.; Ens, W.; Beavis, R.; Schueler, B.; Standing, K. G.; Westmore, J. B.; Wong, C. *Biomed. Environ. Mass Spectrom.* **1987**, *14*, 91–96.
(13) Didonato, G. C.; Busch, K. L. *Anal. Chim. Acta* **1985**, *171*, 233–239.
(14) Field, F. H. *J. Phys. Chem.* **1982**, *86*, 5115–5123.
(15) Keough, T. *Int. J. Mass Spectrom. Ion Processes* **1988**, *86*, 155–168.
(16) Ligon, W. V. *Int. J. Mass Spectrom. Ion Phys.* **1983**, *52*, 189–193.
(17) Stirchak, E. P.; Summerton, J. E.; Weller, D. D. *J. Org. Chem.* **1987**, 4202–4206.
(18) Matteucci, M. D.; Caruthers, M. H. *J. Am. Chem. Soc.* **1981**, *103*, 3185.
(19) Laramée, J. A.; Arbogast, B. C.; Deinzer, M. L. *Anal. Chem.* **1988**, *60*, 1937–1943.
(20) Laramée, J. A.; Chang, Y-S.; Arbogast, B. C.; Deinzer, M. L. *Biomed. Environ. Mass Spectrom.* **1988**, *17*, 63–67.
(21) Van Holde, K. E. *Physical Biochemistry*; Prentice Hall: Edgewood Cliffs, NJ, 1985; p 192.
(22) Griffin, D.; Laramée, J.; Deinzer, M.; Stirchak, E.; Weller, D. *Biomed. Environ. Mass Spectrom.* **1988**, *17*, 105–111.
(23) Kunii, T.; Kuroda, H. *Theoret. Chim. Acta* **1968**, *11*, 97–106.
(24) Page, F. M.; Goode, G. C. *Negative Ions and the Magnetron*; Wiley-Interscience: London, 1969.
(25) Farragher, A. L.; Page, F. M. *Trans. Faraday Soc.* **1966**, *62*, 3072–3080.
(26) Bately, M.; Lyons, L. E. *Nature* **1962**, *196*, 573–574.
(27) Chupka, W. A.; Berkowitz, J.; Gutman, D. *J. Chem. Phys.* **1971**, *55*, 2724–2733.
(28) Baede, A. P. M. *Physica* **1972**, *59*, 541–544.
(29) Gaines, A. F.; Kay, J.; Page, F. M. *Trans. Faraday Soc.* **1966**, *62*, 874–876.
(30) Compton, R. N.; Christophorou, L. G.; Hurst, G. S.; Reinhardt, P. W. *J. Chem. Phys.* **1966**, *45*, 4634–4639.
(31) Chaney, E. L.; Christophorou, L. G.; Collins, P. M.; Carter, J. G. *J. Chem. Phys.* **1970**, *52*, 4413–4417.
(32) Becker, R. S.; Chen, E. *J. Chem. Phys.* **1966**, *45*, 2403–2410.
(33) Briegleb, G. *Angew. Chem. Int. Ed. Engl.* **1964**, *3*, 617–632.
(34) Wentworth, W. E.; Chen, E.; Lovelock, J. E. *J. Chem. Phys.* **1966**, *70*, 445–458.
(35) Naff, W. T.; Compton, R. N.; Cooper, C. D. *J. Chem. Phys.* **1971**, 212–222.
(36) Hedges, R. M.; Matsen, F. A. *J. Chem. Phys.* **1958**, *28*, 950–953.
(37) Lloyd, J. R.; Cotter, M. L. *Biomed. Environ. Mass Spectrom.* **1986**, *13*, 447.

RECEIVED for review May 18, 1989. Accepted June 23, 1989. This work is supported by the National Institutes of Health (NIEHS ES00210, NIEHS 03874, and NIHGM 36030). This is publication no. 8639 from the Oregon Agricultural Experiment Station.

Pyruvate Carboxylase as a Model for Oligosubstituted Enzyme–Ligand Conjugates in Homogeneous Enzyme Immunoassays

Sylvia Daunert, Bryan R. Payne, and Leonidas G. Bachas*

Department of Chemistry, University of Kentucky, Lexington, Kentucky 40506-0055

Theoretical models suggest that the detection capabilities of homogeneous enzyme immunoassays can be improved by the use of oligosubstituted enzyme–ligand conjugates rather than the traditionally used multisubstituted ones. The natural form of pyruvate carboxylase contains four covalently bound biotins (one per subunit) and it can be considered as an oligosubstituted enzyme–biotin conjugate. The enzyme is nearly completely inhibited in the presence of the natural binder for biotin, avidin. When the enzyme is incubated with avidin and free biotin, a competition occurs between the free biotin and the prosthetic group of the enzyme for the avidin. Steep dose–response curves are obtained by relating the observed inhibition to the free biotin concentration. By variation of the amount of avidin or enzyme in the assay, the detection limits of the system can be altered allowing for sensitive determinations over a wide range of biotin concentrations. Such data from real sample analysis of several vitamin supplements are reported.

INTRODUCTION

Homogeneous enzyme immunoassays of the EMIT type have emerged as one of the methods of choice when fast, simple, and selective analytical techniques are being sought (*1, 2*). In these assays the binding of the ligand-specific binder to the enzyme-labeled ligand (conjugate) modifies the enzymatic activity. This modification is caused either by sterically hindering the active site of the enzyme or by inducing a conformational change within the enzyme molecule (*3*). Unlabeled ligand reduces the binder-induced modulation of the enzymatic activity by competing for the specific binder, leaving the enzyme-labeled ligand free to react with the substrate(s). Presently, there are certain inherent limitations to these techniques that can diminish the assay performance and limit their potential usefulness. Indeed, two main problems that now exist in these assays are antibody recognition of the bridging group, which covalently links the ligand to the enzyme label, and use of enzyme–ligand conjugates with

0003-2700/89/0361-2160$01.50/0 © 1989 American Chemical Society

more than one ligand attached per enzyme molecule (i.e., multisubstituted conjugates) (*4*).

Although the problem of bridging group recognition is well characterized and several approaches have been proposed to overcome it (*5–8*), the use of multisubstituted (multivalent) enzyme–ligand conjugates has drawn limited or no attention. We believe that the latter problem is of equal or greater importance than the former in obtaining dose-response curves with better detection limits and higher sensitivity. Indeed, the bridging group recognition problem is limited only to cases where the antibody recognizes this bridging group, whereas the multivalency of the enzyme–ligand conjugate will affect the assay characteristics independent on what type of binder is being used.

In this report, we explore the possibility of using oligosubstituted rather than multisubstituted enzyme–ligand conjugates in the development of enzyme-linked homogeneous competitive binding assays. Pyruvate carboxylase (EC 6.4.1.1), an enzyme that in its natural form possesses biotin as a covalently attached prosthetic group (*9*), is being used as a model system in this study. Since there is only one biotin molecule coupled per subunit, the enzyme can be considered as an oligosubstituted enzyme–ligand conjugate. Avidin is a slow binding inhibitor of pyruvate carboxylase (*10*) and this property has been used for the development of an enzyme modulator mediated immunoassay for 5,5-diphenylhydantoin (*11*). Since biological binders should have lower affinities for oligosubstituted conjugates than for multisubstituted ones, theoretically an improvement in detection limits could be achieved without any loss in selectivity.

EXPERIMENTAL SECTION

Reagents. Baker's yeast (type II), malate dehydrogenase (from bovine heart), glucose-6-phosphate dehydrogenase (G6PDH) (from *Leuconostoc mesenteroides*), D-biotin-*N*-hydroxysuccinimide, and all other materials used were obtained from Sigma (St. Louis, MO). The biotin and avidin standards were prepared in assay buffer (0.100 M Tris–sulfate, 0.10% (w/v) sodium azide, pH 7.8) containing 0.10% (w/v) gelatin.

Isolation of Pyruvate Carboxylase. Pyruvate carboxylase was isolated from baker's yeast (*Saccharomyces cerevisiae*) by the method described by Rohde et al. (*12*). Specifically, a suspension of 300 g of baker's yeast in lysis buffer (0.100 M Tris-acetate, 0.010 M $MgCl_2$, pH 7.2) was lysed in a Branson (Model 2200) sonicator for 12 min at 4 °C. The pH of the lysate was adjusted to 7.2 with 1.0 M Trizma base. After centrifugation (22000g, 30 min, Sorvall RC-5 Superspeed Refrigerated Centrifuge) the lipids were extracted three times with volumes of 1,1,2-trichlorotrifluoroethane equal to one-third of the volume of the supernatant. Nucleic acids were removed from the lipid-free solution with a protamine sulfate treatment and the proteins were precipitated with ammonium sulfate The proteins were then desalted with poly(ethylene glycol) 8000 and the protein solution was chromatographed on a DEAE-Sephacel column. A linear gradient from 0 to 0.20 M ammonium sulfate was used to elute the pyruvate carboxylase. The enzyme-containing fractions were pooled and dialyzed twice against assay buffer. The enzyme solution was kept at −15 °C with approximately 80% recovery of activity after storage; the enzyme was stable for extended periods of time at this temperature. A Lowry analysis (*13*) determined a protein concentration of 0.83 mg/mL in the stored solution (a Beckman Model 26 spectrophotometer was used for this analysis). It should be noted that an enzyme preparation from bovine liver is now commercially available from Sigma. This last enzyme was used to prepare the pyruvate carboxylase–biotin conjugate.

Enzyme Activity. Pyruvate carboxylase activity was determined spectrophotometrically with a SYVA S-III spectrophotometer (the temperature-controlled cuvette was thermostated at 30 °C) interfaced with a SYVA CP-5000 Plus clinical processor, using a modified version of the method of Young et al. (*14*). A mixed substrate solution (solution A) was prepared daily by combining 2.0 mL of 0.139 M $MgSO_4$, 4.0 mL of 0.0032 M NADH, and 4.0 mL of 0.200 M $NaHCO_3$. Similarly, solution B contained 5.0 mL of 0.100 M pyruvate, 10.0 mL of 0.0165 M ATP, and 10.0 mL of buffer (0.500 M Tris–sulfate, 0.10% (w/v) NaN_3, pH 7.8). Activities were determined by adding 500 μL of solution B, 250 μL of solution A, 100 μL of pyruvate carboxylase solution, 50 μL of malate dehydrogenase solution (100 units/mL), and sufficient additional assay buffer to bring the total volume to 1250 μL. The pyruvate carboxylase solution was kept in an ice bath at 4 °C prior to all measurements. The activity of the enzyme was determined by measuring the change in absorbance at 340 nm.

The activity of the enzyme from bovine liver was determined as suggested by Sigma.

Stability Studies. Stability studies of the enzyme were performed on solutions of pyruvate carboxylase stored at 22 and 4 °C. The activity of the samples was determined immediately after the solutions were removed from the deep freezer, and regularly afterward.

Association Study. The effect of the incubation time between pyruvate carboxylase and avidin on the enzymatic activity was determined. An amount of 2.0 μg of avidin and 1.6 milliunits of pyruvate carboxylase were incubated together in a total volume of 150 μL for periods of time ranging from 0 to 30 min. Five hundred microliters of solution B, 250 μL of solution A, 50 μL of malate dehydrogenase (100 units/mL), and assay buffer were then added to make a total volume of 1250 μL, and the activity was measured as described above.

Inhibition Studies. The avidin concentration in the assay was varied while holding enzyme concentration and incubation time constant. Pyruvate carboxylase (1.8 milliunits) was incubated for 15 min at room temperature with quantities of avidin ranging from 0 to 50 μg. After the incubation the substrates and buffer were added to a total volume of 1250 μL, and the activity was measured as described above.

Dose–Response Curves. Dose–response curves were prepared by using a single incubation method (*15*). Volumes of 50 μL each of avidin and varying concentrations of biotin standards were incubated for 15 min with 100 or 200 μL of enzyme solution. Enzyme activity was measured as described above. Dose–response curves were obtained by plotting the percent inhibition against the logarithm of the biotin concentration.

Analysis of Vitamin Preparations. Four vitamin preparations containing biotin (Bio-Genics, Stress B Complex; Parke-Davis, ABDEC; Thompson, Biotin; Perrigo, Biotin) were analyzed. Five tablets of each preparation were powdered and the equivalent of one tablet was weighed and shaken with 5.00 mL of 1.0 M NaOH. The solution was centrifuged for 10 min at 2400 rpm (IEC Centra-7R Model Centrifuge). Four milliliters of each supernatant was neutralized with HCl. Each was then diluted to a volume of 25.0 mL with assay buffer containing 0.10% gelatin. Appropriate dilutions of these solutions were prepared and analyzed as described above. ABDEC is sold in liquid form, and therefore dilutions were made directly from the product with the Tris–sulfate/gelatin buffer.

For the recovery studies either 500 or 250 μL of 1.00×10^{-4} M biotin standard were added to 1.00 mL of the ABDEC vitamin supplement increasing the amount of biotin present in the solution by 5.00 and 2.50 μmol, respectively. Biotin analysis was performed as described previously.

Preparation of the Pyruvate Carboxylase–Biotin Conjugate. The pyruvate carboxylase–biotin conjugate was prepared by reacting 12.5 units of the commercial enzyme with a 60-times excess of the biotin-*N*-hydroxysuccinimide ester (dissolved in methyl sulfoxide). The conjugation reaction was run for 45 min at 4 °C with stirring, while the active site of the enzyme was protected by adding an excess of sodium pyruvate and adenosine diphosphate compared to the amount of enzyme present (*7*). The conjugate was isolated by gel filtration on a Sephadex-15 column (1.5 cm × 40 cm). The assay buffer was used as the eluent. Fractions of 2.35 mL were collected (ISCO Fraction Collector Model 328 synchronized with an ISCO Model UA-5 Absorbance Monitor) and the ones that contained the enzyme (based on absorbance at 280 nm) were tested for activity.

G6PDH–Biotin Conjugates. Variably substituted G6PDH–biotin conjugates were prepared and characterized as described previously (*8*). Dose–response curves were obtained by incubating each conjugate with 36 ng of avidin and biotin standards. For experimental details see ref 8. The degree of conjugation was estimated from the concentration of enzyme-bound biotin. The latter was determined by the method of Green (*16*).

RESULTS AND DISCUSSION

It is common for the enzyme conjugates used in homogeneous EMIT-type of assays to be multivalent, which means that they have more than one ligand attached per enzyme molecule. Such multivalency is needed to assure inhibition of the enzymatic activity in the presence of the binder. Indeed, it has been observed that in the case of G6PDH–morphine conjugates the inhibition of the enzymatic activity by excess antibody increases linearly with increasing substitution (*17*) and reaches a plateau after 12 morphines have been attached per enzyme molecule.

A theoretical model assessing the effect of bridging group recognition and the degree of substitution of enzyme-ligand conjugates on the response characteristics of enzyme-linked competitive binding assays has been developed (*4*). This mass action model is dependent on internal parameters of the competitive binding system, such as the concentration of reagents, the association constants between the binder and the ligand (both labeled and unlabeled), etc. The model was used to describe heterogeneous enzyme immunoassays where a multisubstituted conjugate and a ligand are competing for a binder immobilized on a solid support (*4*). It should be noted that in this model the binder can associate with any of the ligands that are conjugated to the same enzyme, but once the binder binds one of these ligands, the other ligands become stereochemically restricted to such a binding and do not participate in any other equilibria. This theoretical model predicts that the use of multivalent conjugates in enzyme immunoassays will increase the ED_{50} value (i.e., the effective dose of unlabeled ligand that displaces 50% of labeled ligand) and, therefore, will worsen the detection limits of the assay. Conventionally, the ED_{50} value is used to express the detection capabilities of a particular assay; i.e., the lower the ED_{50}, the better the detection limits.

Although the assumption that only one binder can associate with the multisubstituted conjugate is probably true in heterogeneous enzyme immunoassays, in homogeneous assays multiple binders may associate with a single multisubstituted conjugate molecule. However, even in this case once the binder binds to one of the ligands on the enzyme, some of the others (not necessarily all) should be sterically constrained from binding to additional binders. As explained in ref 4, this should result in an increase of the association constant between the conjugate and the binder, and consequently an increase in the ED_{50} value. Reducing the number of ligands on the enzyme should lower the association constant between the conjugate and the binder and result in assays with lower ED_{50} values. Therefore, ability to employ oligosubstituted conjugates in enzyme-linked methods is vital for developing assays with optimized detection capabilities.

Furthermore, since the ligands are attached at different sites on the enzyme molecule, the stereochemistry and charge distribution of the neighboring portions of the protein could influence their association with biological binders. Therefore, the binder may have different affinities for each ligand molecule attached to the enzyme (i.e., a heterogeneous population of conjugates may exist) which can affect the dose–response characteristics of the assay. Indeed, sometimes heterogeneity in the interaction between binders and labeled ligands is known to result in poorer dose–response behavior of competitive binding assays (*18*).

The above arguments demonstrate that by using oligosubstituted conjugates the overall dose–response characteristics of the assays could be improved. Pyruvate carboxylase is an ideal model for an oligosubstituted enzyme–ligand conjugate because the natural prosthetic group of the enzyme is also the ligand that associates with the binder. This prosthetic group is a biotin molecule that is covalently attached to an ϵ-amino group of a lysine residue in the active site of the enzyme (*9*). The nine-carbon, one-nitrogen chain that connects the biotin to the enzyme behaves as a flexible arm that swings between the ATP-bicarbonate site and the pyruvate site and is essential for the enzyme to be active (Figure 1). It also allows for good recognition of biotin by its binder, avidin, and creates ample room for the interaction between these two molecules to occur.

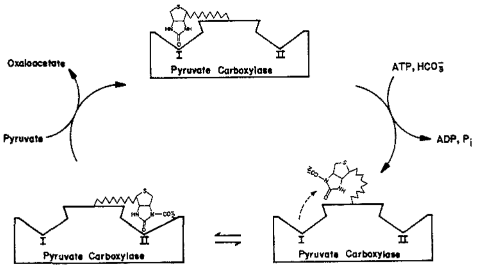

Figure 1. Schematic representation of the catalytic sites present at the active site of pyruvate carboxylase and the mode of action of the enzyme.

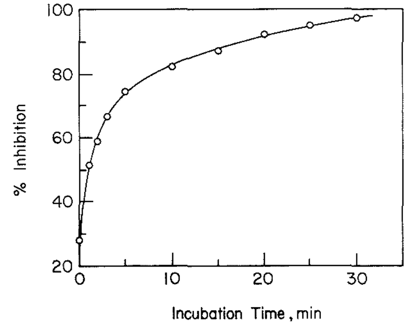

Figure 2. Effect of the incubation time on the inhibition of pyruvate carboxylase using 2.0 μg of avidin and 1.6 milliunits of the enzyme.

At the initiation of this investigation pyruvate carboxylase was not commercially available, and therefore the enzyme was isolated from baker's yeast. Stability studies of pyruvate carboxylase showed that the enzyme was stable for extended periods of time when kept at −15 °C. The stability of the enzyme at 4 and 22 °C was also investigated. At 22 °C the enzymatic activity decreased with a half time of about 10 days. In contrast, the activity was virtually unchanged for at least 15 days when the enzyme was kept at 4 °C.

The kinetics of the association between 2.0 μg (50 μL of 1.0 mg/25 mL) of avidin and 42 μg of pyruvate carboxylase (1.6 milliunits) were studied by following the percent inhibition of the enzyme as a function of the duration of incubation between the two compounds (Figure 2). Inhibition reached a value of 87% after 15 min of incubation, which allowed for reasonably rapid assays. Therefore, the remaining studies were performed by using 15 min as the incubation time. The relatively rapid kinetics associated with the inhibition of pyruvate carboxylase by avidin is due to the high association rate constant between the two reagents (*19*).

The effect of varying the amount of avidin on the inhibition of a fixed amount of enzyme was investigated (Figure 3). This study helped in determining which concentration of avidin

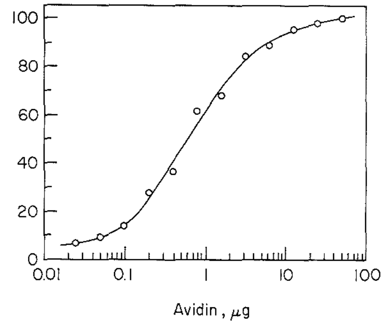

Figure 3. Effect of the avidin concentration on the activity of pyruvate carboxylase.

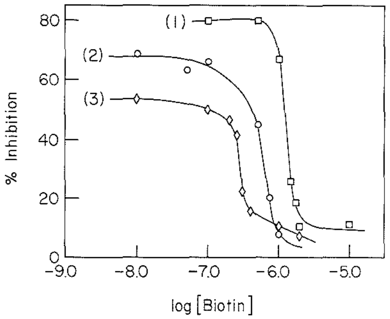

Figure 4. Family of dose–response curves reflecting the effect of varying the amount of avidin and pyruvate carboxylase in the assay: In curve (1) 2.0 μg of avidin and 1.6 milliunits of enzyme were used. In curve (2) the activity of the enzyme was 1.6 milliunits and the avidin concentration was reduced to 0.78 μg. In curve (3) the avidin concentration remained at 0.78 μg but the activity of the enzyme was 2.4 milliunits.

would be best for preparation of dose–response curves. A concentration of avidin that decreases the activity of the enzyme appreciably is desired. However this concentration should be low enough to allow reversibility when small amounts of free ligand are added. The lower the free ligand concentration needed to reverse the inhibition of the enzyme, the more sensitive the assay. A 60–90% inhibition of the enzyme would be in the range where both precision and detection limits are acceptable. Quantities of 3.1 and 0.78 μg of avidin (50 μL of 1.0 mg/16 mL and 50 μL of 1.0 mg/64 mL avidin solutions) were found to inhibit 1.8 milliunits of enzyme by 84 and 61%, respectively. It is within this range that further studies were performed.

When free ligand (biotin) is added to the reaction mixture competition occurs, and dose–response curves can be obtained by varying the amount of free ligand present. Comparison of sequential binding (*20*) and single incubation dose–response curves demonstrated no difference in the ED_{50} value of the two curves (results not shown here). In the sequential binding method avidin and biotin were incubated for 15 min prior to incubation with the enzyme for an additional 15 min. The similarity of the dose–response curves obtained by using these two different protocols is attributed to the fast kinetics of the avidin–biotin interaction. The single incubation method is simpler and faster than the sequential binding method, and therefore, it was used for preparing the remaining dose–response curves and for the real sample analysis. Figure 4 compares dose–response curves obtained by using different concentrations of avidin and/or enzyme. This figure also shows the gain in detection limits obtained when a lower binder concentration was used. However, this gain is concomitant with a decrease in both the magnitude of inhibition and the slope of the steep portion of the curve; the steeper the curve, the more precise the assay. Biotin concentrations of approximately 2×10^{-7} M could be detected when 0.78 μg of avidin and 2.4 milliunits of pyruvate carboxylase were used. In all of our experiments, avidin was in excess over pyruvate carboxylase. This according to Duggleby et al. (*10*) may result in enzyme–binder complexes where not all of the binding sites on avidin are occupied by the biotin-containing enzyme. As a consequence, the detection limits of the assay may be compromised.

Table I

Real Sample Analysis

manufacturer	vitamin preparation	amt of biotin per tablet, μg: found	claimed
Bio-Genics	Stress B Complex	13.4	12.5
Parke-Davis	ABDEC	53.5	50[a]
Thompson	Biotin	144	150
Perrigo	Biotin	300	300

Recovery Study

		μmol of biotin		
Parke-Davis	ABDEC	2.70	2.50	108
Parke-Davis	ABDEC	5.05	5.00	101

[a] This amount refers to biotin present in 1 mL of the liquid preparation ABDEC.

Figure 4 also demonstrates that for the same amount of avidin in the assay, a higher concentration of pyruvate carboxylase results in a dose–response curve with a lower ED_{50} value. Similar effects have been observed in homogeneous assays for folate (*7*) and cyclic AMP (*21*) when the ratios of conjugate/binder were less than one. Moreover, theory suggests that at least in the case of heterogeneous assays, this effect may be predictable (*4*).

Real sample analysis was performed on four commercially available vitamin supplements that contain biotin (Table I). The results of the analysis were on the average 5% different from the biotin content claimed by the manufacturers. The range of this difference was between 0% (Perrigo, Biotin) and 8% (Bio-Genics, Stress B Complex). Recovery studies were performed on the Parke-Davis ABDEC vitamin supplement. The sample was spiked with 2.50 and 5.00 μmol of biotin before analysis. The results showed that 2.70 and 5.05 μmol were recovered (8% and 1% errors, respectively), which indicates that there are virtually no matrix effects associated with this analysis.

In order to prove that the degree of conjugation has an effect on the response characteristics of homogeneous enzyme immunoassays, we attempted to increase the number of biotins per pyruvate carboxylase molecule by conjugating the latter with biotin-*N*-hydroxysuccinimide ester. Our goal was to compare dose–response curves obtained by using the natural form of pyruvate carboxylase and the conjugated enzyme. Unfortunately, this particular enzyme is very sensitive to modification by biotin. Indeed, even when minimally modified, the enzyme retained less than 2% of the original activity which prohibited an accurate comparison.

Glucose-6-phosphate dehydrogenase conjugated with biotin has been used previously for the development of a homogeneous assay for biotin (*8*). In order to demonstrate experi-

Table II. Parameters of G6PDH–Biotin Conjugates

	biotin/enzyme				
conjugate	initial	degree of conjugation	% residual activity	% inhibition	ED_{50}, M
BC-1	100	3	26	98	5.4×10^{-7}
BC-2	200	10	11	100	6.8×10^{-7}
BC-3	500	13	4.8	100	7.8×10^{-7}

mentally that the degree of conjugation affects the response characteristics of the assay, several G6PDH–biotin conjugates prepared with different mole ratios of biotin/enzyme were compared. The various parameters characterizing the conjugates are summarized in Table II. As shown, increasing the initial molar ratio of biotin/enzyme results in a higher degree of conjugation and lower residual activities of the conjugates. It can also be seen in Table II that in the presence of excess avidin the conjugates could be inhibited up to 100% (i.e., zero enzymatic activity). Dose–response curves were obtained by incubating biotin, G6PDH–biotin conjugate, and 36 ng of avidin for 5 min in a single incubation mode of analysis, followed by measurement of the resulting enzymatic activity of the mixture. The data summarized in this table indicate that the ED_{50} value of the dose–response curve is dependent on the degree of substitution of the enzyme–biotin conjugate. In general, the higher the degree of substitution the poorer the ED_{50} value and, therefore, the worse the detection limits of the assay.

It should be noted that in this last experiment the amount of conjugate was controlled so that the same units of enzymatic activity were used in the three assays. This level of enzymatic activity assures the measurement of a sufficiently high absorbance signal over a relatively short period of time; a measurement time of less than 5 min is typical in EMIT-type assays. In the case of conjugates BC-2 and BC-3, it is conceivable that by using lower concentrations of reagents the detection limits of the assays may be improved. However, this will require a longer assay time, which should limit the applicability of the technique.

In conclusion, the results of the real sample experiments and the associated studies show that this assay is effective in determining biotin. More importantly, this assay demonstrates also the feasibility of using oligosubstituted conjugates in homogeneous enzyme immunoassays. Specifically, it demonstrates that 100% inhibition of the enzymatic activity can be obtained even in the presence of only four ligands per enzyme molecule. Furthermore, one of the substrates of this enzyme is bicarbonate, which may allow for potentiometric detection of the enzymatic activity. Such a detection scheme may result in assays with even better detection limits when turbid and/or colored samples are to be analyzed.

LITERATURE CITED

(1) Monroe, D. *Anal. Chem.* **1984**, *56*, 920A–931A.
(2) Ngo, T. T.; Lenhoff, H. M. *Appl. Biochem. Biotechnol.* **1981**, *6*, 53–64.
(3) Rowley, G. L.; Rubenstein, K. E.; Huisjen, J.; Ullman, E. F. *J. Biol. Chem.* **1975**, *250*, 3759–3766.
(4) Bachas, L. G.; Meyerhoff, M. E. *Anal. Biochem.* **1986**, *156*, 223–238.
(5) Van Weemen, B. K.; Schuurs, A. H. W. M. In *Immunoenzymatic Techniques*; Feldman, G., Druet, P., Bignon, J., Avrameas, S., Eds.; Elsevier: New York, 1976; pp 125–133.
(6) Meyerhoff, M. E.; Rechnitz, G. A. *Anal. Biochem.* **1979**, *95*, 483–493.
(7) Bachas, L. G.; Meyerhoff, M. E. *Anal. Chem.* **1986**, *58*, 956–961.
(8) Daunert, S.; Bachas, L. G.; Meyerhoff, M. E. *Anal. Chim. Acta* **1988**, *208*, 43–52.
(9) Moss, J.; Lane, M. D. *Adv. Enzymol.* **1971**, *35*, 321–442.
(10) Duggleby, R. G.; Attwood, P. V.; Wallace, J. C.; Keech, D. B. *Biochemistry* **1982**, *21*, 3364–3370.
(11) Bacquet, C.; Twumasi, D. Y. *Anal. Biochem.* **1984**, *136*, 487–490.
(12) Rohde, M.; Lim, F.; Wallace, J. C. *Eur. J. Biochem.* **1986**, *156*, 15–22.
(13) Lowry, O. H.; Rosebraugh, N. J.; Farr, A. L.; Randall, R. J. *J. Biol. Chem.* **1951**, *193*, 265–275.
(14) Young, M. R.; Tolbert, B.; Utter, M. F. *Methods Enzymol.* **1969**, *13*, 250–263.
(15) Zettner, A. *Clin. Chem.* (*Winston-Salem, N.C.*) **1973**, *19*, 699–705.
(16) Green, N. M. *Biochem. J.* **1965**, *94*, 23c–24c.
(17) Ullman, E. F.; Maggio, E. T. In *Enzyme-Immunoassay*; Maggio, E. T., Ed.; CRC Press: Boca Raton, FL, 1980; pp 105–134.
(18) Borth, R. *Math. Biosci.* **1980**, *51*, 187–197.
(19) Green, M. *Adv. Protein Chem.* **1975**, *29*, 84–133.
(20) Zettner, A.; Duly, P. E. *Clin. Chem.* (*Winston-Salem, N.C.*) **1974**, *20*, 5–14.
(21) Carter, M. L. C., Ph.D. Thesis, University of Michigan, 1986.

RECEIVED for review September 12, 1988. Revised manuscript received March 20, 1989. Accepted July 5, 1989. This research was supported in part by grants from the American Association for Clinical Chemistry (Research and Endowment Fund) and from the National Institutes of Health (Grant No. R29-GM40510).

Anal. Chem. 1989, 61, 2165–2171

Contribution of Interfacial Resistance to Plate Height in Open Tubular Gas Chromatography

Agneta K. Bemgård*,[1] **and Lars G. Blomberg**

Department of Analytical Chemistry, University of Stockholm, S-106 91 Stockholm, Sweden

Anders L. Colmsjö

Department of Analytical Chemistry, National Institute of Occupational Health, S-171 84 Solna, Sweden

A method for the determination of the contribution of interfacial resistance to mass transfer in open tubular gas chromatography is demonstrated. When a term accounting for such mass transfer resistance is included in the Golay–Giddings equation, the agreement between theoretically calculated and experimentally measured height equivalent to a theoretical plate (HETP) vs v_0 plots is greatly improved. Under the conditions studied, the relative significance of the interface resistance term increases with decreasing film thickness. When the stationary-phase film thickness is lower than 2 μm, the contribution from interfacial mass transfer resistance to the HETP value, at optimal mobile-phase velocity, is thus larger than the resistance to mass transfer in the stationary phase. Determination of diffusion coefficients, D_l, in the stationary phase from the Golay–Giddings equation can be erroneous when the interfacial resistance term is excluded.

INTRODUCTION

For several decades, theories for the description and explanation of the chromatographic processes developed in columns, based on for example a gas–liquid phase system, have been deduced and applied to experimental work. In 1941, Martin and Synge (*1*) introduced the concept of HETP (height equivalent to a theoretical plate). Since then, this concept has been used as a basic tool for measuring the performance of chromatographic behavior. In 1958, Golay (*2*) deduced a relationship especially for capillary gas chromatography where the HETP value could be described in terms of axial and radial diffusion in the mobile phase and radial diffusion in the stationary phase. These three concepts were further regarded as presenting the main contribution to band broadening in a capillary gas chromatographic system. Golay's equation has frequently been used since then with the inclusion of terms that correct for the pressure drop over a column.

In 1962, Khan (*3*) mathematically adapted the theory of interfacial resistance (*4*) to be included in the Golay equation. Thus, by inclusion of an additional term, the nonequilibrium state in a column, produced by resistance to mass transfer between the mobile and stationary phases, could be taken into account. This effect would, if it could be proven to be of significant magnitude, obstruct the free interchange of molecules between the stationary and mobile phases, thus contributing to band broadening and increased HETP values. As the magnitude of this term was difficult to measure in simple experiments, no clear acceptance or rejection of its importance could be stated, and it is today still a matter of debate. Krige and Pretorius (*5*) showed in 1963 that the desorption step from the stationary phase was the rate-controlling mechanism if both desorption and adsorption for interfacial resistance were regarded. They suggested that "...Khan overestimates the relative importance of interfacial resistance". James et al. (*6*) also summarized that "...the contribution of interfacial resistance to plate height for columns normally encountered is negligible".

The reason for the difficulty in establishing the importance of this effect, which even if proven to be of small importance (quote not negligible), could be found in the linear dependence between interfacial resistance and resistance to mass transfer in the stationary phase; i.e. the relative contributions of these two effects are impossible to separate in a one-column experiment, unless exact data on diffusion coefficients for the compounds involved are available. Nevertheless, numerous authors have during the past decades attempted to ascertain diffusion coefficients from the Golay equation, without consideration of the interfacial resistance. Most of these results have shown a similar pattern, where the experimentally measured values of the total resistance to mass transfer have been significantly larger than the theoretically derived values by a factor of 2–6 (*7, 8*). This could be explained by a significant contribution from the injection, detection, and electronic systems. However, recent accurate measurements have shown that theoretical and experimental data deviate, even though these effects are taken into account (*9, 10*), and the diffusion coefficients in the stationary phase appear to vary with film thickness (*11, 12*).

During recent years, increased interest has been shown in computer-aided optimization in gas chromatography (*12*). Basic requisites for such optimization are a sufficiently accurate theory to describe the chromatographic process and accurate data for the calculations.

In this study, the influence of interfacial resistance in ordinary capillary gas chromatography has been evaluated by using a method where several similar columns, differing only in film thickness, were used under identical conditions. This method presents a theoretical possibility of distinguishing the relative contributions of interfacial resistance and resistance to mass transfer in the stationary phase for a chromatographic system. By means of high-speed microcomputer registration, the principles, outlined by Giddings et al. (*13*) and Purnell et al. (*14*), for subtracting any contribution of *extra*column effects are also regarded in order to accurately establish the HETP curve as a pure function of *intra*column effects.

THEORY

The original equation, framed by Golay (*2*) for open tubular chromatography, expressed HETP as

$$H = B/v + Cv \tag{1}$$

where

$$B = 2D_g \tag{2}$$

---

[1] Current address: Department of Analytical Chemistry, National Institute of Occupational Health, S-171 84 Solna, Sweden.

0003-2700/89/0361-2165$01.50/0 © 1989 American Chemical Society

and the resistance to mass transfer is divided into

$$C = C_g + C_l \tag{3}$$

$$C_g = \frac{r^2(11k'^2 + 6k' + 1)}{24(1 + k')^2 D_g} \tag{4}$$

$$C_l = \frac{2k' d_f^2}{3(1 + k')^2 D_l} \tag{5}$$

where r is the column radius, k' the capacity factor, d_f the stationary-phase film thickness, D_g and D_l the diffusion coefficients in the mobile and stationary phases, and v the average mobile-phase velocity.

Equation 1 shows the additive contributions to the plate height of the longitudinal diffusion in the gas phase, the resistance to mass transfer in the gas phase, and the liquid phase, respectively. Some years later eq 1 was modified by Giddings (*15*) who introduced the f_1 factor accounting for the band broadening obtained by the expansion of the mobile phase throughout the column. Another f factor (f_2), originally derived by James and Martin (*16*), transfers the average gas velocity to the velocity at the column outlet (v_o).

$$f_1 = \frac{9(P^4 - 1)(P^2 - 1)}{8(P^3 - 1)^2} \tag{6}$$

$$f_2 = \frac{3(P^2 - 1)}{2(P^3 - 1)} \tag{7}$$

$$P = p_i / p_o \tag{8}$$

were p_i and p_o are the column inlet and outlet pressures.

If the average diffusion coefficient in the gas phase, D_g, is replaced by the diffusion coefficient at column outlet pressure D_{go}, and the average velocity is replaced by the outlet velocity according to

$$v = v_o f_2 \tag{9}$$

$$D_g = D_{go} f_2 \tag{10}$$

proper averaging of the plate height, the diffusion coefficient in the mobile phase, and the gas velocity along the column length leads to the introduction of the f_1 factor:

$$H = 2D_{go} f_1 / v_o + (C_{go} f_1 + C_l f_2) v_o \tag{11}$$

However, the theory of Golay presupposes the existence of interfacial equilibrium at any place and time in the chromatographic process. In practice this is not obtainable except at the peak maximum of a compound. The correction term introduced by Khan (*3*) for the contribution of nonequilibrium to band broadening is expressed by

$$C_i = \frac{2k' d_f}{(1 + k')^2 k_d} \tag{12}$$

where k_d is the desorption rate constant.

This additional term has also been described by other authors (*9, 15, 17, 18*). When eq 11 is extended by the C_i term, the plate height can be expressed as

$$H = 2D_{go} f_1 / v_o + (C_{go} f_1 + (C_l + C_i) f_2) v_o \tag{13}$$

The consequence of this extra band broadening contribution is an increased HETP value and an increased slope at velocities above $v_{o,opt}$ if H is plotted versus v_o.

EXPERIMENTAL SECTION

Columns. Fused silica tubing of 0.32-mm i.d. (Quartz et Silice, Paris) was used as column material in lengths of approximately 20 m. In order to measure the inner diameter, the tubes were weighed before and after filling with CCl_4, by which the i.d. was found to be 0.320 ± 0.002 mm. After being flushed with dry nitrogen, the capillaries were deactivated by reaction with decamethylcyclopentasiloxane at 370 °C (*19*). The capillaries were then rinsed with dichloromethane (p.a. grade), dried with nitrogen, and coated statically with a poly(dimethylsiloxane)–(5–6%)–(diphenyl)–(0.1–0.3%)–(methylvinylsiloxane) copolymer gum, PS 264 (Fluka, Buchs, Switzerland) dissolved in dichloromethane in appropriate concentrations.

After solvent evaporation, the columns were dried by flushing with nitrogen overnight, and the column lengths were carefully measured. In order to avoid any alteration in stationary-phase properties or film thickness, the stationary phase was not immobilized and the columns were thus not rinsed with solvent. Further, before testing, the columns were subjected to a mild conditioning only and were thus programmed at 5 °C/min to 250 °C, this temperature being maintained for 30 min.

Determination of Stationary-Phase Film Thickness. Prior to coating, the stationary phase was dissolved in dichloromethane in a concentration giving a film thickness of 2.00 μm (assuming the density of PS 264 to be 1.0 g/cm^3 at 125 °C). This solution was further diluted to concentrations giving film thicknesses of 1.00 and 0.50 μm. The column coated with the solution corresponding to d_f = 2.00 μm was set to 2.00, and the other film thicknesses were calculated by use of the relation $K = \beta k'$. One column with thicker film (d_f = 4.14 μm) was prepared from a new coating solution.

Solutes. All solvents and solutes were of analytical grade. For testing of the column coated with the thickest stationary-phase film, *n*-alkanes from *n*-undecane to *n*-tetradecane and biphenyl were used while *n*-undecane to *n*-hexadecane and biphenyl were used for the other columns. The solutes were dissolved in *n*-hexane, and the concentration of each compound was approximately 200 ng/μL.

Apparatus. All chromatographic experiments were performed on the same instrument, a Carlo-Erba, Mega gas chromatograph (Milan, Italy) equipped with a flame ionization detector. Hydrogen was used as carrier gas. Column inlet pressure was measured by a digital pressure gauge, (Chrompack, Middelburg, The Netherlands).

Testing Conditions. For HETP vs v_o measurements, 1.5 μL of the test solution was injected manually (75-mm needle) in split mode at a ratio of 1:100. On each column, the sample was injected at least twice at selected inlet pressures, ranging from 1.15 to 1.70 atm. Measurements were made for at least 10 different inlet pressures. Injector temperature was 220 °C, column temperature 125 °C, and detector temperature 300 °C.

Signal Registration and Treatment. All registration of chromatograms was performed by ELDS881 (Chromatography Data Systems, Kungshög, Stenhamra, Sweden), using a sampling rate yielding at least 300 data points for each peak. Retention times, half peak widths, tailing factors, mathematical dead times, k' values, and other chromatographic parameters of interest were calculated by the computer system. The number of theoretical plates was calculated in two different ways, either from the peak width at half height or from the moment method (*20*). The results from these methods were in good agreement, thus indicating symmetrical peak shapes. Mathematical dead times, which were calculated according to Guardino et al. (*21*), were then used for the calculation of k' values. The acquired data were subsequently transferred to an ABC-800 microcomputer for further calculations. Average gas-phase velocity, v, was calculated from retention time according to

$$v = L(k' + 1)/t_r \tag{14}$$

and the outlet velocity, v_o, could then be obtained from eq 9. L is the column length and t_r the retention time. Subsequently a least-squares fit of the measured values (H_i, $v_{o,i}$) to $H = B_o/v_o + Cv_o$ was performed according to

$$\min \sum (H_i - B_o/v_o - Cv_o)^2 \tag{15}$$

B_o and C were further optimized by linear programming of D_{go}, D_l, and k_d to fit eq 15. This was necessary, as the B and C terms in eq 15 also depend on v_o via the f_1 and f_2 factors. These factors were measured in every registered data point. A typical curve fit performed for biphenyl is shown in Figure 1. The correlation

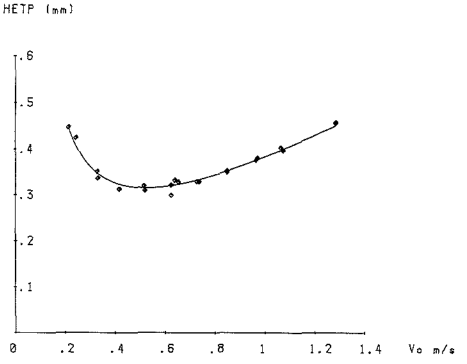

Figure 1. HETP curve fit for biphenyl on a column with 0.49-μm film thickness after computer optimization of D_{go}, D_l, and k_d: carrier gas, H_2; temperature, 125 °C; k', 18.97.

of the HETP plot to the calculated HETP curve was further used as a measure of the significance of the result.

$$\mathrm{ERR} = \sqrt{\Sigma(H_i - H_{calc})^2/n} \qquad (16)$$

H_i are the measured values, H_{calc} are values derived from the calculated HETP curve, and n is the number of data points in that particular experiment. This factor was typically a few micrometers. Furthermore, D_{go} could be estimated from the B term regardless of the significance of the interfacial resistance term.

$$D_{go} = B_o/2f_1 \qquad (17)$$

(In practice, f_1 equals unity for all measurements in this study.) Assuming negligible interfacial resistance, the D_l term can instantly be calculated by using this D_{go} and the C term:

$$C = (11k'^2 + 6k' + 1)r^2f_1/24(1 + k')^2D_{go} + 2k'd_f^2f_2/3(1 + k')^2D_l \qquad (18)$$

On the other hand if interfacial resistance is included, the C term equals

$$C = (11k'^2 + 6k' + 1)r^2f_1/24(1 + k')^2D_{go} + 2k'd_f^2f_2/3(1 + k')^2D_l + 2k'd_ff_2/(1 + k')^2k_d \qquad (19)$$

yielding one equation and two unknown constants, i.e. D_l and k_d. This is overcome by using two columns, differing only by film thickness, but otherwise evaluated under identical conditions. Two equations of type 19 are thus achieved with only two unknown quantities (D_l and k_d).

Extracolumn Effects. In order to take into account the extra band broadening effects (*22*) yielded by the injector, detector, amplifier, and data acquisition system, bandwidths were extrapolated back to zero column length (*13, 14*). This could be done by measuring the peak widths at half-height for a certain compound on identical columns, differing only in column lengths. The square of the peak widths correlates linearly to the column length, thus permitting the assessment of the extracolumn contributions to the peak width of a certain compound. The theoretical plate height was further calculated according to

$$N = 5.54(t_r^2/(W_m^2 - W_0^2)) \qquad (20)$$

where W_m is the registered peak width at half height for a certain compound and W_0 is the peak width at half-height at zero column length. In practice, these extracolumn effects had to be taken into consideration only in the cases of n-undecane and n-dodecane on the d_f = 0.49 μm column. Under the conditions used in this paper, i.e. column dimensions, temperature, and test solutes, extracolumn effects constituted such a considerable part of the band broadening that no accurate measurements of C_{go}, C_l, or C_i could be made on columns coated with thinner films of stationary phase.

Table I. D_{go} Values ($\times 10^6$ m^2/s) at 125 °C in H_2 for *n*-Undecane to *n*-Tetradecane Calculated According to Fuller–Schettler–Giddings, Compared to the Values Derived from Curve Fitting to HETP Plots

compound	F-S-G	measd
n-undecane	39.09	32.68
n-dodecane	37.41	32.30
n-tridecane	35.91	31.04
biphenyl	42.12	41.00

RESULTS AND DISCUSSION

If the interfacial resistance of any solute/column system is nonnegligible, the estimation of D_l from the Golay equation would be erroneous. Thus, in order to investigate the significance of the term defined by eq 12, a number of identical capillary columns were manufactured, differing only in film thickness (4.14, 2.00, 0.93, and 0.49 μm). This would theoretically present the opportunity to calculate D_{go}, D_l, and k_d and to determine the significance of interfacial resistance in capillary gas chromatography.

Initially, the assessment of D_{go} must be made very accurately, as the contribution of the terms involving D_{go} is predominant at all realistic velocities and usually represents 75–90% of the HETP value at optimum v_o (the two first terms in eq 11). Thus, by use of the method for best curve fit described above, a number of D_{go} values could be calculated according to eq 15–17. These values differ from other reported values of D_{go} calculated from, for example, the Fuller–Schettler–Giddings equation (*23*). The deviations, listed in Table I, are of such magnitude that any attempt to employ the values calculated according to ref 23 would severely influence all further calculations. For all calculations made in this investigation, D_{go} values derived from computer-optimized mean values were used. Thus, a fixed D_{go} for each compound at the temperature applied (125 °C) was established and used in further assessment of the C_l and C_i terms.

The slight variations of D_{go}, registered on different columns, may be an effect of statistical fluctuations or could also depend on slight variations of the column temperature. Nevertheless, a fixed D_{go} value for each compound is necessary in order to determine correct D_l and k_d values. If the model *excluding* interfacial resistance is used in one realistic case with a film thickness of 0.49 μm, a deviation of +7% in the D_{go} value would transfer an error in the assessment of D_l of approximately +20%. The error function is shown in Figure 2a, where a slightly increased dependence of ΔD_l versus ΔD_{go} can be noted. A relative error of +20% in D_l (excluding interfacial resistance) would further transfer an error in C_l of approximately −10%.

The D_l and k_d values were further derived from the C_l value from the Golay equation by means of eq 21 and 22. A relative error of −10% in the C_l value would, if this value in absolute terms is divided equally between the C_l (according to the Khan theory) and C_i, transfer an error of +7% in k_d and +35% in D_l for the model including interfacial resistance. In practice this means that the assessment of D_{go} and k_d will be relatively correct if the experiment is very accurately performed, whereas a high-precision assessment of D_l from HETP plots is a difficult task. The values used in Figure 2 a correspond to biphenyl on the d_f = 0.49 μm column. Higher values of d_f will drastically decrease the error in D_l.

The assessment of D_l and k_d from two different $C_l + C_i$ values can be derived from

$$C_l + C_i = 2k'd_f^2/3(1 + k')^2D_l + 2k'd_f/(1 + k')^2k_d \qquad (21)$$

which can be expressed as

$$d_f/3D_l + 1/k_d = (C_l + C_i)(1 + k')^2/2k'd_f \qquad (22)$$

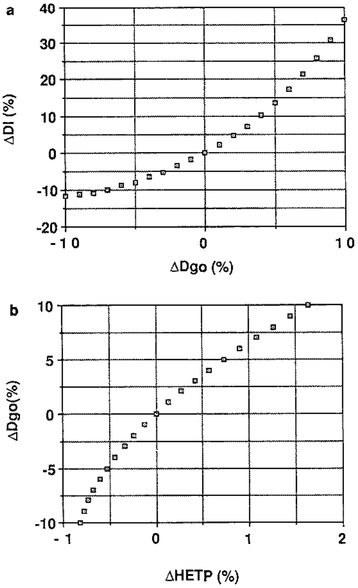

Figure 2. (a) Relative error in D_l as a function of the relative error in D_{go} according to the theory *excluding* interfacial resistance. Conditions: d_f = 0.49 μm; v_o = 0.5 m/s; compound, biphenyl; f_1 = 1; f_2 = 1.1; k' = 10.04; r = 0.16 mm. (b) Relative error in D_{go} as a function of the relative error in HETP. Conditions are the same as in a.

As the intercept between two different lines in a $1/D_l - 1/k_d$ plot falls near the $1/k_d$ axis, k_d will in most cases be determined with a higher accuracy than D_l.

Experimentally, the difference in HETP curves based on the two theories can be observed in a steeper increase in HETP for gas velocities greater than optimum, for the theory including interfacial resistance (steeper slope). The theory for interfacial resistance also postulates a poorer optimal HETP value. Based on the calculated values in this investigation for the d_f = 4.14 μm column, theoretically derived values from the other columns can be compared to the measured values. In Table II, the calculated C_l values for a number of columns are listed together with the measured values based on the curve-fitting method. In the case *excluding* interfacial resistance (Table IIa), the measured values exhibit an increased slope of the HETP curve (larger C_l values) for $v_o > v_{o,opt}$ compared to those predicted by the theory. This is visualized in Figure 3 based on the calculated values derived from the d_f = 4.14 μm column (D_l calculated = 0.98×10^{-9} m^2/s). In this figure are shown the experimental and calculated HETP curves (*excluding* interfacial resistance) plotted for *n*-dodecane on the four columns, based on the assumption that the D_l value is in agreement with the d_f = 4.14 μm column. The relative error in the deviations of the experimental from theoretical curves increases with decreasing film thickness. For example the measured C_l value of *n*-dodecane on the 0.49-μm column is more than 3 times as large as the expected value.

If the same comparison is made for the theory *including* interfacial resistance (Table IIb), a much better agreement is observed between measured and calculated values. In the latter case, the values from Table IV have been used for all film thicknesses; i.e. the same k_d and D_l value can be used for obtaining reasonable values for C_i and C_l, independent of film thickness. In Figure 4, the measured curves are the same as in Figure 3. In this case, the measured value for C_l of *n*-decane on the column with d_f = 0.49 μm is almost the same as the calculated value.

Table II

a. Measured and Theoretically Calculated Values for C_l According to the Model *Excluding* Interfacial Resistance

compd	d_f, μm	C_l, μs calcd	C_l, μs measd
n-undecane	4.14	588	588
	2.00	253	343
	0.93	93.0	174
n-dodecane	4.14	360	360
	2.00	163	229
	0.93	65.5	130
	0.49	27.6	89
n-tridecane	4.14	188	188
	2.00	87.3	138
	0.93	37.2	81.0
	0.49	17.1	68.0
biphenyl	4.14	93.0	93.0
	2.00	43.9	60.0
	0.93	19.3	39.0
	0.49	9.3	33.0

b. Measured and Theoretically Calculated Values for C_l and C_i According to the Model *Including* Interfacial Resistance[a]

compd	d_f, μm	C_l, μs calcd	C_l, μs measd	C_i, μs calcd	C_i, μs measd
n-undecane	4.14	440	418	170	170
	2.00	190	199	151	143
	0.93	69.6	76.6	119	97.3
n-dodecane	4.14	266	254	101	106
	2.00	120	140	94.8	89.2
	0.93	48.4	48.8	82.1	81.7
	0.49	20.4	19.5	65.6	69.4
n-tridecane	4.14	156	147	71.1	71.1
	2.00	72.3	79.2	68.4	65.7
	0.93	30.8	27.0	62.7	54.0
	0.49	14.2	13.3	54.7	54.7
biphenyl	4.14	62.4	60.8	30.4	31.8
	2.00	29.4	28.7	29.7	31.1
	0.93	12.9	14.2	28.1	28.1
	0.49	6.2	6.1	25.6	26.8

[a] T = 125 °C.

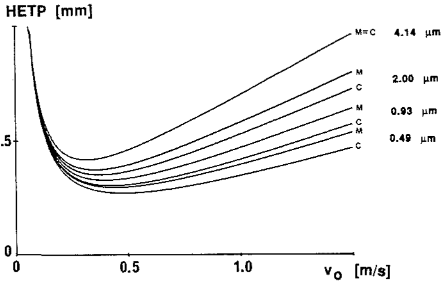

Figure 3. Calculated (C) and measured (M) HETP vs v_o plots for *n*-dodecane on the four columns: calculations according to the model *excluding* interfacial resistance; $D_l = 0.98 \times 10^{-9}$ m^2/s; derived from the data on the column with d_f = 4.14 μm; carrier gas, H_2; temperature, 125 °C.

It is evident that the interfacial resistance can be of importance whenever high-precision calculations are to be made on chromatographic processes in capillary chromatography. The obvious effect of neglecting the interfacial term in the HETP equation is that the D_l value apparently varies with film thickness. In Table IIIa, the values of C_{go}, C_l, and D_l

Table III.

a. Constants Calculated According to the Model *Excluding* Interfacial Resistance for Some Compounds, Using the Same Phase But with Different Film Thicknesses[a]

d_f, μm	compd	k'	C_{go}, μs	C_l, μs	10^6D_{go}, m^2/s	10^9D_l, m^2/s
4.14	*n*-undecane	17.17	331	588	32.68	1.01
	n-dodecane	30.24	347	360	32.30	0.98
	n-tridecane	53.16	368	188	31.04	1.10
	BiPhe	84.41	281	93	41.00	1.43
2.00	*n*-undecane	8.30	305	342	32.68	0.75
	n-dodecane	14.61	330	229	32.30	0.70
	n-tridecane	25.68	358	138	31.04	0.70
	BiPhe	40.75	276	60	41.00	1.04
0.93	*n*-undecane	3.88	260	174	32.68	0.54
	n-dodecane	6.81	299	130	32.30	0.49
	n-tridecane	11.97	337	81	31.04	0.51
	BiPhe	18.97	266	39	41.00	0.70
0.49	*n*-dodecane	3.63	258	89	32.30	0.30
	n-tridecane	6.34	307	68	31.04	0.28
	BiPhe	10.04	250	33	41.00	0.40

b. Constants Calculated According to the Model *Including* Interfacial Resistance for Some Compounds, Using the Same Phase but with Different Film Thicknesses[a]

d_f, μm	compd	k'	C_{go}, μs	C_l, μs	C_i, μs	10^6D_{go}, m^2/s	10^9D_l, m^2/s	10^3k_d, m/s
4.14	*n*-undecane	17.17	331	418	170	32.68	1.36	2.45
	n-dodecane	30.24	347	254	106	32.30	1.39	2.44
	n-tridecane	53.16	368	147	71.1	31.04	1.35	2.01
	BiPhe	84.41	281	60.8	31.8	41.00	2.18	3.02
2.00	*n*-undecane	8.30	305	199	143	32.68	1.37	2.48
	n-dodecane	14.61	330	140	89.2	32.30	1.15	2.71
	n-tridecane	25.68	358	79.2	65.7	31.04	1.16	2.09
	BiPhe	40.75	276	28.7	31.1	41.00	2.18	3.02
0.93	*n*-undecane	3.88	260	76.6	97.3	32.68	1.32	2.69
	n-dodecane	6.81	299	48.8	81.7	32.30	1.36	2.57
	n-tridecane	11.97	337	27.0	54.0	31.04	1.45	2.33
	BiPhe	18.97	266	14.2	25.1	41.00	1.94	3.52
0.49	*n*-dodecane	3.63	258	19.5	69.4	32.30	1.41	2.39
	n-tridecane	6.34	307	13.3	54.7	31.04	1.35	2.01
	BiPhe	10.04	250	6.1	26.8	41.00	2.17	3.02

[a] r = 0.16 mm. L = 20 m. T = 125 °C.

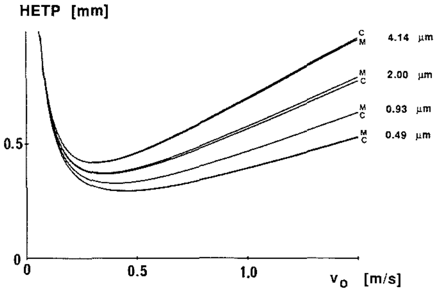

Figure 4. Calculated (C) and measured (M) HETP vs v_0 plots of *n*-dodecane on the four columns: calculations according to the model *including* interfacial resistance; D_l = 1.33 × 10^{-9} m^2/s and k_d = 2.53 × 10^{-3} m/s (Table IV); carrier gas, H_2; temperature, 125 °C.

Table IV. Mean Values for k_d and D_l on Four Columns[a]

compd	10^6D_{go}, m^2/s	10^3k_d, m/s	10^9D_l, m^2/s
n-undecane	32.68	2.54	1.35
n-dodecane	32.30	2.53	1.33
n-tridecane	31.04	2.11	1.33
BiPhe	41.00	3.15	2.12

[a] r = 0.16 mm. L = 20 m. T = 125 °C.

obtained from the equation excluding interfacial resistance are listed. The decrease in D_l values with decreasing stationary-phase film thickness is noticeable. However, this is in accordance with the results presented by Cramers et al. (*11*) who also observed a trend of film thickness dependent stationary-phase diffusion coefficients. Ettre (*24*) reported rather high deviations between calculated and measured HETP values on a thick-film column, which seemed to increase with increasing gas velocities. In that study, the value of D_l used was 1.41 × 10^{-9} m^2/s for *n*-undecane in SE-30 at 130 °C. The calculations were made without inclusion of an interfacial resistance term. Possibly this deviation could to some extent be explained by an interfacial resistance phenomenon.

The liquid-phase diffusion coefficient should be constant for a given combination solute/stationary phase at a given temperature in capillary gas chromatography. If the D_l values are calculated from experimental data with the model including interfacial resistance, the values explored are fairly constant over the film thickness interval regarded in this work (Table IIIb). In Table IV are listed the calculated mean values of D_l and k_d.

Table V illustrates the relative contributions to the HETP values at optimal v_0 divided in axial and radial band broadening in the gas phase, the contribution due to the stationary phase, and the contribution due to the interfacial resistance (nonequilibrium). These data are further plotted in Figure 5 as the B/v_0 term and the three Cv_0 terms including f factors. In Figure 5a, the B and C terms for *n*-undecane on the column with a film thickness of 4.14 μm are shown, and in Figure 5b the same solute on the column with 0.93-μm film thickness is represented. With a decrease in film thickness, the re-

Table V. HETP at v_{opt} Divided into Contributions from Axial and Radial Gas-Phase Diffusion, Stationary-Phase Diffusion, and Interfacial Resistance for Some Compounds on the Same Phase with Different Film Thicknesses[a]

d_f	compd	HETP, mm	B/v_o, %	C_gv_o, %	C_lv_o, %	C_iv_o, %	v_{opt} m/s
4.14	*n*-undecane	0.489	49.3	18.4	22.9	9.33	0.283
	n-dodecane	0.415	49.0	26.6	17.2	7.18	0.312
	n-tridecane	0.358	49.9	35.9	9.58	4.63	0.329
	BiPhe	0.347	49.4	39.2	7.07	3.98	0.483
2.00	*n*-undecane	0.409	48.9	24.5	15.5	11.10	0.342
	n-dodecane	0.371	49.2	31.7	11.6	7.41	0.348
	n-tridecane	0.339	49.8	39.0	6.1	5.09	0.349
	BiPhe	0.330	50.0	41.9	3.73	4.34	0.501
0.93	*n*-undecane	0.348	49.1	28.8	8.72	11.10	0.400
	n-dodecane	0.321	49.4	38.0	4.66	7.81	0.399
	n-tridecane	0.315	49.6	42.8	2.51	5.02	0.377
	BiPhe	0.316	49.8	44.4	1.67	4.19	0.527
0.49	*n*-dodecane	0.294	49.7	39.1	2.47	8.77	0.435
	n-tridecane	0.302	49.9	42.2	1.56	6.40	0.391
	BiPhe	0.304	50.1	44.7	0.90	4.32	0.545

[a] L = 20 m. r = 0.16 mm. Extracolumn effects are subtracted.

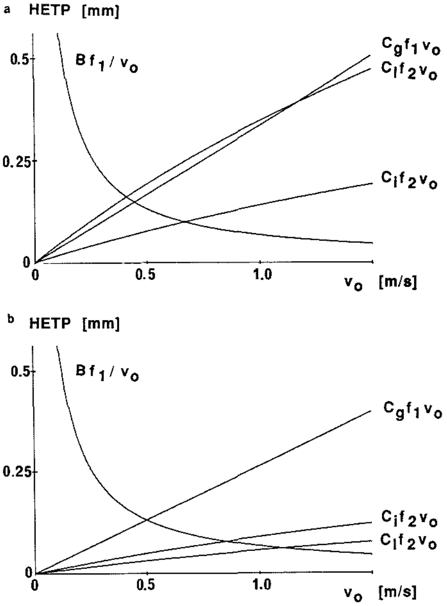

Figure 5. Effects of the B and C terms (the pressure-correcting factors are included) on HETP versus v_o for n-undecane on the columns with (a) d_f = 4.14 μm and (b) d_f = 0.93 μm. Conditions: carrier gas, H_2; temperature, 125 °C.

sistance to mass transfer in the stationary phase, C_l, decreases rapidly, while the contribution to plate height from interfacial resistance remains relatively constant (see also Table V).

On the other hand, if biphenyl is regarded (Figure 6), the contributions to plate height from C_l and C_i are not of the same magnitude as that for *n*-undecane. This is mainly due to a higher k' value and desorption rate constant, k_d, apart from the better diffusivity in the stationary phase for biphenyl than for *n*-undecane (Table IV). The contribution from interfacial resistance to H_{min} is only approximately 4% for biphenyl and 10% for *n*-undecane. For columns with film thicknesses around 0.5 μm, the contribution of interfacial resistance to the HETP value may be 10 times as large as the contribution from resistance to mass transfer in the stationary phase. This emphasizes the difficulties associated with the assessment of phase characteristics in thin-film systems.

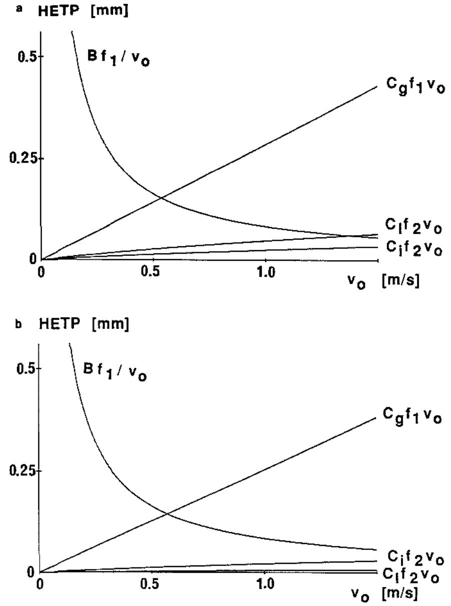

Figure 6. Effects of the B_o and C terms (the pressure-correcting factors are included) on HETP versus v_o for biphenyl on the columns with (a) d_f = 4.14 μm and (b) d_f = 0.49 μm. Conditions: carrier gas, H_2; temperature, 125 °C.

ACKNOWLEDGMENT

The authors thank Beryl Holm for reviewing the manuscript.

LITERATURE CITED

(1) Martin, A. J. P.; Synge, R. L. M. *Biochem. J.* **1941**, *35*, 1358.
(2) Golay, M. J. E. In *Gas Chromatography 1958*, Desty, D. H., Ed.; Butterworths: London, 1958; pp 36–55.
(3) Khan, M. A. In *Gas Chromatography 1962*; van Swaay, M., Ed.; Butterworths: London, 1962; pp 3–17.
(4) Aris, R. *Proc. R. Soc. London*, *A* **1956**, *235*, 67.
(5) Krige, G. J.; Pretorius, V. *Anal. Chem.* **1963**, *35*, 2009.
(6) James, M. R.; Giddings, J. C.; Eyring, H. *J. Phys. Chem.* **1964**, *68*, 1725.
(7) Scott, R. P. W.; Hazeldean, G. S. F. In *Gas Chromatography 1960*; Scott, R. P. W., Ed.; Butterworths: Washington, DC, 1960; pp 144–161.
(8) Desty, D. H.; Goldup, A. In *Gas Chromatography 1960*; Scott, R. P. W., Ed.; Butterworths: Washington, DC, 1960; pp 162–183.
(9) Tijssen, R.; Bleumer, J. P. A.; Smit, A. L. C.; van Kreveld, M. E. *J. Chromatogr.* **1981**, *218*, 137.
(10) Tijssen, R.; van den Hoed, N.; van Kreveld, M. E. *Anal. Chem.* **1987**, *59*, 1007.
(11) Cramers, C. A.; van Tilburg, C. E.; Schutjes, C. P. M.; Rijks, J. A.; Rutten, G. A.; de Nijs, R. *J. Chromatogr.* **1983**, *279*, 83.
(12) Villalobos, R.; Annino, R. in *Proceedings of the 9th International Symposium on Capillary Chromatography*; Sandra, P., Ed.; Hüthig: Heidelberg, FRG, 1988; pp 59–85.
(13) Giddings, J. C.; Robinson, R. A. *Anal. Chem.* **1962**, *34*, 885.
(14) Purnell, J. H.; Sawyer, D. T. *Anal. Chem.* **1964**, *36*, 668.
(15) Giddings, J. C.; Seager, S. L.; Stucki, L. R.; Stewart, G. H. *Anal. Chem.* **1964**, *36*, 741.
(16) James, A. T.; Martin, A. J. P.; Biochem. *J.* **1952**, *50*, 679.
(17) Wong, A. K.; McCoy, B. J.; Carbonell, R. G. *J. Chromatogr.* **1976**, *129*, 1.
(18) Pethö, A. In *Handbuch der Gas Chromatographie*; Leibnitz, E., Struppe, H. G., Eds.; Geest & Portig: Leipzig, GDR, 1966; pp 70–102.
(19) Buijten, J. Immobilized Stationary Phases for Capillary Gas Chromatography. Ph.D. Thesis, University of Stockholm, 1984.

Anal. Chem. **1989**, *61*, 2171–2175

(20) Arnold, F. H.; Blanch, H. W.; Wilke, C. R. *J. Chromatogr.* **1985**, *330*, 159.

(21) Guardino, X.; Albaigês, J.; Firpo, G.; Rodriguez-Vinals, R.; Gassiot, M. *J. Chromatogr.* **1976**, *118*, 13.

(22) Gaspar, G.; Annino, R.; Vidal-Madjar, C.; Guiochon, G. *Anal. Chem.* **1978**, *50*, 1512.

(23) Fuller, E. N.; Schettler, P. D.; Giddings, J. C. *Ind. Eng. Chem.* **1966**, *58*, 19.

(24) Ettre, L. S.; McClure, G. L.; Walters, J. D. *Chromatographia* **1983**, *17*, 560.

RECEIVED for review October 25, 1988. Accepted June 19, 1989. This investigation was kindly supported by the Swedish Natural Science Research Council.

Separation of Styrene–Acrylate and Styrene–Methacrylate Copolymers According to Composition by Liquid Adsorption Chromatography

Sadao Mori* and Masaaki Mouri

Department of Industrial Chemistry, Faculty of Engineering, Mie University, Tsu, Mie 514, Japan

Styrene copolymers of methyl, ethyl, and *n*-butyl acrylates and ethyl and *n*-butyl methacrylates were prepared and separated. A column of 4.6 mm i.d. × 50 mm length packed with silica gel having a pore size of 30 Å was used. The mobile phase was a mixture of chloroform and ethanol. Ethanol content in the mobile phase and column temperature controlled the retention of the copolymers. Acrylate- or methacrylate-rich copolymers required higher ethanol content in the mobile phase or a lower column temperature to elute from the column. In copolymers having the same styrene content, the copolymers that required much ethanol in the mobile phase to elute from the column at a constant column temperature were in the order of methyl, ethyl, and *n*-butyl acrylate (and methacrylate). Similarly, methacrylate copolymers required more ethanol in the mobile phase than acrylate copolymers having the same styrene content and the same ester group. Linear gradient elution was effective in separating the copolymers according to the composition. The initial mobile phase (A) was a mixture of chloroform and ethanol (99.0:1.0 (v/v)), and the composition of the final one (B) was 93.0:7.0. The composition of the mobile phase was changed from 100% A to 100% B in 30 min. Molecular weight dependence on retention volume was not observed.

INTRODUCTION

Synthetic random copolymers usually have a molecular weight distribution (MWD) and a chemical composition distribution (CCD). The accurate determination of CCD is important for the characterization of copolymers as well as the determination of MWD. Several attempts have been reported for the determination of CCD. Among the techniques for measuring CCD, high-performance liquid chromatography (HPLC) holds great possibilities for measuring CCD precisely and rapidly because of its high efficiency. There are several published papers in this area, e.g., separations of styrene–methyl acrylate (*1*), styrene–methyl methacrylate (*2–4*), styrene–acrylonitrile (*5*), and styrene–butadiene (*6*) copolymers by HPLC. The essence of their techniques was the use of a combination of good and poor solvents for the copolymers as the mobile phase, except the method developed by Danielewicz and Kubin (*2*). They used a combination of dichloroethane and tetrahydrofuran, both of which are good solvents for styrene–methyl methacrylate copolymers.

In our previous papers (*7–12*), separation of styrene–methyl methacrylate random copolymers according to chemical composition by high-performance liquid adsorption chromatography (LAC) was reported. A combination of chloroform/ethanol (99.0:1.0 (v/v)) and chloroform/ethanol (95.5:4.5 (v/v)) was used as the mobile phase. These two mixed solvents are good solvents for the copolymers. The copolymers containing more styrene eluted earlier, and molecular weight dependence on retention volume was not observed in the separation of the copolymers by LAC.

In the present report, our method was applied for the separation of copolymers of styrene–acrylate (methyl, ethyl, and *n*-butyl) and styrene–methacrylate (ethyl and *n*-butyl), which were prepared by solution polymerization at a low degree of conversion. Operational variables such as ethanol content in the mobile phase and column temperature, the relationship between the composition of the copolymers and retention volume, and molecular weight dependence on retention volume were investigated.

EXPERIMENTAL SECTION

Apparatus. A TRIROTAR-VI high-performance liquid chromatograph (Jasco, Japan Spectroscopic Co., Ltd., Hachioji, Tokyo, Japan) with a Model TU-300 column oven and a Model VL-614 variable loop injector (both from Jasco) was used in this work. An ultraviolet (UV) absorption detector (Model UVIDEC-100 VI) (Jasco) at a wavelength of 254 nm was used. The equipment for carrying out gradient elution was a type of low-pressure-mixing gradient system with one pump. Silica gel with a pore size of 30 Å and a mean particle diameter of 5 μm (Nomura Chemical Co., Seto, Aichi, Japan) was packed in 4.6 mm i.d. × 50 mm length stainless-steel tubing. This column was thermostated at a specified temperature in the column oven. The number of theoretical plates of the column was 1500 as determined by injecting 10 μL of a 0.1% benzene solution at a flow rate of 0.2 mL/min, with chloroform including 1% ethanol used as the mobile phase.

Sample. Comonomers of styrene (S) were methyl acrylate (MA), ethyl acrylate (EA), *n*-butyl acrylate (BA), ethyl methacrylate (EMA), and *n*-butyl methacrylate (BMA). Copolymers were prepared by solution polymerization at a low degree of conversion. A total volume of 25 mL of a mixture of freshly distilled styrene monomer and respective acrylate or methacrylate monomer at a specified molar ratio was dissolved in 50 mL of benzene, and 20 mg of azobis(isobutyronitrile) (AIBN) was added. Polymerization was performed at 60 °C for 10 h under nitrogen atmosphere. The polymerization solution was then poured into

0003-2700/89/0361-2171$01.50/0 © 1989 American Chemical Society

Table I. Styrene Content of Styrene–Acrylate and Styrene–Methacrylate Copolymers

sample	styrene content, mol %	sample	styrene content, mol %
S–MA		S–EMA	
I	65.7	I	69.1
II	51.3	II	50.2
III	35.6	III	30.4
IV	19.0	IV	15.5
S–EA		S–BMA	
I	68.6	I	69.6
II	52.6	II	50.3
III	36.7	III	30.7
IV	20.7	IV	14.5
S–BA			
I	75.5		
II	59.2		
III	41.0		
IV	15.8		

excess methanol to produce a precipitate that was purified by reprecipitation with a combination of chloroform and methanol. The yield of the polymer products was between 10% and 20%. In the case of copolymers P(S–EA) and P(S–BA), polymerization solutions were cooled to about 0 °C and most of the benzene was evaporated under reduced pressure. Then, the solution was poured into 1-hexanol to produce a precipitate. This procedure was mostly required for the EA- or BA-rich copolymers.

The composition of the copolymer samples was measured by UV spectrophotometry. The copolymer samples were dissolved in chloroform, the absorbance at 260 nm was measured, and then the composition was calculated from a calibration curve that was constructed by using polystyrene. Measurement conditions of the UV spectrophotometer (UVIDEC-610C, Jasco) were as follows: bandwidth, 0.1 nm; time constant, 8 s; wavelength set, 240–310 nm; scan speed, 4 nm/min. The abbreviations and the styrene content of the copolymers prepared in this work are given in Table I. Molecular weight averages of these copolymers measured by size exclusion chromatography (SEC) were between 1.0×10^5 and 3.0×10^5 for $\bar{M}_w$ and 0.5×10^5 and 1.5×10^5 for $\bar{M}_n$ as polystyrene equivalent molecular weight. Although these values of molecular weight averages are not correct, nor proportional to the true values since retention in SEC effectively depends on the radius of gyration and not directly on molecular weight, it is possible to know the rough sizes of the copolymers.

Elution. The mobile phase was a mixture of chloroform and ethanol. Ethanol contained in commerical chloroform as a stabilizer was removed before use by washing chloroform with water and drying it with anhydrous calcium chloride, followed by distillation, and therefore, chloroform as defined in this report does not contain any ethanol unless otherwise specified.

Elution was performed by both isocratic and gradient elution modes. An isocratic elution mode was applied to investigate the elution behavior of the copolymers by changing the column temperature from 30 to 80 °C every 10 °C and by changing the composition of the mobile phase. Samples were dissolved in the mobile phase in a concentration of 0.1%, and the injection volume was 0.025 mL. The flow rate of the mobile phase was 0.5 mL/min.

Linear gradient elution was applied to separate the copolymers according to their composition and was performed as follows: The initial mobile phase (A) was a mixture of chloroform and ethanol (99.0:1.0 (v/v)); the composition of the final mobile phase (B) was 93.0:7.0 (v/v) chloroform/ethanol; and the composition of the mobile phase was changed from 100% A to 100% B in 30 min linearly, and then the mobile phase was returned to 100% A in another 10 min. Samples were dissolved in the initial mobile phase in a total concentration of 0.1%; i.e., sample concentration was 0.02% each for samples I–III and 0.04% for sample IV for each copolymer. A sample solution was injected 1 min after the start of the gradient. The flow rate of the mobile phase was 0.5 mL/min, and the injection volume of the sample solution was 0.1 mL. Lag time in the gradient elution was not determined, but it was assumed to be about 2 min (1 mL) by the experimental results (*8*).

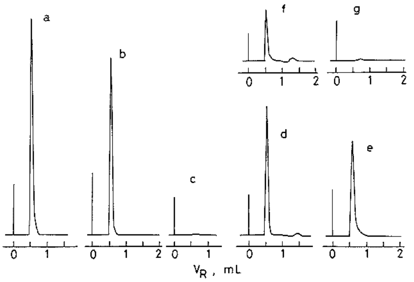

Figure 1. Effect of ethanol content in chloroform on the elution of copolymers S–EA II (a–c) and III (d–g): column temperature, 50 °C; chloroform/ethanol mobile phase (v/v), (a) 97:3, (b) 98:2, (c) 99:1, (d) 95:5, (e) 96:4, (f) 97:3, (g) 98:2.

Fractionation by SEC. Fractionation of some copolymers by SEC was performed as follows. Two Shodex A80M HPSEC columns (50 cm × 8 mm i.d.) (Showa Denko Co., Minato-ku, Tokyo) packed with polystyrene gels for polymer analysis were used with chloroform containing 1% ethanol as the mobile phase. The flow rate was 1 mL/min. A 0.2% solution of each sample copolymer in chloroform containing 1% ethanol was injected into the SEC system. The injection volume was 0.2 mL. The volume of one fraction from each chromatogram was 1.5 mL, and three major fractions were obtained from one chromatogram. The fractionated solutions were dried under reduced pressure and redissolved in the initial mobile phase for LAC and injected into a LAC system.

RESULTS AND DISCUSSION

Isocratic Elution. In the previous paper (*8*), it was reported that styrene–methyl methacrylate (S–MMA) copolymers tended to be retained in the column when chloroform was used as the mobile phase and that the copolymers eluted from the column with increasing ethanol content in the mobile phase. The copolymers having more of the methyl methacrylate component required a higher ethanol content in the mobile phase and a lower column temperature for elution.

In the present work, the elution behavior of styrene–acrylate and styrene–methacrylate copolymers was examined at column temperatures of 30, 40, and 50 °C by changing the ethanol content in the chloroform used as the mobile phase. Ethanol content was increased every 1% from 1% to 7%. The examples for styrene–ethyl acrylate copolymers S–EA II and S–EA III at a column temperature of 50 °C are shown in Figure 1. Copolymer S–EA II did not elute from the column when the ethanol content in the mobile phase was 1% (Figure 1c). This means that copolymer II is retained in the column when chloroform containing less than 1% ethanol is used as the mobile phase. At 2% ethanol concentration in the mobile phase, copolymer S–EA II eluted 80% of the total from the column, and at 3% ethanol concentration, the copolymer eluted 100%. Copolymer S–EA III was retained in the column with the mobile phase containing ethanol up to 2%, and the peak height increased as the ethanol content in the mobile phase was increased from 3% to 5%. The copolymer eluted 100% from the column when the mobile phase contained 5% ethanol.

Copolymer S–EA II could elute 100% with the mobile phase containing more than 3% ethanol, and copolymer S–EA III could elute from the column with the mobile phase containing more than 5% ethanol. The incomplete elution of the copolymers in Figure 1 (b, e, and f) was caused by the difference in the composition of the copolymers, not by the difference in molecular weight (*9*); e.g., the fraction of copolymer S–EA III eluted with the mobile phase chloroform/ethanol (97.0:3.0 (v/v)) (Figure 1f) had higher styrene content than that re-

Table II. Percentage of Styrene–Acrylate (and –Methacrylate) Copolymers Eluted from a Silica Gel Column with a Mobile Phase of Chloroform and Ethanol at a Column Temperature of 50 °C

sample	chloroform/ethanol mobile phase, % (V/V)						
	93:7	94:6	95:5	96:4	97:3	98:2	99:1
S–MA							
I	100	100	100	100	100	100	0
II	100	100	86	66	46	0	0
III	100	77	63	46	20	0	0
IV	100	82	65	35	0	0	0
S–EA							
I	100	100	100	100	100	100	88
II	100	100	100	100	100	80	0
III	100	100	100	73	40	0	0
IV	100	100	78	63	50	0	0
S–BA							
I	100	100	100	100	100	100	100
II	100	100	100	100	100	100	80
III	100	100	100	100	100	100	0
IV	100	100	100	100	100	100	0
S–EMA							
I	100	100	100	100	100	100	30
II	100	100	100	85	58	47	0
III	100	100	68	55	43	0	0
IV	100	83	63	50	30	0	0
S–BMA							
I	100	100	100	100	100	100	52
II	100	100	100	100	100	100	0
III	100	100	100	100	100	70	0
IV	100	100	100	100	100	54	0

tained in the column. This means that the copolymers may have some CCD, and this will be discussed in a later section. One of the characteristics of the elution of the copolymers in this isocratic elution mode was that ethanol content in the mobile phase did not affect the peak retention volume for the copolymers and that the retention volume of the copolymers was always at the interstitial volume of the column when they could elute from the column. As a result, every peak was very sharp, even though the copolymers have CCD. This elution behavior was the same as previously observed for copolymers S–MMA (*8*).

The precentage of the copolymers eluted from the column is listed in Table II. Column temperature was 50 °C, and ethanol content in the mobile phase was changed from 1% to 7% every 1%. Peak height when a sample copolymer eluted completely from the column was expressed as 100%, and other peak heights were shown by percentage. Complete elution of the copolymer was based on the peak height of polystyrene and the composition of the sample copolymer injected. All samples were dissolved in the mobile phase tested. It can be estimated from Table II as follows: Copolymer S–MA I elutes 100% from the column with the mobile phase containing more than 2% ethanol, S–MA II with more than 6%, and S–MA III and IV with more than 7%. Similarly, copolymer S–MA I is retained in the column completely with the mobile phase containing less than 1% ethanol, S–MA II and III with less than 2%, and S–MA IV with less than 3%.

It can also be observed from Table II qualitatively that the copolymer species having a lower alkyl ester group of an acrylate or methacrylate unit required more ethanol in the mobile phase to elute from the column than those having a higher alkyl ester group, e.g., S–MA > S–EA > S–BA, and S–EMA > S–BMA. Similarly, copolymers of styrene–methacrylate required a more ethanol-rich mobile phase to elute from the column than did styrene–acrylate copolymers having the same type of an ester group. For example, copolymers S–MA II, S–EA II, S–EMA II, and S–BMA II are similar in styrene content, having about 50% styrene. In each of the pairs S–MA II and S–EA II, S–EMA II and S–BMA II, and S–EMA II and S–EA II, the former required more ethanol in the mobile phase to elute from the column than did the latter.

Elution behavior of the copolymers at different column temperatures was also investigated. For example, at a constant composition of the mobile phase (chloroform/ethanol, 99.0:1.0 (v/v)), copolymer S–BA II eluted 100% from the column at column temperatures of 30 and 40 °C. Peak height at 50 °C decreased to 80% of that at 30 °C, and that at 60 °C to 24%. The copolymer was retained in the column at a column temperature of 70 °C. The peak retention volume was unchanged with column temperature, and it corresponded to the interstitial volume of the column system. This observation, that the peak retention volume of the copolymers that could elute from the column was always the equivalent position to the interstitial volume of the column, was the same as that in Figure 1 and also as that observed for copolymers S–MMA (*8*).

In a manner similar to that of copolymer S–MMA (*8*), copolymers examined in this experiment tended to adsorb in the column with decreasing ethanol content in the mobile phase and with increasing column temperature. Ethanol content in the mobile phase required for the copolymers to elute 100% from the column at column temperatures 30, 40, and 50 °C is shown in Table III. It can be seen that the lower the styrene content in the copolymers and the higher the column temperature, the more ethanol in the mobile phase was required to elute the copolymers from the column.

Linear Gradient Elution. To separate the copolymers according to composition, linear gradient elution was performed as in the previous work (*8*). The examples for the separation of copolymers S–EA and S–EMA are shown in Figures 2 and 3, respectively. Gradient conditions are given in the Experimental Section. In Figure 2, copolymer S–EA I appeared at the interstitial volume at a column temperature of 40 °C. This means that copolymer S–EA I was not retained in the column at this column temperature. When the column

Table III. Ethanol Content (%) in the Mobile Phase Required for Copolymers to Elute 100% from a Silica Gel Column at Different Column Temperatures

	column temp, °C				column temp, °C		
sample	30	40	50	sample	30	40	50
S–MA				S–EMA			
I	2	3	4	I	2	2	2
II	3	5	6	II	2	4	5
III	5	6	7	III	4	5	6
IV	5	6	7	IV	4	6	7
S–EA				S–BMA			
I	1	1	2	I	2	2	2
II	2	2	3	II	2	2	2
III	3	4	5	III	2	2	3
IV	4	6	7	IV	2	3	3
S–BA							
I	1	1	1				
II	1	1	2				
III	2	2	2				
IV	2	2	2				

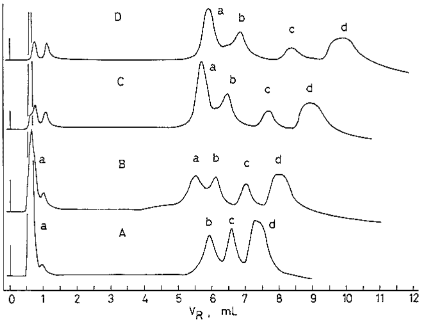

Figure 2. LAC chromatograms of S–EA copolymers obtained by the linear gradient elution method: column temperature (°C), (A) 40, (B) 50, (C) 60, (D) 70; sample, (a) S–EA I, (b) II, (c) III, (d) IV; detector attenuation, ×0.16 AUFS.

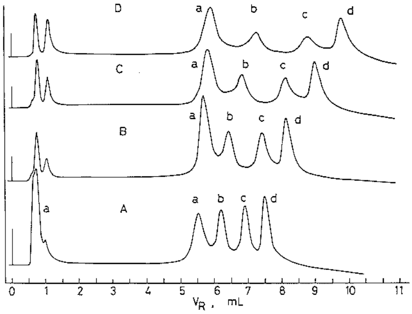

Figure 3. LAC chromatograms of S–EMA copolymers obtained by the linear gradient elution method: column temperature (°C), (A) 40, (B) 50, (C) 60, (D) 70; sample, (a) S–EMA I, (b) II, (c) III, (d) IV; detector attenuation, ×0.16 AUFS.

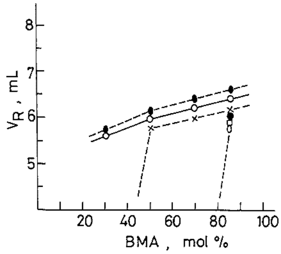

Figure 4. Relationship of retention volume vs BMA content of S–BMA copolymers at different column temperatures (°C): (⬮) 80, (○) 70, (×) 60, (●) 50, (□) 40, (0) 30.

temperature was increased to 50 °C, one-third of copolymer S–EA I eluted at a retention volume of around 5.5 mL and the rest at the interstitial volume. The composition of both fractions is assumed to be different, and that eluted later may have a higher ethyl acrylate content than that eluted earlier (*9*). At a column temperature of 60 °C, 100% copolymer S–EMA I eluted at around 5.5 mL, and as a result, a mixture of copolymers S–EA I, II, III, and IV was separated into four peaks. The resolution was increased when the column temperature was raised to 70 °C. In Figure 3, part of copolymer S–EMA I eluted at the interstitial volume at a column temperature 40 °C. When the column temperature was increased to 50 °C, the four copolymers S–EMA I, II, III, and IV were retained in the column at first and then eluted at the appropriate retention volumes. Resolution was increased with increasing column temperature.

Each peak in Figures 2 and 3 is broad compared with that in Figure 1. This broadening is assumed to be mainly due to CCD of the copolymers, not to MWD. Because the solutes that appear at the interstitial volume as in Figure 1 are not retained in the column and flow through interstices of silica gel beads in the column, and the difference in retention volume of each solute in Figures 2 and 3 is due to the difference in the composition of the solutes. The copolymers prepared in this work may have CCD as in the case of copolymer S–MMA (*10*). Molecular weight dependence of the retention volume is discussed later.

As the peaks are symmetrical, it is possible to assume that each peak retention volume represents the average composition of the copolymers. By use of this assumption, a calibration curve of the composition of the copolymers vs retention volume can be constructed. The approximate range of composition for copolymers S–EA I, II, III, and IV can be estimated as styrene mole percent as follows by using this calibration curve: I, 55–80; II, 42–70; III, 30–40; IV, 10–25. Similarly, for copolymers S–EMA I, II, III, and IV, the following values are estimated: I, 53–83; II, 40–65; III, 15–35; IV, 5–22. Peak resolution in Figures 2 and 3 was incomplete because of the broad CCD of the sample copolymers.

In gradient elution, the increase in the column temperature generally resulted in the improvement of peak resolution in addition to the retardation of solutes. In the case of S–BMA copolymers, however, peak resolution was not improved by the increase in the column temperature. Figure 4 shows the relationship between the composition and retention volume for copolymer S–BMA. The slopes of the plots at column temperatures of 60, 70, and 80 °C were almost the same, and the improvement of peak resolution was not observed. Dotted lines in Figure 4 mean that copolymer S–BMA I at a column temperature 60 °C and copolymers S–BMA I, II, and III at column temperatures of 30, 40, and 50 °C eluted at the interstitial volume.

Figure 5 shows the relationship of retention volume and column temperature for copolymer S–MA. The retention volume difference between two adjacent peaks increased with increasing column temperature and peak resolution was improved at higher column temperature as in the case of copolymers S–EA and S–EMA. Copolymer S–MA I at a column temperature of 30 °C eluted at the interstitial volume.

Fractionation by SEC. To determine the molecular weight dependence of peak retention volume, copolymers

Table IV. Characteristics of SEC Fractions of Copolymers S–EMA II and S–BMA II

fracn	V_R in SEC, mL	styrene compn,[b] mol %	mol wt[c] $10^{-4}\bar{M}_w$	$10^{-4}\bar{M}_n$	V_R in LAC, mL	peak width,[d] mL
			S–EMA II			
1	26.5–28.0	48.0	9.7	9.4	6.70	0.30
2	28.0–29.5	48.0	5.4	5.3	6.62	0.33
3	29.5–31.0	50.0	3.0	2.9	6.60	0.42
a	24.0–33.5	50.2	12.0	7.3	6.70	0.33
			S–BMA II			
1	25.5–27.0	49.0	14.9	14.4	5.72	0.26
2	27.0–28.5	48.5	7.8	7.7	5.68	0.26
3	28.5–30.0	52.0	4.0	3.8	5.67	0.29
a	24.0–32.5	50.3	13.8	7.1	5.70	0.26

[a] Unfractionated. [b] Composition (styrene mol %) was measured by infrared spectrophotometry. [c] Polystyrene equivalent molecular weight averages. [d] Peak width at half height.

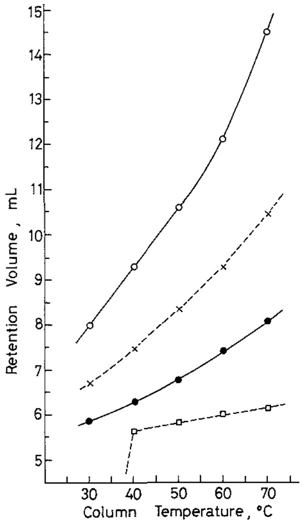

Figure 5. Plot of column temperature vs retention volume of S–MA copolymers: sample, (□) I, (●) II, (X) III, (O) IV.

S–EMA II and S–BMA II were fractionated by SEC. Three fractions in the middle of each chromatogram were obtained, and the rest of both ends of the chromatogram was neglected. Characteristics of these fractions are listed in Table IV. LAC was performed at a column temperature of 60 °C. The composition of copolymers in SEC fractions was measured by infrared spectrophotometry. Fractions were dried on a KBr disk, and film formed on the disk was subjected to the measurement of infrared spectra. The absorbance ratio of 1725 to 699 cm^{-1} was determined and the composition of a styrene content was calculated by using a calibration curve that was constructed with copolymers S–MMA of known composition by a similar method. An SEC calibration curve was constructed with a polystyrene standard of known molecular weight.

Peak retention volume of each fraction separated by LAC is almost the same, signifying negligible molecular weight dependence. The composition of fractions measured by infrared spectrophotometry is slightly different from that of unfractionated copolymers. This is probably caused by the use of a calibration curve constructed with S–MMA copolymers, but for comparison purposes, it does not disturb the conclusion.

ACKNOWLEDGMENT

We express our gratitude to T. Kawase for his technical assistance.

Registry No. (S)(MA) (copolymer), 25036-19-5; (S)(EMA) (copolymer), 26634-88-8; (S)(BMA) (copolymer), 25213-39-2; (S)(EA) (copolymer), 25066-97-1; (S)(BA) (copolymer), 25767-47-9.

LITERATURE CITED

(1) Teramachi, S.; Hasegawa, A.; Shima, Y.; Akatsuka, M.; Nakajima, M. *Macromolecules* **1979**, *12*, 992–996.
(2) Danielewicz, M.; Kubín, M. *J. Appl. Polym. Sci.* **1981**, *26*, 951–956.
(3) Glöckner, G.; van den Berg, J. H. M. *J. Chromatogr.* **1986**, *352*, 511–522.
(4) Sato, H.; Takeuchi, H.; Tanaka, Y. *Macromolecules* **1986**, *19*, 2613–2617.
(5) Glöckner, G.; van den Berg, J. H. M.; Meijerink, N. L. J.; Scholte, T. G.; Koningsveld, R. *Macromolecules* **1984**, *17*, 962–967.
(6) Sato, H.; Takeuchi, H.; Suzuki, S.; Tanaka, Y. *Macromol. Chem., Rapid Commun.* **1984**, *5*, 719–722.
(7) Mori, S.; Uno, Y.; Suzuki, M. *Anal. Chem.* **1986**, *58*, 303–307.
(8) Mori, S.; Uno, Y. *Anal. Chem.* **1987**, *59*, 90–94.
(9) Mori, S. *J. Chromatogr.* **1987**, *411*, 355–362.
(10) Mori, S.; Uno, Y. *J. Appl. Polym. Sci.* **1987**, *34*, 2689–2699.
(11) Mori, S. *Anal. Chem.* **1988**, *60*, 1125–1128.
(12) Mori, S. *Anal. Sci.* **1988**, *4*, 365–369.

RECEIVED for review January 31, 1989. Accepted May 19, 1989.

Voltammetric Reduction and Determination of Hydrogen Peroxide at an Electrode Modified with a Film Containing Palladium and Iridium

James A. Cox* and Robert K. Jaworski

Department of Chemistry, Miami University, Oxford, Ohio 45056

Cyclic voltammetry of a mixture containing 0.2 mM Na_2IrCl_6, 0.1 mM $PdCl_2$, 0.2 M K_2SO_4, and 0.1 M HCl between 1.2 and −0.3 V vs Ag/AgCl for five cycles at 50 mV s^{-1} yields a stable film on a glassy carbon electrode. The reduction of hydrogen peroxide in 0.1 M KCl is diffusion controlled at that modified electrode. Calibration curves obtained at a 100 mV s^{-1} scan rate are linear in the range 0.2–1.8 mM H_2O_2. The slope, 28 μA L $mmol^{-1}$, is independent of film thickness. Since dissolved oxygen is reduced at about the same potential as H_2O_2, −0.3 V, at the modified electrode, it will act as an interferent in solutions that are not deaerated; however, the currents are additive. A second limitation of the described procedure is that with the KCl electrolyte the immobilized film must be reoxidized prior to each measurement. Preliminary data are described which suggest that this problem is alleviated by switching to a basic supporting electrolyte.

INTRODUCTION

The electrochemical determination of hydrogen peroxide often is used in dip-type sensors and amperometric detectors for biomolecules which yield this species upon enzymatic oxidation. Present systems monitor the hydrogen peroxide by its oxidation at Pt, which was initially reported as a quantitative method by Harrar (*1*). Because the oxidation is performed at a quite positive potential, ca. 0.9 V vs SCE, severe interference can occur unless selectivity is achieved with an attendant separation method or through a chemical step. Oxidation by linear scan voltammetry at a glassy carbon electrode avoids some interference by metals which is observed at platinum (*2*); however, reduction at low overpotential perhaps would offer a better approach, in general.

The direct reduction of hydrogen peroxide at bare electrodes is not suited for analytical applications. A reverse pulse method in which the hydroxide that is produced upon the reduction of hydrogen peroxide depolarizes mercury permits quantitative determinations based upon the anodic current (*3*); however, this approach is incompatible with solutions which contain high concentrations of anions that also depolarize mercury. Immobilization of cytochrome *c* peroxidase (CCP) by adsorption onto pyrolytic graphite yields an electrode at which a cathodic current that is related to the hydrogen peroxide is produced. Armstrong and Lannon reported that voltammetric peak currents were proportional to hydrogen peroxide concentration up to at least 70 μM when gentamycin was present as a promoter (*4*), but a cathodic current was not observed in the absence of a promoter. Another limitation was that thermal denaturation of CCP was indicated at 25 °C. Paddock and Bowden (*5*) have reported direct electron transfer between a CCP-modified electrode and hydrogen peroxide. The half-wave potential at a rotating disk electrode was at 0.7 V vs SHE, a value related to the CCP couple. The system gradually became more irreversible at 4–7 °C; however, some electrocatalytic activity was observed after 2 months in storage. The use of a phosphate buffer rather than *N*-(2-hydroxyethyl)piperazine–*N*-2-ethanesulfonic acid and/or the difference in the polishing procedures may account for the disagreement between these reports on CCP.

Immobilization of $Ru(NH_3)_6^{2+}$ into a montmorillonite clay coating on graphite resulted in an electrode that mediated the reduction of hydrogen peroxide at −0.2 V vs SSCE (*6*). In this mechanistic study, only high concentrations of hydrogen peroxide were used, and the ruthenium complex at the micromolar level was included in the electrolyte to minimize its loss from the coating. Alkylsilanization of a gold electrode permitted the simultaneous detection of O_2 and H_2O_2 in a mixture because of the suppression of the first cathodic peak in the linear scan voltammetry of the latter species (*7*). Difficulty in obtaining complete surface coverage of the modifier was suggested, and analytical data were not reported.

Updike et al. (*8*) devised an indirect amperometric sensor for hydrogen peroxide that was based upon the use of an inorganic catalyst for its decomposition to oxygen. A catalyst, such as a sulfide or oxide of ruthenium, was impregnated into the membrane which coats a Clark-type oxygen electrode. The resulting system was suggested to have greater stability than would be realized with an enzyme such as catalase.

The present study describes a procedure based upon a modified electrode which has the necessary characteristics for measuring H_2O_2 with an amperometric flow cell. Because it promotes reduction of H_2O_2 at only −0.2 V vs SCE, has long-term stability, and can be used at ambient temperature, this electrode may be advantageous relative to other reported electrodes for this purpose.

EXPERIMENTAL SECTION

All chemicals used were ACS reagent grade, and they were not further purified. The $PdCl_2$ was obtained from Morton Thiokol, Inc.; Na_2IrCl_6, from Strem Chemicals, Inc.; and 30% H_2O_2, from Mallinckrodt, Inc. Other reagents were obtained from Fisher Scientific Co. The water was distilled in-house and then further purified with a Sybron/Barnstead NANOpure II system.

The experiments were performed with BAS 100 electrochemical analyzer (Bioanalytical Systems, Inc.). All potentials were measured and reported vs the Ag/AgCl reference electrode.

Glassy carbon electrodes (3.0 mm diameter, Bioanalytical Systems, Inc.) were polished with 1–15 μm (Morton Thiokol, Inc.), 0.3 μm, and 0.1 μm (Fisher Scientific Co.) alumina on a polishing cloth with water as the lubricant. The electrode was rinsed under a stream of water for 5 min before changing the size of the alumina and after the final polishing. Electrochemical pretreatment of the bare electrode before modification did not improve the properties of the modified electrode (*9*) and also did not have any effect on the hydrogen peroxide reduction reaction on the modified electrode; hence, it was not generally employed.

The electrode modification procedure was slightly different from that previously described (*9*). The plating solution was 0.2 mM Na_2IrCl_6, 0.1 mM $PdCl_2$, 0.2 M K_2SO_4, and 0.1 M HCl. A polished glassy carbon surface was cycled therein 5 times between 1.2 and −0.3 V at 50 mV s^{-1}. This resulted in a film of an iridium oxide that contained some Pd(II), presumably by isomorphic replacement (*9*). As the plating solution aged, more cycles were

0003-2700/89/0361-2176$01.50/0 © 1989 American Chemical Society

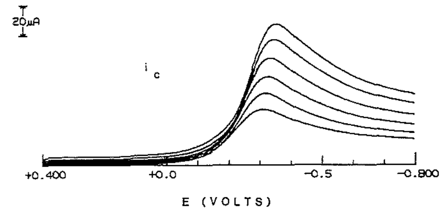

Figure 1. Effect of scan rate on the voltammetry of 1 mM H_2O_2, 0.1 M KCl at the modified electrode. Scan rates, 0.10, 0.16, 0.25, 0.36, 0.49, and 0.64 V s^{-1} for curves with the lowest-to-highest currents, in order.

needed to obtain a given film thickness, as indicated by the peak current for the reduction of the immobilized species. The plating solution was not deaerated. The modified electrode was stable for at least 12 days, whether stored in an electrolyte or used in the experiments. Over two hundred cyclic voltammetry experiments on H_2O_2 were performed with a single surface without any change in sensitivity; the film was intentionally destroyed after this sequence. Before recording a linear scan voltammogram the modified electrode was cycled between −0.8 and 0.9 V in the test solution; the number of cycles and the cathodic potential excursion were not important, but it was necessary to have the film in its oxidized state before initiating a reduction of the test species. This required a positive potential excursion beyond 0.5 V. Unless otherwise stated, all solutions were deaerated by purging with prepurified nitrogen.

RESULTS AND DISCUSSION

Linear scan voltammetry of the modified electrode from 0.4 to −0.7 V vs Ag/AgCl is featureless in deaerated 0.1 M KCl except for a peak at −0.2 V, which is apparently due to an immobilized species. In the presence of H_2O_2 the current near −0.2 V is increased and the corresponding anodic process at ca. 0.4 V is decreased. At a bare electrode, a current for the reduction of H_2O_2 is not observed in this range. These results suggest that a mediated reduction occurs at the modified electrode.

Figure 1 illustrates linear scan voltammograms for the mediated reduction in 0.1 M KCl. Over the scan rate range of 0.10–1.00 V s^{-1}, the peak current function varied only from 114 to 106 $\mu A\ s^{1/2}\ V^{-1/2}$ with a mean and relative standard deviation of 110 ± 2 $\mu A\ s^{1/2}\ V^{-1/2}$ at $n = 8$. The same results were obtained with K_2SO_4 as the supporting electrolyte. In this series of experiments, the film was only about 40% of the typical thickness so that the contribution of the current due to the reduction of the immobilized mediator was not a significant fraction of the total cathodic current (less than 10% of the peak current in the worst case, 1.00 V s^{-1}). Apparently, the current due to the reduction of H_2O_2 is limited by diffusion of the analyte in the bulk solution rather than penetration into the film, electron diffusion within the film, or the kinetics of the cross-exchange reaction.

Glassy carbon cannot be modified in a plating solution that does not contain Pd(II); however, platinum can be coated with an iridium oxide film in a mixture that contains 0.2 M K_2SO_4 and 0.2 mM Na_2IrCl_6 (*9*). The film is not stable, but the reduction of H_2O_2 by linear scan voltammetry at this surface is similar to that at the Pd-containing film. The role of palladium either is limited to stabilizing the film or is duplicated by the presence of the underlayer of platinum.

The above data allow two predictions. Because the current is limited by mass transport, a linear calibration curve is expected. Second, as the film apparently is highly conductive and possesses a sufficient concentration of mediator on its surface to obviate the need for substrate penetration, the slope of the working curve should be independent of the thickness of the immobilized layer.

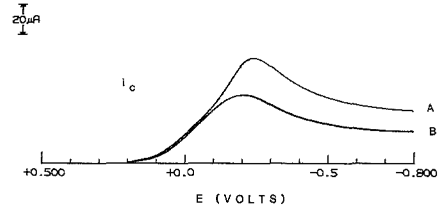

Figure 2. Linear scan voltammetry of 1.0 mM H_2O_2 in the presence and absence of dissolved oxygen at the modified electrode: curve A, air-saturated; curve B, deaerated; scan rate, 0.1 V s^{-1}; electrolyte, 0.1 M KCl.

A calibration curve was prepared in 0.1 M KCl at a scan rate of 100 mV s^{-1}. Total faradaic currents were measured at nine points in the range 0.20 to 1.80 mM H_2O_2. A linear least-squares fit yielded the following: slope, 28.0 ± 0.4 μA L $mmol^{-1}$; y intercept, 4.3 ± 0.5 μA; correlation coefficient, 0.999. The intercept current represents the current due to the immobilized mediator at the peak potential observed for the H_2O_2 reduction. With a film that was ca. 30% thinner (i.e., yielded a y intercept of 2.8 μA rather than 4.3 μA), the slope was essentially the same, 27.8 μA L $mmol^{-1}$. With KCl as the supporting electrolyte, the peak potential for the H_2O_2 reduction varied from −0.20 to −0.35 V from film to film. At any given modified electrode, it is constant. As suggested above, the sensitivity for H_2O_2 was also constant.

There are two general limitations of the method at its present stage of development. First, the reduction of dissolved oxygen overlaps that of H_2O_2. This is illustrated by Figure 2. A comparison of linear scan voltammograms of oxygen-containing and deaerated H_2O_2 solutions shows that the presence of dissolved oxygen increases the current at all potentials that are useful for determining H_2O_2. The slight shift in the peak potential results from the reduction peak for O_2 occurring at a more negative value than that for H_2O_2.

The currents due to the reductions of oxygen and hydrogen peroxide in Figure 2 are additive; for example, the slopes of calibration curves for hydrogen peroxide in the presence and absence of oxygen are 27.7 ± 0.6 and 27.8 ± 0.3 μA L $mmol^{-1}$, respectively. Because the peak potentials for the curves in Figure 2 are not coincidental, the former data are obtained at −0.24 V, and the latter, at −0.21 V. The correction procedure, subtraction of the contribution of the reduction of oxygen from the total current, requires knowledge of the oxygen concentration, which is readily obtained by an identical experiment but with an unmodified electrode. Use of a flow cell with a dual indicator electrode is the suggested approach. It is noteworthy that the reduction of oxygen at this modified electrode occurs in a single, four-electron step rather than through a pair of two-electron steps, the mechanism at a bare electrode, because the peroxide which is a product of the first step is electroactive at the modified electrode at potentials that are positive of −0.3 V.

The second problem is that, as mentioned in the Experimental Section, in 0.1 M KCl a preoxidation of the film must be employed in order to activate the modified surface. This would preclude the use of this electrode as a potentiostatic indicator in an amperometric sensor for high-performance liquid chromatography; a pulsed system would be required. However, we have preliminary data which suggest that this problem can be alleviated by use of basic solutions rather than neutral KCl solutions as the supporting electrolyte. In neutral KCl, cyclic voltammetry of the modified electrode results in cathodic and anodic peak potentials of −0.2 and 0.4 V, respectively, whereas at pH 12, the peak potentials are nearly coincidental at −0.3 V.

Table I. Linear Scan Voltammetry of H_2O_2 at the Modified Electrode in Basic Solution[a]

scan rate, V s^{-1}	$i_pv^{-1/2}$, $\mu A\ V^{-1/2}\ s^{1/2}$	E_p, V
0.01	32	–0.386
0.04	31	–0.419
0.09	31	–0.426
0.16	33	–0.428
0.25	33	–0.432
0.36	32	–0.436
0.49	33	–0.437
0.64	33	–0.439
0.81	32	–0.436
1.00	32	–0.439

[a] Solution 1.0 mM H_2O_2 in 1.0 M KOH.

The reduction of H_2O_2 at the modified electrode is dependent upon pH. In an acidic media or in buffered solutions at pH values below 10, measurable currents for the reduction of millimolar levels of H_2O_2 are not observed at potentials more positive than –0.5 V, the range where the mediated process is expected at the modified electrode. In neutral or basic unbuffered solutions and in buffers of pH 10 or greater, the reduction of H_2O_2 occurs, and the process is diffusion-controlled, the ideal case for an electroanalytical procedure. For example, the results for the reduction of H_2O_2 at the modified electrode in 1 M KOH, which are summarized in Table I, show that the function, $i_pv^{-1/2}$, is independent of scan rate, v, over a wide range. The peak potential does not change markedly with v and is only about 200 mV more negative than that in neutral solution. These observations suggest that KCl is a suitable supporting electrolyte only because the electrolysis consumes protons thereby causing the interfacial pH to increase. A detailed study of the behavior of this electrode in basic solution is presently under way.

LITERATURE CITED

(1) Harrar, J. E. *Anal. Chem.* **1963**, *35*, 893.
(2) Lundback, H.; Johanson, G. *Anal. Chim. Acta* **1981**, *128*, 141.
(3) Brestovisky, A.; KirowaEisner, E.; Osteryoung, J. *Anal. Chem.* **1983**, *55*, 2063.
(4) Armstrong, F. A.; Lannon, A. M. *J. Am. Chem. Soc.* **1987**, *109*, 7211.
(5) Paddock, R. M.; Bowden, E. F. *J. Electroanal. Chem.* **1989**, *260*, 487.
(6) Oyama, N.; Anson, F. C. *J. Electroanal. Chem.* **1986**, *199*, 467.
(7) Fujihira, M.; Muraki, H.; Aoyagui, S. *Bull. Chem. Soc. Jpn.* **1986**, *59*, 975.
(8) Updike, S. J.; Shults, M. C.; Kosovich, J. K.; Treichel, I.; Treichel, P. M. *Anal. Chem.* **1975**, *47*, 1457.
(9) Cox, J. A.; Gadd, S. E.; Das, B. K. *J. Electroanal. Chem.* **1988**, *256*, 199.

RECEIVED for review May 1, 1989. Accepted July 3, 1989. This work was supported by the National Institutes of Health through Grant 1R15GM39948-01.

Polarographic Methods for Ultratrace Cobalt Determination Based on Adsorption–Catalytic Effects in Cobalt(II)–Dioxime–Nitrite Systems[1]

Andrzej Bobrowski

Academy of Mining and Metallurgy, Institute of Material Science, Al. Mickiewicza 30, 30-059 Cracow, Poland

Polarographic curves obtained in the new systems Co(II)–dioxime/nioxime, α-benzil dioxime, dimethylglyoxime (DMG), α-furil dioxime/$NaNO_2$ are shown to be of an adsorption–catalytic nature. The direct current and differential pulse peak currents of cobalt increase in the Co(II)–dioxime–$NaNO_2$ systems by as much as 3 to 4 orders of magnitude, which enables the determination of ultratraces of Co with high sensitivity, precision, and selectivity. The catalytic effect does not appear in a solution containing the Ni(II)–dioxime complexes and $NaNO_2$. The highest sensitivity of the determination is obtained in the system Co(II)–nioxime–$NaNO_2$. The reduction of the Co(II)–nioxime complex in the presence of nitrite ions has been investigated and the effects of pH, buffer capacity, ionic strength, electrolyte composition, and instrumental parameters have been studied. The optimum conditions for the determination of cobalt in the presence of a great excess of Ni and Zn have been established. The determination limit, restricted by the amount of Co in the blank test, was 3×10^{-10} M Co. In the method a considerably smaller influence of Ni and Zn on Co determination was observed compared with the well-known adsorption voltammetric method of Co determination in the form of a Co–DMG complex.

During the last decade the adsorption–voltammetric method (AV) based on the adsorption accumulation of the dimethylglyoximate of Ni or Co on stationary electrodes such as a hanging mercury drop electrode (HMDE)/(*1–10*) mercury film electrode (*11, 12*), or a chemically modified electrode (*13*) have found wide application in trace analysis.

Opposite opinions exist concerning the mechanism of the electrode process involving the mentioned complexes. Some investigators (*14–20*) maintain that the reduction process of the complexes is accompanied by a catalytic evolution of hydrogen; others believe that the increase of the current observed for Ni and Co in the presence of dimethylglyoxime (DMG) is due exclusively to the adsorptive accumulation of the complexes on the electrode surface (*1, 8, 12, 21, 22*).

Although the AV method for Ni in the presence of DMG proved to be the most sensitive and suitable analytical technique, a great excess of zinc as well as nickel makes Co determination impossible (*4, 10, 14, 23, 24*). This limitation prompted the development of a still more sensitive and selective method for Co determination. The aim of earlier investigations carried out by the author (*25, 26*) using modern polarographic techniques (differential pulse, normal pulse, linear potential fast sweep) was to determine the polarographic properties of the Co–DMG complex as well as Co complexes with other dioximes such as 1,2-cyclohexanedione dioxime

---

[1] Dedicated to the memory of Professor W. Kemula.

0003-2700/89/0361-2178$01.50/0 © 1989 American Chemical Society

Table I. Influence of Dioxime and Nitrite on Co(II) Wave in 0.2 M Ammonia Buffer

		2 × 10^{-4} M α-furil dioxime		2 × 10^{-4} M DMG		2 × 10^{-5} M α-benzil dioxime		2 × 10^{-4} M nioxime	
	DPP	DPP	SDC	DPP	SDC	DPP	SDC	DPP	SDC
				Dioxime					
E_+ ($E_{1/2}$), V	−1209	−1067	−1059	−1180	−1171	−1057	−1041	−1180	−1182
$W_{1/2}$, mV	66	49	–	38	–	32	–	34	–
$I_p^{\text{Co–dioxime}}/I_p^{\text{Co}}$		153	88	31	7,6	120	30	115	30
				Dioxime + 0.5 M $NaNO_2$					
$W_{1/2}$, mV	81	48		47		39		38	
$I_p^{\text{Co–oxime–}NO_2^-}/I_p^{\text{Co–oxime}}$		2.3	2.5	66	57	13	21	45	190
$I_p^{\text{Co–oxime–}NO_2^-}/I_p^{\text{Co}}$	17.5	350	220	2050	430	1600 (2090)[a]	630	5200	5800

[a] 4 × 10^{-5} M α-benzil dioxime.

(nioxime) and α-furil dioxime. Although the Co complexes with α-furil dioxime and nioxime were examined by Nagniot (*21*) and Prokhorova et al. (*16*) using the direct current (DC) polarographic method, no distinct differences in the values of DC limiting currents of Co in the presence of DMG, nioxime, and α-furil dioxime were observed. The authors of the above papers, after comparing the properties of the Co–dioxime complexes found the Co–DMG complex to be the most suitable for Co determination. From the author's investigations (*25, 26*) it follows that an addition of nixoime or α-furil dioxime to ammonia buffer containing cobalt(II) ions causes an increase of the differential pulse peak current of Co by 2 orders of magnitude. The increase is significantly higher than that observed in a solution containing DMG. The observations have been recently confirmed by Donat and Bruland's work (*27*), in which the Co(II)–nioxime complex was chosen over Co(II)–DMG complex for the direct differential pulse adsorption voltammetric determination of Co ultratraces in seawater. However, the application of nioxime or α-furil dioxime for the Co polarographic determination enables about 100-fold increase of the sensitivity by the differential pulse or linear potential fast sweep technique, the detection limit of Co determination still being 1 × 10^{-8} M.

The purpose of the present paper is to examine the polarographic properties of the new adsorption–catalytic Co(II)–dioxime–$NaNO_2$ system with special attention to the most sensitive system Co(II)–nioxime–$NaNO_2$. In particular the conditions required for the polarographic and differential pulse adsorption voltammetric determination of lower cobalt concentration in the presence of a great excess of Ni and Zn in Co(II)–dioxime–NO_2^- systems are considered.

EXPERIMENTAL SECTION

Instrumentation. Sample direct current, differential pulse, and normal pulse polarographic and voltammetric curves were recorded by using a Digital PP-04 pulse polarograph (Unitra-Telpod, Poland) and XY recorder, KP-6801 (Kabid-Press, Poland). The DC polarograms were recorded by means of an OH-105 polarograph (Radelkis, Hungary), with the linear potential fast sweep polarograms obtained by using the OP-4 or OP-5 Digital Polarograph (Unitra-Telpod) with a variable voltage scan rate 0.275–40 V·s^{-1} and a digital read-out of the peak current and peak potential. All polarographic and voltammetric curves were recorded in a three-electrode system with dropping mercury electrode (DME), SMDE, or hanging mercury dropping electrode (HMDE) as a working electrode, a saturated calomel electrode as the reference, and a Pt wire as a counter electrode. The flow rate of the DME was 1.97 mg·s^{-1}. An N-517 Digital pH-meter (Mera-Elwro, Poland) was used for pH measurements. All measurements were carried out at 20 ± 2 °C.

Reagents. A stock 1 M ammonia buffer solution was prepared from Merck "Suprapur" grade ammonia and ammonium chloride. Other reagents were of analytical-grade purity. Dimethylglyoxime, nioxime, and α-furil dioxime were recrystallized from ethanol and their 0.01 M solutions were prepared by dissolving an appropriate amount in 96% ethanol.

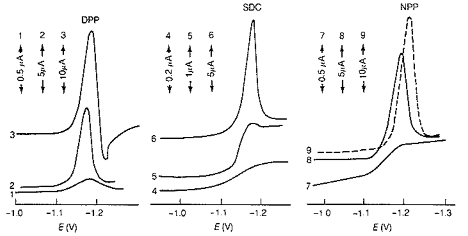

Figure 1. Magnitude and specificity of the nioxime and $NaNO_2$ enhancement. Polarogram of 5 × 10^{-6} M Co in 0.1 M ammonia buffer (curves 1, 4, 7) and in 0.1 M ammonia buffer, 1 × 10^{-4} M nioxime (curves, 5, 8); 1 × 10^{-7} M Co in 0.1 M ammonia buffer, 1 × 10^{-4} M nioxime, 0.5 M $NaNO_2$ (curves 3, 6, 9). Technique: DPP, curves 1–3; SDC, curves 4–6; NPP, curves 7–9.

The stock solution of α-benzil dioxime was prepared as a saturated solution in 96% ethanol.

$NaNO_2$ was recrystallized from water.

Double distilled water (quartz apparatus) was used.

Techniques. Solutions were purged with argon for 10 min before measurement and blanketed with argon during the experiment. Current–potential curves were recorded in the direct current (DC), sample DC (SDC), normal pulse (NPP), differential pulse (DPP), and linear potential fast sweep (LPSP) modes. A drop time of 2 s (SDC, NPP, and DPP), pulse amplitude (ΔE) of 50 mV (DPP), sampling time (ST) of 40 ms (DPP, NPP), and scan rates (v) of 27 mV·s^{-1} (DPP, NPP, and SDC) or 1 V·s^{-1} (LPSP) were employed in most investigations. Voltammetric and cyclic experiments were carried out at a HMDE or SMDE (Laboratorni Pristroje, Czechoslovakia), which was used in the hanging mercury drop electrode mode. Scan rates from the range of 10–200 mV·s^{-1} were applied in voltammetric studies.

RESULTS AND DISCUSSION

Preliminary Investigations. The hexamminocobaltous ions $Co(NH_3)_6^{2+}$ are irreversibly reduced in a supporting electrolyte of 0.1 M ammonia buffer. Thus the sensitivity of Co determination in this solution is rather small even using the DPP technique. When nioxime is present, a nearly 100-fold increase of the DPP peak current of Co is observed (Figure 1).

Addition of 0.5 M sodium nitrite causes a 45-fold increase of the Co peak current in relation to the peak current of the Co–nioxime complex, and nearly a 5200-fold increase in relation to the peak current of cobalt (Figure 1, Table I).

In all the polarographic techniques, a current increase is observed but the highest occurs for the SDC technique. The presence of $NaNO_2$ in ammonia-buffered solutions containing other, very strong Co(II)–dioxime complexes such as Co–DMG, Co–α-furil dioxime, or Co–α-benzil dioxime also causes the appearance or catalytic curves and a great increase in current (Figure 2). The latter together with the E_p (or $E_{1/2}$) values

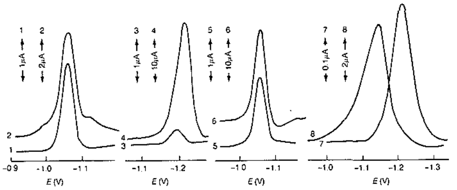

Figure 2. Enhancement effect of 0.5 M $NaNO_2$. The DPP curves of 5 × 10^{-7} M Co in 0.2 M ammonia buffer with addition: 2 × 10^{-4} M α-furil dioxime (curve 1); 2 × 10^{-4} M α-furil dioxime, 0.5 M $NaNO_2$ (curve 2); 2 × 10^{-5} M α-benzil dioxime (curve 3); 2 × 10^{-5} M α-benzil dioxime, 0.5 M $NaNO_2$ (curve 4); 2 × 10^{-4} M DMG (curve 5); 2 × 10^{-4} M DMG, 0.5 M $NaNO_2$ (curve 6); 1 × 10^{-5} M Co, 0.2 M ammonia buffer (curve 7); 1 × 10^{-5} M Co, 0.2 M ammonia buffer, 0.5 M $NaNO_2$ (curve 8).

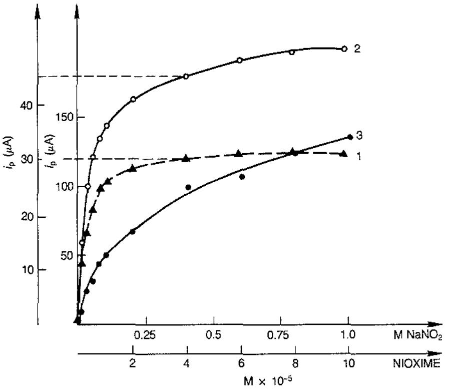

Figure 3. Peak current dependence of Co(II) on nioxime and $NaNO_2$ concentration. Relationship of SDC (curve 1) and DPP (curve 2) peak current i_p^{Co} vs $C_{nioxime}$ for 2 × 10^{-7} M Co(II) in supporting electrolyte 0.1 M ammonia buffer, 0.5 M $NaNO_2$. Relationship of DPP peak current i_p^{Co} vs C_{NaNO_2} for 1 × 10^{-6} M Co(II) in supporting electrolyte 0.1 M ammonia buffer, 1 × 10^{-4} M nioxime.

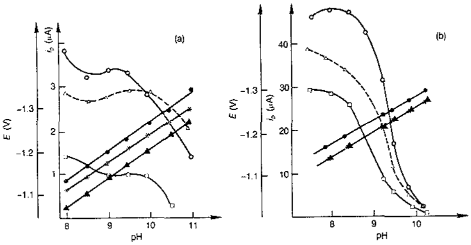

Figure 4. Dependence of Co(II) peak current and peak potential on pH. Effect of pH on the SDC limiting current (□) and half-wave potential (▲), DPP peak current (○) and peak potential (*), or LPSP peak current (△) and peak potential (●) for 1 × 10^{-6} M Co in 2 × 10^{-4} M nioxime, 0.1 M ammonia buffer (a) and for 1 × 10^{-7} M Co in 1 × 10^{-4} M nioxime, 0.5 M $NaNO_2$, 0.1 M ammonia buffer (b).

and the DPP peak widths ($W_{1/2}$) of cobalt after the introduction of dioxime or dioxime and $NaNO_2$ into the ammonia buffer solutions are listed in Table I. In the presence of dioxime the current effects increase as follows: Co–DMG < Co–nioxime = Co–α-benzil dioxime < Co–α-furil dioxime. With added 0.5 M $NaNO_2$ the peak currents increase in the order Co–α-furil dioxime–NO_2^- < Co–α-benzil dioxime–NO_2^- = Co–DMG–NO_2^- < Co–nioxime–NO_2^-. Table I also contains the data characterizing a simple system Co(II)–$(NH_3)_6$–NO_2^-, from which it follows that an addition of 0.5 M $NaNO_2$ to the solution of cobalt in ammonia buffer causes a 17.5-fold increase of its peak current (Figure 2, curves 7 and 8).

The effect of the complex adsorption is pronounced on the NPP curves (Figure 1, curve 8). In the ammonia buffer solution containing both dioxime and $NaNO_2$, the shape of the DC polarographic curves is in a peaked wave form (Figure 1, curve 6), which might indicate the adsorption–catalytic character of the electrode process. The greatest current effect of cobalt occurs in the Co(II)–nioxime system (Table I). For this reason further investigation was concentrated on this system.

Polarographic Properties of the Co(II)–Nioxime–NO_2^- System and Characteristics of the Enhancement Phenomenon. The Effect of $NaNO_2$ and Nioxime Concentration. Figure 3 shows the dependence of the peak current of Co in the Co(II)–nioxime–NO_2^- system on the concentration of sodium nitrite (curve 3) and on nioxime concentration (curves 1 and 2). The Co peak current showed a strong dependence on the $NaNO_2$ concentration in the range 0.01–1 M. The catalytic effect (Δi_{cat}) expressed as the difference between DPP peak current of Co in the presence and absence of NO_2^- ions can be presented by the following equation (calculated by the least-squares method):

$$\Delta i_{cat} = 10^{2.15} C_{NaNO_2}^{0.52}$$

The above relationship is very close to the theoretical dependence of the catalytic current on the oxidant concentration $\Delta i_{cat} \approx Z_{x=0}^{1/2}$ for the pseudo-first-order polarographic catalytic process (*28*, *29*). Within the concentration range 1 × 10^{-2} to 1 M $NaNO_2$ the peak potential of Co is a linear function of log C_{NaNO_2}, and the change in the peak potential ΔE_p determined by either the DPP or LPSP technique equals −20 mV × Δ log C_{NaNO_2}. In the presence of a constant nitrite concentration, the Co peak current distinctly increases with increasing concentration of nioxime, attaining an almost constant value in the nioxime concentration range of 5 × 10^{-5} to 1 × 10^{-4} M. The above dependence is similar in form to the Langmuir adsorption isotherm. The peak potential of Co in the examined concentration range of nioxime 1 × 10^{-6} to 1 × 10^{-4} M) becomes slightly shifted by about 20 mV toward more negative potentials.

Effects of pH, Buffer Capacity, and Ionic Strength. The effect of pH on the peak potential and the peak current of cobalt in a solution containing 1 × 10^{-7} M Co, 0.1 M ammonia buffer, 1 × 10^{-4} M nioxime, and 0.5 M $NaNO_2$ was examined by SDC, DPP, and LPSP. Appropriate pH values were established by adding hydrochloric acid or sodium hydroxide. For the sake of comparison, an analogous dependence of i_p vs pH was obtained also for the Co(II)–nioxime system (Figure 4A). As seen from Figure 4, the electrode processes for the Co(II)–nioxime and Co(II)–nioxime–NO_2^- systems are pH dependent and this is particularly pronounced for the Co(II)–nioxime–NO_2^- system. For this system the maximal current effects are observed at pH ≈ 8, and above this pH the peak currents sharply decrease. At pH = 10 they attain merely a few percent of the current values obtained at pH = 8. The above dependence differs from the one for the Co(II)–nioxime system, for which the maximal peak currents appear for the pH range 8.5–9.5. In this system a significant decrease of peak current is observed above pH = 10. The peak potentials (or half-wave potentials) are linearly shifted toward more negative potentials with increasing pH for the system Co(II)–nioxime and Co(II)–nioxime–NO_2^- (Figure 4). For the Co(II)–nioxime–NO_2^- system the slope $\Delta E_p/\Delta pH$ is equal to −53.6 mV/pH (SDC), −57.1 mV/pH (DPP), and −56.4 mV/pH (LPSP), whereas for the Co(II)–nioxime system the following values of the slope were obtained: −62.6 mV/pH (SDC), −63.7

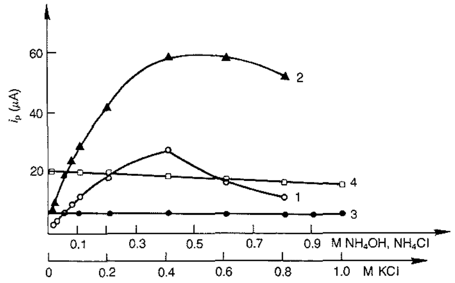

Figure 5. Influence of buffer concentration (curves 1 and 2) and ionic strength (curves 3 and 4) on Co peak current in Co(II)–nioxime–NO_2^- system: SDC (curve 1) and DPP (curve 2) of 1 × 10^{-7} M Co in 1 × 10^{-4} M nioxime, 0.5 M $NaNO_2$; SDC (curve 3) and DPP (curve 4) of 5 × 10^{-8} M Co in 1 × 10^{-4} M nioxime, 0.1 M ammonia buffer, 0.5 M $NaNO_2$.

mV/pH (DPP), and −66.2 mV/pH (LPSP). The decrease of the Co peak currents with increasing pH in the Co(II)–nioxime and Co(II)–nioxime–NO_2^- systems is likely to be due to decreased concentration of hydrogen ions taking part in the electrode reaction. It may be assumed that the rate of chemical reaction causing the occurrence of a catalytic current in the system Co(II)–nioxime–NO_2^- depends on hydrogen ion concentration and hence the rapid drop in current above pH 8. The change of Co peak potential with changing pH is also evidence of the protonation reaction in the overall electrode process.

The effects of buffer capacity and ionic strength on the Co peak current in the Co(II)–nioxime–NO_2^- system are illustrated in Figure 5. The ionic strength was fixed by addition of KCl and the buffer capacity was controlled by varying the concentration of ammonia buffer. An increase of the buffer capacity produced a change in the shape of the Co polarographic curves and caused a great increase of the peak current within the buffer concentration range of 0.01–0.4 M. With further increases in the ammonia buffer concentration, the competitive reaction of the formation of ammonia complexes of cobalt brought about a decrease of the peak currents in the Co(II)–nioxime–NO_2^- system.

Effect of Temperature and Instrumental Parameters. Within the temperature range 20–40 °C a very slight influence of temperature on the current effects of Co was observed when employing the SDC and DPP techniques in a solution containing 5 × 10^{-8} M Co, 1 × 10^{-4} M nioxime, 0.05 M $NaNO_2$, and 0.1 M ammonia buffer. In this range the temperature coefficient of the SDC peak current amounts to +0.2% and that of the DPP peak current is negative and amounts to −0.3%.

The effect of the head mercury on the peak current of cobalt $i_p = kh^p$ was examined by DPP in a solution containing 5 × 10^{-7} M Co, 1 × 10^{-4} M nioxime, 0.5 M $NaNO_2$, and 0.2 M ammonia buffer. The exponent p has the value 0.08 for the Co(II)–nioxime–NO_2^- system as well as the Co(II)–DMG–NO_2^- system. These low values of p are evidence of a catalytic reaction in the Co(II)–dioxime–NO_2^- system. The DPP peak current of Co increases linearly with pulse amplitude from 5 to 50 mV. When the influence of the voltage scan rate (from 0.3 to 2 V.s^{-1}) on the Co peak currents was investigated, a slightly modified value of the Semerano coefficient in the form $S = [[\Delta \log i_p)/A]/\Delta \log v$ was determined to compensate for the influence of the increase of the DME surface during the scan on the value of the Co peak current. For 3 × 10^{-4} M Co in 0.1 M ammonia buffer $S = 0.50$; and for 2 × 10^{-6} M Co in 1 × 10^{-4} M nioxime, 0.1 M ammonia buffer $S = 0.64$. The plots i_p vs v are more complicated in the examined system Co(II)–nioxime–NO_2^- and also depend on the Co concentration. For 2 × 10^{-6} M Co, the Semerano coefficient equaled 0.05 in the range v 0.3–1 V·s^{-1} and 0.49 with v 1–2 V·s^{-1}.

Adsorption Properties of the Examined Co System. Both in Co–nioxime, Co–NO_2^- as well as in the complex Co–dioxime–NO_2^- system, cobalt undergoes adsorptive accumulation. The investigations of the adsorptive properties of Co–dioxime complexes in the presence and absence of nitrite were carried out at the HMDE in mixed and nonmixed solutions using the SDC AV, DP AV, and LPS AV technique. The influence of adsorption time on the Co peak current for the Co(II)–dioxime and Co(II)–dioxime–NO_2^- systems is shown in Figure 6. As in the case of the Co(II)–dioxime systems (25), and the Co(II)–dioxime–NO_2^- and Co(II)–NO_2^- systems, adsorption is one of the main factors causing the large Co current increase. The effect is also manifested in pulse and fast sweep polarographic techniques. The adsorption-voltammetric peak currents of Co depend on the accumulation potential and are the greatest for potentials from −0.4 V to −0.8 V, both for the Co(II)–nioxime and Co(II)–nioxime–NO_2^- systems.

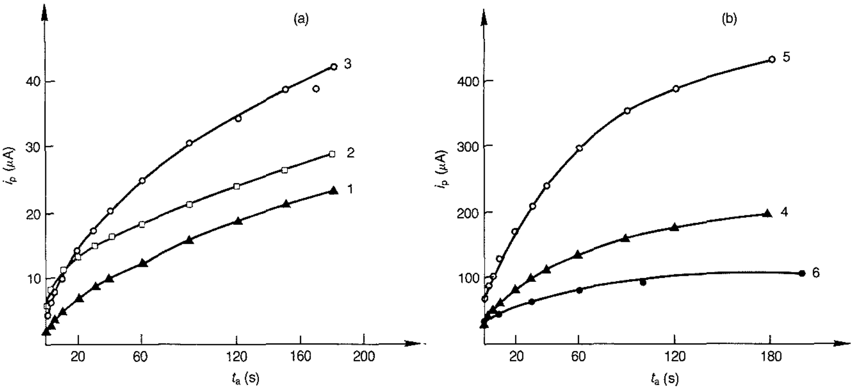

Figure 6. LPSAV (curves 1–5) and DC AV (curve 6) peak current dependence of Co on the time of adsorption t_a in 0.1 M ammonia buffer in absence (A) and presence (B) of nitrite. Scan rate: 1 V·s^{-1} (curves 1–5), 27 mV·s^{-1} (curve 6). 1 × 10^{-6} M Co, 2 × 10^{-4} M DMG (curve 1); 1 × 10^{-6} M Co, 2 × 10^{-4} M α-furil dioxime (curve 2); 1 × 10^{-6} M Co, 2 × 10^{-4} M nioxime (curve 3); 1 × 10^{-6} M Co, 2 × 10^{-4} M DMG, 0.5 M $NaNO_2$ (curve 4); 1 × 10^{-6} M Co, 2 × 10^{-4} M nioxime, 0.5 M $NaNO_2$ (curve 5); 1 × 10^{-7} M Co, 2 × 10^{-4} M nioxime, 0.5 M $NaNO_2$ (curve 6).

Table II. Summary of Regressional Parameters for Co(II) Calibration Plots

data set	supporting electrolyte	technique	concn range, M	slope (m), $\mu A/\mu M$	intercept, μA	corr coeff r	no. of data points N
1	0.1 M ammonia buffer, 1×10^{-4} M nioxime, 0.5 M $NaNO_2$	DPP	2.5×10^{-9} to 2×10^{-8}	4.4×10^2	0.37	0.9996	5
2		DPP	2.5×10^{-9} to 1×10^{-7}	2.5×10^2	1.63	0.9967	9
3		SDC	2.5×10^{-9} to 2×10^{-8}	1.07×10^2	0.06	0.9995	5
4	0.025 M ammonia buffer, 1×10^{-4} M nioxime, 0.5 M $NaNO_2$	DPP	5×10^{-10} to 6×10^{-9}	1.96×10^2	0.06	0.9996	8
5[a]	0.1 M ammonia buffer, 1×10^{-4} M nioxime	DPP	1×10^{-8} to 2×10^{-7}	2.4	0.04	0.9995	7
6[a]	0.1 M ammonia buffer	DPP	5×10^{-7} to 5×10^{-5}	3.8×10^{-2}	0.05	0.9996	8

[a] Different capillaries were used in sets 1–4, 5, and 6.

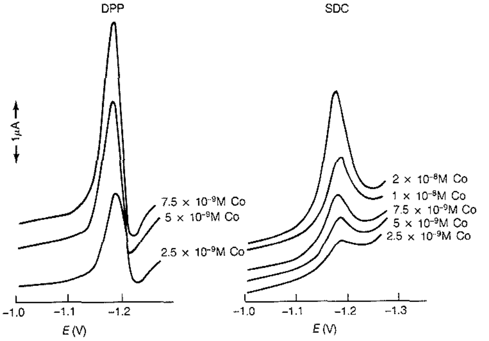

Figure 7. Typical DPP and SDC polarograms for a series of Co(II) concentrations in supporting electrolyte 0.1 M ammonia buffer, 1×10^{-4} M nioxime, 0.3 M $NaNO_2$.

Analytical Applications. Sensitivity, Linear Range, and Detection Limit. From the data listed in Table I it follows that in the Co(II)–dioxime–NO_2^- system there occurs an increase in the analytical signal of Co by 10^3 to 10^4, that is responsible for the fast that, by using the polarographic techniques such as SDC, DPP, and LPSP, excellent peak characteristics and high values of the peak current are obtained even at 10^{-10}–10^{-9} M Co (Figure 7). Because of the adsorptive character of the waves, the concentration dependence is nonlinear (Figure 8, Table II), although a linear dependence is obtained in the range 1×10^{-9} to 1×10^{-8}, M Co with detection up to 10^{-6} M Co possible. Regression parameters calculated for several calibration curves for Co obtained by DPP and SDC polarography in various supporting electrolytes are summarized in Table II. The slope of the calibration curves in the presence of nioxime and $NaNO_2$ was over 100 times larger than that observed in the presence of nioxime and about 10 000 times larger than that observed in its absence (Table II). In the solution containing 0.1 M ammonia buffer, 1×10^{-4} M nioxime, and 0.5 M $NaNO_2$ the detection limit restricted by the blank was 0.04 ppb. A drop in the concentration of ammonia buffer in the supporting electrolyte to 0.025 M allowed a reduction in the amount of Co in the blank (Figure 8). The limit of Co determination by the DPP method in a supporting electrolyte containing 0.025 M ammonia buffer, 1×10^{-4} M nioxime, and 0.5 M $NaNO_2$ (governed by the Co content in distilled water, reagents and laboratory atmosphere) was 3×10^{-10} (0.02 ppb).

The good reproducibility is mostly due to the high values of Co peak currents in the Co(II)–nioxime–NO_2^- system. The relative standard deviation of the DPP or SDC peak currents at cobalt concentrations of the order 10^{-10}–10^{-9} M was $S_r \leqslant 4\%$.

Interferences. In the polarographic determination of Co in the adsorption–catalytic systems Co(II)–dioxime–NO_2^-, interferences may be caused by the competitive adsorption of ions or their complexes on the electrode surface and competitive participation in the catalytic reaction. They may be also the result of the appearance of reduction peaks adjacent to the Co peak. Since in the adsorption–catalytic systems Co(II)–dioxime–NO_2^- the Co peak currents are from 350 (α-furil dioxime) to 5200 (nioxime) times higher than the Co currents observed for simple diffusion processes (Tables I and II), the influence of a large excess of another depolarizer—even with the peak potential very similar to the Co peak potential—on the Co determination will be small. The present study of the influence of other elements on the results of Co determination was focused on the effects of Ni and Zn on Co determination.

The values of the Zn potential and peak current do not

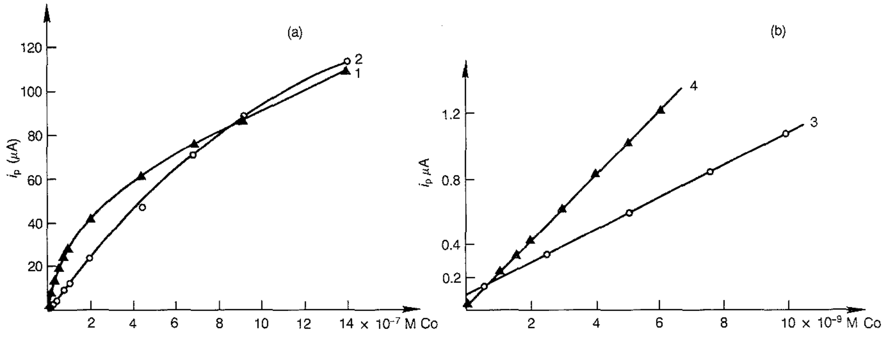

Figure 8. Dependence of DPP (curves 1 and 4) and SDC (curves 2 and 3) Co(II) peak current on the Co(II) concentration in 0.1 M ammonia buffer, 1×10^{-4} M nioxime, 0.5 M $NaNO_2$ (curves 1–3) or in 0.025 M ammonia buffer, 1×10^{-4} M nioxime, 0.5 M $NaNO_2$ (curve 4).

Table III. Differences in DPP Peak Potential (mV) of Ni and Co and Zn and Co

	0.1 M ammonia buffer, 0.5 M $NaNO_2$			
	+1 × 10^{-4} M nioxime	+1 × 10^{-4} M DMG	+2 × 10^{-5} M α-benzil dioxime	+1 × 10^{-4} M α-furil dioxime
E_p^{Ni-Co}	–	+170	–	+180
E_p^{Co-Zn}	–80	–70	–170	–210

change in a supporting electrolyte of 0.1 M ammonia buffer containing the examined dioximes whereas the value of the DPP peak current of Ni in 0.1 M ammonia buffer increases 40 to 100 times after addition of DMG or α-furil dioxime, respectively. An addition of 0.5 M $NaNO_2$ to the solution containing 0.1 M ammonia buffer and 1 × 10^{-4} M dioxime (DMG, α-furil dioxime, nioxime, α-benzil dioxime) does not introduce any changes in the values or the peak currents of Zn ions or the Ni(II)–dioxime complexes. The voltammetric properties of Co(II)–dioxime or Ni(II)–dioxime complexes are similar, whereas in the presence of $NaNO_2$ an observable difference occurs. It is only Co that induces a catalytic reaction in the composite system Co(II)–dioxime–NO_2^-. Table III lists the values of the difference between the Ni and Co peak potentials and those of Co and Zn. The influence of Ni on the determination of Co in the Co(II)–dioxime–NO_2^- system will depend on the chemical nature of the dioxime (Table III). The solution of 0.1 M ammonia buffer, 1 × 10^{-4} M nioxime, and 0.5 M $NaNO_2$ seems to be the most suitable for Co determination in the presence of a very high excess of Ni. In the above solution the Ni wave is not observed, and the limiting factor is the Ni concentration (about 1 × 10^{-5} M Ni), at which nickel nioximate is precipitated, and not the ratio of the Ni and Co concentrations. The precipitated nickel nioximate may cause sorption of Co from the solution and an error in Co determination.

At a 500-fold excess of Ni with respect to Co, no influence of Ni on the DPP peak current of Co was observed in 0.1 M ammonia buffer, 1 × 10^{-4} M nioxime, and 0.5 M $NaNO_2$. With a great excess of Ni present in a simultaneous polarographic determination of Co and Ni one might recommend 0.1 M ammonia buffer, 0.5 M $NaNO_2$ containing 1 × 10^{-4} M DMG or α-furil dioxime (Figure 9).

Zinc has a rather slight influence on the determination of cobalt in solutions containing ammonia buffer, $NaNO_2$, and one of the examined dioximes (Figure 9). The most appropriate is the supporting electrolyte containing 0.1 M ammonia buffer, 2 × 10^{-5} M α-benzil dioxime, and 0.5 M $NaNO_2$ in which the difference between the DPP peak potentials of Co and Zn amounts to $\Delta E \approx 170$ mV, and the Co peak current exceeds the Zn peak current more than 1000 times at equimolar concentration of both elements. In spite of a small difference in the peak potentials ($\Delta E_p \approx 80$ mV) it is possible to determine Co in the presence of a great excess of Zn also in a solution containing 0.1 M ammonia buffer, 1 × 10^{-4} M nioxime, 0.5 M $NaNO_2$. As it has been found experimentally in this solution, the Zn and Co peak currents are not comparable until the Zn concentration exceeds 1000 times that of Co. Hence in ammonia buffer containing nioxime and $NaNO_2$, even a 2000-fold excess of zinc causes only a slight error (≤10%) in the determination of Co.

A 10-fold excess of Fe(III) ions present in the supporting electrolyte 0.1 M ammonia buffer, 1 × 10^{-4} M nioxime and 0.5 M $NaNO_2$ results in an error in cobalt determination. This is due to the formation of a complex system Fe(III)–nioxime–NO_2^- by Fe(III) producing a broad peak. This system has not been examined to a great extent in the present study.

An addition of Triton X-100 to the solution containing 5 × 10^{-8} M Co in 0.1 M ammonia buffer, 1 × 10^{-4} M nioxime, and 0.5 M $NaNO_2$ caused a 60% decrease in the Co DPP peak current, but not until the Triton X-100 concentration exceeded 1 × 10^{-3}%.

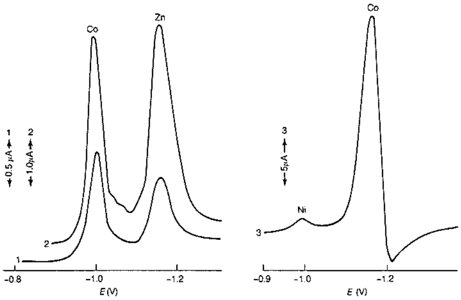

Figure 9. Examples of DPP curves of the following systems: 2 × 10^{-8} M Co, 4 × 10^{-5} M Zn in 0.1 M ammonia buffer, 1 × 10^{-4} M α-furil dioxime, 0.5 M $NaNO_2$ (curve 1); 1 × 10^{-7} M Co + 1.1 × 10^{-4} M Zn in 0.1 M ammonia buffer, 2 × 10^{-5} M α-benzil dioxime, 0.5 M $NaNO_2$ (curve 2); 1 × 10^{-6} M Ni, 5 × 10^{-7} M Co in 0.2 M ammonia buffer, 2 × 10^{-4} M DMG, 0.5 M $NaNO_2$ (curve 3).

Electroactive Process in the Presence of Dioxime and Nitrite. In the Co(II)–dioxime–NO_2^- system, the reduction mechanism seems to be a complex one and only some suggestions can be made concerning the catalytic reaction. Already the description of the reduction mechanism of the Co–DMG or Ni–DMG systems presents many difficulties (*14, 20, 22, 30, 31*), and the Co–DMG mechanism has not been fully explained until now.

Experimental observations indicate that the electrode process of the Co–DMG complex is not a simple adsorption process (*9, 32, 33*). For Co(II)–dioxime and also the Co(II)–dioxime–NO_2^- systems, there occurs a strong adsorption of the cobalt complexes on the electrode surface, induced by the ligand adsorption (Figure 6). It seems probable that in the presence of $NaNO_2$ several different pathways for the reduction of Co species may occur. Besides the adsorption and reduction of the Co(II)–dioxime complexes, catalytic regeneration of the reacting species takes place in the presence of $NaNO_2$.

The above effect is evidenced in the DC polarographic curve (Figures 1 and 7), by the great enhancement of the Co peak current after the introduction of $NaNO_2$ into the solutions containing Co(II)–dioxime complexes (Figure 3), and by the very slight effect of mercury head and voltage scan rate on Co peak current. The catalytic current of the system is related to the reduction of NO_2^-, which is induced by the adsorbed Co complexes.

An additional argument in favor of the catalytic character of the process in the Co(II)–dioxime–NO_2^- system is the current increase in ammonia buffer, containing only $NaNO_2$, as reported in the study by Ngok Khue (*34*); this was confirmed in the present study carried out by the DPP techniques (Figure 2, Table I). Ngok Khue suggests that the zerovalent Co(0), formed on the electrode as a result of the reduction, becomes oxidized by the NO_2^- ions in the catalytic process according to a scheme postulated earlier for the catalytic reduction of chlorate or nitrite with participation of a Fe(0) hydroxo complex deposited at the electrode surface (*35, 36*). The proposed mechanism might also be applied for the description of an electrode process of the system Co(II)–dioxime–NO_2^- according to the scheme

$$\mathrm{Co^{II}(HA)_{2\,(ads)}} + 2e^- \rightarrow \mathrm{Co^{0}(HA)_{2\,(ads)}} \qquad (1)$$

$$\mathrm{Co^{0}(HA)_{2\,(ads)}} + \mathrm{NO_2^-} + m\mathrm{H^+} \rightarrow \mathrm{Co^{II}(HA)_2} + \mathrm{Red} \qquad (2)$$

where HA denotes a neutral molecule of dioxime and Red is a product of the reduction of NO_2^-.

One might also plausibly assume that at a high $NaNO_2$ concentration (0.01–1 M) composite complexes $Co^{II}(HA)_2NO_2$ are formed near the electrode surface as a result of replacing the ammonia in the coordination sphere of cobalt by the NO_2^- ions. The general theory of the catalytic processes assuming the formation of polarographically active composite complexes between the metal complex and inactive oxidant has been presented by Miliavski and Siniakova (*37*, *38*). In the composite complex the NO_2^- group undergoes reduction and an active complex $Co^{II}(HA)_2^*$ is formed, which attaches the subsequent NO_2^- groups

$$Co^{II}(NH_3)_2(HA)_{2\,(ads)} + NO_2^- \rightarrow Co^{II}(NH_3)(HA)_2NO_{2\,(ads)} + NH_3 \qquad (3)$$

$$Co^{II}(NH_3)(HA)_2NO_{2\,ads)} + ne^- - XH^+ \rightarrow Co^{II}(NH_3)(HA)_2^* + \text{Red} \qquad (4)$$

$$Co^{II}(NH_3)(HA)_2^* + NO_2^- \rightarrow Co^{II}(NH_3)(HA)_2NO_2 \qquad (5)$$

where $Co^{II}NH_3(HA)_2NO_2$ is the polarographically active composite complex.

The cyclic regeneration of an electroactive Co(II) species accounts for the enhancement of the Co peak current in the simple Co(II)–NO_2^- system as well as in the composite system Co(II)–dioxime–NO_2^- (Table I).

A similar scheme to that proposed in eq 3–5 has been used by Zarebski to explain the catalytic process in the system Co(II)–En–NO_2^- (*39*) and by other authors to explain the catalytic processes for the systems Fe(II)–H_2O_2, Mo(VI)–complexes–$KClO_3$, and W(IV)–complexes and hydroxylamine (*36*).

In conclusion it may be stated that DPP or even DC polarography offers a simple and sensitive method for the determination of the cobalt ultratraces in the presence of a great excess of nickel and zinc by means of the adsorption–catalytic system Co(II)–dioxime (nioxime, DMG, α-benzil dioxime)–NO_2^-. The highest sensitivity of the determination is obtained in the system Co(II)–nioxime–NO_2^-. In this system the Co peak current is the highest at the ammonia buffer concentration 0.3–0.4 M, pH = 8, nioxime concentration 1×10^{-4} M, and $NaNO_2$ concentration 1 M. Considering the content of Co in the blank, the optimal composition of the supporting electrolyte for the polarographic determination of Co is as follows: 0.025–0.1 M ammonia buffer (pH = 8–9), 1×10^{-4} M nioxime, 0.5 M $NaNO_2$.

Registry No. DMG, 95-45-4; Co, 7440-48-4; $NaNO_2$, 7632-00-0; Zn, 7440-66-6; Ni, 7440-02-0; Co(nioxime)$_2$, 36451-50-0; Co(α-benzil dioxime)$_2$, 63994-24-1; Co(DMG)$_2$, 36451-49-7; Co(α-furyl dioxime)$_2$, 15051-16-8; nioxime, 492-99-9; α-benzil dioxime, 23873-81-6; α-furyl dioxime, 522-27-0.

LITERATURE CITED

(1) Philar, B.; Valenta, P.; Nurberg, H. W. *Fresenius' Z. Anal. Chem.* **1981**, *307*, 337.
(2) Golimowski, J.; Nürnberg, H. W.; Valenta, P. *Lebensmittelchem. Gerichtl. Chem.* **1980**, *34*, 116.
(3) Ostapczuk, P.; Goedde, M.; Stoppler, M.; Nürnberg, H. W. *Fresenius' Z. Anal. Chem.* **1984**, *316*, 252.
(4) Golimowski, J.; Cendrowska, M. *Chem. Anal.* **1985**, *30*, 777.
(5) Nürnberg, H. W. *Pure Appl. Chem.* **1982**, *54*, 853.
(6) Adeloju, S. B.; Bond, A. M.; Briggs, M. H. *Anal. Chem.* **1985**, *57*, 1386.
(7) Adeloju, S. B.; Bond, A. M. *Anal. Chem.* **1985**, *57*, 1728.
(8) Nürnberg, H. W. *Sci. Total Environ.* **1984**, *37*, 9.
(9) Torrance, K.; Gatford, C. *Talanta* **1985**, *32*, 273.
(10) Adeloju, S. B.; Bond, A. M.; Briggs, M. H. *Anal. Chim. Acta* **1984**, *164*, 181.
(11) Eskilsson, H.; Horaldsson, C.; Jagner, D. *Anal. Chim. Acta* **1985**, *175*, 79.
(12) Braun, H.; Metzger, M. *Fresenius' Z. Anal. Chem.* **1984**, *318*, 321.
(13) Baldwin, R. F.; Christensen, I. K.; Kryger, L. *Anal. Chem.* **1986**, *58*, 1790.
(14) Vinogradova, E. H.; Prokhorova, G. V. *Zh. Anal. Khim.* **1968**, *23*, 711.
(15) Vinogradova, E. H.; Prokhorova, G. V. *Zh. Anal. Khim.* **1968**, *23*, 1966.
(16) Prokhorova, G. V.; Vinogradova, E. H.; Pronina, N. V. *Zh. Anal. Khim.* **1970**, *25*, 2073.
(17) Budnikov, G. K.; Miedianceva, E. P. *Zh. Anal. Khim.* **1973**, *28*, 301.
(18) Burger, K.; Syrek, G.; Farsang, G. *Acta Chim. Acad. Sci. Hung.* **1966**, *49*, 113.
(19) Voitenko, L. V.; Prokhorova, G. V.; Agasjan, P. K. *Zh. Anal. Khim.* **1980**, *35*, 702.
(20) Prokhorova, G. V.; Henrion, G.; Schmidt, R. *Z. Chem.* **1982**, *22*, 28.
(21) Nagniot, P. *J. Electroanal. Chem.* **1967**, *14*, 197.
(22) Philar, B.; Valenta, P.; Nürnberg, H. W. *J. Electroanal. Chem.* **1986**, *214*, 157.
(23) Chen, H.; Neeb, R. *Fresenius' Z. Anal. Chem.* **1983**, *314*, 657.
(24) Meyer, A.; Neeb, R. *Fresenius' Z. Anal. Chem.* **1983**, *315*, 118.
(25) Bobrowski, A. *10th International Symposium on Microchemical Techniques*, Antwerp 1986, Book of Abstracts, p 185.
(26) Bobrowski, A. *EUROANALYSIS VI* **1987**, p 114.
(27) Donat, J. R.; Bruland, K. W. *Anal. Chem.* **1988**, *60*, 240.
(28) Koutecky, J. *Chem. Listy* **1953**, *47*, 9.
(29) Koutechy, J. *Collect. Czech. Chem. Commun.* **1953**, *18*, 311.
(30) Flora, C. J.; Nieboer, E. *Anal. Chem.* **1980**, *52*, 1013.
(31) Vienzierl, J.; Umland, F. *Fresenius' Z. Anal. Chem.* **1982**, *312*, 608.
(32) Torance, K. *Analyst* **1984**, *109*, 1035.
(33) Astafeva, V. V.; Prokhorova, G. V.; Salikhdzanova, R. M. F. *Zh. Anal. Khim.* **1976**, *31*, 260.
(34) Ngok Khue, D. *Zh. Anal. Khim.* **1987**, *42*, 511.
(35) Ruvinskii, O. E.; Tur'yan, Va. I.; Neverova, A. K. *Electrokhimija* **1976**, *12*, 1215.
(36) Ruvinskii, O. E. *In Poliarografia, Problemy i Pierspiektivy*; Zinatne: Ryga, 1977; Chapter 2.
(37) Siniakova, S. I.; Miliavskii, Yu. S. *Zh. Niebrg. Khim.* **1967**, *12*, 633.
(38) Siniakova, S. I.; Miliavskii, Yu. S. *Zavodsk. Lab.* **1971**, *37*, 1153.
(39) Zarebski, J. *Chem. Anal.* **1985**, *30*, 699.

RECEIVED for review July 19, 1988. Revised manuscript received January 1, 1989. Accepted May 3, 1989. This work was supported in part by the Central Programme for Basic Research (CPBP No. 01.17).

Anal. Chem. **1989**, *61*, 2185–2188 **2185**

Application of a Quartz-Crystal Microbalance for Detection of Phase Transitions in Liquid Crystals and Lipid Multibilayers

Yoshio Okahata* and Hiroshi Ebato

Department of Polymer Chemistry, Tokyo Institute of Technology, Ookayama, Meguro-ku, Tokyo 152, Japan

Resonance frequency increased abruptly at the phase transition temperature (T_c) from solid to liquid crystalline state of liquid crystals (LCs) or lipid multibilayer films cast on a quartz-crystal microbalance (QCM) electrode when the ambient temperature increased gradually. The large frequency enhancement at the T_c was observed in the case of smectic LC-coated QCM compared with those of nematic and cholesteric LC-coated QCM. Although the frequency enhancement at the T_c of the LC-coated QCM was observed independent of media such as water and air phases, the frequency of the lipid multibilayer-coated QCM increased abruptly at the T_c only in a water phase, but not in an air phase. Frequency enhancements at T_c can be explained by slipping between layered structures of smectic LC and lipid multibilayer in the fluid liquid crystalline state above the T_c. In the case of lipid multibilayers, the penetration of water into interlayers (swelling) occurs at the T_c and then the frequency increase is observed due to slipping between hydrated and fluid layers only in aqueous phases.

Piezoelectric quartz plates are known as a microbalance to detect the amount of substances deposited on the electrode of the quartz from the frequency decrease (*1*). Natural protein-coated quartz-crystal microbalances (QCMs) have been studied as immunoassay procedures using antigen–antibody reactions (*2–5*). We have reported that the lipid multibilayer-coated QCM can detect selective adsorptions of various bitter or odor substances to lipid matrixes both in air and water phases (*6–8*). When the QCM was used as a substrate of Langmuir-Blodgett (LB) techniques in which lipid monolayers were transferred on the QCM plate from a water surface, it was found from the frequency change that LB films were transferred on the substrate with water which gradually evaporated through layers of the films when exposed to air (*9*). The fundamental principle in these studies involves frequency changes due to the surface mass increase or decrease on the QCM by deposition or release.

In this paper, we would like to report that a new application of the QCM for detection of phase transitions from solid to liquid crystalline state of liquid crystals (LCs) and lipid multibilayer films cast on the electrode. Smectic (PCB), nematic (EBBA), and cholesteric (ChD) liquid crystal compounds, and $2C_{16}PE$ phospholipid and polymeric $2C_{18}N^+$-$2C_1/PSS^-$ multibilayer films were cast on the electrode of the QCM (see Figure 1). The frequency of the QCM abruptly increased at the phase transition temperature (T_c) of the coating materials when the temperature was raised gradually in air or water phase. Crane and Fischer have pointed out that the resonance frequency of the shear node quartz crystal is influenced by the fluidity of the coating polymer in air (*10*). Muramatsu and co-workers reported that the frequency shift was observed due to the change of a deficit resistance of a piezoelectric quartz when the quartz was in contact with high-viscosity liquids (*11*).

EXPERIMENTAL SECTION

Materials. Thermotropic liquid crystal compounds, *p*-pentyloxy-*p*′-cyanobiphenyl (PCB, k → s, 43 °C; s → i, 68 °C), *N*-(*p*-ethoxybenzylidene)-*p*′-butylaniline (EBBA, k → n, 36 °C, n → i: 80 °C), and cholesteryl decanoate (ChD, k → ch, 82 °C; ch → i, 91 °C), were purchased for analytical grade chemcials and used without further purification.

Preparations of synthetic phospholipids, 1,3-dihexadecylglycerol-2-phosphoethanolamine ($2C_{16}PE$), and polymeric bilayer-forming amphiphiles of dioctadecyldimethylammonium poly(styrenesulfonate) ($2C_{18}N^+2C_1/PSS^-$) were reported elsewhere (*6–8, 13*). Chloroform solutions of liquid crystals (LCs) and bilayer-forming amphiphiles were cast on the electrode of both sides of the quartz, dried in air, and kept at 10 °C for a day. In the case of lipid multibilayers, the lipid coated QCM was aged in hot water at 60 °C for 30 min and then kept at room temperature for a day. PCB, EBBA, and ChD on the QCM were confirmed to show smectic, nematic, and cholesteric liquid crystalline states at the respective phase transition temperature (T_c). X-ray diffraction analyses showed that $2C_{16}PE$ and $2C_{18}N^+2C_1/PSS^-$ amphiphiles form extended multilamellar structures of a lipid bilayer (3.3–3.9 nm spacing) parallel to the film plane (*6–8, 13*). The multibilayer films on the QCM showed a sharp endothermic peak at 53 °C for $2C_{16}PE$ and 42 °C for $2C_{18}N^+2C_1/PSS^-$ multibilayers from differential scanning calorimetry (DSC) in a water phase, which mean the phase transition from solid to liquid crystalline state of multibilayer films (*6–8, 13*). The polyion complex multibilayer film was used because it was physically stable and did not peel from the QCM plate even at harsh conditions in aqueous solutions.

Apparatus. The experimental apparatus comprised at 9-MHz, AT-cut quartz crystal plate (8 mm diameter) on both sides of which 20 mm² of Ag electrodes had been deposited, and a homemade oscillator designed to drive the QCM at its resonance frequency (*6–9*). The QCM was driven at 5-V dc, and the frequency of the vibrating quartz was measured by an Iwatsu frequency counter (SC 7201 Model) attached to the microcomputer system (NEC, PC 8801 Model). The following equation has been obtained for the AT-cut shear mode QCM (*1*):

$$\Delta F = \frac{-2F_0^{\,2}}{A(\rho_q\mu_q)^{1/2}}\,\Delta m \qquad (1)$$

where ΔF is the measured frequency shift (Hz), F_0 the parent frequency of QCM (9×10^6 Hz), Δm the mass change (g), A the electrode area (0.20 cm²), ρ_q the density of quartz (2.65 g cm^{-3}), and μ_q the shear modulus (2.95×10^{11} dyn cm^{-2}). Calibration of the QCM used in our experiments showed that a frequency change of 1 Hz corresponded to a mass increase of 1.05 ± 0.01 ng on the electrode of QCM (*6–9*)

$$\Delta m = -(1.05 \pm 0.01) \times 10^{-9}\,\Delta F \qquad (2)$$

LC compounds (smectic PCB, nematic EBBA, and cholesteric ChD) or lipid amphiphiles ($2C_{16}PE$ and $2C_{18}N^+2C_1/PSS^-$) were cast to be 15 ± 2 μg (0.5 ± 0.1 μm thick) on electrodes (20 × 2 mm²) of both sides of the QCM. The decrease of vibration frequency (14.3 ± 0.1 kHz) was consistent with the mass deposited on the electrode in line with the calibration value of 1.05 ± 0.02 ng/Hz of eq 2. The LCs- or lipid multibilayers-cast QCM was set in the sealed air vessel or immersed in a water cell and the ambient temperature was raised and lowered gradually in the

---

*To whom all correspondence should be addressed.

0003-2700/89/0361-2185$01.50/0 © 1989 American Chemical Society

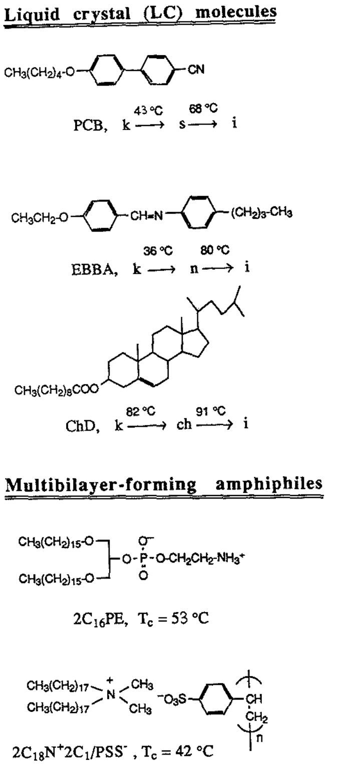
Liquid crystal (LC) molecules
CH3(CH2)4-O ... CN
PCB, k 43 °C → s 68 °C → i
CH3CH2-O ... CH=N ... (CH2)3-CH3
EBBA, k 36 °C → n 80 °C → i
CH3(CH2)8COO
ChD, k 82 °C → ch 91 °C → i
Multibilayer-forming amphiphiles
CH3(CH2)15-O, O-P-O-CH2CH2-NH3+
2C16PE, Tc = 53 °C
CH3(CH2)17 N+ CH3, -O3S, CH, CH2, n
2C18N+2C1/PSS-, Tc = 42 °C

Figure 1. Structures of liquid crystals (LC) and lipid multibilayers cast on the QCM plate.

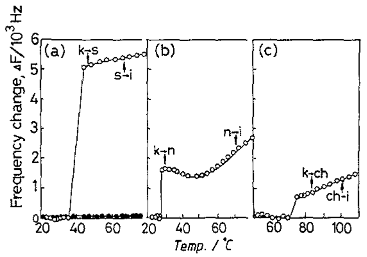

Figure 2. Frequency increases of LC (15 μg)-coated QCMs at the phase transition from solid to liquid crystalline state in air: (a) smectic PBC-coated, (b) nematic EBBA-coated, and (c) cholesteric ChD-coated QCMs. Closed circles show the frequency changes of the uncoated QCM in air. The similar frequency changes at T_c of LC-coated and uncoated QCMs were observed in a water phase.

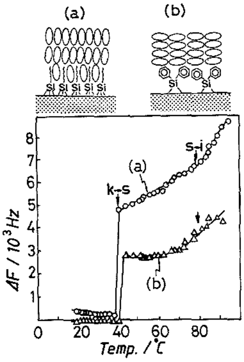

Figure 3. Effect of orientation of smectic PCB liquid crystals on frequency changes at T_c in air. PCB was cast on the surface of the Ag electrodes of the quartz plate which was treated with (a) octadecyltrichlorosilane (OTS) and (b) diphenyldichlorosilane (DPS).

range of 0.1–30 °C min^{-1}. The resonance frequency at each temperature was measured.

RESULTS AND DISCUSSION

Phase Transition of Liquid Crystals (LCs). Figure 2 shows frequency changes of the LC-coated QCM when ambient temperatures are raised gradually at a rate of 1 °C min^{-1} in air phase. The frequency abruptly increased near the respective phase transition temperature from solid to liquid crystalline state (T_c of k $\rightarrow$ s, k $\rightarrow$ n, and k $\rightarrow$ ch) independent of media such as air phase and aqueous solution. The frequency hardly changed at the phase transition from liquid crystal to isotropic state (s $\rightarrow$ i, n $\rightarrow$ i, and ch $\rightarrow$ i). The temperature where the frequency changed was independent of the raising rate of temperatures in the range 0.1–3 °C min^{-1}. After temperatures were raised and then lowered in air and water phases, the frequency reverted to the original value, which means the coating LC materials did not peel from the substrate during experiments.

The magnitude of the frequency enhancement of T_c of the smectic PBC-coated quartz was 2–5 times larger than those of the nematic EBBA- and cholesteric ChD-coated QCMs. This means that the multilayered structure of smectic LCs parallel to the QCM plate plays an important role for the frequency change at T_c in addition to the fluidity or elasticity change from solid to nematic or cholesteric state of LC coatings.

The orientation of smectic LCs is known to be affected with the surface treatment of the substrate (*14, 15*). Figure 3 shows effects of the surface treatment of the electrode of the QCM on the frequency change at T_c of smectic PCB LCs. When the Ag electrode surface was modified with long alkyl chain monolayers of octadecyltrichlorosilane (OTS), the large frequency enhancement was observed at T_c(k $\rightarrow$ s) = 42 °C, in which LC molecules are thought to orient parallel to the long axis of alkyl chains of OTS as shown schematically in Figure 3a. On the contrary, the magnitude of the frequency enhancement reduced about a half when the surface was treated with diphenyldichlorosilane (DPS), in which LC molecules are supposed to orient parallel to the film plane due to the bulky phenyl groups of DPS surfaces (see Figure 3b) (*15*). These results imply that well-oriented layered structures parallel to the QCM plate are important to cause the large frequency change at T_c.

Figure 4 shows the frequency decrease against the cast amount of smectic PCB on the QCM at temperatures below and above T_c (20 and 50 °C, respectively). In the solid state below T_c (at 20 °C), the frequency decreases linearly with increasing the mass of PCB deposited on the electrode in both cases of the OTS- and DPS-treated surface. The slope was calculated to be 1.1 ± 0.2 ng/Hz which is consistent with eq 2. However, in the fluid smectic liquid crystalline state of PCB deposited on the OTS-treated electrode at 50 °C, the frequency hardly decreased proportionally to the cast amount above 5 μg, which means that the QCM scarcely detects the mass above 5 μg of the fluid smectic layered structure on the electrode. In other words, unlike the solid LCs, the fluid or elastic layered structure is thought not to vibrate with the QCM plate. On the contrary, the frequency decreased almost

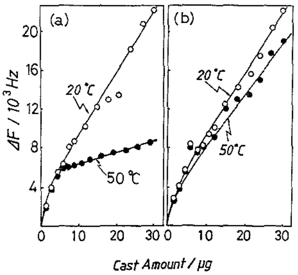

Figure 4. Frequency decreases dependent on the cast amount of PCB liquid crystals on the electrode of the QCM at 20 and 50 °C in air. The electrode surface was treated with (a) octadecyltrichlorosilane (OTS) or (b) diphenyldichlorosilane (DPS).

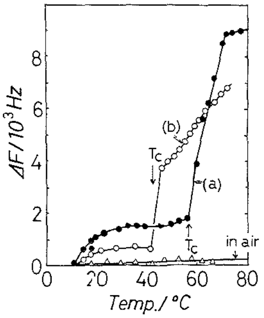

Figure 5. Frequency increases at T_c of (a) the $2C_{16}PE$ and (b) the $2C_{18}N^{+}2C_1/PSS^{-}$ multibilayer (15 µg)-coated QCMs in a water phase. The frequency enhancement and decrease at T_c were observed reversibly when temperatures were raised and lowered in water.

linearly with increasing the cast amount even in the fluid liquid crystalline state at 50 °C when the surface was treated with the bulky DPS (see illustrations in Figure 3).

From these findings, the large, abrupt frequency change at the T_c of smectic PCB on the QCM is explained as follows. In the solid state of LC molecules below T_c, the solid coating vibrates with the QCM plate and the frequency decreases proportional to the surface mass deposited. When LC coatings become fluid above T_c, the multilayered smectic phases may slip between layers and the upper part of LC coatings cannot vibrate with the QCM plate. As a result, the frequency drastically increases at the phase transition temperature (k → s) of the coating LCs. When smectic PCB molecules do not orient perpendicular to the QCM plate on the DPS-treated surface (see Figure 3b) or when the nematic EBBA and cholesteric ChD are deposited on the QCM (see parts b and c of Figure 2, respectively), the frequency changes at T_c are very small because LCs do not form the layered structure parallel to the QCM plate and the slipping is difficult to occur even in the fluid state. The frequency is also affected by the viscoelastisity change of coatings on the QCM; however, the magnitude seems to be small compared with that due to the slipping of layered structures.

Phase Transition of Lipid Bilayers in Water. Figure 5 shows the frequency change of $2C_{16}PE$ and $2C_{18}N^{+}2C_1/PSS^{-}$ bilayer-coated QCM when the temperature was increased gradually at a rate of 5 °C min^{-1} in both water and air phases. The frequency increased immediately at the respective T_c from solid to liquid crystalline state of coating multibilayers only in water, but not in air. The magnitude of the frequency enhancement at T_c of the $2C_{16}Pe$-coated QCM was 2 times larger than that of the polymeric $2C_{18}N^{+}2C_1/PSS^{-}$-coated QCM. In the case of the LC-coated quartz, the frequency change was observed independent of media.

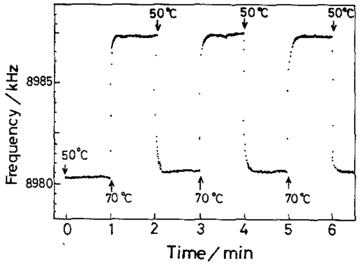

Figure 6. Repeated frequency changes of the $2_{16}PE$ (T_c = 53 °C)-coated QCM when it was immersed into the 50 and 70 °C water baths alternately at the arrow.

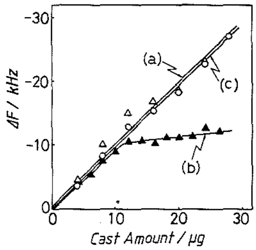

Figure 7. Frequency decreases dependent on the cast amount of $2C_{16}PE$ multibilayers (T_c = 53 °C) on the quartz: (a) at 25 °C in water, (b) at 70 °C in water, and (c) in air independent of temperatures (20–70 °C).

Figure 6 shows the reversible frequency changes of $2C_{16}PE$ multibilayer (T_c = 53 °C)-coated piezoelectric crystal when the QCM was immersed in water phase at 50 and 70 °C repeatedly. The frequency changed reversibly in the range of 20 °C below and above the T_c at least more than 10 times. The similar reversible frequency changes below and above the T_c were also observed in the polymeric $2C_{18}N^{+}2C_1/PSS^{-}$-coated QCM although the magnitude was relatively small.

When the $2C_{16}PE$ multibilayer-coated QCM was covered with hydrophobic polymers such as polystyrene, the frequency change at T_c in a water phase was hardly observed. This clearly indicates that the frequency change at T_c of lipid multibilayers occurred only when the multibilayers contact with aqueous media.

Figure 7 shows the relationship between the frequency decreased and the casting amount of $2C_{16}PE$ (T_c = 53 °C) multibilayers on the QCM. The frequency decreased linearly with increasing the casting amount of the solid bilayers below T_c at 25 °C and the slope (1.0 ng/Hz) was consistent with eq 2, which indicates that all the mass of the solid multibilayers on the electrode vibrate with the QCM. On the contrary, in the case of the fluid liquid crystalline multibilayers at 70 °C, the frequency hardly increased with increasing the mass of multibilayers above 10 µg. This means that the upper layers above 10 µg of the fluid $2C_{16}PE$ multibilayers are slipping between layers in the liquid crystalline state and the weight above 10 µg is not monitored. The similar frequency behaviors were observed for the polymeric $2C_{18}N^{+}2C_1/PSS^{-}$ multibilayer film. In an air phase, the frequency decreased linearly with increasing the mass on the QCM and the frequency decrease due to the slipping was not observed.

Dynamic mechanical measurements of $2C_{18}N^{+}2C_1/PSS^{-}$ films were made with a nonresonance, forced vibration instrument, Rheovibron viscoelastmeter, at 110 Hz in both water and air phases (*16*). In a water phase, the dynamic storage modulus (E') decreased abruptly by about 2 orders of magnitude near T_c = 45 °C. In the tan δ curve narrow peak was found at T_c. The characteristic viscoelastic behavior at T_c of the self-standing multibilayer-immobilized film was not found in air phase.

When the $2C_{16}$PE multibilayer-coated QCM was immersed in water at temperatures above T_c, the frequency gradually decreased with time [$\Delta F = -(60 \pm 10)$ Hz] which indicates the swelling of hydrophilic interlayers of the fluid lipid bilayers with water above T_c. In the solid state of multibilayers, the frequency change due to the swelling was hardly observed (less than −5 Hz). When the polymeric $2C_{18}N^+2C_1/PSS^-$-coated QCM was immersed in an aqueous phase, the similar swelling behavior was observed above the T_c, though the magnitude of the swelling was relatively small [$\Delta F = -(20 \pm 10)$ Hz]. The frequency decrease above the T_c due to the swelling was not clearly observed when the temperature was raised slowly in Figure 5, because the swelling amount (−60 Hz) was very small compared with the frequency enhancement at the T_c (+3000–5000 Hz).

From these findings, the frequency change of lipid multibilayer-coated QCM at the T_c can be explained as follows. When lyotropic lipid multibilayers become fluid above the T_c in aqueous phases, the fluid multibilayers seem to swell slightly with water penetrated into hydrophilic interlayers and slip between fluid and swelled layers, because the frequency change due to T_c was not observed in the absence of aqueous media. When the polymeric $2C_{18}N^+2C_1/PSS^-$-coated QCM was employed in water, the frequency enhancement at T_c and the swelling amount in the fluid state were smaller than those of the $2C_{16}$PE-coated QCM (see Figure 5). In the polyion complex type multibilayers, cationic $2C_{18}N^+2C_1$ amphiphiles form multibilayer structures complexing with PSS^- polyanions at hydrophilic head groups (*6–8*, *13*), and the slipping and swelling between multibilayers seem to be difficult relative to the monomeric $2C_{16}$PE multibilayers.

SUMMARY

It was first found that piezoelectric quartz microbalances can detect the phase transition from solid to liquid crystalline state of the coating layered materials on the electrode by observing frequency changes. The general fluidity or viscoelastic change of coating materials can also be detected from the frequency change, although the magnitude of that is relatively small compared with that due to the phase transition (slipping between layered structures). The obtained results are useful as a new application of piezoelectric crystals as well as a microbalance sensitive to the surface mass deposition.

LITERATURE CITED

(1) Sauerbrey, G. *Z. Phys.* **1959**, *155*, 206.
(2) Ngeh-Ngwainbi, J.; Foley, P. H.; Kuan, S. S.; Guilbault, G. G. *J. Am. Chem. Soc.* **1986**, *108*, 5444.
(3) Muramatsu, H.; Dicks, J. M.; Tamiya, E.; Karube, I. *Anal. Chem.* **1987**, *59*, 2760.
(4) Roederer, J. E.; Bastiaans, G. J. *Anal. Chem.* **1983**, *55*, 2333.
(5) Ebersole, R. C.; Ward, M. D. *J. Am. Chem. Soc.* **1988**, *110*, 8623.
(6) Okahata, Y.; Ebato, H.; Taguchi, K. *J. Chem. Soc., Chem. Commun.* **1987**, 1363.
(7) Okahata, Y.; Shimizu, O. *Langmuir* **1987**, *3*, 1171.
(8) Okahata, Y.; Ebato, H.; Ye, X. *J. Chem. Soc., Chem. Commun.* **1988**, 1037.
(9) Okahata, Y.; Ariga, K. *J. Chem. Soc., Chem. Commun.* **1987**, 1535.
(10) Crane, R. A.; Fischer, G. *J. Phys. D: Appl. Phys.* **1979**, *12*, 2019.
(11) Muramatsu, H.; Tamiya, E.; Karube, I. *Anal. Chem.* **1988**, *60*, 2142.
(12) Skei, T.; Okahata, Y. *J. Microencapsulation* **1985**, *2*, 13.
(13) Okahata, Y.; Taguchi, K.; Seki, T. *J. Chem. Soc., Chem. Commun.* **1985**, 1122.
(14) Kahn, F. J.; Tayler, G. N.; Schonhorn, H. *Proc. IEEE* **1973**, *61*, 823.
(15) Kahn, F. J. *Appl. Phys. Lett.* **1973**, *22*, 386.
(16) Taguchi, K.; Yano, S.; Hiratani, K.; Minoura, N.; Okahata, Y. *Macromolecules* **1988**, *21*, 3336.

RECEIVED for review March 17, 1989. Accepted June 28, 1989.

Anal. Chem. **1989**, *61*, 2189–2192

Amphetamine Selective Electrodes Based on Dibenzo-18-crown-6 and Dibenzo-24-crown-8 Liquid Membranes

Saad S. M. Hassan*,[1] **and Eman M. Elnemma**

Department of Chemistry, Faculty of Science, Qatar University, Doha P.O. Box 2713, Qatar

Two novel membrane electrodes highly sensitive and selective for amphetaminium cation are developed and electrochemically evaluated according to IUPAC recommendations. These electrodes incorporate amphetamine–dibenzo-18-crown-6 (DB18C6) and amphetamine–dibenzo-24-crown-8 (DB24C8) as the active components in 1,2-dichloroethane solvent. Both electrode systems exhibit stable near-Nernstian response over the range 10^{-2}–10^{-5} M amphetaminium cation with a slope in the range of 55–58 mV/decade of concentration. The working pH range is 3–7, the response time varies from 30 to 50 s and the lower limit of detection is ∼3 ppm. The selectivity toward amphetaminium cation is reasonably high relative to many common inorganic cations and alkaloids as well as some amines structurally related to amphetamine. The DB18C6 membrane is 2–14 times more selective for amphetamine in the presence of foreign compounds than DB24C8 based electrode. Determination of 5 μg mL^{-1} to 4 mg mL^{-1} of amphetamine sulfate using the standard addition (spiking) technique shows an average recovery of 98.7% and a mean standard deviation of 1.7%. The method offers several advantages over the standard procedures.

Amphetamine (β-phenylisopropylamine) is one of the most potent sympathomimetic agents with respect to stimulation of the central nervous system. Clinical investigations revealed that patients dependent on amphetamine are prone to aggression, antisocial behavior, and psychotic episodes involving delusions and hallucinations (*1, 2*). Because the liability of amphetamine to abuse constitutes a substantial risk of public health, the World Health Organization (WHO) has recommended international control of this drug (*3*). However, amphetamine has gained popularity as an illicit "street drug" among teenagers, prisoners, students, and truck drivers (*4*). Its illicit use closely parallels that of cocaine in the range of its short-term and long-term effects. Efforts has been devoted toward developing and improving methods for analysis of amphetamine. These methods have involved the use of colorimetry (*5*), spectrophotometry (*6*), fluorometry (*7*), NMR spectrometry (*8*), mass fragmentography (*9*), polarography (*10*), amperometry (*11*), conductometry (*12*), and immunoassay (*13*). Many of these methods suffer from severe interference by amino compounds. Liquid membrane and coated-wire electrodes sensitive for amphetamine (*14*) and methylamphetamine (*15*) based on the use of octadecyl sulfate and dinonylnaphthalenesulfonate as anionic ligand, respectively, have been suggested. Selectivity data for these sensors are either not reported (*14*) or evaluated for only three basic amino compounds (*15*). The poor selectivity coefficient values reported are probably due to the nature of such ligands which complex many other organic cations without discrimination.

It has been reported that crown ether ligands are capable of selective encapsulation of cations depending on the number of oxygen donors and ring size (*16*). These compounds with their exolipophilic/endopolarophic (oxygen donor rich) cavity undergo reversible complexation and hence promote cation transfer between the organic–aqueous phase by carrier translocation. The use of these neutral carriers in the preparation of potentiometric sensors for organic cations and molecules is very limited. The only electrode systems available, so far, are those incorporating dibucaine– and hexylcaine–dibenzo-24-crown-8 (*17*), guanidine–dibenzo-27-crown-9 (*18*), and diquat– and paraquat–dibenzo-30-crown-10 (*19*) as electroactive materials in poly(vinyl chloride) membranes. Applications of chiral crown ethers for selective sensing of some optically active enantiomers of amines (*20*) and amino acid esters (*21*) have been also described. Studies supported by the crystallographic structural data using X-ray analysis (*22, 23*) and stability measurements using the calorimetric technique (*24*) revealed 1:1 binding and complexation between 18-crown-6 and some phenylalkylammonium ions. The present investigation describes two novel electrode systems for selective determination of amphetamine based on the use of dibenzo-18-crown-6 and dibenzo-24-crown-8 ionophores in dichloroethane as liquid membranes. This approach provides a simple and convenient method for determination of amphetamine in pharmaceutical preparations and has the advantages of possible applications to colored and turbid solutions as well as interfacing with automated and computerized recording systems. The proposed electrodes exhibit high selectivity and display fast response for as low as 3 μg mL^{-1} of amphetamine.

EXPERIMENTAL SECTION

Apparatus. All electrode potentials were measured at 25 ± 1 °C with an Orion digital pH/mV meter (Model 701A) using amphetamine–dibenzo-18-crown-6 or amphetamine–dibenzo-24-crown-8 liquid membrane electrodes vs an Orion 90-02 double junction Ag–AgCl reference electrode with 10% (w/v) KNO_3 junction. The following galvanic cell was employed for all electrochemical studies: Ag–AgCl, 10^{-2} M KNO_3–10^{-2} M amphetamine sulfate| 5×10^{-3} M amphetamine–crown ether complex in 1,2-dichloroethane||porous membrane||amphetamine test solution|-Ag–AgCl reference electrode. pH measurements were made with an Orion 91-02 combined glass electrode. Infrared spectra were recorded with a Pye Unicam SP3-100 IR spectrometer.

Reagents. Unless otherwise stated all the reagents used were of analytical reagent grade and doubly distilled water and solvents were used throughout. L-Amphetamine free base and D-amphetamine sulfate were obtained from Sigma Chemical Co. (St. Louis, MO). The purity determined by elemental analysis and the British Pharmacopoeia method (*25*) ranged between 97 and 99%. Dibenzo-18-crown-6 (DB18C6) and dibenzo-24-crown-8 (DB24C8) were obtained from Aldrich Chemical Co. (Milwaukee, WI). Aqueous 10^{-2} M amphetamine sulfate standard solution was freshly prepared. Amphetamine solutions (10^{-3}–10^{-6} M) were prepared by accurate dilutions of the stock solution. Crown ether solutions (10^{-2} M) were prepared in 1,2-dichloroethane. A standard 10^{-2} M aqueous sodium tetraphenylborate solution was prepared, filtered, and standardized by potentiometric titration using the solid-state Ag–Ag_2S membrane electrode (Orion 94-16A) in conjunction with an Orion 90-02 double junction Ag–AgCl reference electrode.

---

[1] Present address: Department of Chemistry, Faculty of Science, Ain Shams University, Cairo, Egypt.

0003-2700/89/0361-2189$01.50/0 © 1989 American Chemical Society

Liquid Sensor Membranes and Electrode Assembly. To a 50-mL separatory funnel were added 5 mL of 10^{-2} M aqueous amphetamine solution and an 8-mL aliquot of 10^{-2} M 1,2-dichloroethane solution of either DB18C6 or DB24C8. A few drops of 1 M HCl and 2 mL of dichloroethane solvent were added, and the mixture was shaken vigorously for 10 min. After phase separation, the organic layer was passed through dry filter paper and used as organic exchange site in an Orion liquid membrane electrode barrel (Model 92). An Orion 92-07-04 porous membrane was used to separate the organic phase from the test solution. The internal filling reference solution was a mixture of equal volumes of 2×10^{-2} M aqueous amphetamine sulfate and 2×10^{-2} M KNO_3 solutions. The assembled electrodes were conditioned by soaking in 10^{-3} M amphetamine sulfate solution for about 24 h. When not in use, the electrodes were kept immersed in the same amphetamine solution and thoroughly washed with doubly distilled water between measurements.

Electrode Calibration and Determination of Amphetamine. Aliquots (ca. 10 mL) of 10^{-2} – 10^{-6} M standard aqueous amphetamine sulfate solution were transferred to 50-mL beakers. The amphetamine–DB18C6 or amphetamine–DB24C8 liquid membrane electrode in conjunction with a double junction Ag–AgCl reference electrode (Orion 90-02) was immersed into the amphetamine sulfate solutions. After equilibration by stirring, the emf was recorded when becoming stable to ±0.1 mV and plotted as a function of the logarithm of amphetamine concentration. The potentials of unknown concentrations of amphetamine solutions were similarly measured and compared with the calibration graph. Alternatively, the known addition technique (*26*) was used by addition of a 1.0-mL aliquot of the standard 10^{-2} M amphetamine solution to the unknown test solution and measuring the change in the potential. Potentiometric titrations were made for 25.0-mL aliquots of the test solutions containing 5–50 mg of amphetamine sulfate using a standard 10^{-2} M aqueous sodium tetraphenylborate solution (NaTPB) and amphetamine–DB18C6 or amphetamine–DB24C8 liquid membrane electrode in conjunction with the double junction reference electrode (1.00 mL of 10^{-2} M NaTPB ≡ 1.36 mg of amphetamine free base). The selectivity coefficients ($k^{pot}_{amph,j}$) were determined with 10^{-3} M solutions at pH 4–6 using the standard separate-solution method (*26*, *27*).

RESULTS AND DISCUSSION

The reaction products of amphetamine with dibenzo-18-crown-6 (DB18C6) and dibenzo-24-crown-8 (DB24C8) were extracted in 1,2-dichloroethane and evaluated, according to the recommendations of IUPAC (*27*), as liquid membranes in electrodes responsive to amphetaminium cation. The infrared spectra of the membrane materials displayed several complex absorption bands at 2200–2400 cm^{-1} assigned to bonded $-^{+}NH$ stretch of ammine salt. The CCO stretch of the polyether ring appeared at 1060 cm^{-1} in the spectra of the pure crown ether solutions was shifted to 1030 cm^{-1} in the spectra of amphetamine–crown ether complexes indicating possible complexation of amphetamine with the cavity oxygen. The strong absorption bands at 1150, 1340, and 960 cm^{-1} in the infrared spectra of DB18C6 and DB24C8 ionophores were either remarkably decreased in their intensity or disappeared in the spectra of their complexes with amphetamine. This is probably due to stabilization of the symmetrical planer conformation of the ether ring as a result of the effective pole–dipole and dipole–dipole interactions with the amphetamine guest species (*28*). A similar reaction between phenacylammonium ion guest and 18-crown-6 host has been reported (*22*).

Amphetamine–Dibenzo-18-crown-6 Liquid Membrane. Table I lists the general performance characteristics of the amphetamine–DB18C6 electrode. The data reveal near-Nernstian response to amphetaminium cation over at least 3 orders of magnitude of concentration. The potentials displayed by the electrode are linearly related to the logarithm of the concentration of amphetamine in the range of 10^{-2}–10^{-5} M with a cationic slope of 58 mV $decade^{-1}$ (Figure 1). Least-squares fit of the observed potentials yields E (mV) = (58 ± 0.8) log [amphetamine] + (330 ± 0.9); the standard deviation is 1.1 mV. Unstable response and variable slopes are obtained, however, by using the less lipophilic 18-crown-6 as an ion carrier in the liquid membrane. 15-Crown-5 does not function as a carrier probably because its cavity is too small to form a just fit stable complex with amphetaminium cation.

Table I. Response Characteristics of Amphetamine–Dibenzo-18-crown-6 (DB18C6) and Amphetamine–Dibenzo-24-crown-8 (DB24C8) Liquid Membrane Electrodes

parameter	amphetamine–DB18C6	amphetamine–DB24C8
slope, mV (log *C*)$^{-1}$	58	55
std dev, mV	0.8	0.9
corr coeff (*r*)	0.999	0.998
intercept, mV	330	280
lower limit of linear range, M	10^{-5}	6×10^{-5}
detection limit, M	8×10^{-6}	3×10^{-5}

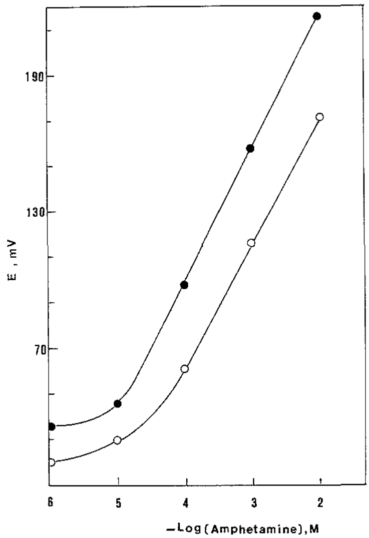

Figure 1. Potential response of (●) amphetamine–DB18C6 and (○) amphetamine–DB24C8 liquid membrane electrodes.

Amphetamine–Dibenzo-24-crown-8 Liquid Membrane. Evaluation of amphetamine–DB24C8 membrane electrode under the same experimental conditions shows a linear response for amphetaminium cation over the concentration range 10^{-2}–10^{-5} M with a slope of 55 mV $decade^{-1}$ (Figure 1). Least-squares analysis of the data gives the relation E (mV) = (55 ± 0.9) log [amphetamine] + (280 ± 0.9); the standard deviation is 1.2 mV. The overall response characteristics of amphetamine–DB18C6 and amphetamine–DB24C8 electrodes are similar (Table I). Little changes were noticed in the electrochemical response of liquid membranes prepared from dichloroethane extracts of different molar ratios of amphetamine and crown ethers (3:1 to 1:3) or by using various counteranions (e.g., SCN^-, ClO_4^-, picrate). These electrodes exhibit linear responses for 10^{-2}–10^{-5} M amphetamine and stable calibration slopes in the range of 53–56 mV $decade^{-1}$. Membranes prepared from 10^{-2} to 10^{-3} M dichloroethane solutions of DB18C6 and DB24C8 alone without amphetamine

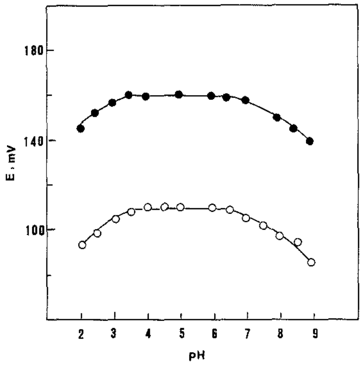

Figure 2. Effect of pH on the response of (●) amphetamine–DB18C6 and (○) amphetamine–DB24C8 liquid membrane electrodes for 10^{-3} M amphetamine sulfate.

Table II. Selectivity Coefficient for Amphetamine–Dibenzo-18-crown-6 (DB18C6) and Amphetamine–Dibenzo-24-crown-8 (DB24C8) Liquid Membrane Electrodes

	$k^{pot}_{amph,j}$	
interferents (j)	amphetamine–DB18C6	amphetamine–DB24C8
epinephrine	6.3×10^{-4}	1.9×10^{-3}
norepinephrine	5.7×10^{-4}	7.2×10^{-4}
ephedrine	6.1×10^{-4}	2.5×10^{-3}
phenylalanine	6.4×10^{-4}	1.1×10^{-3}
tyrosine	8.1×10^{-4}	9.5×10^{-4}
benzamide	5.1×10^{-4}	1.5×10^{-3}
2-aminobenzoic acid	6.1×10^{-4}	1.2×10^{-3}
lidocaine	9.2×10^{-4}	2.4×10^{-3}
caffeine	2.6×10^{-4}	3.7×10^{-3}
brucine	2.4×10^{-3}	4.1×10^{-3}
cinchonine	1.2×10^{-3}	9.5×10^{-3}
quinine	2.1×10^{-3}	8.0×10^{-3}

require a long time for equilibration and conditioning and exhibit unstable response for amphetaminium cation.

Stability of the Membrane Response. Amphetamine–DB18C6 and amphetamine–DB24C8 liquid membrane electrodes give a 95% steady-state response (t_{95}) in about 10 s for 10^{-3} M amphetamine and full response in less than 30 s. Dilute solutions (10^{-4}–10^{-5} M) require a longer time for steady-state response (50–60 s). The electrodes attain the background potential within 1 min when transferred from 10^{-3} M amphetamine test solution into water. The day-to-day stability and reproducibility of the potential reading is ±2 mV. Both electrode systems are usable for at least 6 weeks without loss of response or selectivity. The long-term behavior over this period in terms of potential stability, calibration slope, response time, and recovery time were evaluated by determining replicate calibration graphs ($n = 10$). The drift of the potential readings and calibration slopes does not exceed 3 mV (on the negative side) and 2 mV concentration decade^{-1}, respectively. No significant change in the response time and recovery time was noticed during 5 weeks of continuous use of both electrodes. Changes in the potential of the electrode systems as a function of pH were measured with 10^{-2} M amphetamine sulfate solution. The pH response profiles for the two electrodes (Figure 2) show a useful pH working range of 3–7 over which the potential readings are constant within ±0.1 mV.

Selectivity of the Membranes. The responses of amphetamine electrodes based on DB18C6 and DB24C8 liquid membranes were evaluated toward a number of representative metal cations, alkaloids, and amines structurally related to amphetamine such as α- and β-substituted ethylamines. Potentiometric selectivity coefficient ($k^{pot}_{amph,j}$) values determined by the standard separate-solution method (*26, 27*) at the concentration level of 10^{-3} M are given in Table II. These values show that amphetamine–DB18C6 and amphetamine–DB24C8 membrane electrodes have high preference for amphetamine over many organic cations. The response toward some inorganic cations (NH_4^+, Ba^{2+}, K^+, Na^+) is negligibly low ($k^{pot}_{amph,j}$ 10^{-2}–10^{-4}). The electrodes do not respond to some low molecular weight nitrogeneous compounds such as urea, succinimide, and glycine.

The selectivity characteristics shown in Table II reveal that amphetamine–DB18C6 is about 2 to 14 times less permeable to various interferents than amphetamine–DB24C8 and hence it is more selective for amphetamine. The shape of the cavity of DB18C6 host is slightly flattened by the constraint of the benzo groups which allow a short host–guest contact distance and assist the $-NH_3^+$ site of amphetamine to anchor into the host cavity. The size of DB18C6 cavity is suitable to fit the amphetamine–NH_3^+ group leading to the formation of a relatively more firm complex. It is known that crown ethers are very sensitive to the size of ions. The $-NH_3^+$ cation, with a radius of 1.43 Å (*29*), can fit into the cavity of DB18C6 (radius 1.3–1.6 Å (*30*) easily, and this crown ether is expected to form a relatively strong complex with amphetamine.

Compounds structurally similar to amphetamine (e.g., ephedrine, tyrosine, phenylalanine, epinephrine, and norepinephrine) show variably low effect on the response of both electrodes. The selectivity coefficients range from (5–8) × 10^{-4} with the DB18C6 electrode to (1–2) × 10^{-3} with the DB24C8 electrode. On the grounds of stereochemistry, it is not surprising that the selectivity coefficients vary for various amines with the two-electrode systems. The low symmetry of the protonated amine cation guest offers the possibility of distinguishing these cations by their shape. The nature and position of the substituent groups and the number of hydrogen atoms available in the cation guest for hydrogen bonding interact with the crown ether host, and such an interaction can either destabilize the complex by steric repulsion or stabilize it by hydrophobic bonding and dipole–dipole and charge transfer interactions (*28, 31*).

Although it is more likely to predict poor response for the alkaloids owing to the difficulty of accommodating their bulky cations within the coordination cavity of the crown ethers, brucine, quinine, and cinchonine were found to display relatively higher response than some of the ethylamine derivatives. The degree of response of these alkaloids attested by the selectivity coefficient values is on the order of increasing the analyte lipophilicity. This indicates that the selectivity of amphetamine–crown ether membranes is dominated not only by guest–host structural factors but also by the lipophilic nature of the interfering cation.

Determination of Amphetamine. Different concentrations of standard amphetamine sulfate solutions in the range of 5 μg mL^{-1} to 4 mg mL^{-1} were prepared (four replicates of each) and potentiometrically determined with amphetamine–DB18C6 and amphetamine–DB24C8 electrodes using the known addition spiking technique (*26*). The results obtained (Table III) show average recoveries of 98.7% (mean standard deviation 1.7%) and 98.5% (mean standard deviation 1.8%), with the DB18C6 and DB24C8 membranes, respectively. Addition of some pharmaceutical excipients and additives such as starch, lactose, maltose, gelatine binder, Tween-80, and aspirin in quantities over 100-fold excess of amphetamine did not influence the response of the electrodes. Potentiometric titration of amphetamine with standard so-

Table III. Potentiometric Determination of Amphetamine Using the Standard Addition Technique with Amphetamine–Dibenzo-18-crown-6 (DB18C6) and Amphetamine–Dibenzo-24-crown-8 (DB24C8) Liquid Membrane Electrodes

amphetamine sulfate added, mg mL^{-1}	amphetamine–DB18C6		amphetamine–DB24C8	
	recovery,[a] %	std dev, %	recovery,[a] %	std dev, %
0.005	97.7	2.0	97.2	2.2
0.012	98.4	1.9	97.9	2.1
0.037	99.5	1.7	98.5	1.8
0.092	99.3	1.8	98.4	1.7
0.184	99.0	1.6	99.0	1.8
0.368	98.8	1.8	98.1	1.6
1.840	98.3	1.7	98.6	1.5
2.208	99.2	1.7	99.0	1.7
2.944	99.1	1.5	99.1	1.6
3.680	98.5	1.5	99.2	1.7

[a] Average of four measurements.

dium tetraphenylborate solution can be performed with both electrode systems. Although the inflection break at a stoichiometric 1:1 reaction is relatively small (~50 mV), it is sharp enough for monitoring titration of milligram quantities (5–50 mg) of amphetamine with a relative error of 0.9%.

Determination of amphetamine powder using the British Pharmacopoeia procedure (BP) (*25*), which involves distillation of the sample in the presence of 10 M NaOH and collection of the distillate in a standard 0.1 M HCl solution followed by back titration of the excess acid using methyl red indicator, gives an average recovery of 97.5% and a mean standard deviation of 3.4%. This procedure suffers from serious interference from ephedrine and related compounds (*32*). However, accurate and selective determination of as low as 3.7 μg mL^{-1} (10^{-5} M) of amphetamine sulfate by the present electrode systems can be accomplished directly without pretreatment within 10 min compared with ~1 h and a sample size of 400 mg required for each assay by the BP method (*25*).

In conclusion, the proposed new electrode systems are attractive sensors for monitoring low concentration levels of amphetamine. Methods based on the use of these electrodes offer the advantages of simplicity, rapidity, accuracy and selectivity over many of those previously described instrumental techniques (*5–13*). Although the present electrodes display almost the same linear range of response offered by electrodes based on the use of octadecyl sulfate (*14*) and dinonylnaphthalenesulfonate (*15*), they have the advantages of high selectivity for amphetamine in the presence of compounds of a similar nature, reasonable wide working pH range, and relatively fast response.

Registry No. Amphetamine–DB18C6, 121866-18-0; amphetamine–DB24C8, 121866-19-1; amphetamine, 300-62-9; epinephrine, 51-43-4; norepinephrine, 51-41-2; ephedrine, 299-42-3; L-phenylalanine, 63-91-2; L-tyrosine, 60-18-4; benzamide, 55-21-0; 2-aminobenzoic acid, 118-92-3; lidocaine, 137-58-6; caffeine, 58-08-2; brucine, 357-57-3; cinchonine, 118-10-5; quinine, 130-95-0.

LITERATURE CITED

(1) Wade, A.; Reynolds, J. E. F. *Martindale The Extra Pharmacopoeia*, 27th ed.; The Pharmaceutical Press: London, 1977.
(2) *Remington*'s *Pharmaceutical Sciences*, 17th ed.; Gennaro, A. R., Ed.; Mack: Easton, PA, 1985; pp 1350–1355.
(3) *W.H.O. Tech. Rep. Ser.* **1970**, *No. 437*.
(4) Lawn, J. C.; Hill, C. E.; Feldkamp, R. H.; Hoover, R. D.; Rice, S. T.; Wong, B. J. *Drugs of Abuse*; U.S. Government Printing Office: Washington, DC, 1985; p 40.
(5) Fontani, F.; Morandini, F. *J. Pharm. Pharmacol.* **1970**, *22*, 411–413.
(6) Bhatkar, R. G.; Nevrekar, V. N. *Indian Drugs Pharm. Ind.* **1979**, *14*, 9–10.
(7) Mehta, A. C.; Schulman, S. G. *J. Pharm. Sci.* **1974**, *63*, 1150–1151.
(8) Liu, J. H.; Tsay, J. T. *Analyst* **1982**, *107*, 544–549.
(9) Suzuki, S.; Inoue, T.; Yasuda, T.; Niwaguchi, T., Hori, H.; Inayama, S. *Eisei Kagaku* **1984**, *30*, 23–26. *Chem. Abstr.* **1984**, *101*, 3416x.
(10) Habermann, V.; Habermannova, S. *Farmakol. Toksikol.* **1984**, *47*, 62–66. *Chem. Abstr.* **1984**, *100*, 180048m.
(11) Edward, E.; Lee, F. W.; Joseph, E. S. *Anal. Chem.* **1963**, *35*, 58–61.
(12) Joseph, E. S.; Donald, H. *J. Pharm. Sci.* **1965**, *54*, 805–806.
(13) Colbert, D. L.; Gallacher, G.; Mainwaring-Burton, R. W. *Clin. Chem.* **1985**, *31*, 1193–1195.
(14) Luca, C.; Baloescu, C.; Semenescu, G.; Tolea, T.; Semenescu, E. *Rev. Chim.* **1979**, *30*, 72–74.
(15) Cunningham, L.; Freiser, H. *Anal. Chim. Acta* **1982**, *139*, 97–103.
(16) Yoshio, M.; Noguchi, H. *Anal. Lett.* **1982**, *15*(A15), 1197–1276.
(17) Shirahama, K.; Kamaya, H.; Uedo, I. *Anal. Lett.* **1983**, *16*(B19), 1485–1494.
(18) Bochenska, M.; Biernat, J. *Anal. Chim. Acta* **1984**, *162*, 369–371.
(19) Moody, G. J.; Owusu, R. K.; Thomas, J. D. R. *Analyst* (*London*) **1987**, *112*, 121–127.
(20) Bussman, W.; Lehn, J. M.; Oesch, U.; Plumere, P.; Simon, W. *Helv. Chim. Acta* **1981**, *64*, 657–661.
(21) Shinbo, T.; Yamaguchi, T.; Nishimura, K.; Kikkawa, M.; Sugiura, M. *Anal. Chim. Acta* **1987**, *193*, 367–371.
(22) Maud, J. M.; Stoddart, J. F.; Williams, D. J. *Acta Crystallogr., Sect. C, Cryst. Struct. Commun.* **1985**, *C41*, 137–140.
(23) Cram, D. J.; Cram, J. M. *Acc. Chem. Res. Chem.* **1978**, *11*, 8–14.
(24) Izatt, R. M.; Izatt, N. E.; Bossiter, B. E.; Christensen, J. J.; Haymore, B. L. *Science* **1978**, *199*, 994–996.
(25) *British Pharmacopoeia*; University Press: Cambridge, 1980; Vol. 1, pp 32–33.
(26) Ma, T. S.; Hassan, S. S. M. *Organic Analysis Using Ion Selective Electrodes*; Academic Press: London, 1982; Vol. 1.
(27) IUPAC Analytical Chemistry Division, Commission on Analytical Nomenclature, Recommendations for Nomenclature of Ion Selective Electrodes *Pure Appl. Chem.* **1978**, *48*, 127–132.
(28) Goldberg, I. In *The Chemistry of Ethers, Crown Ethers, Hydroxyl Groups and Their Sulphur Analogues*; Patai, S., Ed.; Wiley: New York, 1980; p 189; Supplement E, Part 1.
(29) Lurie, J. *Handbook of Analytical Chemistry*; Mir: Moscow, 1978; p 24.
(30) Pedersen, C. J.; Frensdorff, H. K. *Angew. Chem., Int. Ed. Engl.* **1972**, *11*, 16.
(31) Jong, F. D.; Reinhoudt, D. N. In *Advances in Physical Organic Chemistry*; Gold, V., Bethell, D., Eds.; Academic Press: New York, 1980; Vol. 17, p 362.
(32) Schoen, K. *J. Am. Pharm. Assoc.* **1944**, *33*, 116–118.

RECEIVED for review February 22, 1989. Accepted June 5, 1989.

Anal. Chem. 1989, 61, 2193–2200

Voltammetry in Supercritical Carbon Dioxide at Platinum Microdisk Electrodes Coated with Perfluorinated Ion-Exchange Membranes

Adrian C. Michael and R. Mark Wightman*[1]

Department of Chemistry, Indiana University, Bloomington, Indiana 47401

It has previously been shown that the resistance of supercritical CO_2 is too high for voltammetry, even with microelectrodes, unless electrolytes and/or polar modifiers are present in the fluid. In a supercritical fluid flow system, such as chromatography, the use of an added electrolyte is not desirable. As an alternative, a film of an ionically conducting polymer, Nafion, placed over an electrochemical probe consisting of both a microdisk working electrode and a quasi-reference electrode, has been used. Undistorted voltammograms of ferrocene, 4-methylcatechol and 3,4-dihydroxybenzylamine dissolved in supercritical CO_2 in the presence of small quantities of H_2O have been obtained without the use of added supporting electrolyte. Experiments carried out in a supercritical fluid flow stream demonstrate the potential utility of membrane coated microelectrodes as chromatographic detectors.

INTRODUCTION

The development of microvoltammetric electrode techniques over the past several years has broadened the scope of voltammetry to previously impractical areas such as low permittivity media, very short time scales, and spatially resolved measurements (*1, 2*). These relatively new features of voltammetric methods are particularly useful for the development of detectors that can be coupled to a variety of chromatographic systems. Small electrode assemblies have been used effectively for on column detection in capillary liquid chromatography and electrophoresis (*3, 4*) and with conventional LC columns to spatially resolve regions of varying efficiency at the column outlet (*5*). Strategies based on microelectrodes have also been used in gas chromatography. For example, Murray and co-workers (*6*), reported the use an electroactive substrate contained within an ionically conducting polymer membrane which responded to modification of transport phenomena caused by the sorption of solvent vapors. Pons and co-workers have used a microelectrode assembly for the direct detection of redox-active eluents (*7*). In the latter work, conduction involved the migration of ions across the surface of the insulator material separating the working and counter electrodes. These reports demonstrate that electrochemical detection can be used even if the chromatographic media are nonconductive. Similar strategies have been utilized for electrochemical studies in lubricants and other nonpolar solvents (*8–10*).

The purpose of the experiments described in this paper is to characterize electrochemical detection in supercritical carbon dioxide (SC-CO_2) with Nafion-coated microelectrode probes. SC-CO_2 is frequently used as a chromatographic mobile phase and as an extraction solvent because it has a readily accessible critical point: $T_c = 31$ °C; $P_c = 73$ atm (*11, 12*). Despite the fact that conventional electrochemical techniques have been applied in various polar supercritical fluids (*13–16*), the extremely low dielectric constant of unmodified SC-CO_2 ($\epsilon < 1.8$ at $T = 50$ °C and $P < 1700$ atm) precludes the use of voltammetry, even with a 5-μm radius microdisk electrode (*17*). Upon addition of water to the fluid, voltammograms of dissolved ferrocene can be recorded but they are distorted by ohmic drop and indicate that the ferricinium cation precipitates on the electrode. Addition of a supporting electrolyte, tetrahexylammonium hexafluorophosphate ($THAPF_6$), to the water-modified SC-CO_2 causes the formation of a conductive molten salt layer over the electrodes (*18*) which results in voltammograms that are not resistively distorted and do not indicate precipitation of ferricinium. However, use of the molten electrolyte to permit undistorted voltammetry in a SC-CO_2 flow system is not likely to be practical.

As an alternative to the use of a supporting electrolyte dissolved in the SC-CO_2, we have investigated the use of an ionically conducting Nafion film over an electrochemical probe consisting of a microdisk working electrode and a macrodisk quasi-reference electrode (QRE) (*19*). Electroactive substrates dissolved in the fluid are detected at the microelectrode after partitioning into the film. The film is useful for electrochemical detection in modified SC-CO_2 because it provides permanent conductivity between the working and quasi-reference electrodes and responds in an interpretable fashion to various experimental parameters such as film thickness, fluid modifiers, voltammetric scan rate, and ionic nature of the redox substrate. The performance of the membrane-coated electrode in a SC-CO_2 flow system is also described and has been considerably improved over that previously reported.

EXPERIMENTAL SECTION

Electrochemical Probe Fabrication. The electrochemical probes used for voltammetry in SC-CO_2 were similar to those described previously (*19*). Briefly, they consisted of a 5-μm radius Pt wire and a 26-gauge Pt wire heat sealed in concentric soft-glass tubes. Polishing the end of the probes produced two coplanar Pt disks imbedded in glass and separated by 300–500 μm. The microdisk served as the working electrode and the larger disk served as the QRE. Because of the small currents in these experiments, an auxiliary electrode was not required. The probe was particularly suitable for this work because (i) the flat face of the probe was easily modified with a polymer membrane and (ii) the Pt to glass seal was very robust and able to withstand repeated exposure to the elevated temperature and pressure of SC-CO_2. Although silver is usually a more suitable QRE, it was not used here because high-quality silver to glass seals could not be obtained. A 5-μm radius of the working electrode was used in all calculations.

Nafion Film Preparation. Films were prepared with a casting procedure from a 0.5 wt % solution of Nafion (H^+ form) dissolved in isopropyl alcohol. Immediately before the coating procedure the solution was sonicated for 10 min. A Hamilton 1-μL syringe mounted in a micromanipulator was used to place a drop of solution on the probe face. The alcohol was evaporated at 80 °C for approximately 1 h and a vacuum was applied for 15 min to assure complete removal of the solvent. This resulted in adherent Nafion films covering the two Pt disks. In contrast to other reports (*20*), the films were not easily removed from the glass by water, even with agitation, and were smooth and free of cracks. Film

---

* To whom correspondence should be addressed.

[1] Present address: Department of Chemistry, University of North Carolina, Chapel Hill, NC 27514.

0003-2700/89/0361-2193$01.50/0 © 1989 American Chemical Society

thicknesses were estimated to be 1–2 μm by optical microscopy (in some instances aided by staining the film with orange Ru(bpy)$_3^{2+}$). However, as previously noted (*21*), films prepared in this fashion were uneven as indicated by visible interference patterns that formed on the probe face. In some experiments, the films were converted to the Na$^+$ form by soaking the coated probes for approximately 30 min in aqueous 1 M NaCl.

Other techniques for preparing Nafion films were also investigated. To produce very thick films the probes were dip coated in a 10 wt % Nafion solution (*22*). The probes were immersed at an angle of approximately 50° from the vertical for several minutes and then slowly removed with a manipulator, allowing for as much drainage as possible from the electrode surface. The probe was then clamped vertically with the electrodes facing upward and cured as described above. The resultant films were 20–30 μm thick as estimated by optical microscopy. Finally, following the reports of Martin and co-workers (*20*), several films were prepared with a 0.5 wt % Nafion solution in DMF and a solvent evaporation temperature of 120 °C. These films gave voltammograms in SC-CO$_2$ that were severely distorted by ohmic drop, an observation that is consistent with the rigid polymer morphology found by Martin (*20*). Because of the apparent distortion, films prepared in this fashion have not been characterized further.

Voltammetric Experiments. For experiments in static SC-CO$_2$ the probes were mounted in a locally constructed 10-mL stainless steel high-pressure cell (*17*) which also contained an electroactive substrate, a fluid modifier, and a stir bar. The fluid temperature was controlled with a GC oven and monitored with a thermocouple positioned near the probe tip. The cell was connected via stainless steel tubing to an HPLC syringe pump and brought to the desired CO$_2$ pressure and temperature while the cell contents were stirred. The fluid pressure was monitored with the transducer in the head of the syringe pump. Experiments were usually performed at 80 °C and 88 atm. At lower temperatures the amplitude of voltammetric currents were generally smaller, while at higher temperatures less stable responses were obtained.

Voltammetry in flowing SC-CO$_2$ was carried out by using the electrochemical flow cell previously described (*19*). The overall flow system, however, was modified slightly by the addition of a second sample vessel in parallel with the vessel used in our earlier work. The vessels were both connected to the syringe pump via a T-connector. One of the vessels contained water-modified SC-CO$_2$, while the other also contained ferrocene. The outlets of the vessels were connected to a valve that was used to select the path of fluid flow to the electrochemical detector. Thus, voltammograms in the presence of ferrocene could be compared with background voltammograms obtained in the presence of modifier only. This arrangement also allows examination of the temporal response of the membrane-coated electrodes to change in the concentration of analyte in the bathing fluid.

Cyclic voltammetry was performed with an AT style personal computer equipped with an analog-to-digital interface (Scientific Solutions, Inc., Solon, OH). The electrode potential was controlled via a digital-to-analog converter (DAC). The microdisk electrode was connected to a Keithley 427 (Keithley Instruments, Cleveland, OH) picoammeter, the output of which was monitored by the computer via an analog-to-digital converter (ADC). All software was developed locally.

RESULTS AND DISCUSSION

Voltammetry in Static SC-CO$_2$ with Nafion-Coated Probes. When voltammetry is performed with the Nafion-coated probes in unmodified SC-CO$_2$, no current is observed, even in the presence of a dissolved electroactive substance such as ferrocene, because of the poor solvation of the counterions in the film by the nonpolar bathing fluid. Under such conditions, the counterions are essentially immobile as they cannot be dissociated from the fixed anionic sites of the film so that ionic conduction cannot occur (*23*). Additionally, this observation shows that the Nafion is not swollen by SC-CO$_2$ to a sufficient extent to permit conduction via segmental motions of the polymer chains. However, if the SC-CO$_2$ is modified with a small amount of water (0.1 M, 20 μL added to the 10-mL cell) a background voltammogram can be obtained (Figure 1A) that is quite similar to the background voltammograms usually obtained with Pt electrodes in aqueous media (*24*). The accessible potential range spans approximately 1.5 V and appears to be limited by the oxidation of water and the reduction of hydrogen ion. The anodic formation of surface oxides and the corresponding cathodic stripping wave are also observed. Frequently, the cathodic stripping process appears as multiple peaks in the background scan, as shown in Figure 1A by the small reduction wave at a more negative potential than the larger stripping peak. As the potential of the surface reduction is well-known to be pH dependent, a likely explanation of this behavior is the presence of regions of differing pH on the electrode surface caused by heterogeneity of the recast Nafion film.

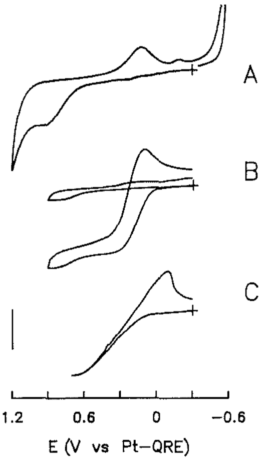

Figure 1. Voltammetry in modified SC-CO$_2$: (A) background voltammogram in SC-CO$_2$ with 0.1 M H_2O added (1 V/s; i = 6 nA); (B) background and ferrocene (2 × 10^{-4} M) voltammogram in SC-CO$_2$ with 0.1 M H_2O added (0.1 V/s; i = 2 nA); (C) voltammogram of ferrocene (2 × 10^{-4} M) in SC-CO$_2$ containing 200 μL of acetonitrile (0.1 V/s; i = 2 nA).

If the positive potential scan is not extended to the surface oxidation region, the cathodic surface waves do not occur as shown by the background voltammogram of Figure 1B. When ferrocene (2 × 10^{-4} M) is dissolved in the water-modified fluid, a distinct voltammogram for the ferrocene/ferricinium couple is observed (Figure 1B). At a scan rate of 0.1 V/s the anodic wave for to the oxidation of ferrocene is sigmoidal indicating radial diffusion of ferrocene to the microdisk electrode. Plots of E vs ln $[(i_d - i)/i]$ for the sigmoidal anodic waves have a slope of 43.1 ± 5.5 mV (mean ± standard deviation; scan rate = 0.1 V/s; n = 4), which is comparable to the 30.4 mV expected for a reversible redox couple at 80 °C (*25*). The cathodic part of the voltammogram, corresponding to the reduction of the ferricinium cation, is peak shaped rather than sigmoidal. As microdisk voltammograms become more peak shaped when the diffusion coefficient of reactant decreases, this behavior indicates slower mass transport of ferricinium than ferrocene in the Nafion film. The slower mass transport of ferricinium is presumably a result of ionic interactions with the fixed anionic sites of the film, as will be discussed in greater detail below.

As mentioned above, the accessible potential range is somewhat limited due to the use of water as a fluid modifier. Therefore, other modifiers were tested for their ability to promote conductivity in the Nafion film. When acetonitrile (200 μL added to the 10-mL cell) is used as the fluid modifier, the voltammogram shown in Figure 1C is obtained. The increased wave slope indicates severe ohmic distortion that could not be alleviated by further addition of acetonitrile. The voltammogram in Figure 1C is actually quite similar in form to the voltammogram of methylviologen dication at a Nafion-coated electrode in liquid acetonitrile, reported by Elliot (*26*). The apparent resistivity of the Nafion with acetonitrile as the modifier or solvent arises from the reduced mobility of ions in the film (*23, 26*). Surprisingly, when methanol or DMF were used as the modifier, voltammograms of ferrocene could not be obtained. As Nafion has been reported to be conductive in both liquid methanol and DMF (*23, 26*), this observation implies that they do not partition into the film from the fluid to a sufficient extent to provide conductivity. Voltammograms obtained by using the Na^+ form rather than the proton form of Nafion also exhibit ohmic distortion, although not as severe as that shown in Figure 1C. This may be due to a lower mobility of Na^+ relative to H^+ in Nafion. Thus, the voltammetric behavior of the Nafion-coated electrode depends on both the nature of the modifier and counterion present in the film. The best voltammetric response, i.e. with the least ohmic distortion, was obtained with the proton form of Nafion and water as the modifier. The increased resistivity of the film under the other conditions investigated outweighed the possible advantage of an increased potential range.

Mass Transfer of Ferrocene to the Microdisk Electrodes. Cyclic voltammetry at microdisk electrodes is conveniently characterized by the dimensionless quantity p (*27, 28*)

$$p = r_0(fv/D)^{1/2} \tag{1}$$

where r_0 is the working electrode radius, D is the apparent diffusion coefficient, v is the scan rate, and $f = nF/RT$. At small values of p (i.e., $p \leq 1$), microdisk voltammograms are sigmoidal due to convergent diffusion of reactant to the electrode surface. As p increases, diffusion of material to the electrode becomes increasingly linear and the voltammograms acquire the familiar peaked shape. An interesting property of voltammetry with microelectrodes is that the qualitative shape of a voltammogram is independent of the concentration of reactant, i.e. p does not contain a concentration term. With a microelectrode, therefore, it is possible to estimate the diffusion coefficient of a species without specifically knowing the concentration. This is particularly useful in these experiments because the concentration of ferrocene in the Nafion film depends on an unknown partition coefficient. Usually, p is experimentally varied by changing the scan rate, but Bard has recently observed a shift from linear to radial diffusion conditions upon changing the temperature of a SO_2 fluid from subcritical to supercritical values (*16*).

Figure 2 shows voltammograms of ferrocene recorded in water-modified SC-CO_2 at 1, 10, and 100 V/s that can be used to estimate the diffusion coefficient operant in the mass transport of ferrocene to the Nafion-coated microdisk electrode. At each scan rate the anodic voltammograms appear sigmoidal. The scans shown have not been background corrected, however, and the voltammogram at 100 V/s may not be purely sigmoidal. Thus, it appears that the p value of 1 lies in the range of 10–100 V/s, which gives an estimated range for the ferrocene diffusion coefficient of $(0.8–8) \times 10^{-4}$ cm^2/s. This range overlaps that found for solutes in supercritical fluids ($(0.5–3.3) \times 10^{-4}$ cm^2/s) and is markedly different from that found in liquids ($(0.5–2.0) \times 10^{-5}$ cm^2/s) (*12*).

The steady-state diffusion current at microdisk electrodes is given by

$$i_d = 4nFrDC^* \tag{2}$$

where C^* is the bulk concentration of reactant. Using the lower end of the estimated diffusion coefficient range and the steady-state current from the 1 V/s scan in Figure 2 in eq 2 yields an estimate of the bulk concentration of ferrocene of 2.07×10^{-4} M, which is close to the actual concentration added to the fluid (2.0×10^{-4} M). These results confirm that the film was sufficiently thin that the voltammograms shown in Figure 2 were controlled by the diffusion coefficient and concentration of ferrocene in the fluid rather than the Nafion.

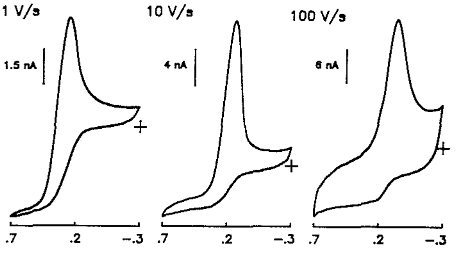

Figure 2. Effect of scan rate on the voltammetry of ferrocene (2×10^{-4} M) in SC-CO_2 with 0.1 M H_2O added.

This is an interesting observation when compared with the voltammetry we previously reported in water-modified SC-CO_2 containing $THAPF_6$ electrolyte in which the voltammograms were found to depend on the properties of a molten salt layer that formed on the electrodes (*18*). The large apparent diffusion coefficient found in the present study also implies that ferrocene diffuses freely through the Nafion film. It has been suggested that recast Nafion films, which imbibe large quantities of water, have an open internal structure and can easily incorporate neutral molecules (*29*) as well as co-ions (*22, 23*). Furthermore, it is also likely that at the elevated temperature of the SC-CO_2, the fluidity of the polymer material is increased, facilitating the motion of solutes.

Thus, with thin Nafion films the shape and amplitude of the voltammograms depend on the diffusion coefficient and concentration of ferrocene in the supercritical fluid. This concurs with the fact that the thickness of the Nafion films used is only a fraction of the disk radius while the diffusion layer extends well into the fluid (approximately $6r_0$ for $C/C^* = 0.9$ (*28, 30*)). The film thickness that resulted from the recasting procedure was found to be variable, however. This was evident in the voltammetry in two significant ways. First, the amplitude of the steady-state limiting current was found to vary between experiments. Second, with purposely thick Nafion films the voltammograms at high scan rates reflect diffusion entirely within the film itself rather than through the fluid. Figure 3A is a voltammogram of ferrocene obtained at 100 V/s using a probe dip-coated with a thick (20–30 μm) Nafion film. The voltammogram is peak shaped on both the anodic and cathodic sweeps and no difference in the amplitude of the anodic and cathodic current is observed, as expected for linear diffusion of both forms of the redox couple. Furthermore, with these thick films, peak-shaped voltammograms are obtained at much slower scan rates (<1 V/s), which also indicates slower diffusion. With films of intermediate thickness, the voltammetric behavior is also intermediate as shown in Figure 3B. This voltammogram was obtained with a Nafion film prepared by using a 1-μL droplet of the 0.5 wt % Nafion solution (as opposed to the 0.5-μL droplet used in Figure 2). Thus, in addition to allowing an estimate of the operant diffusion coefficient, the qualitative features of the microdisk voltammograms can be used to establish a relative scale of film thickness.

Mass Transport of Ferricinium in Nafion Films. The large ferricinium reduction current (Figure 2) suggests that

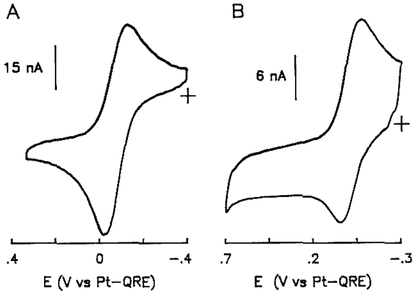

Figure 3. Effect of Nafion film thickness on the voltammetry of ferrocene at 100 V/s in SC-CO_2 with 0.1 M H_2O added: (A) dip-coated electrode, 5 × 10^{-4} M ferrocene; (B) film prepared with 1 μL of the 0.5 wt % Nafion solution, 2 × 10^{-4} M ferrocene.

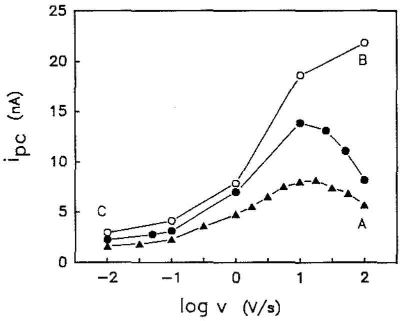

Figure 4. Effect of scan rate and apparent film thickness on the peak current for ferricinium reduction. Relative film thickness judged by lowest scan rate at which sigmoidal voltammograms were obtained for the oxidation of ferrocene: open circles, 100 V/s; closed circles, 25 V/s; closed triangles, 5 V/s.

it could provide the basis of a sensitive detection method when a neutral species is oxidized to a cation. It is of interest, therefore, to examine the ferricinium reduction further. Figures 2 and 3 show that the reduction current is influenced by both the scan rate and film thickness used. A relative film thickness scale can be established based on the slowest scan rate at which the oxidation of ferrocene becomes peak shaped. Thus, the combined effects of scan rate and film thickness on the reduction current can be summarized as in Figure 4. The figure shows that, when the scan rate is varied between 0.01 and 100 V/s, the cathodic peak current exhibits a maximum when thicker films are used (closed symbols) but increases continuously when thin films are used (open circles). Thus, for the purposes of developing a sensitive electrochemical detection scheme, Figure 4 shows that a thin Nafion film in conjunction with a fast scan rate should be utilized. With the thinner film shown in Figure 4, the cathodic current obtained at 10–100 V/s is an order of magnitude larger than the anodic current which represents a significant signal amplification. With even thinner films, however, the resistance was found to increase so that high-speed voltammograms could not be recorded and the advantage of the thinner film was lost.

The peaked reverse wave of the ferrocene voltammograms arises because of the slower mass transport of the ferricinium cation in Nafion. As the amount of ferricinium present in the film is dependent on the amount of ferrocene oxidized during the anodic sweep, the mass transport of ferrocene to the electrode is also a factor that effects the amplitude of the cathodic peak. This explains the decline of the cathodic current at elevated scan rates when thicker films are used. As the scan rate is increased, the size of the ferrocene diffusion layer is correspondingly decreased and eventually approaches the dimensions of the film. The contribution of the rapid diffusion through the fluid phase is reduced and the slower diffusion in the film increasingly dominates the mass transport of ferrocene to the electrode. In contrast, when the film is always smaller than the ferrocene diffusion layer, the rapid mass transport from the fluid is maintained, and the cathodic peak increases with scan rate.

An unusual feature of the thin-film data in Figure 4 is the large amplitude of the cathodic peak. Digital simulations of microdisk voltammetry with slow product diffusion (*28*) show that the ratio of the reverse current to the forward never exceeds approximately 1.2 (both currents measured from the zero current line) which is much smaller than the experimentally observed ratio. At first glance, this behavior might be considered as analogous to a thin layer cell response, especially as the ferricinium cation has been previously reported to be insoluble in water-modified SC-CO_2 (*17*). This is unlikely to be correct, however, as the diffusion coefficients of organic cations in Nafion rarely exceed 1 × 10^{-9} cm^2/s. Thus, on the time scale of a 100 V/s cyclic voltammogram, the ferricinium diffusion layer is not expected to exceed 50 nm which is much less than the film thicknesses used. Even though the Nafion film is considered to be thin compared to the steady-state ferrocene diffusion layer, it is very thick when compared to the ferricinium diffusion layer, especially at short times when the cathodic current is largest.

Two mechanisms of charge transport through Nafion that have been described are electron hopping and the single file diffusion of cations between fixed anionic membrane sites (*31*). Despite the large rate constants reported for the ferricinium–ferrocene self-exchange reaction in various media (*32*), this process does not appear to be involved in the amplification of the cathodic peak. For instance, unequal apparent diffusion coefficients for the oxidized and reduced form of a redox couple have been reported to indicate the dominance of molecular diffusion over hopping (*33*). Furthermore, the electron-hopping mechanism is expected to produce an increase in the apparent rate of mass transport over diffusion alone (*31*) whereas the voltammograms shown in Figure 2 indicate the opposite trend. The mass transport of ferricinium in Nafion, therefore, most likely involves single file diffusion. An important consequence of the single file diffusion model is that the apparent diffusion coefficient of a counterion in the membrane will decrease with increasing concentration as the availability of fixed sites in the membrane is reduced (*31*, *34*). This concentration dependence of the diffusion coefficient, however, is not expected to be evident unless the concentration of the diffusing cation approaches the concentration of membrane sites. In the next section simulated concentration profiles are presented which show that, because of the very rapid diffusion of ferrocene in the fluid phase, very high ferricinium concentrations can in fact be generated in the film.

Digital Simulation of Microdisk Electrodes: The Case of Unequal Diffusion Coefficients. In the previous section it was concluded that the voltammetric behavior of the ferrocene/ferricinium couple at the Nafion-coated electrodes is not fully explained by the simple case of slow product diffusion. It is partially explained on such grounds, however, and when the phenomenon of ion trapping (single file diffusion) is also considered an appropriate model is found. In this section, simulation methods developed elsewhere (*28*) are used to predict voltammograms for a system that involves slow product diffusion. For a qualitative comparison of the simulated and experimental voltammograms, it is not necessary to know the thickness of the Nafion film which can be assumed

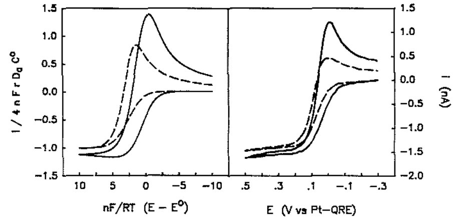

Figure 5. (Left panel) Simulated microdisk voltammograms: solid line, $p_A = 1$, $p_B = 100$; dashed line, $p_a = 0.1$, $p_B = 10$. (Right panel) Voltammograms of ferrocene (2×10^{-4} M) in water-modified SC-CO_2; solid line, 0.1 V/s; dashed line, 0.01 V/s.

to be larger than the ferricinium diffusion layer, as shown in the previous section. In addition, as specific chemical interactions between ferrocene and Nafion are not expected, a change in the film dimensions can be appropriately treated as an alteration of the ferrocene diffusion coefficient. The phenomenon of ion trapping by the Nafion film has not been included in the simulations because such calculations would require several parameters that are not known. Rather, the approach taken here is to attribute differences between the experimental and calculated results to the ionic properties of the film.

For a reaction A $\leftrightarrow$ B + ne^- for which the diffusion coefficients of A (D_A) and B (D_B) are not equal, it is convenient to use the symbols p_A and p_B to indicate the diffusion coefficient used in eq 1. Figure 5A shows simulated voltammograms for $p_A = 0.1$ and 1 with $p_B = 10$ and 100, respectively. If constant values of the disk radius, diffusion coefficients, and temperature are assumed, then the change in p values corresponds to a change in scan rate. Figure 5A shows that as the scan rate increases, the simulated voltammogram shifts to more cathodic potentials and the simulated cathodic current increases. The cathodic current changes because the values of p_B for the two simulations (10 and 100) reflect differing degrees of radial and linear diffusion. At $p_B = 100$ diffusion is virtually linear (27), so a further decrease in D_B would not result in a further increase of the cathodic current. As mentioned above, the cathodic current is only about 20% larger than the anodic current. Figure 5B shows that at slow scan rates the voltammetry of ferrocene is similar to that predicted by simulation. The experimental cathodic peak increases with scan rate but does not exceed the anodic current. There is also a small shift of the wave in the cathodic direction at the faster scan rate but the shift is more clearly evident in Figure 2 where a larger range of scan rates is shown. As the scan rate increases beyond 1 V/s the experimental reverse peak current is much larger that that predicted based solely on a slower diffusion coefficient.

Figure 6 shows the simulated concentration profiles of the electrolysis product taken at the switching potential of cyclic voltammograms with various values of p_A and p_B. Parts A–C of Figure 6 are intended to qualitatively correspond to the points labeled A, B, and C, respectively, in Figure 4. When the Nafion film is thick, D_A is taken to have a small value and the diffusion of A will have a linear component. Figure 6A shows the simulated profile for $p_A = 10$, a value corresponding to substantially linear diffusion, and $p_B = 100$. Figure 6B shows the profile formed when $p_A = 1$ and $p_B = 100$, which corresponds to an increase of D_A (i.e., a decrease in film thickness) assuming D_B and the scan rate remain at the values of Figure 6A. Figure 6C profile for $p_A = 0.1$ and $p_B = 10$, which corresponds to reducing the scan rate with the same diffusion coefficient ratio of Figure 6B.

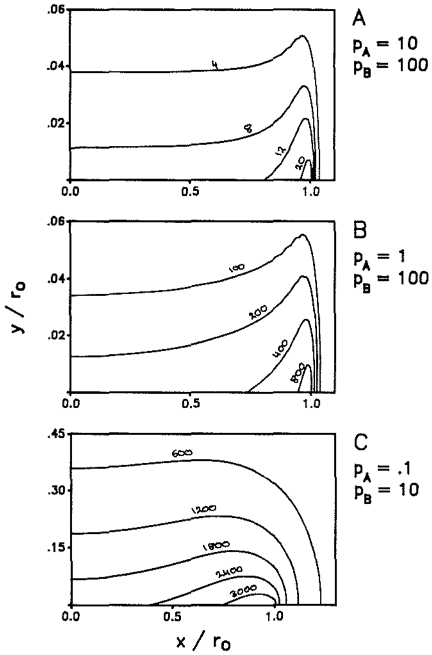

Figure 6. Simulated concentration profiles of the product of a reversible redox reaction taken at the switching potential. The electrode surface lies at $y = 0$ and projects in the x direction.

The concentration profiles in Figure 6 show that, for the conditions simulated, the majority of the product formed during the forward sweep of the voltammogram remains within a short distance of the electrode surface, supporting the assertion made earlier that the Nafion film probably does not form a thin layer cell for the ferricinium cation. Furthermore, when the diffusion of both reactant and product are mostly linear, as in Figure 6A, no extreme concentrations occur in the product diffusion layer so that ion trapping effects are expected to be minimal. In fact, the voltammogram corresponding to Figure 6A bears strong resemblance to the experimental voltammogram of Figure 3B; i.e. both the forward and backward sweeps are peak shaped with the backward peak being slightly more prominent.

When the diffusion coefficient ratio becomes as large as 10^4, as in Figure 6B, radial diffusion of reactant is combined with linear diffusion of product and a highly nonuniform concentration profile develops. In Figure 6B the product concentration is very high near the edge of the electrode and drops off rapidly in all directions. Thus, in the region close to the electrode edge, ion trapping could occur to a significant extent causing the product diffusion coefficient to become concentration dependent. The trapping of ferricinium in a small ring around the circumference of the electrode, as a consequence of both the rapid diffusion of ferrocene in the fluid and the ionic interaction of ferricinium with Nafion, would explain the unexpectedly large reduction current seen in Figure 2.

When the diffusion coefficient ratio is held constant at 10^4 but a slower scan rate is simulated, the nonuniformity of the product concentration profile is greatly reduced (Figure 6C). However, the product concentration near the electrode is extremely high (roughly 3000 times the bulk reactant concentration). Under these conditions, ion trapping is expected to occur about equally near the electrode surface such that a single diffusion coefficient model should again be appropriate, as was in fact shown to be the case in Figure 5. Figure

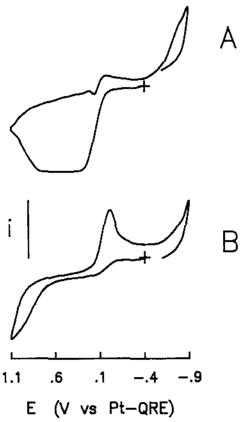

Figure 7. Cyclic voltammograms of ferrocene (2×10^{-4} M) at a coated electrode in SC-CO_2 containing 0.13 M added H_2O: (A) scan rate = 0.01 V s^{-1}; (B) scan rate = 1 V s^{-1}.

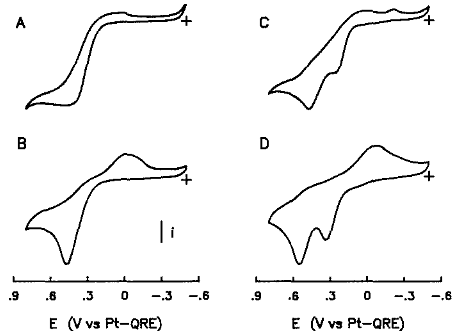

Figure 8. Cyclic voltammetry of 1×10^{-4} M 4-methylcatechol (A, B) and 3,4-dihydroxybenzylamine (C, D) in water-modified SC-CO_2 at 1 V/s (A, C) and 10 V/s (B, D) with Nafion-coated microelectrodes; i = 1.8 nA (A), 5 nA (B), 1.6 nA (C), 5.7 nA (D).

6C suggests the possibility that at some point mobility of the product ion may be inhibited altogether if the concentration of available ionic membrane sites is exceeded. Such behavior has been experimentally observed as shown in Figure 7A, which shows a voltammogram recorded at a very slow scan rate (0.01 V/s) and that was extended to high anodic potential. The current was observed to suddenly decrease before the switching potential was reached. As this behavior was not observed with the same electrode at a faster scan rate (Figure 7B), it is attributed to blockage of the Nafion by ferricinium.

Voltammetry of Catechol Derivatives in Water-Modified SC-CO_2. In the previous sections, the different apparent rates of mass transport of ferrocene and ferricinium in Nafion films were attributed to the differing degree of ionic interaction of the neutral and cationic species with the film material. For this to be correct, the nature of the voltammograms obtained for other redox substrates should be interpretable on a similar basis. Figure 8 shows voltammograms of two substituted catechols, 4-methylcatechol (4-MC) and 3,4-dihydroxybenzylamine (DHBA), at scan rates of 1 and 10 V/s. As with ferrocene, the voltammogram for the oxidation of 4-MC at 1 V/s (Figure 8A) is sigmoidal. In contrast with ferrocene, however, the cathodic part of the 4-MC voltammogram does not exhibit a peaked shape because the quinone product is a neutral species and is able to diffuse away from the electrode. Thus, at 1 V/s the behavior of 4-MC is consistent with that expected on the basis of minimal ionic interaction of the neutral species with the film.

Compared to ferrocene, the diffusion of 4-MC in Nafion appears to be slower as indicated by the peak-shaped voltammogram obtained at 10 V/s (Figure 8B). The slow diffusion of 4-MC is most likely due to hydrophilic interactions of this water-soluble compound with ionic domains in the film. The apparently greater interaction of the more hydrophilic substance with the film is opposite of the behavior reported for Nafion in aqueous media where selectivity for hydrophobic substances is observed (*35*). In contrast to experiments in aqueous media, however, Nafion is more hydrophilic than the supercritical fluid and it is therefore likely that 4-MC readily partitions into the film. The voltammetry of 4-MC preconcentrated in the Nafion can be regarded as the hydrophilic version of the hydrophobic stripping voltammetry recently described by Christian and co-workers (*36*).

The most striking feature of the voltammogram for DHBA (Figure 8C,D) is the appearance of two oxidation peaks, in contrast to the usually straightforward voltammetry of this compound (*37*). Such behavior has been previously reported (*29*, *38*, *39*) and was attributed to interactions of ionic redox couples with polyelectrolyte films (*40*). In this case it appears that the amine group of DHBA is the cause of the observed behavior. Although the two oxidation waves of DHBA are not well resolved at a scan rate of 1 V/s (Figure 8C), it appears that the first wave is sigmoidal and that the second wave is a peak superimposed on the limiting current of the first wave. The oxidation potential of substituted catechols increases with decreasing pH (*41*), which suggests that the second oxidation peak of DHBA arises from molecules that have partitioned into acidic regions of the Nafion film. Apparently, in these regions the amine becomes protonated and then undergoes ionic interactions with the membrane sites causing the peaked shape of the second oxidation wave even at a slow scan rate just as was observed with ferricinium. The existence of regions on the electrode surface with differing pH was also suggested earlier by the appearance of multiple surface reduction waves, shown in Figure 1A. At a scan rate of 10 V/s (Figure 8D) the two DHBA waves are resolved and are both peak shaped, consistent with the assumption that behavior of the first oxidation is similar to that of 4-MC.

Voltammetric Detection in Flowing SC-CO_2. Figure 2 indicates that mass transport of ferrocene across a thin Nafion film can occur on a millisecond time scale. The Nafion-coated electrodes should, therefore, be able to monitor variations in the concentration of ferrocene in the fluid. This point was investigated with the supercritical fluid-flow system as shown in Figure 9. The experiment was carried out with cyclic voltammetry at 10 V/s repeated at 1-s intervals. The two sample vessels contained water-modified SC-CO_2 and one also contained ferrocene (5×10^{-4} M). Each data point plotted in the left panel of Figure 9 was obtained by averaging the cathodic current over the potential range corresponding to the reduction of ferricinium. The valve was initially positioned so that only water-modified SC-CO_2 was flowing through the detector cell. When ferrocene was introduced to the detector, a rapid change in the reduction current was observed. The signal took approximately 3 s to rise to a stable value. The valve was repositioned after 20 s and the faradaic signal returned to base line with a fall time roughly equal to the rise time. The right-hand panel of Figure 9 shows a background-corrected voltammogram that is qualitatively similar to those from the static fluid experiments. The sigmoidal oxidation wave indicates that mass transport of ferrocene across the Nafion film occurs on a time scale of about 100 ms. Thus, the majority of the rise and fall time observed can be

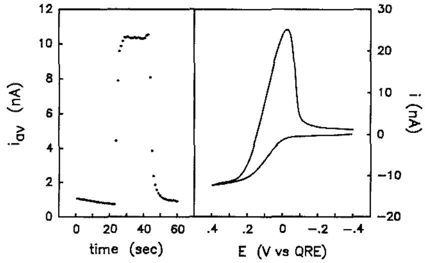

Figure 9. Cyclic voltammograms (10 V/s) of ferrocene (5×10^{-4} M) repeated at 1 s intervals in flowing water modified SC-CO_2: left panel, temporal response of the current averaged over the potential range corresponding to ferricinium reduction; right panel, background-subtracted ferrocene voltammogram.

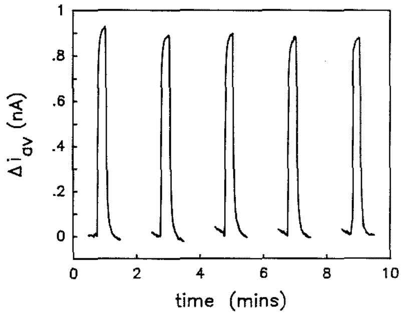

Figure 10. Temporal response observed to ferrocene "injections" of 20-s duration repeated at 2-min intervals.

attributed to the flow dynamics in the electrochemical detector cell. The detector itself has a fairly large dead volume and the experiment was carried out at a slow fluid flow rate (100 μL/min). It therefore appears that the Nafion-coated microelectrodes are able to respond rapidly to concentration changes in the fluid.

Other important properties of a detector include sensitivity and stability. The present design of the flow system does not permit variation of the ferrocene concentration during a single experiment so that a calibration curve cannot yet be reported for this system. However, some comments regarding stability can be made. The left panel of Figure 9 shows the response of the electrode remained stable during the 20 s that ferrocene was present in the flow stream. Additionally, Figure 10 shows that a reproducible response can be obtained when 20-s exposures to ferrocene are repeated at 2-min intervals. Both of these features are a considerable improvement over the results reported previously (*19*). The improved response has at least two sources. In the present work the Nafion-coated electrode was continuously exposed to water-modified SC-CO_2 so that the membrane was equilibrated with the modifier. Also, the voltammetric detection scheme used in Figures 9 and 10 generates only limited amounts of ferricinium in the film. As suggested in Figure 7, larger quantities of ferricinium can interfere with the ionic conduction process in Nafion.

Although the reproducibility shown in Figure 10 is good, the electrodes were found to be less stable in the flow stream than in static SC-CO_2. Visual inspection of the Nafion films after the flow stream experiments showed that they were intact and well adhered to the electrode probes. At the present time it appears that the instability is related to the solubility properties of the water modifier. In the current design of the electrochemical flow cell, the electrode is positioned near a point of decompression as the fluid enters the detector cell. This decompression reduces the solubility of the water in the fluid and eventually causes condensation in the detector cell. Future work will be aimed at eliminating the dead volume of the detector, which should lead to improved response times and stability.

CONCLUSION

The results reported above show that ionically conducting membranes placed over both a microdisk-working electrode and a quasi-reference electrode provide a means via which electrochemical detection can be carried out in modified supercritical carbon dioxide. In the supercritical solvent, Nafion is found to retain the characteristics of an ion exchange polymer, exhibiting selective retention of cationic species such as ferricinium and DHBA. Voltammograms obtained with Nafion-coated electrodes are dependent on the nature of the charge transition that occurs as a result of the redox reaction. The three substrates reported in this work, 4-MC, ferrocene, and DHBA, are each examples of a different ionic transition, namely 0/0, 0/+1, and +1/+1, respectively. The oxidation of ferrocene involves a change in charge number which led to the atypical voltammetric behavior observed for this compound. The ion exchange properties of the membrane influence both the rate of mass transport and the oxidation potential of DHBA. In addition, Nafion exhibits some hydrophilic character in supercritical carbon dioxide, in contrast to its usual behavior in liquid solvents.

ACKNOWLEDGMENT

The software used for the flow stream experiments was developed by Randy Foster of Indiana University.

LITERATURE CITED

(1) Wightman, R. M.; Wipf, D. O. *Electroanalytical Chemistry*; Bard, A. J., Ed.; Marcel Dekker: New York, 1989; Vol. 15.
(2) Pons, S.; Fleischmann, M. *Anal. Chem.* **1987**, *59*, 1391A–1399A.
(3) Knecht, L. A.; Guthrie, E. J.; Jorgenson, J. W. *Anal. Chem.* **1984**, *56*, 479–482.
(4) Wallingford, R. A.; Ewing, A. G. *Anal. Chem.* **1988**, *60*, 258–263.
(5) Baur, J. E.; Kristensen, E. W.; Wightman, R. M. *Anal. Chem.* **1988**, *60*, 2334–2338.
(6) Parcher, J. F.; Barbour, C. J.; Murray, R. W. *Anal. Chem.* **1989**, *61*, 584–589.
(7) Brina, R.; Pons, S.; Fleischmann, M. *J. Electroanal. Chem.* **1988**, *244*, 81–90.
(8) DeWulf, D. W.; Bard, A. J. *J. Electrochem. Soc.* **1988**, *135*, 1977–1985.
(9) Kaaret, T. W.; Evans, D. H. *Anal. Chem.* **1988**, *60*, 657–662.
(10) Wang, S. S. *J. Electrochem. Soc.* **1989**, *136*, 713–715.
(11) Novotny, M.; Springston, S. R.; Peaden, P. A.; Fjelsted, J. C.; Lee, M. L. *Anal. Chem.* **1981**, *53*, 407A–414A.
(12) Lee, M. L.; Markides, K. E. *Science* **1987**, *235*, 1342–1347.
(13) Flarsheim, W. M.; Tsou, Y.-M.; Trachtenberg, I.; Johnston, K. P.; Bard, A. J. *J. Phys. Chem.* **1986**, *90*, 3857–3862.
(14) Crooks, R. M.; Bard, A. J. *J. Electroanal. Chem.* **1988**, *240*, 253–279.
(15) Crooks, R. M.; Bard, A. J. *J. Electroanal. Chem.* **1988**, *243*, 117–131.
(16) Cabrera, C. R.; Garcia, E.; Bard, A. J. *J. Electroanal. Chem.* **1989**, *260*, 457–460.
(17) Philips, M. E.; Deakin, M. R.; Novotny, M. V.; Wightman, R. M. *J. Phys. Chem.* **1987**, *91*, 3934–3936.
(18) Niehaus, D.; Philips, M. E.; Michael, A. C.; Wightman, R. M. *J. Phys. Chem.*, in press.
(19) Michael, A. C.; Wightman, R. M. *Anal. Chem.* **1989**, *61*, 270–272.
(20) Moore, R. B., III; Martin, C. R. *Macromolecules* **1988**, *21*, 1334–1339.
(21) Orata, D.; Buttry, D. A. *J. Electroanal. Chem.* **1988**, *257*, 71–82.
(22) Rubinstein, I.; Bard, A. J. *J. Am. Chem. Soc.* **1981**, *103*, 5007–5013.
(23) Lopez, M.; Kipling, B.; Yeager, H. L. *Anal. Chem.* **1977**, *49*, 629–632.
(24) Adams, R. N. *Electrochemistry at Solid Electrodes*; Marcel Dekker: New York, 1969.
(25) Bard, A. J.; Faulkner, L. R. *Electrochemical Methods*; Wiley: New York, 1980.
(26) Elliot, C. M.; Redepenning, J. G. *J. Electroanal. Chem.* **1984**, *181*, 137–152.
(27) Aoki, K.; Akimoto, K.; Tokuda, K.; Matsuda, H.; Osteryoung, J. *J. Electroanal. Chem.* **1984**, *171*, 219–230.
(28) Michael, A. C.; Wightman, R. M.; Amatore, C. A. *J. Electroanal. Chem.*, in press.

(29) Rubinstein, I. *J. Electroanal. Chem.* **1984**, *176*, 359–362.
(30) Crank, J. *The Mathematics of Diffusion*; Clarendon: Oxford, 1975; pp 42–43.
(31) Buttry, D. A.; Anson, F. C. *J. Am. Chem. Soc.* **1983**, *105*, 685–689.
(32) Neilson, R. M.; McManis, G. E.; Safford, L. K.; Weaver, M. J. *J. Phys. Chem.* **1989**, *93*, 2152–2157.
(33) Buttry, D. A.; Anson, F. C. *J. Electroanal. Chem.* **1981**, *130*, 333–338.
(34) Murphy, W. D.; Rabeony, H. M.; Reiss, H. *J. Phys. Chem.* **1988**, *92*, 7007–7012.
(35) Martin, C. R.; Dollard, K. A. *J. Electroanal. Chem.* **1983**, *159*, 127–135.
(36) Chastel, O.; Kauffmann, J.-M.; Patriarche, G. J.; Christian, G. D. *Anal. Chem.* **1989**, *61*, 170–173.
(37) Baur, J. E.; Kristensen, E. W.; May, L. J.; Wiedemann, D. J.; Wightman, R. M. *Anal. Chem.* **1988**, *60*, 1268–1272.
(38) Tsou, Y.-M.; Anson, F. C. *J. Electrochem. Soc.* **1984**, *131*, 595–601.
(39) Kristensen, E. W.; Kuhr, W. G.; Wightman, R. M. *Anal. Chem.* **1987**, *59*, 1752–1757.
(40) Naegeli, R.; Redepenning, J.; Anson, F. C. *J. Phys. Chem.* **1986**, *90*, 6227–6232.
(41) Deakin, M. R.; Wightman, R. M. *J. Electroanal. Chem.* **1986**, *206*, 167–177.

RECEIVED for review May 4, 1989. Accepted June 26, 1989. This work was supported by NSF-CHE8808122.

Enzyme Dual-Electrode for Analyte Determination

H. Allen O. Hill,* Napthali A. Klein, Ioanna S. M. Psalti, and Nicholas J. Walton

Inorganic Chemistry Laboratory, South Parks Road, Oxford OX1 3QR, England

A dual-band electrode configuration was fabricated using gold, sputtered on to a glass substrate. The experimental response of these electrodes was tested by cyclic voltammetry and, in the generation-collection mode, agreed with theoretical predictions. An additional property of the present electrodes is the adjustability of the interelectrode space. The application of the device to biochemical electroanalysis was successfully demonstrated for the enzymatic reaction of glucose oxidase and glucose, coupled to the electrochemical oxidation of a substituted ferrocene.

Over the last few years, ultramicroelectrodes have been much used in electrochemical studies (*1*). Their small dimensions result in enhanced mass transport, leading to steady-state, or quasi-steady-state, diffusion-controlled currents (*2*). In addition, their properties mean that they can be used in high-resistance media (*3–6*), short time domains (*7*), studies of nucleation processes (*8*), charge transfer kinetics (*8–10*), as a probe within the diffusion layer (*11*), as electrochemical detectors for chromatography (*12*) and in spectroelectrochemistry (*13*). Band microelectrodes, which have an active surface with one dimension in the micrometer range, with the other several millimeters long, retain many of the advantages of ultramicroelectrodes mentioned before. However, by having a much larger surface area, they have two further advantages: first, they do not suffer from the problems caused by a very small total current or imperfections of the active surface of microdisk electrodes and second, they can be constructed of at least two such electrodes, electrically independent but closely spaced. When interelectrode separation is kept in the micrometer range, certain interesting characteristics results (*14*). In such a configuration, each electrode is within the diffusion layer of the other and therefore the reactions taking place at one have an impact on the current passed at the other, and vice versa. Moreover any subsequent chemical reaction of the species generated at one electrode, during the time and space interval of their migration to the other electrode, might cause a measurable change at the second electrode. The theory of such systems has recently been reported and demonstrated experimentally (*15, 16*). These applications of the dual electrode, in the generation-collection mode, used catalytic systems which did not involve enzymes. The present investigation is aimed at pursuing the advantages that the dual microband electrode might hold for biochemical electroanalysis and comparing electrodes with different interelectrode space and their individual responses in a biochemical reaction coupled to an electrochemical one. We have used the system of glucose oxidase (GOx) and glucose with a substituted ferrocene acting as mediator in a non-oxygen-dependent manner (*17*). This is the first report of the application of the dual electrode configuration acting as a simple enzyme electrode.

EXPERIMENTAL SECTION

Reagents. Glucose oxidase (EC 1.1.3.4 from *Aspergillus niger*) was purchased from Sturge Enzymes and further purified (*18*). The final concentration of GOx in stock solution was 3.80 mM as determined spectrophotometrically (*19*).

D-Glucose (Aristar) was purchased from BDH; 1,1′-dimethyl-3-(1-hydroxy-2-aminoethyl)ferrocene (DMHAE-ferrocene) was synthesised in this laboratory by Dr. K. di Gleria.

Buffer solutions were prepared from AnalaR grade reagents (BDH) in Millipore Q deionized water; the supporting electrolyte was 0.1 M $NaClO_4$/0.02 M K_2HPO_4, adjusted to the required pH with $HClO_4$. Glucose solutions were prepared 24 prior to use in order to allow for the equilibration of the α and β anomers.

Apparatus. dc cyclic voltammetry experiments were performed at room temperature in a glass cell which had a working volume of 1 cm^3. The cell contained a dual-microband working electrode, a platinum gauze counter electrode, and a Radiometer type K4112 saturated calomel electrode (SCE) as reference. An Ursar Scientific potentiostat and scan unit were used with a Gould series 60,000 A3 chart recorder.

Fabrication of the Working Electrode. The dual electrode presented here was constructed by using an approach similar to that of Wightman et al. (*20*); the Au/epoxy/Au sandwich configuration is shown schematically in Figure 1. Microscope glass slides provide an easy-to-handle substrate for metal deposition. Though sputtering of gold on to glass normally requires Cr or Ti layers as a precoating on the glass surface, it was found that the gold adheres strongly to the substrate *if* the latter is thoroughly cleaned prior to sputtering. Interdiffusion of Ti (*1*) or Cr (*21*) into the Au film with time is therefore eliminated as a primary culprit for increasing resistance problems and eventual failure of the electrode in the case of Ti, plus the superimposed metal electrochemistry and the residual response of the electrode in the case of Cr. Glass splinters cut from the slides were cleaned before sputtering in Micro detergent solution, rinsed with distilled water

0003-2700/89/0361-2200$01.50/0 © 1989 American Chemical Society

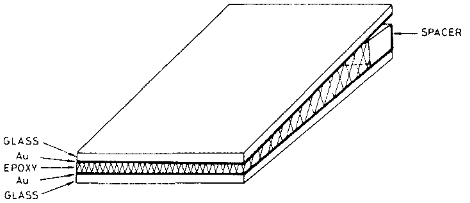

Figure 1. Schematic model of the microband electrode assembly.

followed by ethanol, and subsequently dried under a stream of Ar. Deposition of gold onto the glass was carried out by sputtering at ca. 10^{-5} Torr with an Ion Tech, Ltd. (Middlesex, UK), Microvac coater unit. Such metalized glass splinters were glued in pairs with a two-component epoxy (Araldite MY 753 with Hardener HY 932, Ciba-Geigy Plastics and Additives Co., Cambridge, UK), gold films facing, while the distance was kept to the micrometer range by a spacer 100 μm thick (Adhesive Teflon tape DF-1200, Dilectrix, AZ) at one end (Figure 1). The two splinters were pressed together during the two-stage curing schedule of the epoxy (1 h at 80 °C, then 12 h at 100 °C) and electrical contact to the individual gold films was achieved with copper leads attached with conductive silver paint (Johnson Matthey Chemicals, Royston, UK) to the gold on each splinter. The electrical contacts and the two triangular sides of the sandwich were sealed with two-component epoxy (Araldite, rapid-setting). The "sharp-edge" of the sandwich was polished on 600 and 800 grit sandpaper, then with 0.3-μm aluminum oxide/water slurry on Metron polishing cloth on a polishing wheel, rinsed, then finally polished on a damp cloth. The electrode thus obtained was sonicated for 20 s to remove any alumina present and then repolished using a damp cloth. Electron micrographs were obtained with a Jeol JSM-35X scanning electron microscope (SEM). The electrodes were coated with a thin layer of carbon (50–100 Å) on a Speedivac coating unit, Model 12E6 (Edwards High Vacuum, Ltd., Sussex, UK), at 10^{-5} Torr and mounted with conductive silver paint.

The advantage of this modified version is the fact that the interelectrode gap can be less than 10 μm without the two electrodes being short circuited and it can be brought up to the desired size by simple polishing on emery paper and checking under an optical microscope. The disadvantages that mica presents (*16*), due to its instability during polishing, are also removed as the epoxy is of high mechanical strength (*22*).

Procedure. Electrochemical measurements were carried out in aqueous solutions degassed with Ar in the three-electrode mode (single-band electrode) and in the four-electrode mode (generation collection). A stream of Ar was constantly maintained over the solution in order to eliminate any competition for GOx by oxygen. The dual electrode was polished on damp cloth and placed in the cell prior to any glucose or GOx addition to the DMHAE-ferrocene solution, and the cell was sealed. Additions of glucose and GOx were carried out from degassed stock solutions. After each addition the solution was mixed with a magnetic stirrer and the potential was scanned at the generating electrode at 5 mV s^{-1}. The collecting electrode was kept at zero potential with respect to SCE and the current was recorded.

RESULTS AND DISCUSSION

Electrode Characterization by Cyclic Voltammetry at Single Band Electrodes. The behavior of the microband electrodes for the DMHAE-ferrocene couple, when they are independently addressed, is shown in Figure 2. One electrode is scanned while the other in the dual configuration is left at open circuit. The shape of the voltammograms thus obtained depends on the scan rate used. At low scan rates, up to 50 mV s^{-1}, no peak is observed due to the steady-state mode of the cylindrical diffusion to the electrode. This is consistent with previous reports (*20, 23*). At scan rates higher than 50 mV s^{-1} depletion of the diffusion layer sets in; hence the current becomes scan-rate dependent and the conventional peaks of cyclic voltammetry begin to appear. One should note how well matched the two electrodes in the pair are, as shown by the striking similarity of voltammograms a and b in Figure 2.

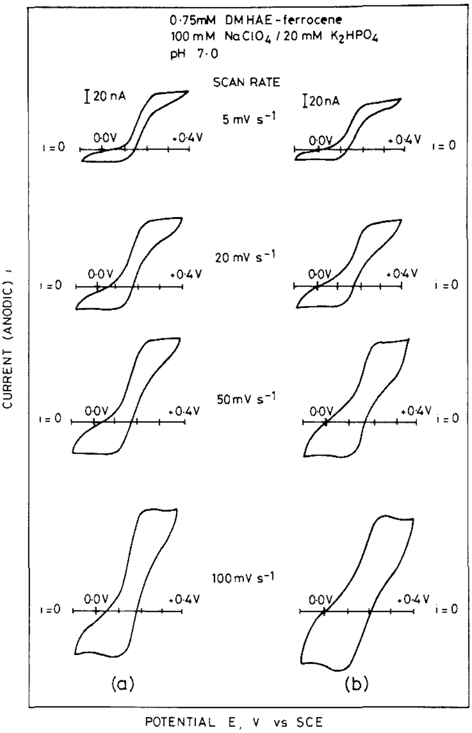

Figure 2. (a) Typical cyclic voltammograms for a single band of a dual electrode. Potential scanned at the scan rates indicated on the figure with the second electrode at open circuit. (b) As in (a) with the second electrode scanning and the first one at open circuit.

For a band electrode the theoretical quasi-steady-state current is given (*24*) by eq 1

$$i = nFDlC[5.553/(\ln \theta) - 6.791/(\ln \theta)^2] \qquad (1)$$

where n is the number of electrons involved, F is the Faraday constant, D is the diffusion coefficient of the electroactive species, l is the electrode length, and C is the concentration of the electroactive species. The dimensionless parameter, θ, is given (*16*) by

$$\theta = 4Dt/W^2 \qquad (2)$$

where W is the electrode width the t the experimental time. The electrode widths used in the calculations were determined from scanning electron microscope (SEM) micrographs whereas the experimental time t (corresponding to RT/Fv where v is the scan rate) was 5 s. The electrodes, when polished, have well-defined geometries of both the gap and the gold microbands, as seen in the SEM photographs (Figure 3). The theoretical shape for the electrodes is that of a rectangle (*16*) and as observed in Figure 3, the electrodes prepared here are indeed of almost perfect rectangular shape. (The portion of the electrode shown in Figure 3a is only a fraction of the actual length; it is however representative of the shape and the well-defined geometry of the whole length of the electrode). It is not therefore surprising that the experimental currents are in good agreement with the theoretical ones, within experimental error (see Table I). The results presented are representative of a set of data obtained with

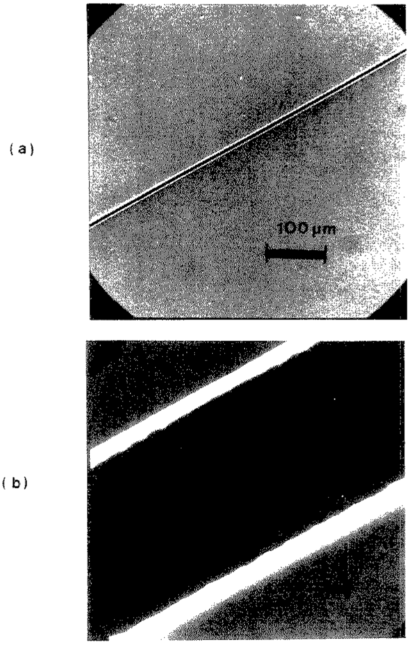

Figure 3. (a) Scanning electron micrograph of the dual microband electrode Au/epoxy/Au with bands 0.8 μm wide and an epoxy film 7 μm wide over a length of 590 μm. (b) SEM of the same electrode at a higher magnification.

Table I. Comparison of t_{rxn} and t_{gap} for the Electrodes of Different W_{gap} Values

W_{gap}, μM	t_{rxn}, s	t_{gap}, s	ϕ_{SS}[a]	ϕ_{SS}[b]
7	0.323	0.075	0.40	0.36
82	0.323	10.345	0.088	0.00

[a] Collection efficiency ϕ_{SS} prior to enzymatic reaction. [b] Collection efficiency ϕ_{SS} after the enzymatic reaction is coupled to the electrochemical one with addition of GOD (1 μM) and glucose (5 mM).

different electrodes manufactured in the same way. The two bands of width W_1 and W_2 respectively belong to the same dual electrode configuration. The resulting currents obtained in a solution of 2 mM DMHAE-ferrocene are 305 nA (for the band of width W_1) and 300 nA (for the band of width W_2), being in agreement with the calculated values of 309 and 305 nA to 99% and 98%, respectively. Theoretical currents were estimated by using eq 1 with $D = 6.5 \times 10^{-6}$ cm^2 s^{-1}, $l = 0.5$ cm, and $W_1 = 8 \times 10^{-5}$ cm, $W_2 = 7.5 \times 10^{-5}$ cm as obtained from the SEM pictures. It can thus be concluded that the width (W) of the electrodes estimated electrochemically is very close to the geometric W of the gold bands; hence it is not necessary to calculate an "effective" electrode width. All estimated widths are less than 1 μm, resulting therefore in sufficiently long θ values ($\theta \geq 100$) and allowing true quasi-state currents. It must be noted, however, that the excellent agreement observed between the theoretically predicted currents and those obtained in the cyclic voltammetric experiments may be fortuitous. The comparison between theory and experiment is useful because, for a band electrode of thickness of the order of a micrometer and a time scale of seconds, the current appears to have reached a constant value, then decaying slowly as $1/(\ln t)$.

Electrode Characterization in the Generation–Collection Mode. Generation–collection experiments are of the general type

generating electrode $\quad R \rightarrow O$

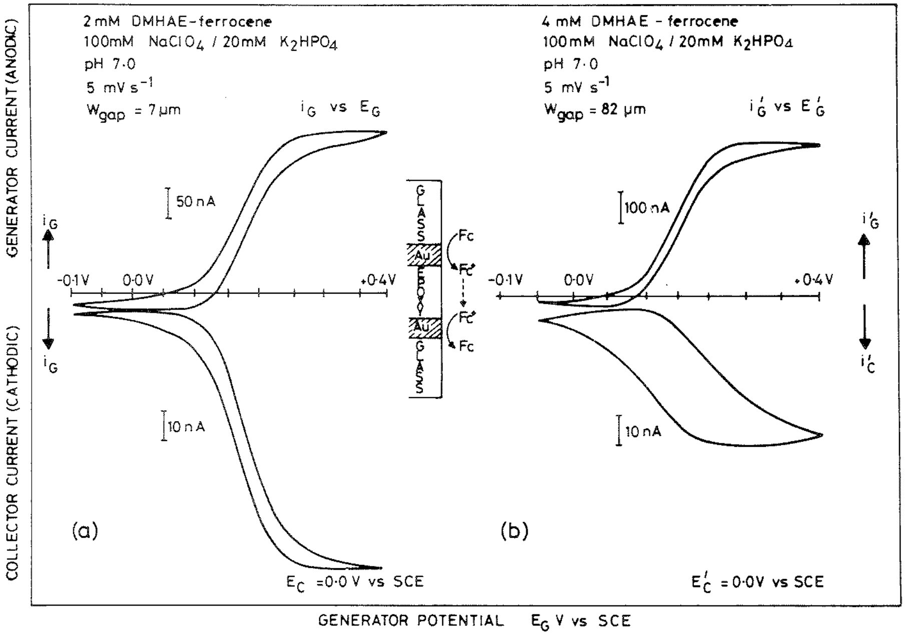

Figure 4. Generation–collection experiment with electrodes of different W_{gap}.

collecting electrode $\quad O \rightarrow R$

where O and R are the oxidized and reduced forms, respectively, of the DMHE-ferrocene. A typical set of curves for the dual electrode working in the generation–collection mode is shown in Figure 4. Ferrocene is oxidized as the potential of one electrode (generating) is scanned from the negative to the positive direction, hence the anodic wave i_G. The adjacent electrode (collecting), kept at 0.0 V vs SCE, shows an increased cathodic current, i_C, as the oxidized ferrocene reaches it through a diffusion-controlled process.

The steady-state collection efficiency ϕ_{SS}, defined *(16)* as the ratio of the collecting current (i_C) to the generating current (i_G), is given by

$$\phi_{SS} = |i_C|/|i_G| \qquad (3)$$

and it is dependent on the interelectrode distance W_{gap} as given *(16)* by

$$\phi_{SS} = 0.033 + 0.21 \log \theta_{gap} - 0.016(\log \theta_{gap})^2 \qquad (4)$$

where the dimensionless parameter θ is given by

$$\theta_{gap} = 4Dt/W_{gap}^2 \qquad (5)$$

and D and t have the same meaning as in eq 2. This dependence of ϕ_{SS} on W_{gap} is clearly presented in Figure 4 where generation–collection curves are shown for electrodes of two different W_{gap} values, as determined from SEM photographs. The smaller interelectrode distance of electrode I (W_{gap} = 7μm) resulted in the larger collection efficiency (ϕ_{SS} = 0.4) for the reduction of DMHAE-ferrocene compared with that obtained for electrode II: ϕ_{SS} = 0.088; W_{gap} = 82 μm under the same experimental conditions. The improved collection efficiency brought about by the smaller W_{gap} is in good agreement with previous reports *(15)*.

The W_{gap} values for the two electrodes were also determined electrochemically as 10 μm for electrode I and 84 μm for electrode II. When these values are compared to those obtained from SEM photographs, a deviation of 3 and 2 μm respectively is apparent. Previous reports *(16)* showed a W_{gap} determined electrochemically up to 5 times higher than W_{gap} determined from an SEM on a polished electrode. It should however be noted that only the electrode of the smaller interelectrode distance has a log θ value between 1.8 and 5.7, being the limits within which eq 4 had been shown to hold *(16)*.

The values of currents obtained electrochemically are always slightly lower than those theoretically predicted. This rather insignificant difference could be due to minor contamination of the electrode surface, resulting thus in a smaller effective working area of the bands, or more probable to an error in the calculation of the diffusion coefficient of the ferrocene or in the estimation of the ferrocene concentration itself. In addition the gap width, W_{gap}, for electrodes I and II determined electrochemically seems to be slightly larger than the values obtained by SEM. This can be accounted for by the uneven removal of metal, glass, and epoxy, a factor which is thought to increase the gap width as reported in ref 16. It appears however that this uneven removal of the different components of the electrode does not have a dramatic effect on the agreement between the theoretical and experimental results. This may demonstrate another advantage of using this particular epoxy as separator instead of, for example, mica.

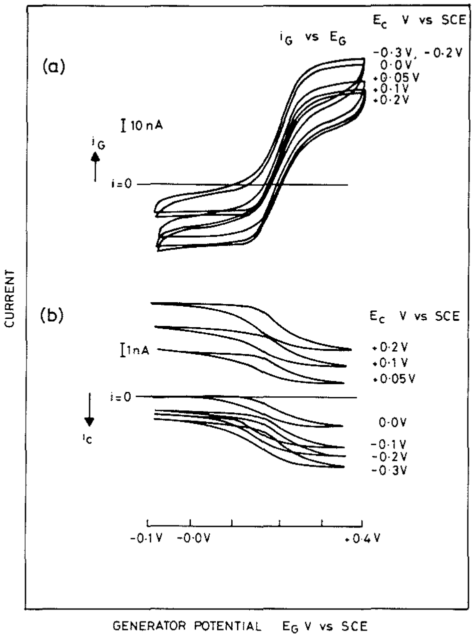

Figure 5. Generation–collection experiment. (a) Generating current curves shown as i_G vs E_G. Potential of the generating electrode scanned at 5 mV s^{-1}. The collecting electrode was kept at a resting potential, E_C indicated on the figure. Solution 0.2 mM DMHAE-ferrocene in phosphate buffer, pH 7.0. (b) Collecting current curves shown as i_C.

Variations in the generating and collecting electrode response due to change of the resting potential can be seen in Figure 5. The sigmoidal shape remains a constant feature of the voltammograms of the generating (Figure 5a) and the collecting (Figure 5b) processes with a slight decrease in size of the current i_C when the collecting electrode was poised at 0.0 and +0.05 V potentials. The major effect observed is the shift of base-line current when the resting potential is changed from positive to negative values. At, for example, +0.2 V, DMHAE-ferrocene is oxidized at the collecting electrode and therefore high positive currents pass. However, when the scanning electrode reaches oxidative potentials, it now also oxidises the DMHAE-ferrocene. Shielding of the diffusion field is imposed on the resting electrode, resulting in diminished oxidative current, whereas the feeding of the oxidized species from the collecting to the generating electrode gives the reduction current observed in the negative region of the scan. Hence the shielding effect (on the oxidatively poised electrode) generates a sigmoidal voltammogram. The maximum shielding effect would be expected to be seen at poised potentials larger than +0.3 V. However no change was observed in the voltammograms of the collector electrode at potentials higher than +0.2 V. It appears that when the poised potential is higher than the half-way potential of the electroactive species (0.175 V vs SCE for DMHAE-ferrocene) the shielding effect is not enhanced any further. When a negative value for the resting potential is considered, for example −0.1 V, the ferrocene at the collecting electrode is kept in its reduced state and therefore no appreciable current passes. However, when the generating electrode reaches oxidative potentials, DMHAE-ferrocene is oxidized and diffusion of the oxidized species toward the resting electrode results in increased reductive currents. The shielding effect is removed and the current plateau observed at the generating electrode increases in the positive region of the scan.

Figure 6 shows the behavior of the two dual electrodes of different interelectrode distance at various scan rates in the generation–collection mode. The striking feature of Figure 6a (as compared to Figure 6b) is that there is a collectable

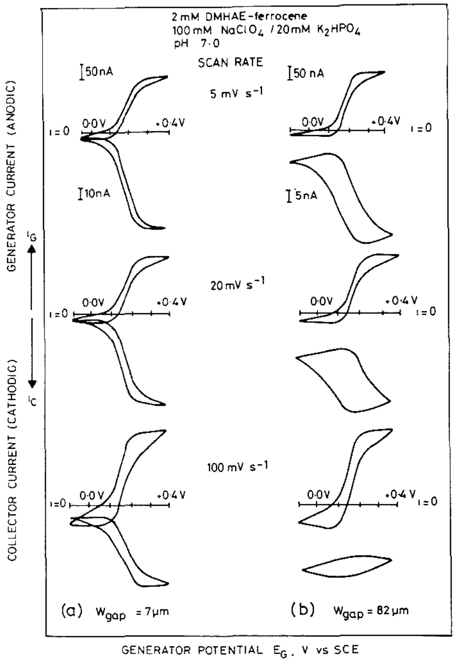

Figure 6. Generation-collection mode in 2 mM DMHAE-ferrocene solution in phosphate buffer, pH 7.0. Potential of the generating electrode scanned at the scan rates indicated on the figure. Collecting electrode poised at 0.0 V vs SCE.

amount of the generated species even at scan rates as high as 100 mV s^{-1} when the interelectrode distance is 7 μm, whereas there is hardly any measurable collection current when the distance is 82 μm at the same high scan rate. In the latter case, the generated species does not have enough time, within the experimental time scale, to diffuse across the gap and be detected on the collecting electrode.

In summary, the dual configuration manufactured by the method presented here performs as expected according to the predictions (*15*, *16*) of the digital simulations. In particular, each band has a regular geometry, allowing for good agreement between prediction and experiment; the collection efficiency depends on the interelectrode distance and can be used to calculate successfully the W_{gap} of a given electrode.

Generation–Collection Experiments following an Enzymatic Reaction. The dual electrodes manufactured here were employed to detect changes in electrode response resulting from the catalytic homogeneous reactions of glucose–glucose oxidase coupled to the electrochemical oxidation of the DMHAE-ferrocene (*17*) in a non-oxygen-dependent manner. In general the electrochemical reaction (eq 6) is coupled to a solution reagent Z (eq 7) as shown below:

$$R \rightarrow O \qquad (6)$$

$$Z + O \xrightarrow{k} R + \text{products} \qquad (7)$$

In the experiments performed here, Z is the reduced form of the enzyme. The processes are summarized in Figure 7a; Figure 7b shows the reactions that take place in the presence of oxygen. The expected effect of the subsequent reaction is to increase the oxidation current at the generator electrode and to decrease the collecting current (*16*). Under the experimental conditions employed, however, the time domain associated with the microelectrodes is too short to allow direct detection of the catalytic enhancement effect on the generating electrode. Most of the ferricinium ions, however, are consumed by the enzyme on their way to the collecting electrode, resulting in a considerable diminution of the collecting current (Figure 8a). The generation and collection currents observed for the ferrocene-alone solution are well apart. Upon addition of glucose, the curve corresponding to the resting electrode (i_C) shifts upward. In the presence of 0.05 μM GOx the shift in the collecting current curve becomes even more pronounced while the diminution of the collection current can be seen with the accompanying flattening of either tail of the curve. All these effects become more pronounced upon further addition of GOx. However, when the interelectrode distance is 7 μm, the enzymatic reaction has a quite different effect upon the collection wave (Figure 8b). The generator and collector waves initially overlap each other while upon addition of glucose the collection wave (i_C) shifts upward in a similar way to that seen for the electrode of the larger gap. Upon addition of 0.05 μM GOx there is only a slight diminution of the current with a further upward shift of the curve. However there is, in addition, a collapse of the normal hysteresis shape into a very thin loop, which eventually leads to inversion of the hysteresis shape upon further addition of GOx. It should be noted that when glucose or GOx alone is added to the ferrocene solution, the collecting wave shifts upward in much the same way. This initial shift could be due to adsorption of glucose or GOx on the electrode surface; however in no case can the diminution of the current or the inversion of the hysteresis shape be achieved by adding increasing amounts of glucose or GOx alone. Concomitant adsorption of both reagents can also be ruled out as the collapse of the hysteresis shape and its subsequent inversion observed for the electrode of W_{gap} equal to 7 μm are characterstics both reversible and reproducible in the sense that if the solution is left unprotected from the oxygen in the air for sometime, the original curves of the ferrocene alone are restored, due to the complete consumption of the substrate in the solution by the enzymatic reaction with

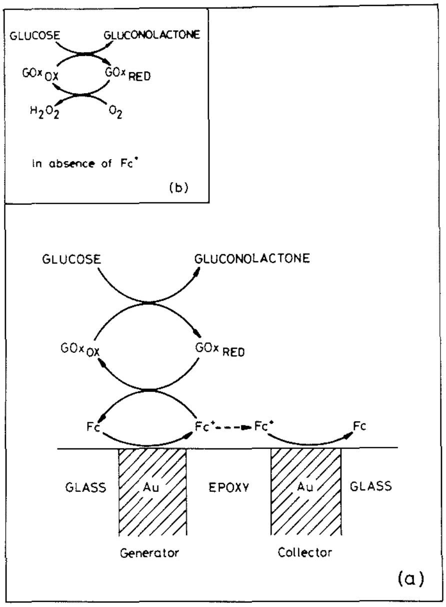

Figure 7. Scheme showing the reaction sequence for the electrochemically coupled enzymatic oxidation of glucose.

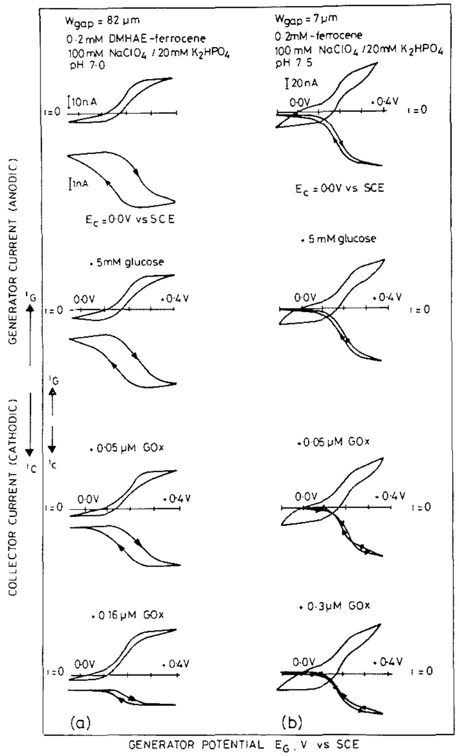

Figure 8. Generation–collection mode with a following enzymatic reaction for electrodes of different W_{gap}: (a) W_{gap} = 82 μm. W_{gap} = 7 μm.

dissolving oxygen (Figure 7b). Deoxygenation of the same solution, followed by addition of substrate, causes once more the inversion of the hysteresis shape and the slight diminution of the collection current.

The half-life of the enzymatic reaction is compared to the time required for the ferrocene to diffuse across gaps of different sizes in Table I. The reaction time t_{rxn} and t_{gap} are estimated (*16*) by using eq 8 and 9

$$t_{rxn} = 1/k[Z] \tag{8}$$

where k is the rate constant for the following reaction and [Z] the concentration of the reduced form of the enzyme

$$t_{gap} = W_{gap}^2/D \tag{9}$$

where W and D have their usual meaning. The rate constant k for the coupled reaction is taken as 3.1×10^6 M^{-1} s^{-1} (*25*). The concentration of the reduced form of GOx ($[GOx]_{RED}$) is taken to be equal to that of the total GOx ($[GOx]_{total}$) added at the beginning of the experiment. In the presence of excess substrate (glucose) all of the enzyme can be considered to be in its reduced form as glucose is converted into gluconolactone. As the cell is sealed from the oxygen in the air and the solution itself is thoroughly degassed, the reduced form of the enzyme cannot be converted into its oxidized form until the electrochemical reaction starts. Therefore the assumption of $[GO_x]_{RED}$ being equal to $[GOx]_{total}$ is valid.

As t_{rxn} (0.323 s) is not that much larger than the t_{gap} for the electrode of W_{gap} equal to 7 μm (i.e. t_{gap} = 0.075), one would expect to observe only a minor effect on the ϕ_{SS} brought about by the chemical step. Indeed the quasi-steady-state collection efficiency ϕ_{SS} remains almost the same with or without the enzymatic reaction following the electrochemical one (Table I) and the effect of the electrochemical step is hardly observed in quantitative terms. However, it can be followed by the progressive change in the hysteresis shape of the collection current wave with further additions of GOx.

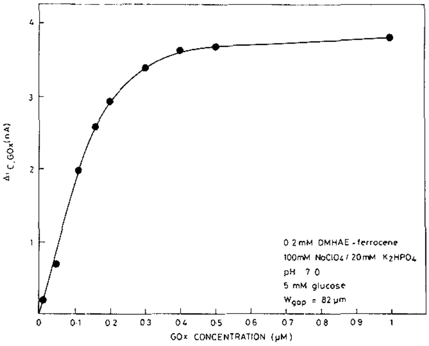

Figure 9. Effect on the collecting current of titration of increasing concentrations of GOx.

It is clearly demonstrated that the presence of the enzymatic reaction induces certain features in the performance of the dual electrode that cannot be fully predicted by the recent theoretical models (*16*). It could well be that the experimental conditions are not strictly pseudo first order or second order as the enzyme is present neither at concentrations much larger (pseudo first order) or of the order of that of the ferrocene (second order). It would be useful in the future to consider some modification of the already existing simulation model (*16*) in order to incorporate the more complicated enzymic cycle.

In order to determine the minimum amount of enzyme required for the catalytic reaction to be detected, a titration of GOx into a DMHAE-ferrocene plus glucose solution was carried out for the two electrodes of different W_{gap} values. It was found that, for W_{gap} equal to 7 μm, the collapse of the hysteresis into a thin loop can be brought about by addition of GOx to a concentration as low 0.005 μM. The same concentration of GOx brings about a significant diminution of the current at an electrode of W_{gap} equal to 82 μm. To collecting current dependence on the concentration of GOx for the electrode of the larger gap can be seen in Figure 9 as $\Delta i_{C,GOx}$ vs concentration of GOx, where $\Delta i_{C,GOx}$ is given by

$$\Delta i_{C,GOx} = i_{[GOx]=0} - i_{[GOx]=X} \tag{10}$$

where $i_{[GOx]=0}$ is the current at zero concentration of GOx and $i_{[GOx]=X}$ is the current at concentration X of GOx. There is a sharp increase in the function $\Delta i_{C,GOx}$ over the range of zero to 0.2 μM of GOx corresponding to a decrease of the current at the collecting electrode. After addition of 0.3 μM the curve reaches a plateau when $i_{[GOx]=X}$ is zero. The behavior seen with the electrode of W_{gap} equal to 7μm is nowhere near as dramatic when compared to that of the larger gap. The function Δi increases only very slightly over the same concentration range of GOx: the term $i_{[GOx]=X}$ of the function Δi never reaches zero; i.e. there is always some oxidized species reaching the collecting electrode. It should also be noted that the quasi-steady-state collection efficiency ϕ_{SS} tends to zero upon addition of 1 μM GOx for the electrode of W_{gap} equal to 82 μm whereas a finite and rather large ϕ_{SS} (equal to 0.36) is obtained for the electrode of the smaller interelectrode distance. It is therefore clear that a large interelectrode gap

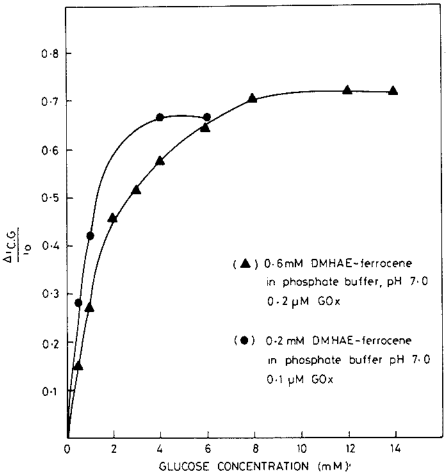

Figure 10. Titration curves showing dependence of the collecting current on glucose concentration with the electrode having W_{gap} equal to 82 μm at different concentrations of DMHAE-ferrocene and GOx.

allows more time for the enzymatic reaction to take place and so to be detected successfully.

The electrode of W_{gap} equal to 82 μm was therefore used for further experiments in order to evaluate the utility of the dual configuration in the generation–collection mode as a detection system of a chosen analyte (glucose). Typical calibration curves for glucose determination are shown in Figure 10. High enzyme concentration (1.25 μM, the level often used with electrodes of conventional size) results in complete canceling of collection current after addition of 0.02 mM glucose, as the difference between t_{gap} and t_{rxn} at this concentration of GOx is much larger than the difference at lower concentrations of GOx. Reducing the concentration of the enzyme about 10-fold to 0.100 μM (● in Figure 10) allowed working within a higher concentration range of the analyte, this range being further extended by an increase of the [GOx] to 0.200 μm (in Figure 10). To achieve a similar increase in the range of currents detected for the calibration curve of the analyte, the ferrocene concentration was also increased, thereby extending even further the dynamic concentration range that the system can determine. Experiments with 0.6 mM DMHAE-ferrocene solutions seem to support this idea (▲ in Figure 10). A limit on the "usable" ferrocene concentration might be imposed by the deposition of ferricinium ion salts onto the electrode as the ferrocene concentration is increased to 2 or 3 mM. The upper detection limit of the system is much lower than that achieved by using a conventional electrode [limit = 30 mM glucose (*26*)]. This may depend on the interelectrode distance. Increase of the W_{gap} to values higher than 100 μm may well provide the solution but it was not possible up to now to manufacture electrodes with such specifications.

CONCLUSIONS

We have reported a modified version of the previously published method of fabrication of gold dual microband electrodes (*20*). Electrodes thus manufactured are stable over a period longer than 18 months. Cyclic voltammetry with the redox couple of a modified ferrocene was used to investigate each single band, while generation–collection experiments were used to characterize further the behavior of the electrode entity.

The simulation models reported (*16*) were used here to predict successfully interelectrode distances and electrode widths. The device was also demonstrated to be successful in detecting the analyte chosen and exhibits the ability to follow the coupled reaction quantitatively. These results demonstrate the feasibility of the use of dual microband electrodes in biochemical electroanalysis.

ACKNOWLEDGMENT

The authors thank Mr. G. Dixon-Brown (Department of Metallurgy and Science of Materials, Oxford) for help with the scanning electron microscope.

LITERATURE CITED

(1) Fleischmann, M.; Pons, S.; Rolison, D. R.; Schmidt, P. P. *Utramicroelectrodes*; Datatech Systems, Inc., Science Publishers: NC, 1987.
(2) Wightman, R. M. *Anal. Chem.* **1981**, *53*, 1125A.
(3) Bond, A. M.; Lay, P. A., *J. Electroanal. Chem.* **1986**, *199*, 285.
(4) Geng, L.; Murray, R. W. *Inorg. Chem.* **1986**, *25*, 3115.
(5) Hedges, W. M.; Pletcher, D. *J. Chem. Soc., Faraday Trans. 1*, w1986, *82*, 179.
(6) Pena, M. J.; Fleischmann, M.; Garrard, N. *J. Electroanal. Chem.* **1987**, *220*, 31.
(7) Fitch, A.; Evans, D. H. *J. Electroanal. Chem.* **1986**, *202*, 83, and references therein.
(8) Scharifker, B.; Hills, G. *J. Electroanal. Chem.* **1981**, *130*, 81.
(9) Howell, J. O.; Wightman, R. M. *Anal. Chem.* **1984**, *56*, 524.
(10) Russel, A.; Repka, K.; Dibble, T.; Ghoroghchian, J.; Smith, J. J.; Fleischmann, M.; Pitt, C. H.; Pons, S. *Anal. Chem.* **1986**, *58*, 2961.
(11) Engstrom, R. C.; Weber, M.; Wunder, D. J.; Burgess, R.; Winquist, S. *Anal. Chem.* **1986**, *58*, 844.
(12) Ghoroghchian, J.; Sarfarazi, F.; Dibble, T.; Cassidy, J.; Smith, J. S.; Russel, A.; Dunmore, G.; Fleischmann, M.; Pons, S. *Anal. Chem.* **1986**, *58*, 2278.
(13) Robinson, R. S.; McCurdy, C. W.; McCreery, R. L. *Anal. Chem.* **1982**, *54*, 2356.
(14) Kittlesen, G. P.; White, H. S. *J. Am. Chem. Soc.* **1985**, *107*, 7373.
(15) Bard, A. J.; Crayston, J. A.; Kittlesen, G. P.; Varco Shea, T.; Wrighton, M. S. *Anal. Chem.* **1986**, *58*, 2321.
(16) Varco Shea, T.; Bard, A. J. *Anal. Chem.* **1987**, *59*, 2101.
(17) Cass, A. E. G.; Davis, G.; Green, M. J.; Hill, H. A. O. *J. Electroanal. Chem.* **1985**, *190*, 117.
(18) Di Gleria, K.; Hill, H. A. O.; McNeil, C. J.; Green, M. J. *Anal. Chem.* **1986**, *58*, 1203.
(19) Duke, R. F.; Weibel, M. K.; Page, D. S.; Bulgrin, V. G.; Luthy, J. *J. Am. Chem.* Soc. **1969**, *91*, 3904.
(20) Wehmeyer, K. R.; Deakin, M. R.; Wightman, R. M. *Anal. Chem.* **1985**, *57*, 1913.
(21) Aoki, K.; Osteryoung, J. *J. Electroanal. Chem.* **1981**, *125*, 315.
(22) Araldite MY 750 and MY 753 with Hardener HY 932, Instruction Sheet No. C26e, Ciba-Geigy, May 1979.
(23) Bond, A. M.; Henderson, T. L. E.; Thormann, W. *J. Phys. Chem.* **1986**, *90*, 2911.
(24) Coen, S.; Cope, D. K.; Tallman, D. E. *J. Electroanal. Chem.* **1986**, *215*, 29.
(25) Frew, J. E., Medisense (UK), Inc., private communication.
(26) Green, M. J.; Hill, H. A. O. *J. Chem. Soc., Faraday Trans. 1* **1986**, *82*, 1237.

Received for review November 4, 1988. Accepted June 26, 1989. The authors thank MediSense, Inc., for generous support and assistance.

Anal. Chem. 1989, 61, 2207-2211

Molecular Formula Determination of Capillary Column Gas Chromatographic Effluents Using Combined Microwave-Induced Plasma Emission and Mass Spectral Data

D. B. Hooker and J. DeZwaan*

7255-209-0, Physical and Analytical Chemistry Research, The Upjohn Company, Kalamazoo, Michigan 49001

The use of elemental composition information derived from microwave-induced plasma emission as a complement to mass spectral data for the determination of molecular formulas of materials eluted from a gas chromatograph was explored. This evaluation was conducted using the atomic emission responses obtained from large (GMW 200–400 range) molecules of varying structure that were composed of three to six elements. The emission responses were calibrated by using a set of small molecules of unrelated chemical structure. The results obtained indicate that, if an accurate mass has been measured, the molecular formula can be determined by using only a subset of the elemental ratios available from the atomic emission. If, however, only a low-resolution determination of the molecular weight has been made, all of the elemental ratios are required for the determination of a molecular formula. Of the examples reported here, all but one molecular formula could be determined unambiguously from the low-resolution molecular weight and the atomic emission data. In that particular case, possible molecular formulas could be limited to three, while an accurate mass determination alone for this molecule would produce 23 molecular formulas.

INTRODUCTION

The determination of a molecular formula is an important step in the characterization or identification of an unknown material. Because of this importance, the molecular formula is one of the first determinations attempted when a new material is isolated. On bulk materials, molecular formulas can be obtained by combining microanalytical data (elemental composition on a weight percent basis) with mass spectral data (molecular weight). If an accurate mass determination (high-resolution mass spectrometry) is made on a material, usually only a limited amount of information on elemental composition is required to obtain the molecular formula. If only a low-resolution molecular weight is available, however, all of the elements composing the material must be specified and accurate microanalytical data for all except one of them must usually be known to obtain the correct molecular formula.

Although highly accurate and reliable microanalytical methods are available for all common elements, these determinations typically require from 1 to 10 mg of pure material for each elemental determination. These sample requirements preclude the use of these classical techniques of analysis for materials that (1) are components of mixtures, (2) are in limited supply, or (3) cannot be purified in sufficient quantity. Because these types of materials can often be obtained in pure form by using capillary column gas chromatography, there has been interest in using microwave-induced plasma (MIP) emission detectors as a means of determining the elemental composition of eluted materials since the initial development of the technique by McCormack (*1*).

This technique has high potential for elemental determinations in organic materials because MIP's sustained in a helium matrix can largely reduce all samples to their elements and provide for efficient excitation of a variety of common nonmetals. The responses obtained have been reported to be both specific for each element and linear over a wide range. Because the possibility exists for observing several of these elemental responses simultaneously, several investigators have explored using MIP emission as a means of empirical formula determination (*2–4*).

MIP emission data alone can provide for only an estimation of the empirical formula and not the molecular formula since only elemental ratios can be determined. When combined with mass spectral information on molecular weight, in much the same way as traditional microanalytical information, these experimentally derived elemental ratios can often yield an unambiguous determination of the molecular formula. The objective of this work was to make a realistic evaluation of the general potential of combined MIP–MS analysis for determining molecular formulas. Because of this objective an attempt was made (1) to avoid homologous series or closely related analogues, (2) to avoid concentrating on small molecules (except for calibration), (3) to avoid striving for unusual levels of precision, and (4) to avoid relying on other types of data to infer a molecular formula.

The elemental composition data reported for the materials studied are evaluated both for the case where an accurate mass is known and for the case where only the molecular weight is available. In the first case, a limited set of data is sufficient to specify a molecular formula. This is consistent with the case of classical procedures discussed earlier and for the determination of molecular formulas of nanograms of a solid sample using MIP emission as reported elsewhere (*5*). In the second case, again as with determinations using classical procedures, if only the molecular weight is known, it is generally true that all elements present in the molecule must be identified before a unique molecular formula can be determined.

In the simple chromatograms arising in this work, it is possible to generate the necessary data by using separate chromatographs, columns, and sample runs for MIP and MS data. Because of the effects of different vacuum levels on the observed retention times, however, a problem in correlating the two data sets can arise with complex mixtures. The data reported here were obtained by using a detector that can monitor the MIP emission and mass spectral (low resolution) data simultaneously from a single sample injection.

EXPERIMENTAL SECTION

This instrumentation consisted of a capillary column gas chromatograph (Hewlett-Packard Model 5890) in which the effluent was split inside the oven (*6*) with part being conducted to the MIP through a heated transfer line and the remainder going

---

*Author to whom correspondence should be addressed.

0003-2700/89/0361-2207$01.50/0 © 1989 American Chemical Society

Table I. Materials Used and Their Source

compound	no.	empirical formula	source
1-chloro-2-fluorobenzene	1	C_6H_4ClF	Aldrich
3-chloroaniline	2	C_6H_6NCl	Aldrich
benzothiazole	3	C_7H_5NS	Eastman
2-chlorobenzothiazole	4	C_7H_4NClS	Eastman
2-fluorobiphenyl	5	$C_{12}H_9F$	Aldrich
benzophenone	6	$C_{13}H_{10}O$	Aldrich
diphenyl ether	7	$C_{12}H_{10}O$	Aldrich
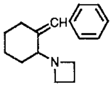	8	$C_{16}H_{21}N$	Upjohn
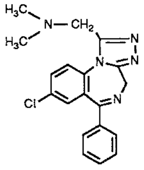	9	$C_{19}H_{18}N_5Cl$	Upjohn
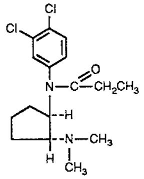	10	$C_{16}H_{22}N_2OCl_2$	Upjohn
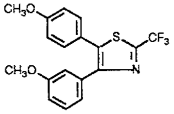	11	$C_{18}H_{14}NO_2SF_3$	Upjohn

to the mass selective detector (Hewlett-Packard Model 5970B). The MIP emission detector used was a Model MPD 850 (Applied Chromatography Systems, Luton, England), which incorporates a low-pressure (5–10 Torr) $^1/_4$-wavelength Evanson type cavity (7) and a $^3/_4$-m (dispersion = 1.39 nm/mm) monochromator. The output from up to eight fixed exit slits was monitored by using a couple of four-channel interface boxes in a MAXIMA 820 chromatography workstation.

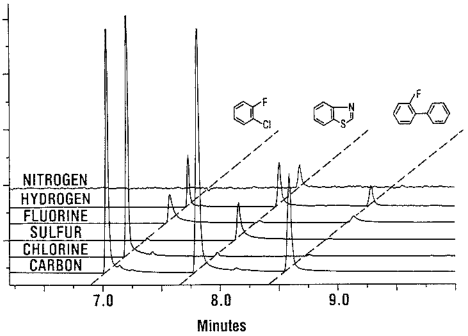

Figure 1. Six individual MIP emission responses observed simultaneously for a chromatogram run on a mixture of compounds **1**, **3**, and **5**.

The compounds used in this study are listed in Table I along with their source. The smaller molecules (compounds 1–7) were selected as calibration materials while compounds **8–11** were used to evaluate the capabilities of this combined procedure for determining molecular formulas.

Mixtures of the calibration compounds were dissolved in methanol and injected into the chromatograph. The sample sizes used were allowed to vary over a fairly wide range to allow for a more realistic estimate of the variability of these determinations. All separations were done with a DB-5 (15 m, 0.25 mm i.d.) J and W fused silica column. The MIP was sustained at a forward power of 150 W (2450 MHz) with minimal reflected power, and the emission was monitored at the wavelengths indicated in Table II. The atomic emission determinations for all elements, except oxygen, were made by using helium containing 0.2% oxygen. The oxygen to carbon ratios were determined by using helium containing 0.2% of a 95% nitrogen–5% hydrogen mixture. Shown in Figure 1 are six elemental responses recorded simultaneously from a single injection of a mixture containing compounds **1**, **3**, and **5**.

RESULTS

The results determined by using oxygen as scavenge gas were all obtained in a single day and results using the hydrogen–nitrogen mixture were all obtained on another day. Examples of the actual data obtained by integrating the emission responses are given in Table II for compounds **8–11**.

Table II. Area Responses Observed for Compounds 8–11 at the Wavelengths (nm) Indicated[a]

compound	carbon (247.9)	hydrogen (486.1)	sulfur (545.4)	chlorine (479.5)	fluorine (685.6)	nitrogen (746.8)	carbon[b] (247.9)	oxygen[b] (777.2)
8	0.842	0.710	0.019	0.029	0.013	0.135	1.13	
	0.367	0.329	0.009	0.011	0.007	0.0786	1.85	
	0.490	0.435	0.012	0.016	0.010	0.0888	1.90	
	0.828	0.722	0.019	0.021	0.015	0.118	1.82	
	0.907	0.786	0.020	0.024	0.015	0.161	2.18	
9	3.63	2.39	0.119	0.945	0.047	2.85	0.943	
	0.580	0.361	0.023	0.146	0.008	0.416	1.21	
	0.463	0.295	0.017	0.107	0.006	0.262	1.35	
	2.37	1.58	0.090	0.594	0.028	1.69	1.24	
	2.66	1.78	0.090	0.621	0.037	2.02	1.56	
10	2.89	2.58	0.062	1.65	0.046	0.955	0.643	0.0552
	0.426	0.388	0.010	0.252	0.006	0.162	0.920	0.0772
	0.556	0.513	0.016	0.333	0.008	0.188	0.958	0.0789
	1.92	1.76	0.052	1.10	0.025	0.573	0.907	0.0843
	2.00	1.82	0.054	1.15	0.026	0.633	1.06	0.0941
11	1.43	0.670	0.336	0.030	1.44	0.232	0.472	0.094
	0.429	0.213	0.107	0.009	0.415	0.067	0.724	0.153
	0.549	0.265	0.129	0.009	0.535	0.077	0.727	0.158
	1.09	0.531	0.265	0.013	1.16	0.177	0.693	0.147
	1.19	0.595	0.294	0.019	1.19	0.189	0.819	0.169

[a] Five determinations were made for each sample at each wavelength. [b] Run on different day with different scavenge gas.

Table III. Molar Responses Relative to Carbon[a]

compound	hydrogen	nitrogen	oxygen	chlorine	sulfur	fluorine
1	0.689 (0.031)	-	*	4.62 (0.11)	-	6.11 (0.18)
2	0.640 (0.011)	2.40 (0.09)	*	4.47 (0.15)	-	-
3	0.602 (0.015)	2.52 (0.17)	*	-	4.55 (0.14)	-
4	0.565 (0.017)	2.23 (0.08)	*	4.44 (0.10)	4.72 (0.11)	-
5	0.674 (0.012)	-	*	-	-	5.83 (0.14)
6	*	*	1.35 (0.04)	*	*	*
7	*	*	1.36 (0.05)	*	*	*
8	0.665 (0.016)	2.8 (0.43)	-	-	-	-
9	0.687 (0.021)	2.69 (0.32)	-	4.66 (0.24)	-	-
10	0.662 (0.008)	2.66 (0.24)	1.39 (0.07)	4.65 (0.10)	-	-
11	0.628 (0.016)	2.81 (0.16)	1.88 (0.07)	-	4.35 (0.12)	6.04 (0.23)
av (total)	0.646 (0.042)	2.59 (0.22)	1.5 (0.26)	4.57 (0.11)	4.54 (0.19)	5.99 (0.13)
RSD, %	6.5	8.5	17.3	2.4	4.2	2.2
av (1-7)	0.634 (0.051)	2.38 (0.15)	1.36 (0.01)	4.51 (0.10)	4.64 (0.12)	5.97 (0.15)
RSD, %	8.0	6.3	0.7	2.2	2.6	2.5

[a] Standard deviations are given in parentheses. Also given are the average values for all samples and the average values for the calibration set (compounds 1-7).

Table IV. Actual and Experimental Elemental Ratios for Compounds 8-11[a]

compd	C/H	C/N	C/O	C/Cl	C/S	C/F	GMW
8							
actual	0.762	16.0					
LB	0.726	13.6		158	197	352	227
FB	0.740	14.8		156	202	352	
9							
actual	1.05	3.2		19.0			
LB	0.974	3.36		18.4	133	460	351
FB	0.992	3.66		19.0	130	461	
10							
actual	0.727	8.0	16.0	8.0			
LB	0.696	7.2	15.7	7.8	186	427	328
FB	0.709	7.8	17.3	7.9	182	428	
11							
actual	1.29	18.0	9.0		18.0	6.0	
LB	1.30	15.3	6.5	265	19.2	5.98	365
FB	1.33	16.6	7.2	269	18.8	5.99	

[a] Experimental values were calculated by using the full basis (FB) and the calibration on limited basis (LB) to establish relative response.

As indicated, five independent determinations were made for each molecule at each wavelength. The magnitude of the carbon signals reported in Table II provides a good means of assessing the variations in sample size, both between and within samples, that occurred. Area responses were observed even if the element was not contained in the molecule and are reported in Table II to one or two significant figures. These "ghost signals" are commonly observed in these types of experiments (*8*), but they are small when compared to the elemental emission signal observed if the element was present in the sample. Only in the case of the oxygen response for compounds 8 and 9 were ghosting signals not observed. In these two particular cases very small negative going responses were observed.

The molar response ratios were calculated for all the elements present in samples 1-11 by using the relation

$$\frac{X}{C} = \frac{R_x}{R_c}\frac{N_c}{N_x}$$

In this expression R_X and R_C represent the area responses observed for the element and for carbon, respectively. N_C and N_X are the number of carbon atoms and the number of X atoms in the empirical formulas of the compounds. No corrections of any kind (*9*) were made to the experimentally determined area responses R_X to calculate the response ratios and standard deviations reported in Table III. The numbers reported in Table III should not be associated with relative elemental sensitivities of the MIP detector since the area responses observed depended directly on various instrument settings and the signal to noise ratios of various channels were not the same. Information on sensitivities attainable can be found in ref 6. Based on previous experience in this lab and literature reports, the precision represented by the data in Tables II and III appears to be fairly typical (*10, 11*) and routinely attainable.

Ideally the molar response ratios determined would be totally independent of the compound being analyzed. The data in Table III indicate this to be nearly true with the possible exceptions being the H/C ratio observed for compound 4 and the O/C ratio observed for compound 11. The best estimate of the response factors comes from the average values of all the results (full basis), and these results are reported in Table III. Also reported in Table III are the average response factors obtained from compounds 1-7, which were initially designated as calibration samples.

DISCUSSION

Given in Table IV are the theoretical molar ratios of compounds 8-11 and the values determined experimentally by using both the limited basis (LB) and the full basis (FB) as sources for molar response ratios. Taken on their own, these values can be used to establish which elements are present in a material and which are not, as well as to provide an estimate of the empirical formulas. For example, compound 8 may be seen to be composed only of carbon, hydrogen, and nitrogen with an empirical formula of something near $C_{14}H_{19}N$. Based only on the data of Table IV, several possible empirical

Table V. Empirical Formulas Determined from the Experimental Elemental Ratios and the Molecular Formulas Consistent with the Exact Masses of Compounds 8–11

compd	molecular formula	empirical formula	molecular formulas[a]
8	$C_{16}H_{21}N$	$C_{13.6}H_{18.7}N$	$C_{16}H_{21}N$, $C_{11}H_{21}N_3O$
9	$C_{19}H_{18}N_5Cl$	$C_{18.4}H_{18.9}N_{5.5}Cl$	$C_{18}H_{22}NO_4Cl$, $C_{19}H_{18}N_5Cl$
10	$C_{16}H_{22}N_2Cl_2O$	$C_{15.7}H_{22.6}N_{2.2}O$	$C_{16}H_{22}N_2OCl_2$, $C_{11}H_{22}N_4O_3Cl_2$
11	$C_{18}H_{14}NO_2SF_3$	$C_{19.2}H_{14.8}N_{1.3}O_{2.9}F_{3.2}S$	$C_{21}H_{13}NOF_2S$, $C_{15}H_{15}NO_3F_4S$, $C_{18}H_{14}NO_2F_3S$

[a] The elemental ratio data were used to limit the ranges of allowable values for S, Cl, and F.

formulas could be proposed for each compound. Any information available from mass spectrometry concerning molecular weight, however, can be used to produce much more specific information.

If high-resolution mass spectra data are available, the accurate mass determined can be used to generate a set of possible molecular formulas. However, large molecules with the possibility of many compositional elements can produce a large set of possible molecular formulas. For example, compound **11** produces 23 possible choices for molecular formula within 5 millimass units of its exact mass of 365.0697 subject to the rather broad constraints of $C_xH_yN_{1,3}O_{0-4}S_{0-3}F_{0-4}$. Knowledge of the nitrogen, sulfur, and fluorine compositions presented in Table IV, however, dictates the tighter constraints of $C_xH_yNO_{1-4}F_{2-4}S_1$, which allows for only three possible molecular formulas over the same mass range. These possibilities are given in Table V. Of these three possible choices, only $C_{18}H_{14}NO_2SF_3$ is consistent with all elemental ratios. Also given in Table V are possible molecular formulas for compounds **8–10** that are consistent with the exact mass of these compounds. Constraints on the heteroatoms S, Cl, and F consistent with the MIP data were again used to limit the initial size of the list. Again in these cases, only one of the listed molecular formulas is consistent with all the experimental elemental ratios. On the basis of these samples, it appears that in most cases where an accurate mass has been determined only a subset of elemental ratios is required to establish a molecular formula, and it may usually be possible to obtain the molecular formula without the added difficulty of determining the oxygen content.

Because determination of accurate masses for GC effluents of unknown structue can require extensive set-up time and calibration, in addition to very expensive equipment, usually only a molecular weight and not an exact mass will be available. In these cases, the data obtained in oxygen scavenge gas (i.e., for all elements except oxygen) is usually not sufficient to establish a molecular formula. This is true because, unlike classical determinations where an absolute weight percent of each element is determined, the MIP data give only elemental ratios. Because only elemental ratios are available, an additional constraint (knowledge of all elemental ratios) is required to make molecular formula determinations using MIP–MS data.

Knowing that compounds **8–11** are composed of the elements and only the elements given in the experimentally derived empirical formulas in Table V is important because this constraint allows major refinements of these empirical formulas to be made if the molecular weights of the compounds are known. Forcing the elemental composition and elemental ratio data to be consistent with the molecular weight eliminates many of the possible choices for the molecular formula, because the following obvious constraints must also be met:

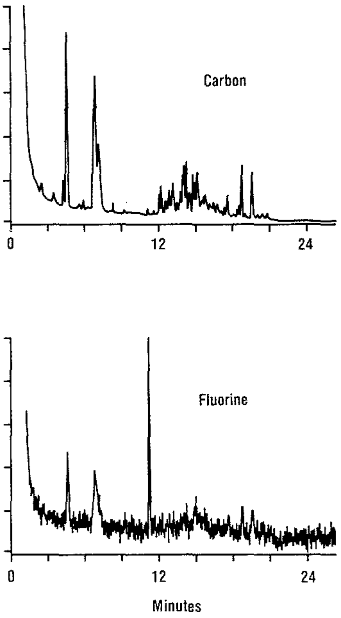

Figure 2. Carbon and fluorine MIP emission responses obtained for a chromatogram of an extracted sample of blood plasma obtained from a rat dosed with compound **11**. The fluorine response clearly identifies the small carbon peak with a retention time of 11 min as the peak of interest.

(1) The molecular formulas must give the measured molecular weight.

(2) In the absence of phosphorus, the number of nitrogens in the molecular formula must have the same parity as the molecular weight.

(3) The molar levels of elements in a molecular formula must be integers.

Somewhat surprising perhaps is the limited number of the potential molecular formulas that remain.

The simplest case reported here is compound **8**, which contains only C, H, and N with a molecular weight of 227. Because the molecular weight is odd, there can be only a single nitrogen in the molecular formula. This is the case because, if there were three nitrogens, the C/N ratio in Table IV would require far more carbon atoms than is possible for a molecular weight of 227. Given the constraints of a molecule with (1) a single nitrogen, (2) a complete composition of C, H, and N, (3) a C/H ratio of approximately 0.73, and (4) a molecular weight of 227, the only possible molecular formula is $C_{16}H_{21}N$.

Compound **9** contains C, H, N, and Cl and nothing else and has a molecular weight of 351. The constraints imposed by the C/Cl ratio and observed molecular weight indicate that the molecular formula can contain only a single chlorine atom. This indicates that the molecular formula should be similar to the empirical formula given in Table V for compound **9**. Applying the constraints given above leads to $C_{19}H_{18}N_5Cl$ as the only possible molecular formula for this material.

Determining a unique molecular formula becomes more difficult as the molecular weight and the number of constituent elements increase, which is also the case when classical microanalytical techniques or accurate mass determinations are used. For compound **10**, which contains five elements, the elemental ratios and molecular weight (GMW = 328) again

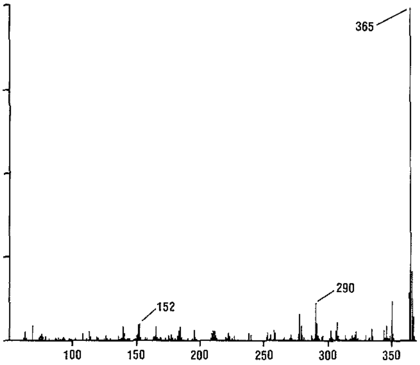

Figure 3. Mass spectrum of the fluorine containing peak in Figure 2, obtained simultaneously from the same injection as the responses in Figure 2.

lead to a unique molecular formula. For compound **11**, which contains six elements, a unique choice of molecular formula is not obtained. In this case, there are three most probable structures, none of which are totally consistent with the data. These possibilities are (1) $C_{18}H_{14}NO_2F_3S$, (2) $C_{17}H_{10}NO_3F_3S$, and (3) $C_{18}H_{17}NO_3F_2S$. An investigator using only the data available in this report would not have a basis for choosing one of these over the others.

The uncertainty in determining the molecular formula of compound **11** arises primarily because the oxygen response observed for this material was 35% greater per mole of carbon than would be expected on the basis of the other compounds studied. Literature available (*3, 11, 12*) on the determination of oxygen by MIP emission is limited, but it indicates that these determinations can be difficult.

In cases where pure, stable samples are available, standard microanalytical procedures are preferable to the MIP emission technique for molecular formula determinations. Even in these cases, however, a significant disadvantage for the classical procedures is the amount of sample required for analysis. If it were known for example that compound **11** was composed of only C, H, N, O, S, and F, approximately 25 mg of pure material would still be required to perform the microanalyses necessary to characterize it completely.

Practical situations, in which knowledge of the molecular formula would be useful but for which samples of the size and purity required for routine microanalytical determinations are not available, are frequently encountered. These situations include determination of trace impurities in bulk chemicals, rapid analysis of reaction mixtures, and analysis of complex mixtures. An example of a complex mixture is shown in Figure 2 where the carbon and fluorine responses produced by a sample of extracted blood plasma taken from a rat that had been previously dosed (intravenously) with compound **11** are shown. The plasma concentration of this material was in the microgram per milliliter range. The MIP emission responses shown not only demonstrate the potential for molecular formula determination (when combined with the mass spectrum of the chromatographic peak which was generated simultaneously and is shown in Figure 3) but also show the potential this experimental arrangement provides for locating the material(s) of interest in a complex matrix.

The results presented above indicate that careful generation of complementary MIP emission and mass spectral data sets can extend the capability of molecular formula determinations into a broad range of GC applications. Successful determinations of molecular formulas using these techniques generally require assurances that (1) a meaningful MIP emission response would be obtained for each element that may be present, (2) that the molecular ion associated with each peak of interest is identified, and (3) that the molar response observed for each element is independent of its chemical environment.

LITERATURE CITED

(1) McCormack, A. J.; Tong, S. G.; Cooke, W. D. *Anal. Chem.* **1965**, *37*, 1470.
(2) Uden, P. C.; Slatkavitz, K. J.; Barnes, R. M. *Anal. Chim. Acta* **1986**, *180*, 401–416.
(3) KehWei, Z.; Qing-Yu O.; Guo-Chuen, W.; Wei-Lu, Y. *Spectrochim. Acta* **1985**, *40B*, 349.
(4) Windsor, D. L.; Denton, M. B. *Anal. Chem.* **1979**, *51*, 1116.
(5) Hooker, D. B.; DeZwaan, J. *J. Res. NBS* **1988**, *93*, 245–249.
(6) Hooker, D. B.; DeZwaan, J. *J. Pharm. Biomed. Anal.*, in press.
(7) Fehsenfeld, F. C.; Evanson, K. M.; Broida, H. P. *Rev. Sci. Instrum.* **1965**, *36*, 294–298.
(8) Brenner, K. S. *J. Chromatogr.* **1978**, *167*, 365.
(9) Hass, D. L.; Caruso, J. A. *Anal. Chem.* **1985**, *57*, 846.
(10) Slatkavitz, K. J.; Uden, P. C.; Hoey, L. D.; Barnes, R. M. *J. Chromatogr.* **1984**, *302*, 277.
(11) Tanabe, K.; Haraguchi, H.; Fuwa, K. *Spectrochim. Acta* **1981**, *36B*, 1829.
(12) Bradley, C.; Carnahan, J. W. *Anal. Chem.* **1988**, *60*, 858.

RECEIVED for review April 25, 1989. Accepted July 11, 1989.

Comparison of Sampling Techniques for Combined Supercritical Fluid Chromatography and Fourier Transform Infrared Spectrometry with Mobile Phase Elimination

Roger Fuoco

Istituto di Chimica Analitica Strumentale del CNR, Universita di Pisa, Via Risorgimento 35, 56100 Pisa, Italy

Stephen L. Pentoney, Jr.,[1] and Peter R. Griffiths*

Department of Chemistry, University of California, Riverside, California 92521-0403

Six potential sampling techniques for combined supercritical fluid chromatography and Fourier transform infrared spectrometry measurements involving mobile phase elimination are compared. These are conventional (i) transmission and (ii) external reflection spectrometry of the sample deposited on a flat ZnSe plate, (iii) reflection–absorption spectrometry of the sample deposited on a smooth metallic substrate, diffuse reflection spectrometry of the sample deposited on a thin layer of powdered NaCl on either (iv) a metallic or (v) an infrared transmitting (ZnSe) substrate, and (vi) diffuse transmittance spectrometry for samples deposited on the latter substrate. For external reflection measurements of thin films of organic molecules deposited on flat surfaces, the optical constants of the substrate determine the nature of the spectrum. When the film thickness exceeds about a quarter of a wavelength, the effect of diffuse reflectance becomes apparent. The signal-to-noise ratio and base-line flatness of diffuse reflectance or diffuse transmittance spectra of samples deposited on powdered substrates are too poor to allow either technique to be used beneficially for supercritical fluid chromatography/Fourier transform infrared spectrometry measurements. Conventional transmission spectra of samples on flat infrared windows give the best compromise between high sensitivity, faithful representation of relative band intensities, and adherence to the Beer–Lambert law.

INTRODUCTION

Two different approaches to coupling supercritical fluid chromatography (SFC) with Fourier transform infrared spectrometry (FT-IR) have been demonstrated over the past 6 years. The first approach involves passing the chromatographic effluent through a high-pressure flow cell and measuring the spectrum of each component in the presence of the mobile phase (*1–8*). This approach has worked well for separations performed with a mobile phase consisting of supercritical carbon dioxide, which is transparent over most of the useful mid-infrared spectral region, or xenon, which is completely transparent. Wieboldt et al. (*8*) recently described an improved flow cell interface for SFC/FT-IR and presented infrared spectra of methyl palmitate measured from as little as 10 ng of material injected onto the column. The signal-to-noise ratio (SNR) exhibited by many of these spectra was excellent, and the greatest remaining obstacle to SFC/FT-IR flow cell work, for separations performed with carbon dioxide or xenon, appears to be reduction of the cell volume to a value that is compatible with the small-bore (50–100 μm) capillary columns generally employed for SFC analyses (*9*), especially in light of the degradation of resolution caused by the SFC/FT-IR flow cell demonstrated by Wieboldt et al. (*8*).

The utility of SFC for the solution of real chemical problems will depend, in part, upon the extension of the technique to more polar mobile phases. Many of the separations performed by packed column SFC require the addition of small amounts (1–5%) of polar organic modifiers, such as methanol, formic acid, or water, to carbon dioxide (*10*). In addition, several current research interests focus on the investigation of more polar supercritical fluids including ammonia (*11*), chlorofluorocarbons (*12*), and sulfur dioxide (*13*) for the elution of compounds that are not sufficiently soluble in supercritical carbon dioxide. The utility of FT-IR spectrometry for the identification of compounds separated by using these more polar fluids will, in turn, depend upon the compatibility of the interface with these strongly absorbing fluids. Although the mechanical simplicity of the flow cell interface makes it an attractive approach for CO_2-based separations, a more versatile approach is required in order to encompass a wider range of mobile phases.

In an attempt to design a more versatile SFC/FT-IR interface that would be applicable to polar fluids, Griffiths et al. (*14–19*) and Jinno et al. (*20, 21*) have favored the solvent elimination approach, which relies upon the fact that supercritical mobile phases are all gaseous at ambient pressure and therefore are readily separated from less volatile solutes. In the mobile phase elimination approach to SFC/FT-IR, the effluent expands from the tip of an appropriate pressure/flow restrictor and solutes are collected upon the surface of a slowly moving substrate as the mobile phase evaporates away. Solute spectra may then be measured either in real time as the substrate passes through the IR beam, or off-line by returning the collected sample to the beam after the separation is complete for extended signal-averaging. Several important advantages have been realized with this type of interface, including applicability to more polar mobile phases (*14, 15, 19*), increased sensitivity gained through unrestricted spectral acquisition time (*15, 17, 18, 22*), and the ability to measure spectra over the entire mid-infrared spectral region without interference from the mobile phase.

It is worth noting that the development of SFC/FT-IR has paralleled that of both GC/FT-IR and HPLC/FT-IR, with flow cell interfaces being demonstrated (and widely accepted in the case of GC/FT-IR) first (*23, 24*) and identification limits subsequently being reduced by deposition techniques (*25–27*). An additional benefit of the solvent elimination approach to SFC/FT-IR is that the interface can be designed in such a manner as to be equally applicable to separations performed by SFC, GC, and HPLC. This is because cell volume and path length requirements, which differ greatly for each of the three separation techniques, are dismissed when the mobile phase is eliminated. Chromatographic resolution and sensitivity can

---

* Author to whom correspondence should be addressed.

[1] Current address: Department of Chemistry, Stanford University, Stanford, CA 94305.

0003-2700/89/0361-2212$01.50/0 © 1989 American Chemical Society

be optimized for each of the separation techniques (provided that the mobile phase is effectively eliminated) by simply adjusting the rate at which the substrate is translated. This "universal" approach to the chromatography/FT-IR interface has recently been described (*28*).

Despite the similarity of the hardware for the GC/FT-IR (*27*), SFC/FT-IR (*16, 17*), and HPLC/FT-IR (*29*) interfaces, several significant differences should still be noted. For example, in the GC/FT-IR interfaces described by Haefner et al. (*27*) and Brown et al. (*30*), the analytes condense on the substrate directly from the vapor phase. Although asymmetrical molecules are deposited with no preferred orientation, when certain polar molecules with a C_2 symmetry axis are deposited on a crystalline substrate, there is evidence (*31*) that they can condense with their C_2 axis aligned with one of the cleavage planes of the substrate. Because the beam emerging from most interferometers of contemporary FT-IR spectrometers has some residual polarization, it is possible that this effect could lead to differences between GC/FT-IR spectra of certain analytes and their KBr disk reference spectrum.

It is well recognized (*32, 33*) that SFC eluites often form clusters immediately on emerging from the restrictor. Clusters formed in this manner are less likely to deposit in an oriented manner on crystalline substrates. It is therefore possible that the GC/FT-IR and SFC/FT-IR spectra of symmetrical molecules on certain substrates will show small differences. This topic is under active investigation in our laboratory, and results will be reported in the near future.

The situation for HPLC/FT-IR measurements is complicated by the fact that the analytes are usually still in solution (albeit as an aerosol) when they reach the substrate. In this case, the spectrum of the analyte may depend on the rate at which the solvent evaporates. The slower is the rate of evaporation, the more likely is the analyte to form an oriented crystal on any smooth substrate. By use of a substrate with a rough surface, e.g. a thin layer of an infrared-transparent powder on a suitable backing, the effect of sample orientation should be completely eliminated. Only for the "MAGIC" HPLC/FT-IR interface (*34*) is the solvent eliminated before reaching the substrate. In this case, it is possible (but not proven) that the solute spectra may be similar to SFC/FT-IR spectra obtained with the same substrate.

In summary, therefore, even though the optics for the GC/FT-IR, SFC/FT-IR, and HPLC/FT-IR interfaces can be identical (*28*), the spectra may be quite different. It is also possible that the spectrum of a given analyte separated by either GC, SFC, or HPLC and measured by using a mobile phase elimination technique will be strongly dependent on the nature of the substrate. In this paper, the effect of various substrates is investigated for SFC/FT-IR depositions. The advantages and disadvantages of each substrate technique is discussed with respect to the development of a sensitive and versatile SFC/FT-IR interface. Although our conclusions may pertain in part to the corresponding GC/FT-IR and HPLC/FT-IR interfaces, the results for each one should be studied individually before conclusions as to the similarity of the measured spectra can be drawn.

EXPERIMENTAL SECTION

Separations were performed by using a Computer Chemical Systems Model 5000 SFC/GC chromatograph. A 100 μm i.d. × 20 m fused silica WCOT capillary column coated with a 0.4-μm film of 5% phenylmethylsilicone (DB-5, J&W Scientific) was mounted in the chromatograph. Sample introduction was accomplished in a split fashion with a 20-nL sample volume being delivered onto the head of the column. The column was routed directly to the FT-IR interface by passing it through a 1.2-m length of heated transfer line. The end of the capillary column was connected to a heated frit restrictor (Lee Scientific). The transfer line and restrictor assembly were connected to a micrometer which allowed the tip of the restrictor to be positioned precisely above the surface of appropriate infrared substrates.

The translation stage assembly of the interface (*16, 17*) was removed so that various substrates could be positioned below the restrictor during depositions. All depositions described in this paper were made with the substrate held stationary. Acenaphthenequinone was selected as the probe molecule both because it is known to be extremely nonvolatile and because its use allowed for comparison with previous measurements made in a similar manner by SFC (*14–16*), HPLC (*29*), and GC (*27*). All separations were performed at a pressure of 2000 psi, and the oven and transfer line were maintained at 70 °C. The restrictor was maintained at 200 °C in accordance with the manufacturer's operating specification.

Infrared spectra were measured off-line by using a Perkin-Elmer Model 1800 FT-IR spectrometer equipped with a medium-range MCT detector with a 250-μm square element. A Spectra-Tech IR Plan microscope, which operates in both the transmittance and reflectance modes, was used for all reported measurements.

The sampling techniques investigated for SFC/FT-IR depositions of acenaphthenequinone include transmittance and external reflectance for samples deposited onto a flat ZnSe window, reflection–absorption for samples deposited onto a front-surface mirror, diffuse reflectance for samples deposited onto a layer of powdered NaCl that had been laid on the surface of a ZnSe plate or front-surface mirror, and diffuse transmittance and diffuse reflectance for samples deposited onto the thin layer of NaCl formed on the surface of the ZnSe window.

The ZnSe window (Harrick Scientific, Ossining, NY) was 38 mm long by 19 mm wide and 2 mm thick. NaCl was finely ground in a Wig-L-Bug grinder (Crescent Mfg. Co., Chicago, IL) and was slurried in methanol for deposition either upon the ZnSe window for diffuse transmittance and diffuse reflectance measurements, or into a 50-μm-deep groove of an aluminum plate for diffuse reflectance measurements. In either case the deposited slurry was placed in an oven and dried at 110 °C for 30 min, after which time the surface was scraped smooth by using the edge of a razor blade. The ZnSe window was placed in a specially designed aluminum holder prior to scraping the NaCl surface. The sides of the holder immediately adjacent to the ZnSe window extended 50 μm above the upper surface of the window so that the resulting NaCl layer was approximately 50 μm thick.

RESULTS AND DISCUSSION

To test the relative advantages of different substrates for SFC/FT-IR measurements, a series of injections of 100 ng of acenaphthenequinone (AQ) dissolved in CH_2Cl_2 was made. During elution from the column, the AQ eluite was deposited on the five different substrates described above, each of which was mounted 50 μm below the end of the pressure/flow restrictor.

The first substrate was simply a ZnSe window, with depositions being made in an analogous fashion to that of our previous work (*14–19, 22*). The transmission spectrum measured by using a microscope with an aperture diameter of 50 μm is shown in Figure 1. It is apparent that not only is the SNR excellent (better than the corresponding spectra in Figures 2–5), but band shapes are also symmetrical. Relative band intensities are close to those observed in the transmission spectrum of a KBr disk containing AQ.

When the deposition was made on a front-surface aluminized mirror, the reflection–absorption (R–A) spectrum also showed good SNR, but there is some evidence of band asymmetry (see Figure 2). The asymmetry increased as the quantity injected was increased, indicating the effect of front-surface reflection from the analyte rather than from the surface of the mirror. The effect of front-surface reflection is also manifested by the somewhat reduced intensity of the C═O stretching band at 1717 cm^{-1} relative to that of the sharp band at 1277 cm^{-1}.

As noted in the Introduction, the magnitude of the relative band intensities could be altered by the effect of molecular orientation. For example, we have reported (*22, 28*) that the

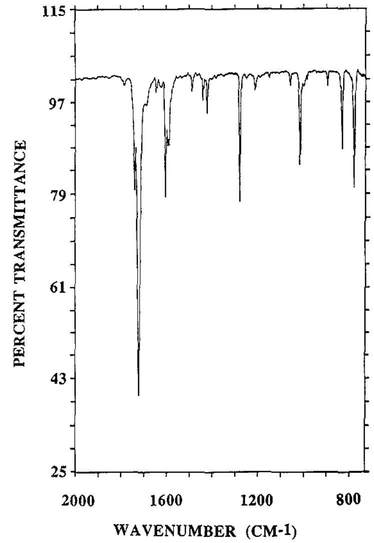

Figure 1. Transmission spectrum measured from 100 ng of AQ deposited onto the surface of a ZnSe window.

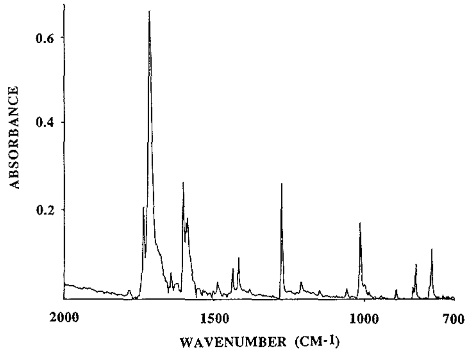

Figure 2. Reflection–absorption (R–A) spectrum measured from 100 ng of AQ deposited onto the surface of an aluminized mirror.

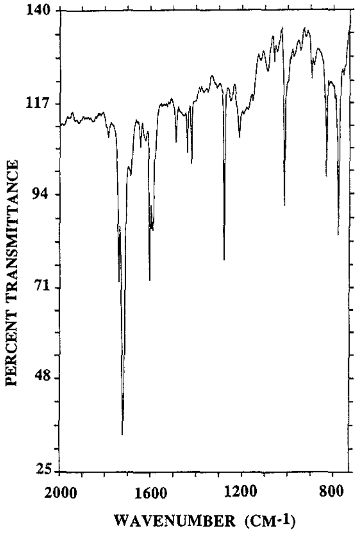

Figure 3. Diffuse transmittance (DT) spectrum measured from 100 ng of AQ deposited onto a 50 μm thick layer of NaCl formed from a methanol slurry upon the surface of a ZnSe window.

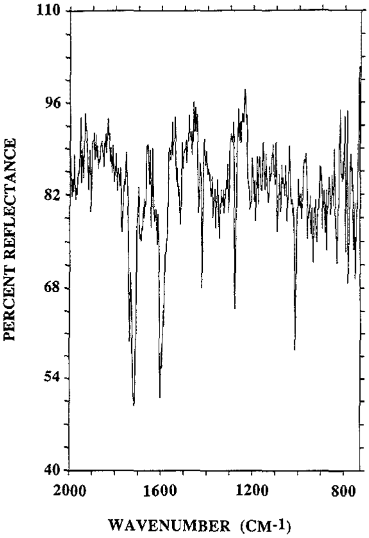

Figure 4. Diffuse reflectance (DR) spectrum measured from 100 ng of AQ deposited onto a 50 μm thick layer of NaCl formed from a methanol slurry upon the surface of a ZnSe window.

relative band intensities of the transmission and R–A spectra of certain analytes deposited on flat substrates can be different from those in the transmission spectrum of the corresponding analytes prepared as KBr disks, whereas the relative band intensities when the analyte was deposited on a powdered substrate and diffuse reflectance (DR) or diffuse transmission (DT) spectra were measured are similar to those in the transmission spectrum of a KBr disk. We have therefore investigated the effect of measuring the spectrum of the AQ eluite deposited on powdered substrates of two types. Firstly, a layer of NaCl powder, approximately 50 μm in thickness, was laid down on a ZnSe plate from a methanol slurry; this substrate is subsequently referred to as NaCl/ZnSe. Both DR and DT spectra of SFC eluites deposited on this substrate could be measured. For the second, a layer of NaCl of approximately the same thickness was laid down on a front-surface aluminized mirror (NaCl/Al); only DR spectra could be measured with this substrate.

The spectra measured are shown in Figures 3, 4, and 5. When a microscope with a 50-μm-diameter aperture is used to measure either DR or DT spectra, the single-beam spectral energy is reduced significantly below the level of transmission or R–A measurements from a nonscattering substrate made with the same aperture setting. The poorest noise level of all was found for DR measurements made with the NaCl/ZnSe substrate (see Figure 4), as much of the incident beam appeared to pass through the NaCl layer without being back-reflected significantly from the ZnSe backing. Any radiation passing through the ZnSe substrate will, of course, not be detected. Not surprisingly, therefore, the diffuse transmittance measurement of the same sample had the highest SNR of these three measurements (see Figure 3) and the DR

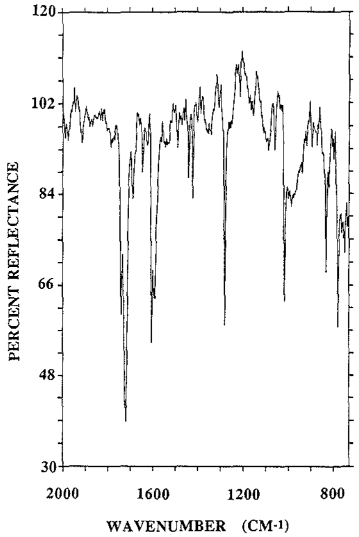

Figure 5. Diffuse reflectance (DR) spectrum measured from 100 ng of AQ deposited onto a 50 μm thick layer of NaCl formed from a methanol slurry upon the surface of an aluminized mirror.

Table I. Intensities of the 1717- and 1277-cm^{-1} Bands of AQ on Various Substrates

substrate	technique	log (1/T) or log (1/R) 1717 cm^{-1}	log (1/T) or log (1/R) 1277 cm^{-1}	intensity ratio
ZnSe	transmission	0.422	0.122	3.47
Al	R–A	0.656	0.263	2.49
NaCl/ZnSe	DT	0.686	0.285	2.40
NaCl/ZnSe	DR	0.205	0.149	1.38
NaCl/Al	DR	0.407	0.252	1.61

measurement from NaCl/Al had an intermediate noise level (see Figure 5).

For the diffuse reflectance measurements, the band intensities in the spectrum of AQ on NaCl/Al were about twice as great as those of the same quantity of AQ on NaCl/ZnSe, again indicating the double-passing effect of the aluminum substrate with such a thin layer of NaCl powder. The intensities of two bands in the spectrum, at 1717 and 1277 cm^{-1}, for each measurement shown in Figures 1–5 are listed in Table I. For the sake of consistency, these intensities are given as log (1/T) or log (1/R), for transmission and reflectance spectra, respectively, and were measured after base-line correction.

We have noted in some fundamental studies related to DR and DT measurements through relatively thick (0.1–1.5 mm) layers of alkali halide powders (*35*) that band intensities in diffuse transmission spectra are often greater than the corresponding intensities in diffuse reflectance spectra of the same sample. Although this effect was also observed in these SFC/FT-IR measurements, we found this result quite surprising in view of the fact that a significant fraction of the signal in the DR measurement from the NaCl/Al substrate was due to radiation that had passed through the sample twice. Thus it might have been expected that the measured band intensities in the DR spectrum of AQ on NaCl/ZnSe would be about twice the corresponding values in the DT spectra from the same substrate rather than being smaller.

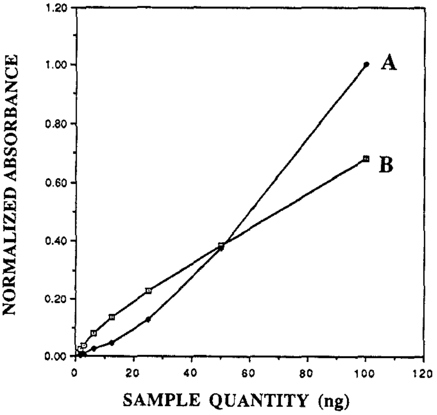

Figure 6. Normalized absorbance of the 1717-cm^{-1} band plotted as a function of injected AQ quantity: (A) reflection–absorption measurements from an aluminized mirror surface and (B) transmission measurements from a flat ZnSe substrate.

When band intensities in the spectra measured by conventional transmission (Figure 1) and diffuse transmission (Figure 3) measurements are compared, it can be seen that the bands in the DT spectrum are more intense than those in the conventional transmission spectrum. The effect of the layer of NaCl is to scatter the radiation, thereby increasing its effective path length through the sample (*36*). However, the increased noise in the DT and DR measurements means that the SNR of the conventional transmission spectrum is superior to that of the DT or DR spectra.

The relative intensities of the 1717- and 1277-cm^{-1} bands show a fairly large variation from one technique to the next, as shown in the final column of Table I. This effect is not surprising because diffuse reflectance spectra do not obey the same quantitative laws as spectra measured by using the other three techniques. For samples of "infinite depth", band intensities of DR spectra are best described by using the Kubelka–Munk (KM) function rather than log (1/R). It is noteworthy that in other diffuse reflectance measurements from our laboratory (*35*), we have found that the depth of NaCl powder (of approximately the same particle size as the powder used in these measurements) required to fulfill the infinite depth criterion for DR spectrometry is about 100 μm. If the DR spectra (Figures 4 and 5) are converted into the KM format, the relative band intensities are increased to 1.91 (for the NaCl/ZnSe substrate) and 2.72 (for NaCl/Al), which is closer to the relative band intensities for the conventional transmission, R–A, and DT spectra. The smaller value of the band intensities for the DR spectrum of AQ on NaCl/ZnSe should probably be ascribed to the fact that the layer thickness (50 μm) is somewhat less than "infinite". The effect of double-passing from the metallic surface is apparently to increase the layer thickness to a value closer to that of an "infinite" depth.

The change in band intensity with injected quantity for conventional transmission measurements from a flat ZnSe substrate for R–A measurements from a mirror surface was also investigated, and the results are summarized in Figure 6. As expected, log (1/T) varies approximately linearly with injected quantity, for transmission spectra; i.e. the Lambert law is being followed. For R–A spectra, the plot of log (1/R) vs injected quantity is nonlinear, with values being smaller than the corresponding intensities obtained by transmission spectrometry for low sample quantities (<50 ng injected) and larger for injected sample quantities greater than 50 ng. For low injected quantities, the layer thickness is less than a

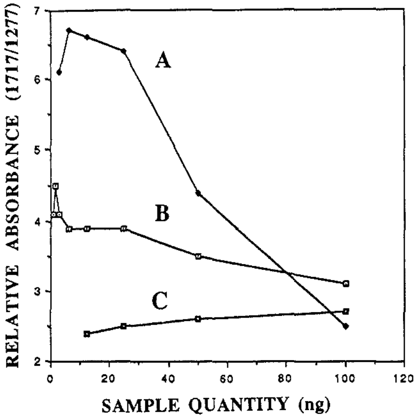

Figure 7. Relative absorbance of 1717/1277 cm^{-1} plotted versus injected AQ sample quantity: (A) reflection-absorption measurements; (B) transmission measurements; (C) diffuse transmission measurements.

quarter of a wavelength ($\lambda/4$). For such thin layers on metallic substrates, not only is the s-polarized component of the incident radiation not absorbed at all, but even the absorption of the p-polarized component is weak at the approximately 45° incidence angle of a typical FT-IR microscope. When the thickness exceeds $\lambda/4$, both polarizations are absorbed, and when the thickness is much greater than $\lambda/2$, the band intensities of an R–A spectrum should be about double those of a transmission spectrum of a sample of the same thickness. As shown in Figure 6, this behavior is verified in practice. Since the wavelength of the C=O stretching band of AQ is 5.82 μm, it can be predicted that the average thickness of the layer produced from a 100-ng injection under the deposition conditions used in this study is about 3 μm. This prediction is in line with the band intensities of the corresponding transmission spectrum shown in Figure 1.

The relative intensities of bands in R–A spectra at wavelengths λ_1 and λ_2 would be expected to change with the injected sample quantity since the layer thickness, d, changes. If $\lambda_2 \gg \lambda_1$ and $\lambda_1/d < 0.5$ while $\lambda_2/d > 0.5$, the relative intensity of the band at λ_1 would be expected to be greater than that at λ_2. As shown in Figure 7, however, the relative intensities of the 1717- and 1277-cm^{-1} bands of AQ vary with injected quantity by more than a factor of 2.5, even though the ratio of the wavelengths is only 1.34. We therefore believe that an additional mechanism must contribute to the magnitude of band intensities in the R–A spectra of samples prepared in this way. Because of the microcrystalline nature of the deposit, it is possible that some scattering could be occurring despite the fact that the average diameter of the crystallites must be smaller than the wavelength of the incident radiation and that the layer thickness was only on the order of one wavelength, so that band intensities could be enhanced by diffuse reflectance.

To study this effect, samples of 100 ng of AQ (injected) were deposited on a KBr window and external reflection spectra were measured at several points across the spot. The average reflectance of KBr at an incidence angle of 45° (near Brewster's angle for KBr) is only about 4.6% (9.2% for s-polarized radiation and approximately zero for p-polarized radiation), so that the intensity of radiation reflected from the substrate is minimized. For an injected quantity of 100 ng, the spot of AQ has an approximately Gaussian thickness profile, as measured by transmission microspectrometry using a 15-μm-diameter microscope aperture. The full width at half-maximum thickness is 90 μm, while the full width at 10% of the maximum thickness is about 300 μm.

External reflection spectra of this spot, measured by using a 50-μm-diameter aperture, vary dramatically with the region from which radiation is being collected, as shown in Figure 8. In the center of the spot, absorption bands are manifested as reflection minima, and the spectrum is similar to the diffuse reflectance spectrum of a neat sample (see Figure 8A). The

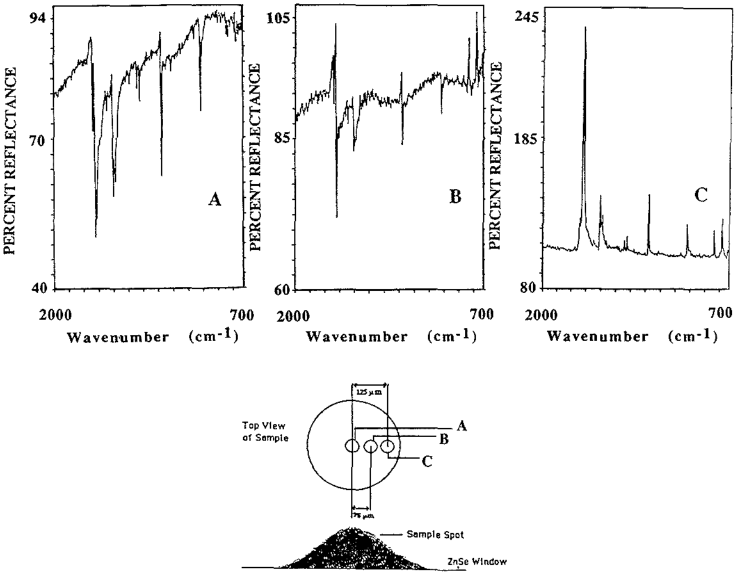

Figure 8. External reflection spectra measured at three different regions from a single deposition of 10 ng of AQ upon a KBr window. The microscope aperture setting was 50 μm, and spectra A–C were measured from the regions indicated in the figure.

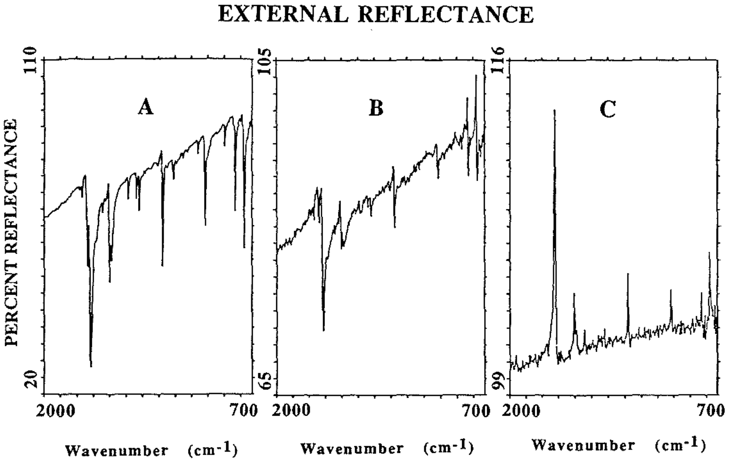

Figure 9. External reflectance spectra measured from (A) 50, (B) 25, and (C) 3.1 ng of AQ deposited onto a ZnSe window. Spectra were measured at the center of the AQ spot with an aperture setting of 50 μm.

bands are somewhat asymmetrical, as would be expected for samples where an external reflection mechanism (see below) also contributes to the spectrum. Nevertheless, this spectrum lends credence to the claim made earlier that the intensities of bands in R–A spectra of thick deposits are enhanced by diffuse reflectance.

At a distance of 125 μm from the center of the spot, where the sample is very thin, the external reflection spectrum consists of reflection *maxima* at the wavelengths of each absorption band (see Figure 8C). This behavior is exactly what would be predicted on the basis of the calculations reported by Dluhy (*37*) for thin organic films on substrates of low refractive index. Seventy-five micrometers from the center of the spot, the thickness of the AQ deposit is such that the effects of diffuse reflectance from a microcrystalline deposit and external reflectance from a thin film on KBr compensate each other, with the result that most bands in the spectrum are dispersive in appearance (see Figure 8B).

It is also interesting to note that the effect of reducing the quantity of analyte deposited on a transparent substrate of low refractive index is very similar to obtaining the spectrum of a large quantity of the eluite at different distances from the center. Representative data are shown in Figure 9. The external reflection spectrum measured from a 50-ng injection of AQ measured with a 50-μm-diameter microscope aperture has the typical appearance of a diffuse reflection spectrum (see Figure 9a), even though the thickness of this deposit is believed to be only about $\lambda/2$ at 1700 cm^{-1} (vide supra). When the injected quantity is less than 5 ng, the external reflection spectrum (Figure 9C) is similar to that in Figure 8C; i.e., absorption bands appear as reflection maxima.

It should be recognized that the effect of the substrate on external reflection spectra of thin films will depend strongly on its optical constants, n and k. For thin films on aluminum ($n = 10.8$, $k = 42.6$ at $\lambda = 6$ μm), the external reflection spectra will have a totally different appearance from the corresponding spectrum of an equally thick film of the same material on ZnSe ($n = 2.5$, $k = 0$) or KBr ($n = 1.5$, $k = 0$). As is well-known, absorption bands of thin films on metallic substrates appear as reflection minima, the intensity of which can be predicted by using the methods originally developed by Greenler (*38*). For relatively thick films, the band intensities in the R–A spectrum will be largely governed by a double-pass transmittance mechanism, but the effects of diffuse reflectance from the bulk and specular (Fresnel) reflectance from the front surface also contribute. Relative band intensities of R–A spectra of SFC eluites deposited on metallic substrates would therefore be expected to be strongly dependent on the thickness of the layer and its microcrystallinity, as well as on the angle of incidence of the radiation.

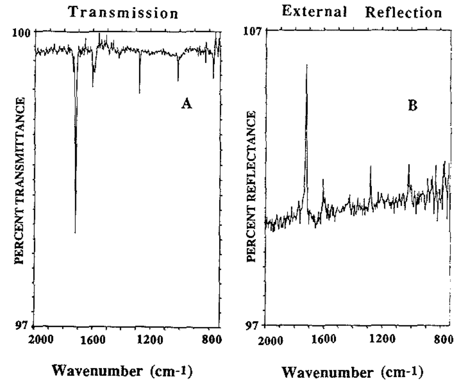

Figure 10. (A) Transmittance and (B) external reflectance spectrum measured from 800 pg of AQ deposited onto a ZnSe window.

From Figure 7 it can also be seen that the relative absorbances of the 1717- and 1277-cm^{-1} bands in conventional transmission spectra show a small variation with the quantity of analyte injected. The magnitude of this variation is by no means as great as that for R–A spectrometry, but the effect is reproducible and is undoubtedly real. Several reasons for this behavior may be postulated; but we believe that the most likely explanation is that as the thickness of the film decreases, the loss of transmitted radiation by external reflection at the wavelengths of absorption bands becomes relatively more important. To illustrate this effect, an 800-pg injection of AQ was deposited on a flat ZnSe plate and the transmittance and external reflectance spectra were measured; the spectra are shown in Figure 10. ΔR for the 1717-cm^{-1} band of AQ is about 5%, whereas ΔT is only 2%, so that an appreciable fraction of photons interacting with the sample are manifested in the reflection spectrum rather than the transmission spectrum. Since only 19% of the incident radiation is reflected from ZnSe at 45° incidence (30% for s-polarized radiation and 8% for p-polarized radiation) while 81% is transmitted, the SNR of the transmission spectra is still superior to that of the R–A spectrum. Thus the effect of external reflection, which is strongly dependent on the optical constants of both the analyte and the substrate, might also cause a change in the relative band intensities in the transmission spectra of thin films. It is, perhaps, also noteworthy that the data shown in Figure 10 are the first reported SFC/FT-IR spectra of a subnanogram injected quantity of an SFC eluite. It is also possible that the effect of scattering might lead to deviations from the Beer–Lambert law when the injected quantity is large. Other work from our laboratory (*30*) indicates this to be unlikely for such thin films, and the deviation would be expected to be positive rather than negative. Finally, it is possible that the diameter of the spot may be increasing slightly as the injected quantity is increased.

In summary, the data in this paper indicate that for SFC/FT-IR measurements involving mobile phase elimination, the use of flat infrared-transparent substrates and the measurement of conventional transmission spectra lead to fewer spectral artifacts than deposition on a flat metallic substrate and measurement of the R–A spectrum. When the size of each sample spot is small and microscope optics are used for the measurement, the sensitivity of transmission or R–A spectrometry is significantly higher than that of either diffuse reflection or diffuse transmission measurements. Thus conventional transmission spectrometry would appear to be the technique of choice for solvent elimination SFC/FT-IR measurements.

LITERATURE CITED

(1) Shafer, K. H.; Griffiths, P. R. *Anal. Chem.* **1983**, *55*, 1939–1942.
(2) Olesik, S. V.; French, S. B.; Novotny, M. *Chromatographia* **1984**, *18*, 489–495.
(3) Johnson, C. C.; Jordan, J. W.; Taylor, L. T.; Vidrine, D. W. *Chromatographia* **1985**, *20*, 717–723.
(4) Jordan, J. W.; Johnson, C. C.; Taylor, L. T. *J. Chromatogr. Sci.* **1986**, *24*, 82–88.
(5) Skelton, R. J.; Johnson, C. C.; Taylor, L. T. *Chromatographia* **1986**, *21*, 3–8.
(6) French, S. B.; Novotny, M. *Anal. Chem.* **1986**, *58*, 164–166.
(7) Later, D. W.; Bornhop, D. J.; Lee, E. D.; Henion, J. D.; Wieboldt, R. C. *LC–GC* **1987**, *5*, 804–816.
(8) Wieboldt, R. C.; Adams, G. E.; Later, D. W. *Anal. Chem.* **1988**, *60*, 2422–2427.
(9) Fields, S. M.; Markides, K. E.; Lee, M. L. *Anal. Chem.* **1988**, *60*, 802–806.
(10) Gere, D. R. *Science* **1983**, *222*, 253–258.
(11) Kuei, J. C.; Markides, K. E.; Lee, M. L. *HRC CC, J. High Resolut. Chromatogr. Chromatogr. Commun.* **1987**, *10*, 257–262.
(12) Pariente, G. L.; Griffiths, P. R. In *Supercritical Fluid Chromatography*; White, C. M., Ed.; Dr. A. Heuthig Verlag: Heidelberg, FRG, in press.
(13) Pentoney, S. L., Jr.; Griffiths, P. R., unpublished results, 1987.
(14) Shafer, K. H.; Pentoney, S. L., Jr.; Griffiths, P. R. *HRC CC, J. High Resolut. Chromatogr. Chromatogr. Commun.* **1984**, *7*, 707–709.
(15) Shafer, K. H.; Pentoney, S. L., Jr.; Griffiths, P. R. *Anal. Chem.* **1986**, *58*, 58–64.
(16) Pentoney, S. L., Jr.; Shafer, K. H.; Fuoco, R.; Griffiths, P. R. *HRC CC, J. High Resolut. Chromatogr. Chromatogr. Commun.* **1986**, *9*, 168–171.
(17) Pentoney, S. L., Jr.; Shafer, K. H.; Griffiths, P. R. *J. Chromatogr. Sci.* **1986**, *24*, 230–235.
(18) Griffiths, P. R.; Pentoney, S. L., Jr.; Giorgetti, A.; Shafer, K. H. *Anal. Chem.* **1986**, *58*, 1349A–1366A.
(19) Griffiths, P. R.; Pariente, G. L.; Pentoney, S. L., Jr. *Proc. 31st IUPAC Congr.* (Sofia, Bulgaria), 1987.
(20) Fujimoto, C.; Hirata, Y.; Jinno, K. *J. Chromatogr.* **1985**, *332*, 47–56.
(21) Jinno, K. *Chromatographia* **1987**, *23*, 55–62.
(22) Pentoney, S. L., Jr. Ph.D. Dissertation, University of California, Riverside, December, 1987.
(23) Erickson, M. D. *Appl. Spectrosc. Rev.* **1979**, *15*, 261–297.
(24) Griffiths, P. R.; de Haseth, J. A.; Azarraga, L. V. *Anal. Chem.* **1983**, *55*, 1361A–1387A.
(25) Reedy, G. T.; Ettinger, D. G.; Schneider, J. F.; Bourne, S. *Anal. Chem.* **1985**, *57*, 1602–1609.
(26) Fuoco, R.; Shafer, K. H.; Griffiths, P. R. *Anal. Chem.* **1986**, *58*, 3249–3254.
(27) Haefner, A. M.; Norton, K. L.; Griffiths, P. R.; Bourne, S.; Curbelo, R. *Anal. Chem.* **1988**, *60*, 2441–2444.
(28) Griffiths, P. R.; Pentoney, S. L., Jr.; Pariente, G. L.; Norton, K. L. *Mikrochim. Acta* (*Wien*) **1987**, *III*, 47–62.
(29) Fraser, D. J. J.; Norton, K. L.; Griffiths, P. R. In *Infrared Microspectroscopy: Theory and Applications*; Messerschmidt, R. G., Harthcock, M. A., Eds.; Marcel Dekker, Inc.: New York, 1988, Chapter 4, pp 197–210.
(30) Brown, R. S.; Wilkins, C. L. *Anal. Chem.* **1988**, *60*, 1483–1488.
(31) Tripathi, G. N. R.; Katon, J. E. *J. Chem. Phys.* **1979**, *70*, 1383–1388.
(32) Smith, R. D.; Kalinoski, H. T.; Udseth, H. R. *Mass Spectrom. Rev.* **1987**, *6*, 445–496.
(33) Smith, R. D.; Wright, B. W.; Yonker, C. R. *Anal. Chem.* **1988**, *60*, 1323A–1336A.
(34) Robertson, R. M.; de Haseth, J. A.; Browner, R. F. *Mikrochim. Acta* (*Wien*) **1987**, *II*, 199–202.
(35) Fraser, D. J. J.; Norton, K. L.; Griffiths, P. R., submitted for publication in *Anal. Chem.*
(36) Kortüm, G. *Reflectance Spectroscopy: Principles, Methods, Applications*; Springer-Verlag: New York, 1969.
(37) Dluhy, R. A. *J. Phys. Chem.* **1986**, *90*, 1373–1379.
(38) Greenler, R. G. *J. Chem. Phys.* **1966**, *44*(1), 310–315.
(39) Greenler, R. G. *J. Chem. Phys.* **1969**, *50*(5), 1963–1968.

RECEIVED for review May 11, 1989. Accepted June 7, 1989.

Anal. Chem. 1989, 61, 2219–2224

CORRESPONDENCE

Canonical Correlation Technique for Rank Estimation of Excitation–Emission Matrices

Sir: One of the major problems that has challenged analytical chemists for a long time is to determine the number of components in a multicomponent sample. Often the sample data occur in the form of a matrix whose rank, in the absence of noise, is equal to the number of components. The presence of random noise in the data, however, will generally cause the rank of the mixture matrix to exceed the number of components in the mixture. The problem then is to estimate what the rank would be if the noise were removed.

An eigenanalysis in the form a singular value decomposition of the measured mixture matrix provides information that is useful for estimating rank. Most methods that have been proposed utilize information from the eigenvalues and ignore the information contained in the eigenvectors (*1–6*). An exception is the frequency analysis method proposed by Rossi and Warner (*7*), which relies on the prior expectation that the Fourier transforms of noise eigenvectors will have heavily weighted coefficients for the high frequencies.

In this communication we will report a new approach to this problem which incorporates eigenvector information without requiring prior expectations about the nature of the eigenvectors. It utilizes the multivariate statistical technique of canonical correlations. We will present the methodology in the context of fluorescent mixtures and will also assume that the readers are familiar with the excitation–emission matrix (EEM). For information on the formulation of the EEM and its basic properties, see ref 8 and 9.

GENERAL CONSIDERATION

The mathematical formulation of the EEM for a k-component sample in the noise-free case can be expressed as

$$\mathbf{S} = \mathbf{XDY}^{\mathrm{T}} \tag{1}$$

where $\mathbf{S}$ is an m by n matrix, $\mathbf{X}$ is the m by k matrix whose jth column is the excitation spectrum for the jth component, $\mathbf{Y}$ is the n by k matrix whose jth column is the emission spectrum for the jth component, and $\mathbf{D}$ is a k by k diagonal matrix whose elements depend on the concentrations of the fluorescence emitters, fluorescence quantum efficiency, molar absorptivity, etc. We assume that both the columns of $\mathbf{X}$ and the columns of $\mathbf{Y}$ are linearly independent, which implies that the rank of $\mathbf{S}$ is equal to k, the number of components in the mixture. If $\mathbf{M}$ is the measured EEM, then $\mathbf{M}$ will typically contain a noise term $\mathbf{N}$ in addition to the signal $\mathbf{S}$, i.e.

$$\mathbf{M} = \mathbf{S} + \mathbf{N} \tag{2}$$

A common method for estimating k (the rank of $\mathbf{S}$) is to inspect the singular values from the singular value decomposition of $\mathbf{M}$. If the noise is low compared to the signal, one would expect to see a large drop between the kth and $(k + 1)$st singular values and much smaller drops between the $(k + 1)$st and later singular values. When the noise level is not low, however, this method is likely to fail, especially when the mixture contains more than two or three individual components and/or the individual components are highly correlated, i.e. have high spectral overlap.

We propose an alternative method for estimating k. This alternative approach utilizes canonical correlations and can be applied whenever there are at least two measured EEMs for mixtures containing the same k constituents. The method does not require that the constituents be present in the same proportions in both mixtures. However, for simplicity and ease of exposition, we will illustrate the method for replicate measurements on the same mixture.

Let **M1** and **M2** be m by n EEM's of a k-component mixture obtained under the same experimental conditions. We assume that $k < m \le n$. Write **M1** and **M2** as

$$\begin{aligned}\mathbf{M1} &= \mathbf{XDY}^{\mathrm{T}} + \mathbf{N1}\\ &= \mathbf{U}_1\mathbf{L}_1\mathbf{V}_1^{\mathrm{T}}\\ \mathbf{M2} &= \mathbf{XDY}^{\mathrm{T}} + \mathbf{N2}\\ &= \mathbf{U}_2\mathbf{L}_2\mathbf{V}_2^{\mathrm{T}}\end{aligned} \tag{3}$$

where **N1** and **N2** denote random noise and the $\mathbf{U}_i\mathbf{L}_i\mathbf{V}_i^{\mathrm{T}}$ $(1 \le i \le 2)$ are the singular value decompositions for **M1** and **M2**.

Traditional methods of rank estimation utilize the information contained in the singular values, which appear in the diagonal matrices $\mathbf{L}_1$ and $\mathbf{L}_2$. However, there is also useful information in the eigenvectors, the columns of the $\mathbf{U}_i$ and $\mathbf{V}_i$ matrices. We will show how that information can be extracted, using the statistical technique of canonical correlations.

In the absence of noise $\mathbf{L}_1 = \mathbf{L}_2$, $\mathbf{U}_1 = \mathbf{U}_2$, $\mathbf{V}_1 = \mathbf{V}_2$, and the singular values from $k + 1$ to m are equal to zero. Furthermore, the first k columns of $\mathbf{U}$ span the same subspace of the m-dimensional space as the columns of $\mathbf{X}$ do, and the first k columns of $\mathbf{V}$ span the same subspace of the n-dimensional space as the columns of $\mathbf{Y}$ do.

In the presence of noise we expect that $\mathbf{L}_1$ and $\mathbf{L}_2$ will differ and that in each case all m singular values will be positive. However, if the noise is low, all singular values from $k + 1$ to m should be close to zero. Traditional methods for estimating k exploit this expectation by looking for a pattern in the singular values in which all those from $k + 1$ to m are near zero.

With noise we also expect differences between $\mathbf{U}_1$ and $\mathbf{U}_2$ and between $\mathbf{V}_1$ and $\mathbf{V}_2$. If the noise is low, we expect that the subspace spanned by the first k columns of $\mathbf{U}_1$ and the subspace spanned by the first k columns of $\mathbf{U}_2$ will each be close to the subspace spanned by the columns of $\mathbf{X}$, and therefore close to each other. When we include the $(k + 1)$st columns of $\mathbf{U}_1$ and $\mathbf{U}_2$, the contribution is mainly the result of noise. Since the noise matrices $\mathbf{N}_1$ and $\mathbf{N}_2$ are independent, there is no reason to expect any relationship between the directions they contribute to an eigenanalysis.

These considerations lead us to an expectation about the structure of the subspaces spanned by the first $k + 1$ columns of $\mathbf{U}_1$ and $\mathbf{U}_2$, i.e. there are k dimensions in which these two subspaces nearly coincide, but their $(k + 1)$st dimensions are nearly orthogonal. Canonical correlations (*10–12*) have an interpretation as the cosines of the angles between two subspaces. If we calculate canonical correlations between the first $k + 1$ columns of $\mathbf{U}_1$ and $\mathbf{U}_2$, we expect to see k high correlations and one low correlation. If this pattern does in fact appear in the data, it provides us with an estimate of k.

Similar statements apply to the columns of $\mathbf{V}_1$ and $\mathbf{V}_2$. We would therefore expect that an estimate of k obtained from a canonical correlation analysis of the eigenvectors of $\mathbf{M1M1}^{\mathrm{T}}$ and $\mathbf{M2M2}^{\mathrm{T}}$ would be confirmed by a canonical correlation analysis of the eigenvectors of $\mathbf{M1}^{\mathrm{T}}\mathbf{M1}$ and $\mathbf{M2}^{\mathrm{T}}\mathbf{M2}$.

This methodology might be described as rank estimation by canonical correlation analysis of matrix pairs (RECCAMP). It may be helpful to point out some of the similarities and

0003-2700/89/0361-2219$01.50/0 © 1989 American Chemical Society

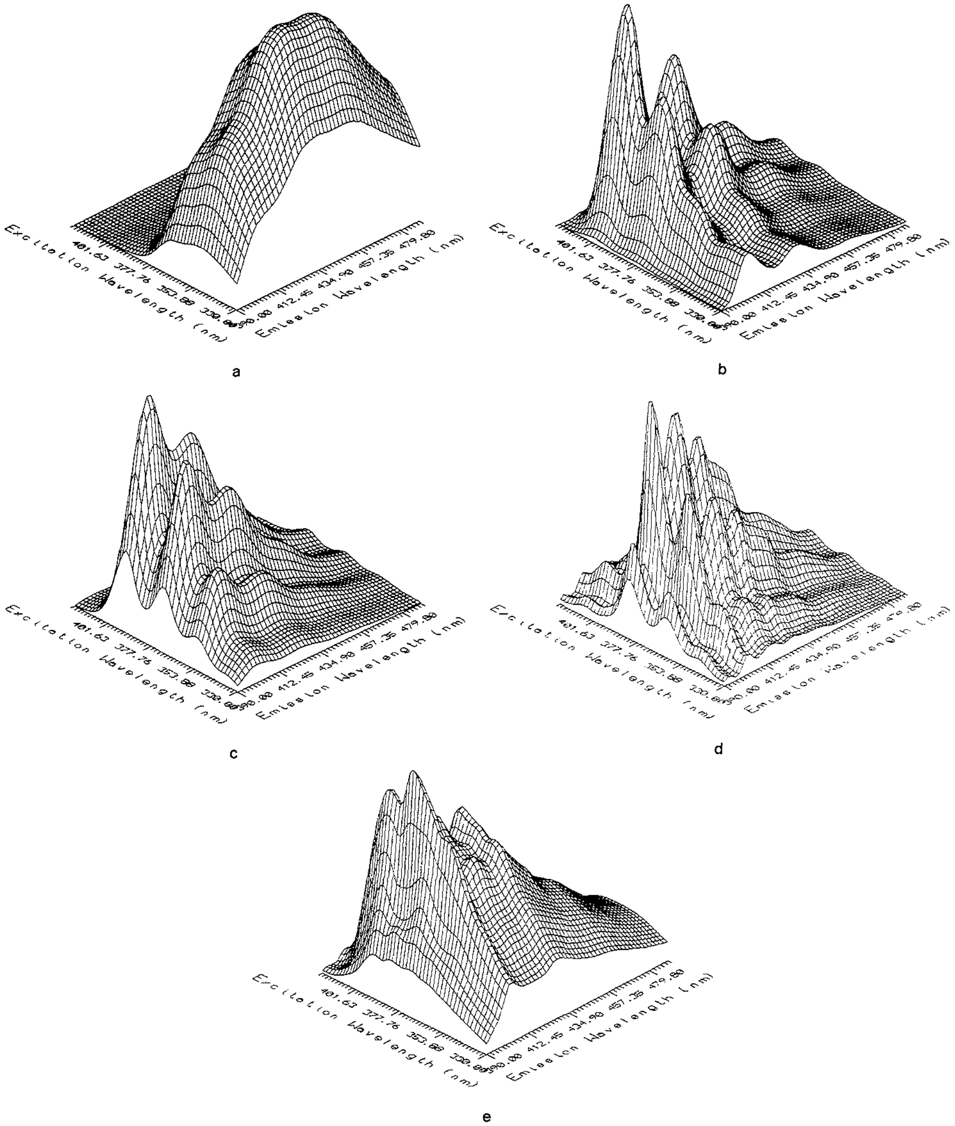

Figure 1. Plots of the noise-free EEM's for (a) B(b)F; (b) B(k)F; (c) BgP; (d) DPA, and (e) mixture of B(b)F, B(k)F, BgP, and DPA.

Table I. Uncorrected Matrix Correlations between the EEM's of the Individual Components in the Simulated Mixture

	B(b)F	B(k)F	BgP	DPA
B(b)F	1	0.364	0.538	0.45
B(k)F		1	0.742	0.816
BgP			1	0.763
DPA				1

differences between RECCAMP and GRAM, the generalized rank annihilation method (*13*, *14*), before proceeding to the next section. On the surface the methods may appear quite similar because both require two data matrices and both rely on eigenanalyses. The similarity ends there, however. GRAM is a calibration method, not a method for rank estimation. The two matrices used in GRAM need not have the same rank as long as all of the components in one of the matrices (the sample) appear also in the other (calibration or calibration + sample). It is pointless to apply GRAM to replicate measures of the same sample. By contrast RECCAMP requires that the two matrices have the same constituent components and necessarily, therefore, the same rank. It is sensible to use RECCAMP on replicate measures of the same sample.

RESULTS AND DISCUSSION

The canonical correlation technique described here was

Table II. Eigenvalues of $c^2\mathbf{S}^T\mathbf{S}$ and the Seven Leading Eigenvalues of $\mathbf{M1}^T\mathbf{M1}$, $\mathbf{M2}^T\mathbf{M2}$, and $\bar{\mathbf{M}}^T\bar{\mathbf{M}}$, Where $\bar{\mathbf{M}} = (1/2)(\mathbf{M1} + \mathbf{M2})$[a]

	eig1	eig2	eig3	eig4	eig5	eig6	eig7
			$c = 25$ $r = 0.6\%$				
$c^2\mathbf{S}^T\mathbf{S}$	6995.7	85.723	5.035	4.093			
$\mathbf{M1}^T\mathbf{M1}$	7000.2	86.043	5.068	4.275	0.179	0.152	0.1374
$\mathbf{M2}^T\mathbf{M2}$	6995.2	87.49	5.033	4.085	0.152	0.142	0.1365
$\bar{\mathbf{M}}^T\bar{\mathbf{M}}$	6997.6	86.712	5.005	4.129	0.08	0.0713	0.0706
			$c = 10$ $r = 1.7\%$				
$c^2\mathbf{S}^T\mathbf{S}$	1119.3	13.72	0.806	0.655			
$\mathbf{M1}^T\mathbf{M1}$	1121.2	13.9	0.861	0.791	0.178	0.152	0.137
$\mathbf{M2}^T\mathbf{M2}$	1119.2	14.48	0.874	0.709	0.149	0.141	0.135
$\bar{\mathbf{M}}^T\mathbf{M}$	1120.1	14.14	0.821	0.696	0.0797	0.0712	0.0702
			$c = 6$ $r = 2.9\%$				
$c^2\mathbf{S}^T\mathbf{S}$	402.95	4.938	0.290	0.2357			
$\mathbf{M1}^T\mathbf{M1}$	404.11	5.093	0.372	0.3443	0.177	0.151	0.137
$\mathbf{M2}^T\mathbf{M2}$	402.896	5.438	0.387	0.3067	0.146	0.139	0.133
$\bar{\mathbf{M}}^T\bar{\mathbf{M}}$	403.46	5.2103	0.324	0.2745	0.079	0.071	0.0695
			$c = 5$ $r = 3.5\%$				
$c^2\mathbf{S}^T\mathbf{S}$	279.83	3.43	0.201	0.1637			
$\mathbf{M1}^T\mathbf{M1}$	280.81	3.576	0.2989	0.2599	0.176	0.151	0.137
$\mathbf{M2}^T\mathbf{M2}$	279.796	3.863	0.3088	0.2402	0.1458	0.141	0.132
$\bar{\mathbf{M}}^T\bar{\mathbf{M}}$	280.26	3.664	0.2426	0.2008	0.0787	0.071	0.069
			$c = 4$ $r = 4.3\%$				
$c^2\mathbf{S}^T\mathbf{S}$	179.09	2.195	0.1289	0.1048			
$\mathbf{M1}^T\mathbf{M1}$	179.89	2.334	0.2423	0.1935	0.173	0.1493	0.136
$\mathbf{M2}^T\mathbf{M2}$	179.08	2.562	0.2493	0.1889	0.145	0.1393	0.131
$\bar{\mathbf{M}}^T\bar{\mathbf{M}}$	179.44	2.392	0.1781	0.1407	0.078	0.0708	0.0686
			$c = 3$ $r = 5.8\%$				
$c^2\mathbf{S}^T\mathbf{S}$	100.74	1.234	0.073	0.059			
$\mathbf{M1}^T\mathbf{M1}$	101.36	1.367	0.205	0.172	0.149	0.141	0.135
$\mathbf{M2}^T\mathbf{M2}$	100.75	1.536	0.209	0.155	0.143	0.138	0.131
$\bar{\mathbf{M}}^T\bar{\mathbf{M}}$	101.01	1.395	0.131	0.0978	0.075	0.0699	0.068

[a] r is calculated as the ratio of the standard deviation of the simulated normal noise to the maximum element of $c\mathbf{S}$.

applied to a four-component simulated mixture. The signal spectra were composed of four individual components obtained from the steady-state EEMs of benzo[*b*]fluoranthene [B(b)F], benzo[*k*]fluoranthene [B(k)F], benzo[*ghi*]perylene (BgP) and 9,10-diphenylanthracene (DPA). Each EEM has 50 rows and 50 columns, corresponding to excitation wavelengths from 330 to 420 nm and emission wavelengths from 390 to 490 nm. The normalized rank-one fits of these EEMs are plotted in Figure 1. The normalization condition was $Tr(\mathbf{MM}^T) = 1$, i.e. the Frobenius matrix norm $\|\cdot\|_F$ (*15, 16*). The uncorrected matrix correlations (*17*) between the EEMs for the individual components are listed in Table I. The noise-free EEM of the simulated mixture is the sum of these rank-one fits and is also plotted in Figure 1.

The data used for the simulation were obtained in the following form:

$$\mathbf{M1} = c\mathbf{S} + \mathbf{N1}, \text{ and} \qquad (4)$$

$$\mathbf{M2} = c\mathbf{S} + \mathbf{N2}$$

where S is the noise-free EEM of the mixture, c is a scalar used to control the signal-to-noise ratio, and **N1** and **N2** are simulated white noise matrices. The entries of **N1** and **N2** were generated independently from a normal distribution function with mean 0 and variance 0.001. By varying c in (4), we can also see how the methodology is affected by changes in the signal-to-noise ratio.

Any reasonable method of rank estimation will work well when the noise level is very low and poorly when the noise level is very high. To discern meaningful differences between competing methods, we must evaluate their performances at intermediate levels of noise. By simulating the noise as we have done, we can explore these critical intermediate levels of the signal-to-noise ratio. Notice, though, that our simulated noise has been applied to a signal derived from real data.

For the six selected values of c (25, 10, 6, 5, 4, and 3) the four eigenvalues of $c_2\mathbf{S}^T\mathbf{S}$ (or $c_2\mathbf{SS}^T$) and the leading seven eigenvalues of $\mathbf{M1}^T\mathbf{M1}$ (or $\mathbf{M1M1}^T$) and $\mathbf{M2}^T\mathbf{M2}$ (or $\mathbf{M2M2}^T$) are listed in Table II. These eigenvalues are the squares of the singular values of **S**, **M1**, and **M2**. The EEMs of **M1** for these values of c are plotted in Figure 2 (the EEMs of **M2** are similar to those of **M1** and therefore are not plotted).

Rank estimation based on eigenvalues (or singular values) requires only a single measured EEM, not two. If two measured EEMs are available, it is logical to average them to reduce the noise. Therefore, Table II also contains the eigenvalues obtained from $\bar{\mathbf{M}}$, the average of **M1** and **M2**.

A visual inspection of the eigenvalues in Table II shows that the selected range for c is appropriate for the rank estimation problem based on eigenvalues. At $c = 25$ the break between the fourth and fifth eigenvalues is dramatic, suggesting a confident estimate of 4 for the value of k. At $c = 3$ the break between the fourth and fifth eigenvalues is scarcely noticeable.

To implement the canonical correlation procedure, let $\mathbf{C}_1{}^i$ and $\mathbf{C}_2{}^i$ denote the subspaces spanned by the respective i leading eigenvectors of $\mathbf{M1M1}^T$ and $\mathbf{M2M2}^T$. Then, for i = 1, 2, 3, etc., calculate canonical correlations between $\mathbf{C}_1{}^i$ and $\mathbf{C}_2{}^i$. These correlations will necessarily fall in the range between 0 and 1. A correlation not significantly different from 0 is an indication that we have reached the noise. Therefore, at the ith step we test the statistical significance of the ith canonical correlation coefficient (*18, 19*). If the significance level, i.e. P value is sufficiently small, continue. If not, stop and declare $k = i - 1$. Confirm by repeating the process for $\mathbf{R}_1{}^i$ and $\mathbf{R}_2{}^i$, the subspaces spanned by the respective i leading eigenvectors of $\mathbf{M1}^T\mathbf{M1}$ and $\mathbf{M2}^T\mathbf{M2}$.

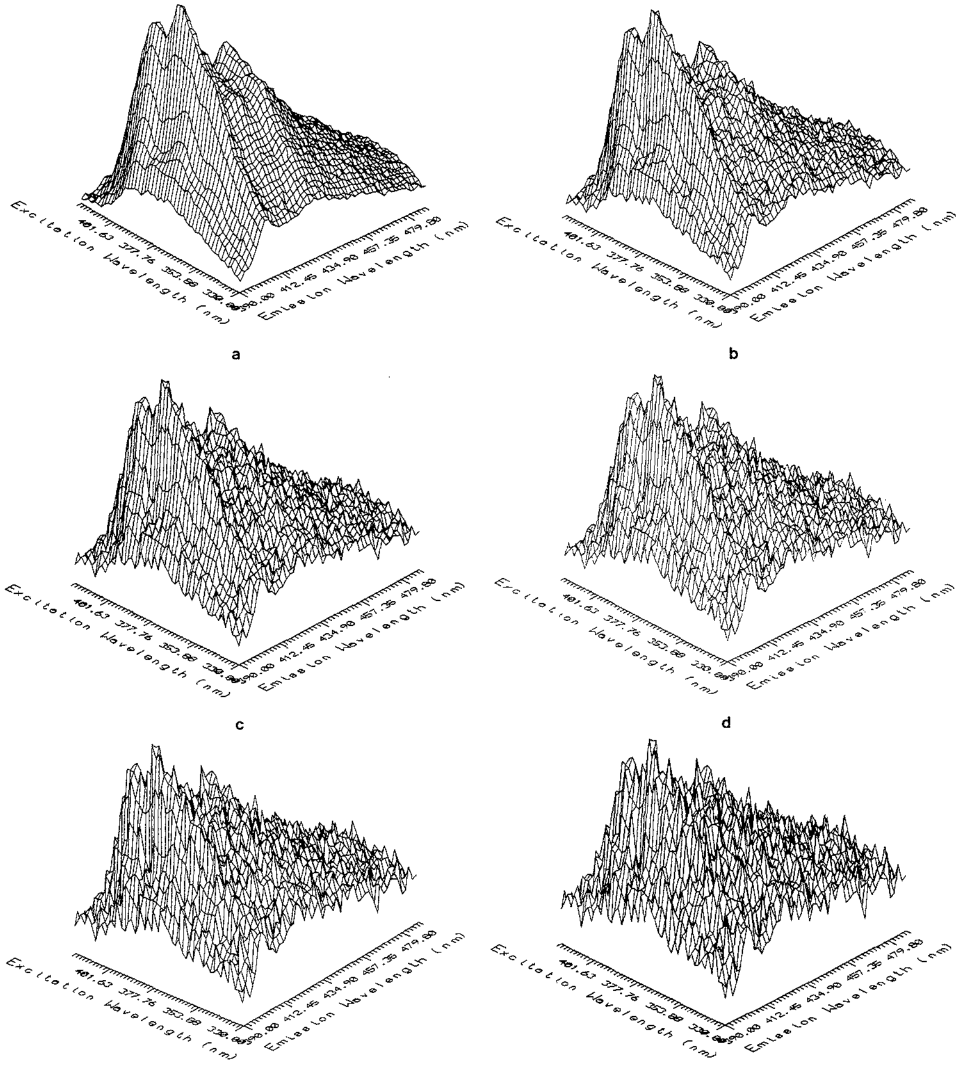

Figure 2. Plots of the noise-simulated EEM **M1** at (a) $c = 25$; (b) $c = 10$; (c) $c = 6$; (d) $c = 5$; (e) $c = 4$, and (f) $c = 3$.

These computations were performed for our simulated data using the SAS statistical program PROC CANCORR. The results for $c = 3, 4, 5$ are presented in Table III and Table IV. Exactly what significance level to use as a cutoff criterion is a fine-tuning question, the answer to which will have to wait for more experience. However, the results are clear in this example. In the general practice of statistical significance testing, the most commonly used cutoff levels for declaring "statistical significance" are 0.10, 0.05 and 0.01. If any of these are applied here the algorithm correctly identifies $k = 4$ when $c = 4$ or 5. At $c = 3$ it picks up three components and misses the fourth.

Is there any reason to continue the calculations for larger values of i once a nonsignificant results has been obtained? Again, a definitive answer will have to wait for more experience, but under certain conditions the answer may be yes. Notice that the third and fourth eigenvalues derived from the signal are not very different. When these eigenvalues are equal, or nearly so, it is possible in the presence of noise that the third canonical correlation would be insignificant at $i = 3$, but that the third and fourth canonical coefficients both become significant when we move to $i = 4$. Despite the closeness of the third and fourth eigenvalues in our example, that phenomenon did not occur in our simulation. It could still happen for some future data set. For completeness the canonical correlation calculations at $i = 6$ and $i = 7$ are included in Tables III and IV. The first seven canonical correlations for all the selected values of c are listed in Table V.

Table III. Canonical Correlations between the Column Subspaces C_2^i and C_2^i and the Corresponding P Values for the Hypothesis That the Current and the Smaller Canonical Correlations Are 0

	$c = 3$		$c = 4$		$c = 5$	
	can. corr	P value	can. corr	P value	can. corr	P value
$i = 1$	0.9996	0.0001	0.9997	0.0	0.9998	0.0
$i = 2$	0.9996	0.0	0.9997	0.0	0.9998	0.0
	0.9554	0.0001	0.9743	0.0001	0.9833	0.0001
$i = 3$	0.9996	0.0	0.9997	0.0	0.9998	0.0
	0.9585	0.0001	0.9766	0.0001	0.9850	0.0001
	0.4300	0.0020	0.6124	0.0001	0.7161	0.0001
$i = 4$	0.9996	0.0	0.9997	0.0	0.9998	0.0
	0.9601	0.0001	0.9771	0.0001	0.9852	0.0001
	0.5207	0.0059	0.7433	0.0001	0.8445	0.0001
	0.0462	0.7550	0.4708	0.0007	0.6546	0.0001
$i = 5$	0.9996	0.0001	0.9998	0.0	0.9998	0.0
	0.9606	0.0001	0.9774	0.0001	0.9853	0.0001
	0.5336	0.0706	0.7586	0.0001	0.8528	0.0001
	0.1404	0.9211	0.5195	0.0073	0.6686	0.0001
	0.0287	0.8476	0.0002	0.9987	0.0151	0.9193
$i = 6$	0.9996	0.0001	0.9998	0.0	0.9998	0.0
	0.9617	0.0001	0.9784	0.0001	0.9862	0.0001
	0.6096	0.0550	0.7770	0.0001	0.8553	0.0001
	0.3075	0.7645	0.5196	0.0773	0.6709	0.0010
	0.1722	0.8386	0.2002	0.7629	0.2026	0.7598
	0.0527	0.7276	0.0404	0.7894	0.0324	0.8304
$i = 7$	0.9996	0.0001	0.9998	0.0	0.9998	0.0
	0.9656	0.0001	0.9808	0.0001	0.9876	0.0001
	0.6482	0.1478	0.7894	0.0001	0.8656	0.0001
	0.3580	0.9022	0.5684	0.2024	0.7147	0.0049
	0.2051	0.9444	0.2196	0.9213	0.2328	0.9114
	0.1912	0.8068	0.1977	0.7827	0.1901	0.8028
	0.0257	0.8669	0.0340	0.8241	0.0398	0.7949

Table IV. Canonical Correlations between the Row Subspaces R_2^i and R_2^i and the Corresponding P Values for the Hypothesis That the Current and the Smaller Canonical Correlations Are 0

	$c = 3$		$c = 4$		$c = 5$	
	can. corr	P value	can. corr	P value	can. corr	P value
$i = 1$	0.9994	0.0001	0.9997	0.0	0.9998	0.0
$i = 2$	0.9995	0.0	0.9997	0.0	0.9998	0.0
	0.9620	0.0001	0.9787	0.0001	0.9864	0.0001
$i = 3$	0.9995	0.0	0.9997	0.0	0.9998	0.0
	0.9657	0.0001	0.9807	0.0001	0.9877	0.0001
	0.3407	0.0166	0.5482	0.0001	0.6744	0.0001
$i = 4$	0.9995	0.0	0.9997	0.0	0.9998	0.0
	0.9676	0.0001	0.9811	0.0001	0.9877	0.0001
	0.3712	0.1485	0.6268	0.0001	0.7750	0.0001
	0.0228	0.8774	0.4993	0.0003	0.6593	0.0001
$i = 5$	0.9995	0.0001	0.9997	0.0	0.9998	0.0
	0.9729	0.0001	0.9818	0.0001	0.9886	0.0001
	0.4327	0.2011	0.6556	0.0001	0.7783	0.0001
	0.2350	0.5576	0.5292	0.0049	0.6636	0.0001
	0.1026	0.4922	0.0779	0.6026	0.0468	0.7545
$i = 6$	0.9995	0.0001	0.9997	0.0	0.9998	0.0
	0.9773	0.0001	0.9866	0.0001	0.9913	0.0001
	0.4706	0.1945	0.6858	0.0001	0.7903	0.0001
	0.4174	0.3732	0.5745	0.0232	0.7071	0.0002
	0.1621	0.8439	0.1599	0.7654	0.1543	0.7918
	0.0746	0.6218	0.1273	0.3991	0.1213	0.4219
$i = 7$	0.9995	0.0001	0.9997	0.0	0.9998	0.0
	0.9820	0.0001	0.9900	0.0001	0.9937	0.0001
	0.5581	0.2062	0.7059	0.0007	0.7970	0.0001
	0.4253	0.5477	0.5875	0.0802	0.7189	0.0022
	0.2977	0.7181	0.2957	0.6909	0.2810	0.7456
	0.2178	0.6859	0.2377	0.6276	0.2335	0.6540
	0.0695	0.6497	0.0536	0.7264	0.0388	0.8002

For comparison purposes Table VI presents the results for our data from the imbedded error function and factor indicator function rank estimation methods described by Malinowski (*4, 5*). Both these methods are based exclusively on the eigenvalues. As Table VI shows, both methods correctly identify $k = 4$ when $c = 25$ or $c = 10$. At $c = 6$ the IE method misses two of the components, and at lower values of c both methods incorrectly give 2 as the value of k.

In summary, when at least two data matrices are available for linear mixtures containing the same constituents, infor-

Table V. Canonical Correlations between the Column Subspaces C_1^7 and C_2^7 and between the Row Subspaces R_1^7 and R_2^7 and the Corresponding P Values for the Hypothesis That the Current and the Smaller Canonical Correlations Are 0

column space		row space		column space		row space	
can. corr	P val	can. corr	P val	can. corr	P val	can. corr	P val
$c = 25$				$c = 10$			
1.0000	0.0	1.0000	0.0	1.0000	0.0	1.0000	0.0
0.9995	0.0	0.9997	0.0	0.9969	0.0001	0.9984	0.0001
0.9950	0.0001	0.9909	0.0001	0.9686	0.0001	0.9448	0.0001
0.9883	0.0001	0.9879	0.0001	0.9261	0.0001	0.9245	0.0001
0.2611	0.8970	0.2938	0.8641	0.2525	0.9009	0.2894	0.8443
0.1647	0.8765	0.1372	0.9371	0.1729	0.8519	0.1642	0.8835
0.0308	0.8407	0.0066	0.9654	0.0390	0.7991	0.0105	0.9451
$c = 6$				$c = 5$			
0.9999	0.0	0.9999	0.0	0.9998	0.0	0.9998	0.0
0.9914	0.0001	0.9957	0.0001	0.9876	0.0001	0.9937	0.0001
0.9092	0.0001	0.8540	0.0001	0.8656	0.0001	0.7970	0.0001
0.8005	0.0001	0.7995	0.0001	0.7147	0.0049	0.7189	0.0022
0.2406	0.9059	0.2795	0.7925	0.2328	0.9114	0.2810	0.7456
0.1845	0.8182	0.2130	0.7348	0.1901	0.8028	0.2335	0.6540
0.0420	0.7837	0.0269	0.8603	0.0398	0.7949	0.0388	0.8002
$c = 4$				$c = 3$			
0.9998	0.0	0.9997	0.0	0.9996	0.0001	0.9995	0.0001
0.9808	0.0001	0.9900	0.0001	0.9656	0.0001	0.9820	0.0001
0.7894	0.0001	0.7059	0.0007	0.6482	0.1478	0.5581	0.2062
0.5684	0.2024	0.5875	0.0802	0.3580	0.9022	0.4253	0.5477
0.2196	0.9213	0.2957	0.6909	0.2051	0.9444	0.2977	0.7181
0.1977	0.7827	0.2377	0.6276	0.1912	0.8068	0.2178	0.6859
0.0340	0.8241	0.0536	0.7264	0.0257	0.8669	0.0695	0.6497

Table VI. Values of the Imbedded Error Function (IE) and the Factor INDicator Function (IND) Calculated from the Eigenvalues of $\bar{T}^{T}\bar{M}$, Where Asterisk Indicates the Number Determined by the Respective Criterion

IE	IND	IE	IND
c = 25		*c* = 10	
0.071 452 22	0.000 549 225 7	0.029 573 8	0.000 227 322 4
0.033 220 82	0.000 195 297 7	0.016 358 37	0.000 096 167 17
0.029 432 07	0.000 153 292 1	0.016 651 65	0.000 086 727 36
0.014 836 16*	0.000 072 864 8*	0.014 822 12*	0.000 072 795 83*
0.016 207 69	0.000 077 816 7	0.016 194 21	0.000 077 751 94
0.017 387 01	0.000 083 635 9	0.017 372 44	0.000 083 565 79
0.018 341 97	0.000 090 057 3	0.018 330 81	0.000 090 002 48
c = 6		*c* =5	
0.018 839 17	0.000 144 809 5	0.016 279 75	0.000 125 136 2
0.012 901 66*	0.000 075 845 9	0.012 214 1*	0.000 071 803 95*
0.014 299 05	0.000 074 474 2	0.013 838 56	0.000 072 075 85
0.014 798 52	0.000 072 679 9*	0.014 783 17	0.000 072 604 55
0.016 171 71	0.000 077 643 9	0.016 157 43	0.000 077 575 34
0.017 347 47	0.000 083 445 6	0.017 331 64	0.000 083 369 52
0.018 310 1	0.000 089 900 8	0.018 296 46	0.000 089 833 82
c = 4		*c* = 3	
0.013 826 32	0.000 106 277 6	0.011 547 13	0.000 088 758 38
0.011 624 5*	0.000 068 377 8*	0.011 148 95*	0.000 065 542 2*
0.013 438 51	0.000 069 992 2	0.013 104 95	0.000 068 254 94
0.014 754 58	0.000 072 464 1	0.014 683 68	0.000 072 115 93
0.016 131 74	0.000 077 452	0.016 072 22	0.000 077 166 27
0.017 303 53	0.000 083 234 3	0.017 242 63	0.000 082 941 38
0.018 271 4	0.000 089 710 8	0.018 213 31	0.000 089 425 57

mation useful for rank estimation can be extracted from canonical correlations of the eigenvectors. The example presented here suggests that an algorithm incorporating canonical correlations of the eigenvectors will outperform traditional methods, but more experience is needed to fine tune the parameters of the algorithm.

LITERATURE CITED

(1) Rasmussen, G. T.; Isenhour, T. L.; Lowry, S. R.; Ritter, G. L. *Anal. Chim. Acta* **1978**, *103*, 213.
(2) Tway, P. C.; Cline Love, L. J.; Woodruff, H. B. *Anal. Chim. Acta* **1980**, *117*, 45.
(3) Gold, H. S.; Rasmussen, G. T.; Mercer-Smith, J. A.; Whitten, D. G.; Buck, R. P. *Anal. Chim. Acta* **1980**, *122*, 171.
(4) Malinowski, E. R.; Howery, D. G. In *Factor Analysis in Chemistry*; Wiley: New York, 1980.
(5) Malinowski, E. R. *Anal. Chem.* **1977**, *49*, 612.
(6) Gabriel, K. R. *Biometrika* **1971**, *58*, 453.
(7) Rossi, T. M.; Warner, I. M. *Anal. Chem.* **1986**, *54*, 810–815.
(8) Warner, I. M. In *Contemporary Topics in Analytical and Clinical Chemistry*; Hercules, D. M., Hieftje, G. M., Snyder, L. R., Evenson, M. A., Eds.; Plenum Press: New York, 1982; Vol. 4.
(9) Warner, I. M.; Neal, S. L.; Rossi, T. M. *J. Res. Natl. Bur. Stand.* (*U.S.*) **1985**, *90*, 487.
(10) Mardia, K. V.; Kent, J. T.; Bibby, J. M. *Multivariate Analysis*; Academic Press: London, 1972.
(11) Johnson, R. A.; Wichern, D. W. *Applied Multivariate Statistical Analysis*; 2nd ed.; Prentice Hall: Engelwood Cliff, NJ, 1988.
(12) Tatsuoka, M. M. *Multivariate Analysis*; John Wiley and Sons: New York, 1971.
(13) Sanchez, E.; Kowalski, B. R. *Anal. Chem.* **1986**, *58*, 496–499.
(14) Sanchez, E.; Kowalski, B. R. *J. Chemom.* **1988**, *2*, 247–263 and 265–280.
(15) Golub, G.; Van Loan, C. *Matrix Computations*; The Johns Hopkins University Press: Oxford, 1983.
(16) Stewart, G. W. *Introduction to Matrix Computations*; Academic Press: New York, 1973.
(17) Burdick, D. S.; Tu, X. M. *J. Chemom.* **1989**, *3*, 431–441.
(18) Rao, C. R. *Linear Statistical Inference*; John Wiley and Sons: New York, 1973.
(19) Kshirsagar, A. M. *Multivariate Analysis*; Marcel Dekker: New York, 1972.

Xin M. Tu
Donald S. Burdick*
Institute of Statistics and Decision Sciences
Department of Mathematics
Duke University
Durham, North Carolina 27706

David W. Millican
Linda B. McGown
Department of Chemistry
Duke University
Durham, North Carolina 27706

RECEIVED for review April 10, 1989. Accepted June 14, 1989. L. B. McGown is grateful for support for this project from the Department of Energy (Grant Number DE-FG05-88ER13931).

CORRECTION

Separation of Two Components of Horse Myoglobin by Isoelectric Focusing Field-Flow Fractionation

J. Chmelík, M. Deml, and J. Janča (*Anal. Chem.* **1989**, *61*, 912–914).

The manuscript received and accepted dates for this correspondence were inadvertently omitted on publication. The correct dates are as follows: Received for review April 11, 1988. Revised manuscript received December 30, 1988. Accepted January 17, 1989.

For Over
Six Decades...

INDUSTRIAL and ENGINEERING CHEMISTRY
ANALYTICAL CHEMISTRY
FEBRUARY 1949
analytical chemistry
Information Retrieval and Data Management
MARCH 1984
PRODUCT TAMPERING: TRACING THE SOURCE
Analytical CHEMISTRY
DECEMBER 1, 1987
ICP Still the Panacea for Trace Metals Analysis? 1345 A

The Leader in the Field.

ANALYTICAL CHEMISTRY, the world's foremost publication in the vital field of measurement science, comes to you semi-monthly packed with *more* research articles, special features and application papers.

Keeping pace with the changes has continued to make *ANALYTICAL CHEMISTRY* the pinnacle of publications in the field . . . for over 6 decades.

For your personal subscription:

CALL TOLL FREE (800) 227-5558 (U.S. only)
Outside U.S. (202) 872-4363

Telex: 440159 UI
89 2582 ACSPUBS

American Chemical Society
1155 16th St., NW
Washington, DC 20036

Determine Free Carbon, Amorphous Carbon, Graphitic Carbon, Free Moisture, Crystalline Moisture and Total Moisture with a single unit... the LECO® RC-412 Multiphase Carbon/Hydrogen/Moisture Determinator

RC - 412
CAUTION
HOT
LECO
LECO
CAUTION
HOT

- **Irons**
- **Aggregates**
- **Mold Powders**
- **Chemicals**

Today's analytical laboratory requires not only the knowledge of total carbon and moisture contents, but also the forms in which they are present. The LECO® RC-412 fills these requirements. The RC-412 couples an integral microprocessor system with menu-driven software for flexibility and ease of operation, while a resistance heated reaction chamber combined with a highly sensitive infrared detector forms the basis for carbon and moisture accuracy of ±3%.

LECO® Corporation 3000 Lakeview Avenue
St. Joseph, MI 49085-2396 U.S.A. Phone: (616) 983-5531

LECO®

CIRCLE 90 ON READER SERVICE CARD